



HAL
open science

**Background studies and design optimisation of the
SuperNEMO demonstrator module: search for $2\nu\beta\beta$ and
 $0\nu\beta\beta$ decays of ^{116}Cd into the excited states of ^{116}Sn
with NEMO-3**

Thibaud Le Noblet

► **To cite this version:**

Thibaud Le Noblet. Background studies and design optimisation of the SuperNEMO demonstrator module: search for $2\nu\beta\beta$ and $0\nu\beta\beta$ decays of ^{116}Cd into the excited states of ^{116}Sn with NEMO-3. Nuclear Experiment [nucl-ex]. Université Grenoble Alpes, 2017. English. NNT : 2017GREAY102 . tel-02127033

HAL Id: tel-02127033

<https://theses.hal.science/tel-02127033>

Submitted on 13 May 2019

HAL is a multi-disciplinary open access archive for the deposit and dissemination of scientific research documents, whether they are published or not. The documents may come from teaching and research institutions in France or abroad, or from public or private research centers.

L'archive ouverte pluridisciplinaire **HAL**, est destinée au dépôt et à la diffusion de documents scientifiques de niveau recherche, publiés ou non, émanant des établissements d'enseignement et de recherche français ou étrangers, des laboratoires publics ou privés.

THÈSE

Pour obtenir le grade de

DOCTEUR DE LA COMMUNAUTÉ UNIVERSITÉ GRENOBLE ALPES

Spécialité : **Physique Subatomique et Astroparticules**

Arrêté ministériel du 25 mai 2016

Préparée au sein de **Laboratoire d'Annecy-le-Vieux de Physique des Particules**
et de l'école doctorale de **Physique de Grenoble**

Background studies and design optimisation of the SuperNEMO demonstrator module Search for $2\nu\beta\beta$ and $0\nu\beta\beta$ decays of ^{116}Cd into the excited states of ^{116}Sn with NEMO-3

Présentée par

Thibaud LE NOBLET

Thèse dirigée par **Dominique DUCHESNEAU**
et codirigée par **Alberto REMOTO**

Thèse soutenue publiquement le **26 septembre 2017**,
devant le jury composé de :

M, Damir BUSKULIC

Professeur, USMB, LAPP - Annecy

Président

M, Claudio GIGANTI

Chargé de recherche, LPNHE - Paris

Rapporteur

M, Ruben SAAKYAN

Professor, UCL - Londres

Rapporteur

Mme, Jaime DAWSON

Chargée de recherche, APC - Paris

Examinatrice

M, Laurent SIMARD

Maître de conf, Univ. Paris-Sud / LAL - Orsay

Examineur

Mme, Edwige TOURNEFIER

Directrice de recherche, LAPP - Annecy

Examinatrice

Acknowledgments

Je ne sais pas s'il y a des mots pour décrire la sensation que l'on ressent lorsque l'on finit sa thèse. C'est un mélange de bonheur, de soulagement et de fierté, le tout mélangé à un sentiment nostalgique en se disant que, décidément, ces trois années sont décidément passées bien vite ! Bien que ce manuscrit soit écrit en anglais, je me permets ici d'utiliser le français pour remercier les personnes qui m'ont, de près comme de loin, encouragé pendant ce travail et ont participé grandement à l'améliorer.

Je tiens, dans un premier temps, à remercier chaleureusement tous les membres de mon jury, qui de par leurs questions et leurs remarques ont participé à l'amélioration de mon travail. Merci beaucoup à Claudio Giganti et à Ruben Saakyan qui ont accepté d'être les rapporteurs de ma thèse malgré la quantité de travail supplémentaire que cela représente. Merci également à Jaime Dawson et Edwige Tournefier qui ont accepté sans hésitation de faire partie de mon jury. Je remercie particulièrement Laurent Simard pour toutes les discussions que l'on a pu avoir en amont lors des réunions analyse. Elles m'ont été très utiles et m'ont permis de perfectionner des points de mon analyse. Je n'oublie pas ta gentillesse et ta bienveillance. Enfin, un grand merci à Damir Buskulic. On se connaît depuis mes premières années de licence et je suis très heureux que tu aies accepté de présider mon jury, merci pour ton enthousiasme communicatif et tes questions "naïves".

Je remercie bien évidemment le LAPP qui m'a accueilli pendant ces trois années. Ce fut un grand plaisir de faire ma thèse dans ce cadre magnifique. J'en profite pour en remercier la direction ainsi que tout le personnel administratif qui m'a bien aidé et notamment Brigitte et Myriam. Je remercie également le groupe neutrino de m'avoir si bien intégré en son sein. Un grand merci à Dominique Duchesneau, le responsable d'équipe et également mon directeur de thèse. Un immense merci à Alberto Remoto qui a encadré et guidé mon travail pendant ces trois années. Tu m'as transmis beaucoup, notamment l'exigence envers mon travail. Merci à tous les deux, j'ai beaucoup appris à vos côtés. Je remercie aussi le reste du groupe et celles et ceux qui ont fait partie ces dernières années : Isabelle, Laura, Viktoriya, Wassila, David, Henri, Jean et Pablo. Je n'oublie pas bien sûr Luis avec qui j'ai failli me faire dévorer par un ours au Canada et Anne avec qui j'ai partagé mon bureau pendant plus de deux ans. Le canapé et l'îlot central resteront certainement parmi mes meilleurs idées de ma thèse. Je remercie également tous les ingénieurs et techniciens avec qui j'ai été amené à travailler : Éric, Jean-Luc, Sophie, Richard et Thierry. Je n'oublie pas Andrea et Jean-Marc avec qui j'ai passé pas mal de temps en salle blanche. Vous avez toujours été de bonne humeur et d'excellente compagnie malgré la tâche délicate et complexe que représentait la fabrication des feuilles sources, leur grande qualité vous doit beaucoup.

Je veux aussi remercier la collaboration NEMO ainsi que celles et ceux que j'y ai croisés. Ce fût un grand plaisir de travailler à vos côtés. Merci à Cédric, Christine, Fabrice, François, Frédéric et j'en oublie sûrement, pour les moments que l'on a partagé pendant les réunions de collaborations. Merci à

l'équipe du LAL de m'avoir accueilli plusieurs fois, merci à Pia, Mathieu, Laurent (encore), Serge et les deux Xavier. Merci également à l'équipe du Texas qui m'a accueilli plusieurs semaines à Austin. J'ai beaucoup appris dans votre environnement très stimulant. Merci beaucoup à Karol de m'avoir fait venir. Merci également à Marek, Ramon et tous les autres membres de cette équipe. Merci à Shiv qui m'a fait découvrir les fêtes et la nourriture indienne. Un immense merci à John qui m'a hébergé pendant ces mois, j'ai énormément appris à tes côtés. Je n'oublierai pas le match des Spurs de San Antonio pendant Thanksgiving et la visite magique de la NASA à Houston. Je tiens aussi à remercier toutes les personnes que j'ai côtoyées pendant les semaines où j'ai participé à l'installation du détecteur (Christian, Rémi et pleins d'autres). Il me reste à remercier toutes les doctorantes et tous les doctorants que j'ai croisés pendant ces trois années. Merci à Xin pour la découverte des bars de Londres, merci à Summer, Delphine, Benjamin et Guillaume. Un grand merci à mes grosses têtes : Arnaud, Guillaume et Steven, pour nos parties de billard et nos discussions légèrement enivrés tard dans la nuit.

Je remercie également tous les amis du laboratoire (LAPP et LAPTh), doctorants, post-docs et permanents pour nos sorties et soirées. Je remercie Vincent avec qui on partage une passion commune pour les séries (les bonnes comme les mauvaises), Jordan et MÉRIL pour les matches enflammés de ping-pong. Anne (encore) qui m'a supporté surtout les derniers mois. Merci également à Éric pour les randonnées et à Nicolas le grand amateur de jeux qui m'en a fait découvrir beaucoup. Merci également à Yoann, Mathieu et Romain. Je n'oublie pas non plus les anciens : Léo et Nicolas. Merci également à mes anciens professeurs de l'université Savoie Mont-Blanc et plus particulièrement à Richard Taillet et Pierre Salati. Merci à vous tous pour ces moments partagés. J'en profite aussi pour remercier tous mes proches de m'avoir soutenu pendant cette thèse. Merci à François dont j'ai eu le plaisir d'être le témoin de mariage (déjà cette année 2017 a été bien riche). Merci à Simon qui m'a toujours soutenu et encouragé parfois pendant longues heures au téléphone. Merci également à Laure, qui malgré la distance, est toujours restée très présente dans ma vie. J'en profite pour remercier aussi toutes les personnes présentes le jour de ma soutenance.

Enfin, je termine ces remerciements en témoignant ma gratitude à ma famille pour leur soutien sans faille. Ils m'ont toujours appuyé dans mes démarches. Merci à mes parents, à mon frère et à ma sœur. Je pense également à ma grand-mère et mon oncle Manu qui m'ont fait la surprise de venir assister à ma soutenance.

Contents

Introduction	8
1 Neutrino physics	11
1.1 Neutrino history	11
1.2 Neutrino in the Standard Model	12
1.3 Neutrino mixing	13
1.3.1 Neutrino oscillation	13
1.3.2 Observation status	15
1.3.3 Summary and open questions	18
1.4 Massive neutrino	20
1.4.1 Origin of neutrino mass	20
1.4.2 Mass measurement	22
2 Double beta decay	25
2.1 Beta decay	25
2.2 Two Neutrino Double Beta Decay	27
2.3 Neutrinoless Double Beta Decay	28
2.3.1 Neutrino Mass Mechanism	29
2.3.2 Other mechanisms	31
2.3.3 Nuclear Matrix Element	34
2.4 Experimental search for $\beta\beta$ decays	36
2.4.1 Half-life sensitivity for $0\nu\beta\beta$	36
2.4.2 Maximising signal	37
2.4.3 Minimising background	37
2.5 Double Beta Experiments	38
2.5.1 Semiconductor experiments	39
2.5.2 Scintillation experiments	41
2.5.3 Bolometer experiments	43
2.5.4 Scintillating bolometer experiments	44
2.5.5 Time projection chamber experiments	44
2.5.6 Tracker-calorimeter experiments	45
2.6 Summary and status of the $\beta\beta$ researches	45

3	NEMO detectors	51
3.1	Modane underground laboratory	51
3.2	NEMO-3	52
3.2.1	Source foils	55
3.2.2	The ^{116}Cd source foil	56
3.2.3	Tracker	57
3.2.4	Calorimeter	59
3.2.5	Trigger and DAQ	61
3.2.6	Energy and time calibration	61
3.2.7	Magnetic coil and shielding	63
3.2.8	Results and measurements	64
3.3	The SuperNEMO demonstrator module	65
3.3.1	Source foils	66
3.3.2	Tracker	67
3.3.3	Calorimeter	69
3.3.4	Calibration system	70
3.3.5	Shieldings	71
3.3.6	Prospects	71
4	Source foil design optimisation	73
4.1	Source foil design	73
4.1.1	Foil geometry	74
4.1.2	Foil composition	74
4.1.3	Material radiopurity	74
4.1.4	Foil parameters	75
4.1.5	Designs under consideration	75
4.1.6	Discussion	77
4.2	Monte-Carlo simulations	78
4.2.1	Source foils modelisation	78
4.2.2	Event generation	78
4.2.3	Energy distribution	78
4.3	Sensitivity study	79
4.3.1	R.O.I method	80
4.3.2	Selection efficiency	80
4.3.3	The Feldman & Cousins 90% C.L.	83
4.3.4	1d vs 2d R.O.I. optimisation	83
4.3.5	Validation of the background level	84
4.3.6	Estimation of the systematic uncertainty	85
4.4	Source foil design and detector performance	86
4.4.1	Radio-purity vs background level	86
4.4.2	Sensitivity vs. foil designs	89
4.4.3	Optimising the amount of PVA	90
4.4.4	Foil uniformity	91
4.5	Conclusion	94

5	Radon in SuperNEMO	97
5.1	Computation of the expected activity	99
5.1.1	Activity source the foil	99
5.1.2	Activity from the tracker	100
5.2	Simulation and Reconstruction	100
5.2.1	Generation of the ^{214}Bi events	100
5.2.2	Detector response simulation	103
5.2.3	Reconstruction of the simulated events	103
5.3	Reconstruction of the α particle	104
5.3.1	The Alpha Finder algorithm	105
5.3.2	The alpha emission time t_0	106
5.4	Selection of the $1e1\alpha$ channel	107
5.4.1	$1e1\alpha$ events from the source foil	108
5.4.2	$1e1\alpha$ events from the tracker	117
5.5	Measurement	121
5.6	Results and Conclusion	123
5.6.1	Source selection	124
5.6.2	Tracker selection	125
6	Search for $\beta\beta$ decay of ^{116}Cd into the excited states of ^{116}Sn	127
6.1	Excited states of ^{116}Sn	127
6.2	Analysis technique	130
6.2.1	MC simulation	130
6.2.2	Event reconstruction	130
6.2.3	Particle identification	131
6.2.4	Time of flight information	133
6.2.5	Data set	136
6.2.6	Statistical analysis	136
6.3	Background to the search for the excited states	141
6.3.1	Internal backgrounds	141
6.3.2	External backgrounds	143
6.3.3	Background model	144
6.4	Event preselection	153
6.4.1	Signal efficiency	154
6.4.2	Number of expected background	155
6.5	Cut optimisation using a multivariate approach	157
6.5.1	Discriminating variables	157
6.5.2	Choice of the rectangular method	158
6.5.3	Reduction of the number of variables	159
6.6	Sources of systematic uncertainties	161
6.6.1	Sources of systematic uncertainties	161
6.6.2	Systematic uncertainty on the selection efficiency	163
6.7	$\beta\beta$ decay of ^{116}Cd via the excited state (2^+) of ^{116}Sn	165
6.7.1	2ν decay mode	166
6.7.2	0ν decay mode	170
6.8	$\beta\beta$ decay of ^{116}Cd via the excited state (0^+) of ^{116}Sn	172
6.8.1	2ν decay mode	173

CONTENTS

6.8.2 0ν decay mode	175
6.9 Summary	178
Conclusion	179
Bibliography	181

Introduction

Neutrinos are elementary particles of the Standard Model belonging to the lepton group and representing an important part of the matter in the Universe. Their existence has been postulated by Pauli, in 1930, to explain the conservation of energy, momentum and angular momentum in beta decay. Since their detection by Cowan and Reines in 1956, many experiments studied their properties. These searches demonstrated the existence of three neutrino flavours associated to the charged leptons which are produced by weak interaction : electron, muon and tau. These experiments also showed that neutrinos can change flavour during their propagation by a mechanism called neutrino oscillation. As the neutrinos interact only via the weak interaction, their detection and their study are very challenging and, despite the huge efforts of the neutrino community, many of their properties are still yet to be discovered.

Contrary to the other particles of the Standard Model, the neutrino mass has not been measured yet and for a long time physicists thought they were massless. Thanks to the discovery of their oscillation, which is possible only for massive neutrinos, we know now that neutrinos have a mass but the mechanism by which they acquire it is still unknown. It could be via the Higgs mechanism as for the other particles, but other theories exist such as models involving Majorana neutrinos. As they are electrically neutral, the neutrinos could be their own anti-particle (Majorana neutrinos) or their anti-particles could differ (Dirac neutrinos) from them. Since it has been proven that the neutrinoless double beta decay is possible only for Majorana neutrinos, many experiments have been designed to search for this hypothetical decay. Its observation would not only prove the Majorana nature of the neutrinos but would also give us information about the mass scale of the neutrinos. This Majorana neutrino scenario could also bring some clues to the explanation of the asymmetry between matter and antimatter observed in the Universe.

It is in this context that the NEMO experiments which are the basis of this thesis work, have been designed. The NEMO detectors provide a unique approach in the double beta field combining a calorimetric and a tracking measurement of double beta events emitted by a separated isotopic source. This feature allows for searching for double beta decays among several isotopes with good background discrimination. Furthermore, the NEMO experiments are able to measure all kinematic parameters of the event(s) which might allow to determine the process underlying the neutrinoless double beta decays.

Three main contributions have been addressed in this work : the optimisation of the SuperNEMO source, the α -finder algorithm and an analysis of the NEMO-3 data. Chapter 1 presents the description of the neutrino in the theoretical framework of the Standard Model. The neutrino oscillation phenomenon will also be discussed followed by an introduction to the theory of massive neutrino. The process of double beta decay will be presented in Chapter 2 as well as the different technologies to study this decay and a status of the different searches. Chapter 3 gives a detailed description of the NEMO-3 detector which

has been used for the analysis developed in this thesis which is the search for double beta decay of ^{116}Cd into the excited states of ^{116}Sn . In a second part, its successor SuperNEMO, which is currently under construction and based on the same technique, is also described to introduce the detector optimisation and the particle identification study performed for this thesis. In this framework, Chapter 4 presents the study realized to optimise the SuperNEMO sensitivity and the design of its source foil. The background induced by radon in the beta decay experiment will be discussed in Chapter 5. This chapter introduces the algorithm which has been developed and implemented to reconstruct and identify the alpha particles within SuperNEMO software. This alpha particle reconstruction and the identification of the $1e1\alpha$ channel will be presented to discuss the measurement of the radon contamination. Finally, Chapter 6 presents the original search for two neutrinos and neutrinoless double beta decay of ^{116}Cd via the excited states of ^{116}Sn realized with the NEMO-3 data.

Chapter 1

Neutrino physics

Important milestones in our understanding of the neutrino properties have been achieved these last decades. The discovery of their oscillation, rewarded in 2015 by the physics Nobel prize, proves that neutrinos are massive particles and that the lepton flavour is not conserved. This challenges the Standard Model and opens questions on the nature of neutrinos. The neutrino discovery and their history are briefly presented in Section 1.1. Their description in the framework of the Standard Model can be found in Section 1.2. The neutrino oscillation phenomenon is described in Section 1.3. Finally, Section 1.4 discusses the massive neutrinos and the different methods which could give access to its mass.

1.1 Neutrino history

The history of neutrino physics started in 1914 when J. Chadwick measured the energy spectrum of the electron emitted in β decay [1]. At that time, this decay was considered, as the α and γ decays, as the emission of a single particle and the observation of a continuous spectrum instead of a monoenergetic line went against the fundamental principle of the energy conservation. To solve this problem, W. Pauli proposed that a part of the energy is carried away by a second, electrically neutral, weakly interacting and very light particle [2]. To distinguish this new particle from the heavier neutron, E. Amaldi called it neutrino. This name has then been widely spread by E. Fermi during the Paris and Solvay conferences in 1932 and 1933 respectively. Twenty six years after its prediction, the neutrino has finally been discovered by Cowan and Reines with an experiment installed near a nuclear reactor [3].

In 1934, E. Fermi provided a theoretical description of the beta decay [4] in which four fermions directly interact at a common vertex. The Fermi interaction was the precursor to the theory of the weak interaction introduced by S. Glashow, A. Salam and S. Weinberg [5–7]. In these models, the electron and the neutrino are deeply linked since they are always created together. In 1936, the discovery of a second lepton flavour, the muon μ [8], suggested the existence of a second neutrino ν_μ , discovered in 1962 at Brookhaven [9]. In the same way, the detection of the lepton τ in 1975 [10] led to the ν_τ discovery in 2000 by the DONUT experiment [11]. Nowadays, thanks to the very precise measurements of the invisible width of the Z boson^a realized at CERN with the LEP collider, we know that there exist three active flavours of light neutrinos (lighter than the Z^0) as shown in Figure 1.1.

^aCorresponding to the channel decay $Z^0 \rightarrow \nu + \bar{\nu}$

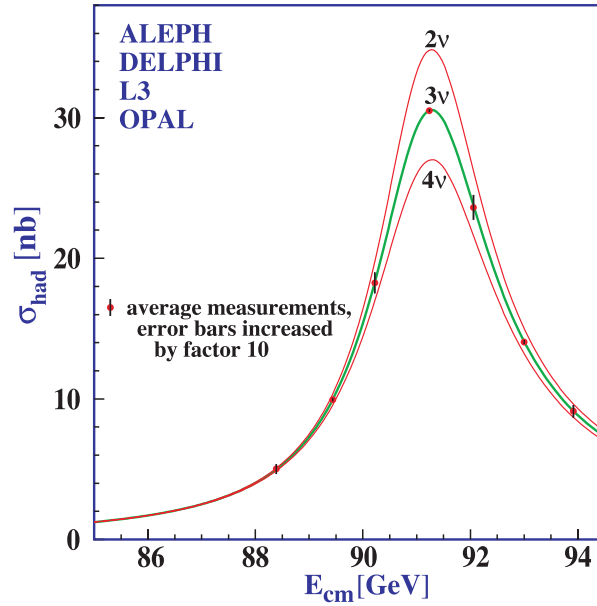


Figure 1.1: Combined LEP cross-section measurement for $e^+e^- \rightarrow \text{hadrons}$ around the Z^0 resonance. $N_\nu = 3$ is clearly favoured [12].

1.2 Neutrino in the Standard Model

The Standard Model (\mathcal{SM}) is the quantum field theory describing the fundamental constituents of the Universe and the way they interact by strong, weak and electromagnetic interactions. The theory is based on the gauge group $SU(3)_c \otimes SU(2)_L \otimes U(1)_Y$ where C,L and Y denote color, left handed chirality and weak hypercharge respectively. In the \mathcal{SM} , the constituents of matter are fermions, with spin 1/2, while the interactions are mediated by bosons, with an integer spin. As shown in Table 1.1, three generations of fermions exist. These generations have the same properties except that the particles of the third generation are heavier than the particles of the second generation themselves heavier than the particles of the first generation. The particles of the third and second generation are unstable and decay to particles of the first generation. The existence of three generations of fermions instead of less or more is not explained in the \mathcal{SM} framework.

	1 st generation	2 nd generation	3 rd generation
quarks	$\begin{pmatrix} u \\ d \end{pmatrix}_L$ u_R, d_R	$\begin{pmatrix} c \\ s \end{pmatrix}_L$ c_R, s_R	$\begin{pmatrix} t \\ b \end{pmatrix}_L$ t_R, b_R
leptons	$\begin{pmatrix} e \\ \nu_e \end{pmatrix}_L$ e_R	$\begin{pmatrix} \mu \\ \nu_\mu \end{pmatrix}_L$ μ_R	$\begin{pmatrix} \tau \\ \nu_\tau \end{pmatrix}_L$ τ_R

Table 1.1: Fermions (quarks and leptons) of the Standard Model. Three generations with the same properties except for different masses.

The strong interaction is mediated by eight massless gluons corresponding to the eight generators of $SU(3)_c$. The electroweak interaction is mediated by four bosons. Three of them are massive (W^+ , W^- and Z) corresponding to the three generators of $SU(2)_L$ and one is massless (γ) corresponding to the generator of $U(1)_Y$. The massive bosons acquire their mass through the Higgs mechanism. All the bosons have a spin 1 except the Higgs scalar boson which has a spin 0.

Quarks are the components of hadrons (baryons and mesons). They have a fractional electrical charge and are sensitive to all the interactions. They never exist as free particles except top quark which decays before hadronisation. Electron (e), muon (μ) and tau (τ) particles are negatively charged leptons which are not sensitive to the strong interaction. Finally, in the \mathcal{SM} , neutrinos are described as neutral fermions^b. Since it has been deduced from the 1958 neutrino helicity experiment that there is no right handed neutrino [13], no mass term coupling between the left and right handed component has been introduced in the \mathcal{SM} , then neutrinos are described as massless.

1.3 Neutrino mixing

In the \mathcal{SM} , neutrinos are massless and there is no mixing between the leptonic flavours since the mass eigenstates are degenerated. In the late 1960s, the Homestake experiment detected for the first time the neutrino emitted by the Sun and measured a deficit in the neutrino flux [14]. This discrepancy between the predicted and measured rates of neutrino detection has been confirmed by other experiments such as SAGE [15] or GALLEX [16] and could be explained by an oscillation phenomenon of the neutrino during its propagation. Another discrepancy between the predicted and measured atmospheric neutrino flux has also been observed [17].

The neutrino oscillation hypothesis has been confirmed at the beginning of the 2000's by the SNO [18] and SuperKamiokande experiments [19] and has been rewarded by a Nobel prize in 2015. Nowadays, the mechanism responsible for neutrino oscillation is well known and described by the theory and the experimental observations. The theoretical framework of the neutrino oscillation is introduced in Section 1.3.1. The observation status in the different sectors is summarized in Section 1.3.2. The open questions and the future of neutrino parameter measurements are introduced in Section 1.3.3.

1.3.1 Neutrino oscillation

In analogy to the $K^0 \leftrightarrow \bar{K}^0$ oscillation in quark sector, Pontecorvo postulated the possibility of the neutrino oscillation $\nu \leftrightarrow \bar{\nu}$ in 1957 [20]. After the discovery of the ν_μ , Maki, Nakagawa and Sakata proposed the possibility of oscillation among the neutrino families [21]. The mechanism of the neutrino oscillation is based on the fact, in a scenario with massive neutrino that, flavour states $|\nu_\alpha\rangle$ and mass states $|\nu_i\rangle$ do not coincide :

$$|\nu_\alpha\rangle = \sum_i U_{\alpha,i}^* |\nu_i\rangle \quad (1.1)$$

where α represents the flavours (e, μ, τ), i enumerates the mass value of the mass state (1,2,3) and U is the PMNS (Pontecorvo-Maki-Nakagawa-Sakata) unitary matrix. The free propagation of the mass eigenstates follows the Schrödinger equation and can be described by plane wave solutions of the form :

$$|\nu_i(t)\rangle = e^{-i(E_i t - p_i L)} |\nu_i(0)\rangle \quad (1.2)$$

^bNeutrinos are the only particles of matter with no electrical charge.

where E_i is the energy of the mass eigenstate i , t is the time from the start of the propagation, p_i is the momentum and L is the propagation distance. By assuming the three mass eigenstates propagate with the same momentum with relativistic energy ($p \simeq E > m$) :

$$E_i = \sqrt{p_i^2 + m_i^2} \simeq p + \frac{m_i^2}{2p} \simeq E = \frac{m_i^2}{2E} \quad (1.3)$$

Equation 1.1 can be written, using the natural units ($c = \hbar = 1$,) as :

$$|\nu_\alpha(t)\rangle = \sum_i U_{\alpha i}^* e^{-i(m_i^2/2E)L} |\nu_i(0)\rangle \quad (1.4)$$

The eigenstates propagate with different frequencies depending on their mass. By reverting Equation 1.1, the mass eigenstate $|\nu_i\rangle$ can be written as a function of the flavour eigenstate $|\nu_\beta\rangle$:

$$|\nu_\alpha\rangle = \sum_{\beta \in (e, \mu, \tau)} \left(\sum_i U_{\alpha i}^* e^{-i(m_i^2/2E)L} U_{\beta i} \right) |\nu_\beta\rangle \quad (1.5)$$

Equation 1.5 shows that a neutrino created with a flavour state α evolves as a linear superposition of the existing lepton states. The probability to observe a neutrino created with flavour α with a different flavour β after a distance L is given by :

$$\begin{aligned} P(\nu_\alpha \rightarrow \nu_\beta)(L, E) &= |\langle \nu_\beta | \nu_\alpha(L) \rangle|^2 \\ &= \sum_i |U_{\alpha i} U_{\beta i}^*|^2 + 2\mathcal{R}e \left(\sum_{i>j} U_{\alpha i} U_{\beta i}^* U_{\alpha j}^* U_{\beta j} e^{-i(\Delta m_{ij}^2/2E)L} \right) \end{aligned} \quad (1.6)$$

where $\Delta m_{ij}^2 = m_i^2 - m_j^2$ is the mass squared difference related via : $\Delta m_{12}^2 + \Delta m_{23}^2 + \Delta m_{13}^2 = 0$. In Equation 1.6, an oscillation term appears as a function of the distance between the neutrino creation point and the detection point, and the neutrino energy. The oscillation frequency is proportional to Δm_{ij}^2 while the oscillation amplitude is proportional to the PMNS matrix elements $U_{\alpha i}$:

$$U = \begin{pmatrix} c_{12} c_{13} & s_{12} c_{13} & s_{13} e^{-i\delta} \\ -s_{12} c_{23} - c_{12} s_{23} s_{13} e^{i\delta} & c_{12} c_{23} - s_{12} s_{23} c_{13} e^{i\delta} & s_{23} c_{13} \\ s_{12} s_{23} - c_{12} c_{23} s_{13} e^{i\delta} & -c_{12} s_{23} - s_{12} c_{23} s_{13} e^{i\delta} & c_{23} c_{13} \end{pmatrix} \quad (1.7)$$

where $c_{ij} = \cos \theta_{ij}$ and $s_{ij} = \sin \theta_{ij}$ with the mixing angles θ_{12} , θ_{23} and θ_{13} , and δ is a CP violation phase. The neutrino oscillation depends on 6 parameters : 3 mixing angles, 2 mass squared differences and a complex CP violation phase. For practical reasons, the mixing matrix is usually factorized in 3 matrices $M_{23} \times M_{13} \times M_{12}$:

$$U = \underbrace{\begin{pmatrix} 1 & 0 & 0 \\ 0 & c_{23} & s_{23} \\ 0 & -s_{23} & c_{23} \end{pmatrix}}_{\text{Atmospheric}} \underbrace{\begin{pmatrix} c_{13} & 0 & s_{13} e^{-i\delta} \\ 0 & 1 & 0 \\ -s_{13} e^{i\delta} & 0 & c_{13} \end{pmatrix}}_{\text{Cross-mixing}} \underbrace{\begin{pmatrix} c_{12} & s_{12} & 0 \\ -s_{12} & c_{12} & 0 \\ 0 & 0 & 1 \end{pmatrix}}_{\text{Solar}} \quad (1.8)$$

An additional matrix is added in case of Majorana neutrinos with two phases λ_1 and λ_2 but does not impact the neutrino oscillation :

$$U = M_{13} \times M_{23} \times M_{12} \times \underbrace{\begin{pmatrix} 1 & 0 & 0 \\ 0 & e^{i\lambda_1} & 0 \\ 0 & 0 & e^{i\lambda_2} \end{pmatrix}}_{\text{In case of Majorana neutrino}} \quad (1.9)$$

The matrix M_{23} is parametrized in terms of θ_{23} which is the mixing angle dominating the $\nu_\mu \rightarrow \nu_\tau$ and related to the atmospheric neutrino. The matrix M_{12} is parametrized in terms of θ_{12} which is the mixing angle dominating the $\nu_e \rightarrow \nu_{\mu,\tau}$ and related to the solar neutrinos. The matrix M_{13} is parametrized in terms of θ_{13} which is the mixing angle dominating the $\nu_\mu \rightarrow \nu_e$

1.3.2 Observation status

In order to easily understand the neutrino oscillation experimental results, we consider the case with only two active neutrinos. This case is equivalent to considering that only one squared mass splitting Δm_{ij}^2 is important compared to the others. This approximation is possible because two of the mass splittings are very close compared to the third and the mixing angle θ_{13} is small. This case is appropriate for the case of atmospheric neutrinos mixing ($\nu_\mu \rightarrow \nu_\tau$) where the ν_e plays little role and also for the solar case and for short baseline reactor antineutrino experiments. Considering two flavour states ν_α and ν_β , two mass states ν_1 and ν_2 and their difference mass splitting $\Delta m^2 = m_2^2 - m_1^2$. The mixing among the neutrino families is described by an unitary 2×2 matrix :

$$\begin{pmatrix} \nu_\alpha \\ \nu_\beta \end{pmatrix} = \begin{pmatrix} \cos \theta & \sin \theta \\ -\sin \theta & \cos \theta \end{pmatrix} \begin{pmatrix} \nu_i \\ \nu_j \end{pmatrix} \quad (1.10)$$

where θ is the rotation angle between the flavour and the mass eigenstate. The oscillation probability is then written :

$$P_{\nu_\alpha \rightarrow \nu_\beta}(L, E) = \sin^2(2\theta) \sin^2\left(\frac{\Delta m^2 L}{4E}\right) \quad (1.11)$$

this last expression can also be written using the physical units :

$$P_{\nu_\alpha \rightarrow \nu_\beta}(L, E) = \sin^2(2\theta) \underbrace{\sin^2\left(1.27 \Delta m^2 [\text{eV}^2] \frac{L[\text{km}]}{4E[\text{GeV}]}\right)}_{\phi} \quad (1.12)$$

In the limit where $\phi \ll 1$, the oscillation probability can be approximated by :

$$P_{\nu_\alpha \rightarrow \nu_\beta}(L, E) \simeq \sin^2 2\theta \left(\frac{\Delta m^2 L}{4E}\right)^2 \quad (1.13)$$

and the measurement of the oscillation probability would give information on the product $\sin^2(2\theta) \times \Delta m^2$. Given L/E , neutrino oscillation experiments then provide two parameters : the oscillation frequency Δm^2 and the mixing angle θ . Depending on the sector they are sensitive to, oscillation neutrino experiments can be classified in solar, atmospheric, reactor and accelerator experiments.

Solar neutrino

The Sun produces an important flux of electron neutrinos during the thermonuclear fusion process, 6×10^{10} neutrinos/cm²/s arrive at the surface of the Earth. The typical energy of the solar neutrino is of the order of 1-10 MeV. In the 1970s, the first observation of these neutrinos was realised by the Homestake experiment [14]. The experiment pointed out a deficit of neutrinos compared to the standard solar model prediction [22], only one third were measured. This deficit has been confirmed by other experiments such as Gallex, SAGE or Kamiokande [15, 16, 23] and was known as the solar neutrino problem. In 2001, the SNO experiment (Sudbury Neutrino Observatory) used a heavy water detector allowing the detection of the three neutrino flavours and proved that the deficit is consistent with the neutrino flavour mixing [18].

The solar sector have also been studied by the KamLAND experiment located in the Kamioka mine in Japan [23]. The KamLAND experiment detects $\bar{\nu}_e$ from nuclear reactor around the Kamioka mine at a mean distance of 180 km. KamLAND showed that to explain all the neutrino deficit of solar neutrinos, the oscillation in vacuum is not enough and that there is an important effect of neutrino oscillation in matter called MSW effect [24]. Combining KamLAND results with different solar experiments, the actual values of the parameters in the solar sector have been determined [25] :

$$\begin{aligned}\Delta m_{21}^2 &= 7.53 \pm 0.18 \times 10^{-5} \text{ eV}^2 \\ \sin^2 \theta_{12} &= 0.307 \pm 0.013\end{aligned}\tag{1.14}$$

Atmospheric neutrino

The interaction of cosmic rays with the atmosphere of the Earth can produce hadronic showers containing pions and kaons. The decays of these particles create high energy muons and muon neutrinos. Muons at low energy (< 1 MeV) decay before hitting the Earth's surface into electron, ν_e and ν_μ :

$$\begin{aligned}\pi^\pm &\rightarrow \mu^\pm + \nu_\mu (\bar{\nu}_\mu) \\ \mu^\pm &\rightarrow e^\pm + \nu_e (\bar{\nu}_e) + \bar{\nu}_\mu (\nu_\mu)\end{aligned}\tag{1.15}$$

At these energies, we expected to detect twice as much ν_μ ($\bar{\nu}_\mu$) than ν_e ($\bar{\nu}_e$) [26]. Some experiments measured a deficit of ν_μ giving origin to the so called atmospheric neutrino anomaly [27]. Several interpretations have been proposed to solve this anomaly such as Lorentz invariance violation, flavor changing neutral currents or neutrino oscillations. In 1998, the SuperKamiokande experiment, successor of the Kamiokande detector, confirmed the deficit and demonstrated its dependance on the zenith angle as shown in Figure 1.2. In an underground detector as SuperKamiokande the flux of neutrinos going up is expected to be the same as the neutrino going down because the neutrino flux produced in the atmosphere is expected to be isotropic. In Figure 1.2, sub-GeV ν_e have almost no dependance on the zenith angle while the flux of down going ν_μ is higher than the up going neutrino at sub-GeV scale. These results can be interpreted in terms of oscillations : up-going ν_μ are produced at opposite side of the Earth and travelled around 12 000 km more than the down-going ν_μ . It seems that these up-going ν_μ disappear during their propagation while no disappearance of ν_e has been found. This is interpreted as an oscillation of the ν_μ into ν_τ [28].

The hypothesis of neutrino oscillation $\nu_\mu \rightarrow \nu_\tau$ have been confirmed by disappearance experiment measurements such as K2K or MINOS [29, 30]. These experiments studied the ν_μ flux created by an accelerator with a near and a far detector. The near detector allows the measurement of the ν_μ flux going to the far detector. With the knowledge of their energy and the distance between the near and far detector, the oscillation parameters can be extracted. To definitely confirm the $\nu_\mu \rightarrow \nu_\tau$ oscillation, the OPERA experiment searched and found the ν_τ appearance in a pure ν_μ beam [31]. The global fit concerning the parameters in the atmospheric sector have been determined to be :

$$\begin{aligned}\Delta m_{23}^2 &= 2.45 \pm 0.05 \times 10^{-3} \text{ eV}^2 \\ \sin^2 \theta_{23} &= 0.51 \pm 0.04\end{aligned}\tag{1.16}$$

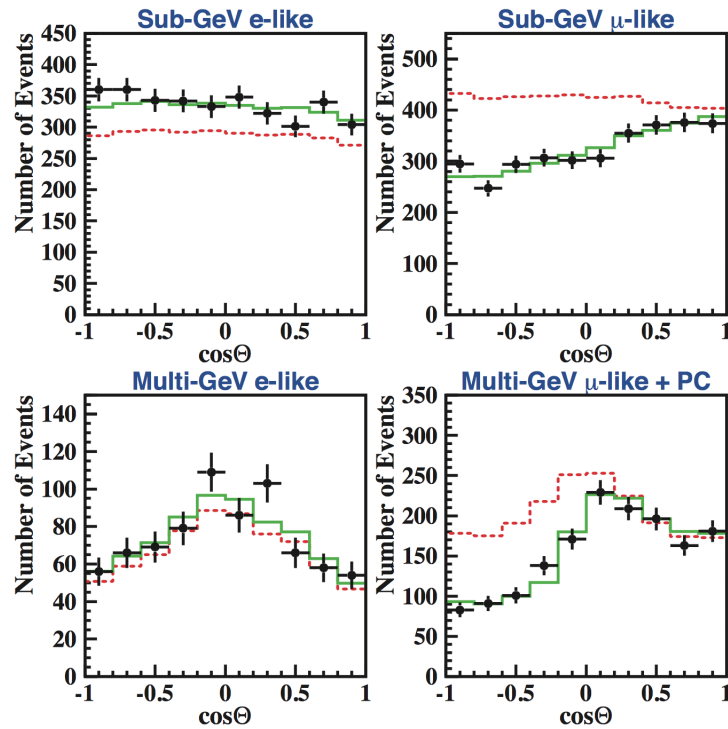


Figure 1.2: Angular distributions of the electron and muon neutrinos produced in the atmosphere measured by SuperKamiokande. The ν_μ neutrino rate presents a clear deficit for the neutrinos crossing the Earth ($\cos \theta < 0$) compared to the predicted flux without no oscillation (red line) [19].

Reactor neutrino

Nuclear reactors are a very intense source of neutrinos. An important part of elements created during the uranium fission decay by β decay leading to a continuous $\bar{\nu}_e$ flux with an energy of the order of MeV. A 1 GW reactor emits around 10^{20} neutrinos/s.

The $\bar{\nu}_e$ oscillation to $\bar{\nu}_\mu$ and $\bar{\nu}_\tau$ can only be measured by the disappearance of the $\bar{\nu}_e$ since the energy is not high enough for the μ and τ creation. Generally the detection of the $\bar{\nu}_e$ is realized by inverse beta decay reaction ($\bar{\nu}_e + p \rightarrow n + e^+$). The coincidence detection of the photons emitted by the positron annihilation and by the neutron capture allows to identify the $\bar{\nu}_e$ interaction in the detector. The first detection of the neutrino in 1956 used this technique which is still used today such as in the KamLAND and the DayaBay experiments [32, 33]. Figure 1.3 shows the oscillation survival probability versus L_{eff}/E_ν .

Reactor neutrino experiments allow the measurement of the Δm_{13}^2 and θ_{13} parameters. Moreover the Δm_{13}^2 parameter can be constrained from atmospheric and accelerator neutrino experiments. The global fit gives :

$$\begin{aligned} \Delta m_{13}^2 &= 2.45 \pm 0.05 \times 10^{-3} \text{eV}^2 \\ \sin^2 \theta_{13} &= 0.021 \pm 0.0011 \end{aligned} \quad (1.17)$$

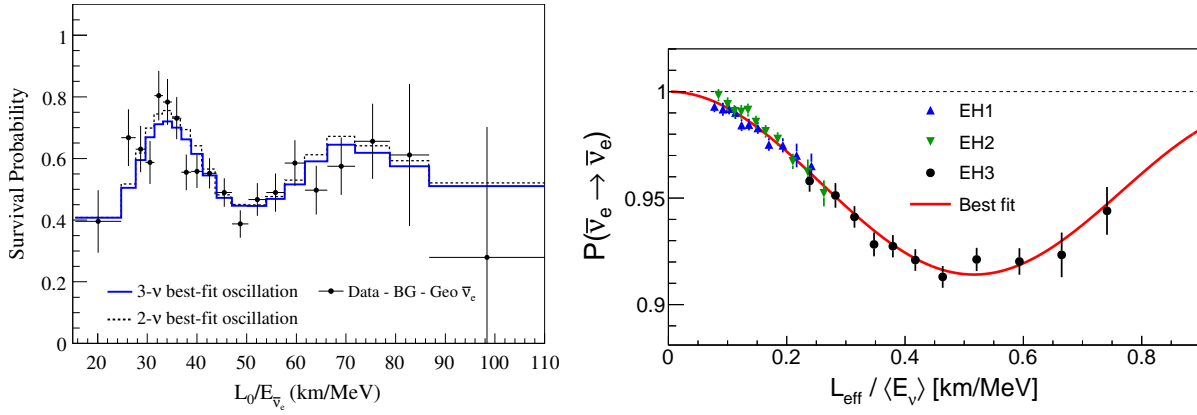


Figure 1.3: Measured reactor $\bar{\nu}_e$ spectral distortion displayed as the oscillation survival probability versus L_{eff}/E_{ν} . Left results from KamLAND [32]. Right : results from DayaBay [33].

Accelerator neutrino

Particle accelerators are used as a source of artificial neutrinos, mainly ν_{μ} . The advantage is that the characteristics of the neutrino beam are well known and can be adapted (energy and $\nu/\bar{\nu}$). To create the ν_{μ} (or $\bar{\nu}_{\mu}$) beam, the principle is to send a proton beam on a target to produce hadrons (pions, kaons,...) which then decay mainly into μ and ν_{μ} . A detector is placed hundred kilometers away to measure the ν_{μ} disappearance or the $\nu_{e,\tau}$ appearance. It has existed and there are still many neutrino accelerator experiments around the world such as MiniBooNE, MINOS, T2K or No ν A. I will not discuss all of them here, their physics program is very wide including the measurement of the mixing angle θ_{13} , the determination of the CP-violating phase, mass ordering or search for sterile neutrinos. One of the previous experiments, OPERA, found 5 ν_{τ} events, after 5 years of data taking confirming the $\nu_{\mu} \rightarrow \nu_{\tau}$ oscillation [31, 34].

1.3.3 Summary and open questions

The neutrino oscillation phenomenon has been studied by many experiments and is fairly well understood by the theory and experiments. The measurement of the three mixing angles are more and more precise and are known today with a precision less than 10%. The two squared mass splittings have also been measured. Future neutrino experiments will focus mainly on the determination of the missing oscillation parameter δ_{CP} and of the sign of the Δm_{31}^2 . Other experiments also investigate the possibility of the existence of sterile neutrinos.

CP violation phase

The last oscillation parameter which is not yet measured is the CP violating phase δ_{CP} . The measurement of this parameter is motivated since it can demonstrate a difference in the behaviour between the neutrino and antineutrino which could explain the matter/antimatter asymmetry in the Universe. The T2K and Nova experiments could reach a sensitivity of 2-3 σ on δ_{CP} after 10 years [35]. The future long baseline experiments such as DUNE or HyperKamiokande should determine this parameter with improved sensitivities in the coming 20 years [36, 37].

Mass ordering

Neutrino oscillations provide information on the mass squared differences and do not allow to access to their mass. Thanks to solar neutrino measurements Δm_{21}^2 has been determined to be positive but we still do not know the sign of Δm_{31}^2 . Two cases are then possible as shown in Figure 1.4, if $\Delta m_{31}^2 > 0$ we talk about normal ordering (or normal hierarchy), if $\Delta m_{31}^2 < 0$ we talk about inverted ordering (or inverted hierarchy). Some experiments are planned in the future to determine the neutrino mass ordering such as JUNO, PINGU or KM3NeT [38–40]. The determination of the neutrino mass ordering is important since it strongly impacts the neutrinoless double beta decay searches and the measurements of δ_{CP} .

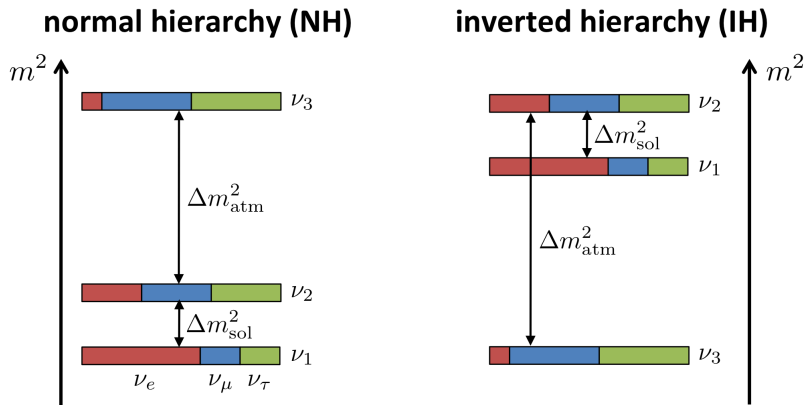


Figure 1.4: Neutrino mass ordering : on the left the normal ordering where $\Delta m_{31}^2 > 0$. On the right the inverted ordering where $\Delta m_{31}^2 < 0$.

Sterile neutrino

Despite the success of the three flavour oscillation theory, some small anomalies in short baseline neutrino experiments have been highlighted which can not be explained in the three neutrino framework. These anomalies could suggest that the theory is incomplete and could point out the existence of sterile neutrinos.

During the development of the last generation of reactor neutrino experiments, the $\bar{\nu}_e$ flux have been reevaluated [41, 42]. A total deficit of approximately 7% has been found between the updated predicted flux and the flux measured by different experiments [43]. This discrepancy is called the reactor antineutrino anomaly [44].

Another anomaly has been measured by the GALLEX [16] and SAGE [15] experiments. These experiments were calibrated with ^{51}Cr and ^{37}Ar sources put inside the detector. The monoenergetic ν_e produced by these sources were detected by their interaction with ^{71}Ga forming ^{71}Ge . A deficit between the measured and the predicted event rates has been found corresponding to a 2.8σ deviation [45]. This anomaly is called gallium anomaly.

In addition to these two anomalies a last one coming from the LSND experiment has been highlighted. This experiment measured an excess of 3.8σ of $\bar{\nu}_e$ events in a beam of ν_μ produced by μ^+ decays [46]. To explain all these anomalies, the existence of a sterile neutrino has been postulated. The best fit values

for the oscillation parameters suggest $\Delta m^2 > 1.5 \text{ eV}^2$ and $\sin^2 2\theta = 0.14 \pm 0.08$ [44]. Experiments are currently running or under construction to exclude or confirm the existence of a light sterile neutrino such as STEREO [47], Solid [48] or SOX [49]. First results should arrive in the coming months.

1.4 Massive neutrino

The observation of neutrino oscillations proves that neutrinos are massive particles which is in direct conflict with their description in the current form of the \mathcal{SM} . The origin of their mass is believed as a low energy manifestation of physics beyond \mathcal{SM} . Section 1.4.1 describes the mechanisms which can give a mass to the neutrino while Section 1.4.2 discusses the different ways which could allow us to measure it.

1.4.1 Origin of neutrino mass

The origin of the neutrino mass has been subject to intense theoretical and experimental investigations. To introduce the neutrino into the \mathcal{SM} , two different types of neutrino mass terms are possible : Dirac and Majorana.

Dirac mass term

A straightforward way to generate a neutrino mass is to use the same Higgs mechanism that gives mass to quarks and charged leptons. In this scenario, the existence of a right handed neutrino has to be postulated. To agree with experimental observations, these right handed neutrinos can not couple to the weak interaction and are called sterile [50]. The Dirac mass term is written as :

$$\mathcal{L}_{\text{mass}}^{\text{D}} = -m_{\text{D}}(\bar{\nu}_{\text{R}} \nu_{\text{L}} + \bar{\nu}_{\text{L}} \nu_{\text{R}}) \quad (1.18)$$

where ν_{R} and ν_{L} are the right and left handed chiral fields for the neutrino and m_{D} is the Dirac mass matrix which can be expressed for the component k in terms of the Yukawa coupling λ_k^ν and the vacuum expectation value v :

$$m_k = \frac{\lambda_k^\nu v}{\sqrt{2}} \quad (1.19)$$

Dirac neutrinos acquire their mass by coupling to the Higgs field and their mass is proportional to v . The main problem of this mechanism is that it does not explain the huge order of magnitude difference between the charged lepton and neutrino masses. There are four distinct fields in Equation 1.18 which implies that neutrino and anti-neutrinos are fundamentally different particles.

Majorana mass term

Another way to introduce a mass term into the \mathcal{SM} is through a Majorana mass term. This term has been proposed for the first time in 1937 by Ettore Majorana [51]. It consists of introducing a Majorana field defined such that $\mathcal{C}|\psi\rangle = |\psi\rangle$ implying there is no distinction between particle and anti-particle. This type of mass term is only possible for electrically neutral particles such as neutrinos. For a fermion field ($\psi = \psi_{\text{L}} + \psi_{\text{R}}$), the Dirac equation $(i\gamma^\mu \partial_\mu)\psi = 0$ is equivalent to the coupled equations [52] :

$$i\gamma^\mu \partial_\mu \psi_{\text{L}} = m\psi_{\text{R}}$$

$$i\gamma^\mu \partial_\mu \psi_{\text{R}} = m\psi_{\text{L}}$$

The equations are coupled by their mass term, but in case of massless field :

$$\begin{aligned} i\gamma^\mu \partial_\mu \psi_L &= 0 \\ i\gamma^\mu \partial_\mu \psi_R &= 0 \end{aligned} \quad (1.20)$$

the equations are not coupled and we have the so-called Weyl equations with ψ_L and ψ_R the Weyl spinors. As discussed in Section 1.2, the neutrino in the \mathcal{SM} was massless and then was described by left handed Weyl spinor ν_L . Majorana wondered if it is possible to make a right handed field from a left handed one to form a mass term [51]. In the case Majorana studied, we want to obtain the first equation of 1.20 from the second one. In order to do that, the Hermitian conjugate of the second equation is taken :

$$-i\gamma^\mu \partial_\mu \overline{\psi_R} = m\overline{\psi_L} \quad (1.21)$$

Then the transverse of the Equation 1.21 is taken and using the property of the charge conjugation matrix $\mathcal{C}\gamma^{\mu T} = -\gamma^\mu \mathcal{C}$:

$$i\gamma^\mu \partial_\mu \mathcal{C}\overline{\psi_R}^T = m\mathcal{C}\overline{\psi_L}^T \quad (1.22)$$

Equation 1.22 has the same structure as the first equation of 1.20, and they are identical if :

$$\psi_R = \xi \mathcal{C}\overline{\psi_L}^T \quad (1.23)$$

with ξ an arbitrary phase factor. Equation 1.23 is the Majorana relation between the ψ_L and ψ_R . The Dirac equation can then be written only in terms of ψ_L :

$$\psi = \psi_L + \psi_R = \psi_L + \mathcal{C}\overline{\psi_L}^T \quad (1.24)$$

implying :

$$\psi^c = (\psi_L + \mathcal{C}\overline{\psi_L}^T)^c = \psi \quad (1.25)$$

Equation 1.25 is called the Majorana condition and implies that a Majorana particle is its own antiparticle. This condition can only be satisfied by a neutral particle since the charge conjugation operator flips the sign of the electric charge. The only fermions that can be Majorana particles are neutrinos. In case of Majorana neutrino, the mass term is written as :

$$\mathcal{L}_{\text{mass}}^M = -\frac{1}{2} m_\nu^M \overline{\nu_L^c} \nu_L + h.c \quad (1.26)$$

As Majorana mass term couples neutrinos to antineutrinos, interactions involving Majorana neutrino violate lepton number conservation by two units.

See-saw mechanism

The see-saw mechanism requires Majorana neutrinos. Based on the Majorana description given in Equation 1.25, two independent fields, which are their own conjugate, can be introduced [53, 54] :

$$\lambda = \frac{\chi_L + (\chi_L)^c}{\sqrt{2}} \quad \Lambda = \frac{\chi_R + (\chi_R)^c}{\sqrt{2}} \quad (1.27)$$

The mass term in the Lagrangian can be written in its more general form :

$$-\mathcal{L}_m = m_L \bar{\lambda} \lambda + m_R \bar{\Lambda} \Lambda + m_D (\bar{\lambda} \Lambda + \lambda \bar{\Lambda}) \quad (1.28)$$

which can also be written in a matrix form as follows :

$$-\mathcal{L}_m = (\bar{\lambda} \ \bar{\Lambda}) \mathcal{M} \begin{pmatrix} \lambda \\ \Lambda \end{pmatrix}, \quad \mathcal{M} = \begin{pmatrix} m_L & m_D^T \\ m_D & m_R \end{pmatrix} \quad (1.29)$$

The fields λ and Λ defined in Equation 1.27 do not have a definite mass because of the non diagonal m_D terms in the mass matrix. These fields are not mass eigenstates and are not physical particles. If we have mass eigenstates ν_1 and ν_2 , the Lagrangian can be written in terms of these mass eigenstates. The \mathcal{M} matrix can be diagonalized by using an unitarity matrix \mathcal{U} :

$$\mathcal{U}^\dagger \mathcal{M} \mathcal{U} = \mathcal{M}' \quad , \quad \mathcal{M}' = \begin{pmatrix} m_1 & 0 \\ 0 & m_2 \end{pmatrix} \quad (1.30)$$

where the masses m_1 and m_2 can be expressed in terms of m_D , m_L and m_R :

$$m_{1,2} = \frac{1}{2} \left[(m_L + m_R) \pm \sqrt{(m_L - m_R)^2 + 4m_D^2} \right] \quad (1.31)$$

As the SM forbids the left handed Majorana term, the mass m_L can be set to 0. With this choice and making the assumption that $m_R \gg m_D$:

$$m_{1,2} = \frac{m_R}{2} \left[1 \pm \sqrt{1 + 4 \frac{m_D^2}{m_R^2}} \right] \simeq \begin{cases} m_R & \text{for heavy neutrino} \\ -m_D^2/m_R & \text{for light neutrino} \end{cases} \quad (1.32)$$

The see-saw mechanism has the advantage to naturally explain the tiny mass of active neutrinos. Indeed, as the mass of the right neutrino is not constrained, a very heavy right handed neutrino can be considered leading to a very small mass for the neutrino.

1.4.2 Mass measurement

The absolute mass scale of the neutrino is an important open question in neutrino physics but also in astrophysics and cosmology. The neutrino oscillation experiments are used to measure the different oscillation parameters but do not give access to the neutrino mass. Other experiments are required to determine or set limits on the neutrino mass value such as the precise measurement of the β spectrum at the end-point. Cosmology can also bring information on the neutrino mass. Furthermore, we will also see in Chapter 2 that the neutrinoless double beta decay experiments can bring information on the neutrino mass scale.

Direct neutrino mass from β decay

A direct measurement of the neutrino mass is possible by a precise study of the β decay kinematic. The energy released in the decay is shared between the electron and the antineutrino. The energy spectrum of the electron is given by :

$$\frac{dN}{dE} \propto p(E + m_e^2)(Q - E) \sqrt{(Q - E)^2 - m_{\bar{\nu}_e}^2} c^4 \quad (1.33)$$

where p , m_e and E are the momentum, mass and energy of the electron, Q is the end point energy and $m_{\bar{\nu}_e}$ is the antineutrino mass defined as the incoherent sum of neutrino mass eigenstates :

$$m_{\bar{\nu}_e} = \sum_{i=1}^3 U_{ei}^2 m_i^2 \quad (1.34)$$

The end point of the electron energy spectrum is distorted depending on the neutrino mass as shown in Figure 1.5. In this region, the number of expected events is very low and can be maximised by using a β emitter with a low Q. With a Q of 18.6 keV and an half-life of 12.3 y, tritium is one of the best candidates. It has been investigated in the past by the Mainz and Troitz experiments which have set limits of 2.3 eV and 2.1 eV on $m_{\bar{\nu}_e}$ respectively [55, 56]. The KATRIN experiment expects to reach a sensitivity of 0.2 eV [57].

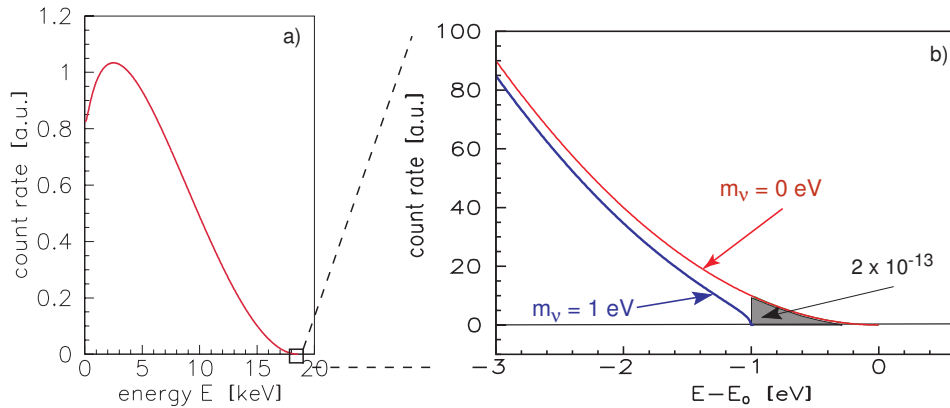


Figure 1.5: Left : full electron energy spectrum in tritium β decay. Right : region around the end point, the case of a massless neutrino is represents in red. The blue curve shows the spectrum in presence of a 1 eV neutrino. [57]

By respectively studying the π and τ decays, upper limits on the ν_μ and ν_τ masses can be set. These limits are less stringent than those obtained by β decay. The best limits obtained today have been set by the PSI and the ALEPH experiments [58, 59] :

$$\begin{aligned} m_{\nu_\mu} &< 0.17 \text{ MeV} \\ m_{\nu_\tau} &< 18.2 \text{ MeV} \end{aligned} \quad (1.35)$$

Cosmology

Due to their huge abundance in the Universe, neutrinos and their mass play a role in its evolution. Neutrinos contribute to the mass density of the Universe [60, 61]. Cosmology can set limit on the total mass of neutrinos ($\sum m_\nu$) by studying how they affect the shape of the matter power spectrum of the Cosmic Microwave Background (CMB). The best and most recent limit on $\sum m_\nu$ has been reported by the Planck collaboration [62]:

$$\sum m_\nu < 0.23 \text{ eV} \quad (1.36)$$

Chapter 2

Double beta decay

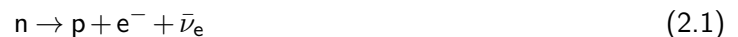
Since the prediction of the neutrino in 1930 and their first detection in 1956, many studies have been carried out to understand their properties. One of the most important achievements is the discovery of their oscillations, proving their non-zero mass which is a first indication of physics beyond the Standard Model. There are still remaining questions in neutrino physics including their nature and how they acquire their masses. Since it has been proven that the neutrinoless double beta decay necessarily involves Majorana neutrinos, the search for this hypothetical decay is one of the most active research topics in neutrino physics. Its observation may also give access to their absolute mass scale.

Some elements on simple beta decay and double beta decay are respectively introduced in Sections 2.1 and 2.2. The neutrinoless double beta decay is discussed in Section 2.3 and their experimental search in Section 2.4. The different double beta decay experiments and the status of the searches are respectively presented in Section 2.5 and 2.6.

2.1 Beta decay

Beta decay is a radioactive decay which transmutes a nucleus into a different one. This decay is mediated by the weak interaction and is always accompanied by a neutrino or antineutrino emission. Beta decays have been sorted in three categories :

β^- **decay**, in which a neutron converts into a proton with the emission of an electron and an antineutrino :



β^+ **decay**, in which a proton converts into a neutron with the emission of a positron and a neutrino :



Electron capture (EC), in which an atomic electron is captured by its nucleus, resulting in the emission of a single neutrino :



Note that there is a competition between the β^+ decay and the electron capture processes. In case the β^+ decay is forbidden or highly suppressed, the electron capture is the only way for a nucleus to become more stable. After an electron capture, a hole appears in the atomic orbital and the reorganisation

of the remaining electrons is accompanied by a cascade of photons and/or Auger electrons. From a kinematic point of view, the released energy in β^\pm decays is shared between the β -particle and the neutrino or the antineutrino while, in electron captures, the emitted neutrino carries away all the released energy. The β^\pm decays can only occur if the mass of the daughter nucleus, $\mathcal{M}(A, Z_f)$, is lower than the mother nucleus, $\mathcal{M}(A, Z_i)$, where A is the number of nucleons and Z is the atomic number. The mass of an atomic nucleus is given by :

$$\mathcal{M}(A, Z) = Zm_p + (A - Z)m_n - E_B \quad (2.4)$$

where m_p is the mass of the proton, m_n is the mass of the neutron and E_B is the binding energy of the nucleus which can be estimated with the semi-empirical mass formula also called Bethe–Weizsäcker formula [63] :

$$E_B = a_v A - a_s A^{2/3} - a_c \frac{Z^2}{A^{1/3}} - a_A \frac{(A - 2Z)^2}{A} + \delta(A, Z) \quad (2.5)$$

where $a_v A$ is known as the volume term. It represents the interaction of a nucleon with its nearest neighbors via the strong nuclear force. It is proportional to A and does not depend on Z . The surface term, $a_s A^{2/3}$, also based on the strong interaction, is a correction to the volume term. It takes into account the fact that the nucleons on the surface of the nucleus have fewer nearest neighbors to interact with compared to the nucleons located inside the nucleus. The third term, $(a_c Z^2)/A^{1/3}$, known as the Coulomb term, takes into account the electrostatic repulsion between protons. The fourth term, $a_A(A-2Z)^2/A$ is the asymmetry term. Based on the Pauli exclusion principle, this term has been added to take into account the asymmetry between the number of protons and neutrons in the nucleus. This term is equal to zero when a nucleus has the same number of protons and neutrons. The last term δ which is called pairing term, takes into account the effect of spin-coupling. Indeed, due to the Pauli exclusion principle, the energy of a nucleus is minimised in the case the number of protons with spin up is equal to the number of protons with spin down. As it is similar for the neutron the pairing term is written :

$$\delta(A, Z) = \begin{cases} +\delta_0 & \text{if } A \text{ is even : } Z \text{ and } (A - Z) \text{ even} \\ 0 & \text{if } A \text{ is odd} \\ -\delta_0 & \text{if } A \text{ is even : } Z \text{ and } (A - Z) \text{ odd} \end{cases} \quad (2.6)$$

Finally, by combining Eq 2.4 and Eq 2.5, the mass of an atomic nucleus can be written as :

$$\mathcal{M}(A, Z) = Zm_p + (A - Z)m_n - a_v A + a_s A^{2/3} + a_c \frac{Z^2}{A^{1/3}} + a_A \frac{(A - 2Z)^2}{A} + \delta(A, Z) \quad (2.7)$$

It can be deduced from 2.7 that at a given A , parabolic curves are generated as a function of Z and provide which β decays are energetically allowed or forbidden. In case A is odd, only one curve exists, but for an even A , two curves exist split by the pairing term as shown in Figure 2.1. It can also be seen that the β^- decays $^{82}\text{Ge} \rightarrow ^{82}\text{As}$ and $^{82}\text{As} \rightarrow ^{82}\text{Se}$ are energetically allowed while the β^- decay $^{82}\text{Se} \rightarrow ^{82}\text{Br}$ is forbidden.

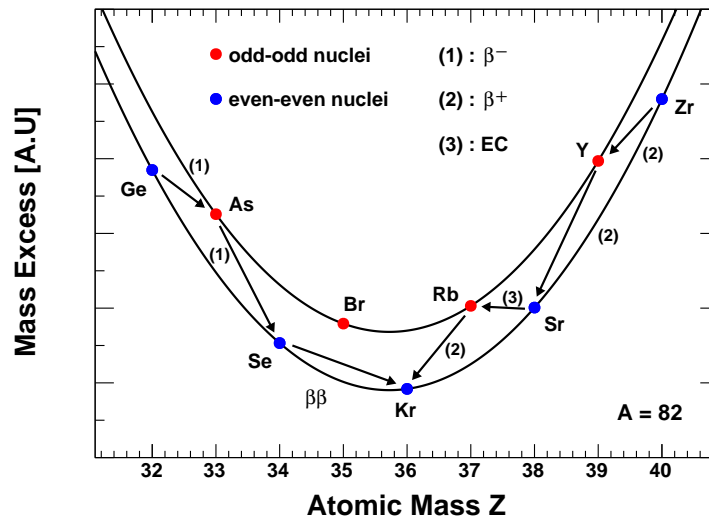
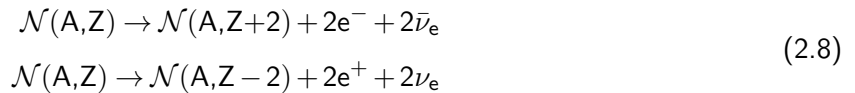


Figure 2.1: Mass excess according to the atomic number Z estimated with the Bethe–Weizsäcker formula at $A = 82$. $2\nu\beta\beta$ decay of ^{82}Se is possible because its simple β decay is energetically forbidden.

2.2 Two Neutrino Double Beta Decay

As shown in Figure 2.1, ^{82}Se is stable against β decay but has the possibility to undergo two neutrino double beta decay ($2\nu\beta\beta$) to reach a more stable state. This decay, proposed by Goeppert-Mayer in 1935 [64], is a rare process in which $2\beta^-$ or $2\beta^+$ decays happen simultaneously :



The $2\nu\beta\beta$ decay is a second order process allowed in SM and possible only for the even-even nucleus, as it can be seen in Figure 2.1. The double β^+ decays are also possible in theory but rarely studied since they are in competition with the double electron capture which makes their half-lives longer than double β^- decays. The Feynman diagram of $2\nu\beta\beta$ decay is shown in Figure 2.2. As the antineutrinos carry away a part of the energy, the total energy of the emitted electrons is a continuous spectrum with an end-point at the nuclear transition energy, $Q_{\beta\beta}$, defined as :

$$Q_{\beta\beta} = \mathcal{M}_i - (\mathcal{M}_f + 2m_e) \quad (2.9)$$

where \mathcal{M}_i is the mass of the mother nucleus, \mathcal{M}_f the mass of the daughter nucleus and m_e is the electron mass. The shape of this spectrum is shown in Figure 2.6. The half-life of $2\nu\beta\beta$ is very long, it depends on the isotope but the orders of magnitude are in the range $[10^{18} - 10^{24}]$ y. The half-life of the decay can be parametrised as :

$$(T_{1/2}^{2\nu})^{-1} = G_{2\nu}(Q_{\beta\beta}, Z) \times |M_{2\nu}|^2 \quad (2.10)$$

where $G_{2\nu}$ is the four-body phase space factor that can be calculated analytically and $M_{2\nu}$ is the nuclear matrix element (NME) for the decay. More details about NME will be given in Section 2.3.3.

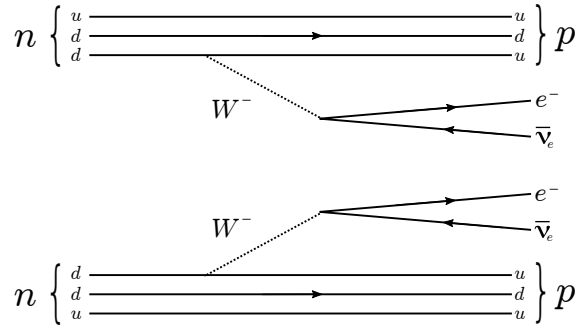


Figure 2.2: Feynman diagram for $2\nu\beta\beta$ decay. In this second order process, 2 neutrons decay simultaneously ($2n \rightarrow 2p + 2e^- + 2\bar{\nu}$). Two electrons and two anti-neutrinos are emitted.

41 natural isotopes capable of $2\nu\beta\beta$ decay exist, 35 by double β^- and 6 by β^+ . The decay rate of 12 of them have been experimentally observed. The transition energy, the natural abundance and the phase space factors of the 35 β^- isotopes are gathered in Table 2.5 at the end of the chapter.

2.3 Neutrinoless Double Beta Decay

The neutrinoless double beta decay ($0\nu\beta\beta$) is a hypothetical process, in which $2\beta^-$ decays occur simultaneously and no neutrino are emitted :

$$\mathcal{N}(A,Z) \rightarrow \mathcal{N}(A,Z+2) + 2e^- \quad (2.11)$$

Violating lepton number conservation this decay is forbidden in SM and has never been observed. As this decay is only possible if neutrinos are massive and are Majorana particles, it constitutes a sensitive method for testing the Majorana nature of neutrinos [65]. All candidates for $2\nu\beta\beta$ decay are also candidates for $0\nu\beta\beta$ decay and, a priori, there is no correlation between the two decay rates.

Many hypothetical mechanisms might mediate the $0\nu\beta\beta$ decay. The most common of them are the neutrino mass mechanism, right-handed current and Majoron emission modes presented in Sections 2.3.1 and 2.3.2. In these mechanisms it is clear that the neutrino must be a Majorana particle. But other mechanisms exist, not presented herein, such as R-parity violating supersymmetry [66]. In some of these mechanisms, no neutrinos are involved and it is not evident that $0\nu\beta\beta$ decay confirms the Majorana nature of neutrino [66]. In 1980, Schechter and Valle introduced a "black box" diagram depicting this decay [53]. This black box is shown in Figure 2.3 and demonstrates that regardless of the underlying mechanism, the $0\nu\beta\beta$ decay requires Majorana neutrinos.

As in $2\nu\beta\beta$, the half-life of $0\nu\beta\beta$ can be parametrised as :

$$(T_{1/2}^{0\nu})^{-1} = G_{0\nu}(Q_{\beta\beta}, Z) \times M_{0\nu}^2 \times \eta^2 \quad (2.12)$$

where $G_{0\nu}$ is a two-body phase space factor which is well known, $M_{0\nu}^2$ is the $0\nu\beta\beta$ NME, and η is a lepton violating number parameter which takes into account all the physics behind the $0\nu\beta\beta$ mechanism. This parameter varies according to the mechanism via which $0\nu\beta\beta$ is mediated.

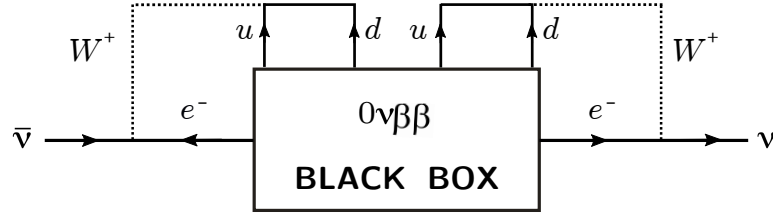


Figure 2.3: Black box representing the fact that whatever the underlying mechanism, the observation of the $0\nu\beta\beta$ decay implies Majorana neutrino.

2.3.1 Neutrino Mass Mechanism

The most common decay model which deviates the least from the SM is the neutrino mass mechanism. In this mechanism, $0\nu\beta\beta$ is mediated by the exchange of a light neutrino. A Feynman diagram using only SM vertices can be drawn, as shown in Figure 2.4. A right helicity Majorana neutrino is emitted from a W boson and absorbed by another as a left helicity Majorana neutrino.

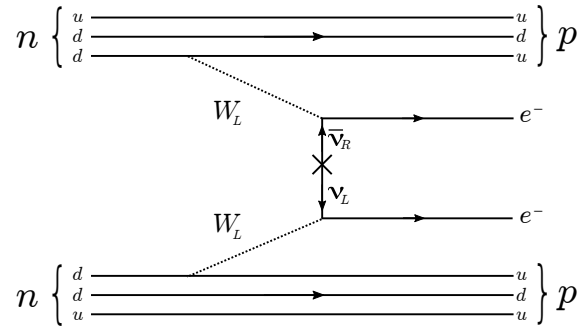


Figure 2.4: Feynman diagram of $0\nu\beta\beta$ decay in case of light Majorana neutrino exchange. The emitted electrons carry over all the energy, the experimental signature is given by a peaked distribution at the $Q_{\beta\beta}$ value.

In this model, the η parameter is given by the effective neutrino mass ($m_{\beta\beta}$) and the half-life can be expressed as:

$$(T_{1/2}^{0\nu})^{-1} = G_{0\nu}(Q_{\beta\beta}, Z) \times M_{0\nu}^2 \times \left(\frac{m_{\beta\beta}}{m_e} \right)^2 \quad (2.13)$$

where m_e is the electron mass, and $m_{\beta\beta}$ can be written as a function of PMNS matrix elements and neutrino masses (m_{ν_i}):

$$\begin{aligned} m_{\beta\beta} &= \left| \sum_i U_{ei}^2 m_{\nu_i} \right| \\ &= \cos^2\theta_{12} \cos^2\theta_{13} m_1 + \sin^2\theta_{12} \cos^2\theta_{13} e^{2i\lambda_1} m_2 + \sin^2\theta_{13} e^{2i(\lambda_2-\delta)} m_3 \end{aligned} \quad (2.14)$$

where θ_{12} and θ_{13} the mixing angles of PMNS matrix, δ is the Dirac CP-violating phase, and λ_1 and λ_2 the Majorana phases. The available values for $m_{\beta\beta}$ as a function of the lightest neutrino mass using the

best fit values of oscillation parameters are plotted in Figure 2.5. It is interesting to note that neutrino oscillation experiments do not give access to the neutrino nature or mass scale but are intimately linked with $0\nu\beta\beta$ searches via $m_{\beta\beta}$.

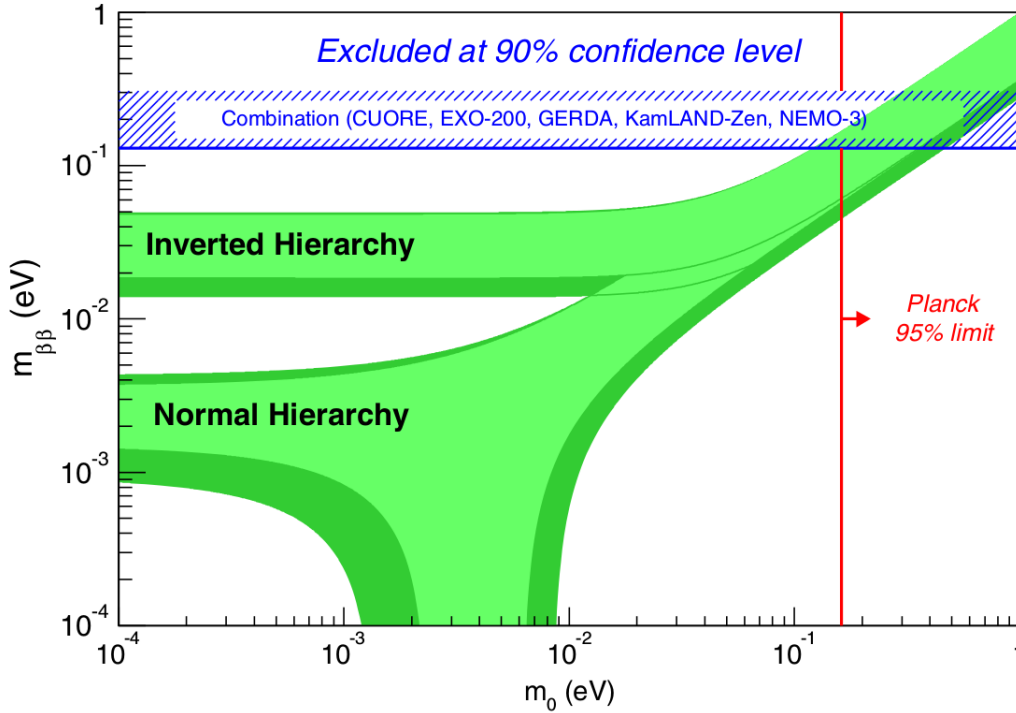


Figure 2.5: Neutrino effective mass for inverted and normal hierarchy with respect to the lightest neutrino mass determined by the best fit oscillation parameters and their uncertainties from [67]. The disfavoured regions from cosmology and $0\nu\beta\beta$ decay experiments are indicated [68].

The green bands represent the allowed values of the parameters for $m_{\beta\beta}$ in case of normal and inverted ordering of neutrino mass. The width of each of these bands is governed by the uncertainty over the parameters of the PMNS matrix. The $0\nu\beta\beta$ experiments put limits on $m_{\beta\beta}$ (y-axis), while direct and indirect neutrino mass measurements set limits on the lightest neutrino mass (x-axis). The coming $0\nu\beta\beta$ projects could probe the inverted ordering or excluding $0\nu\beta\beta$ mediated by the mass mechanism (in case nature chose the inverted ordering).

As no neutrinos are emitted, the electrons carry away all the released energy. The total energy distribution of the emitted electrons is expected to be peaked at the $Q_{\beta\beta}$ value as shown in Figure 2.6 (here the peak is replaced by a gaussian to illustrate the impact of the energy resolution of the detector). The measurement and the study of the total energy spectrum for the total energy provide the best way to observe $0\nu\beta\beta$.

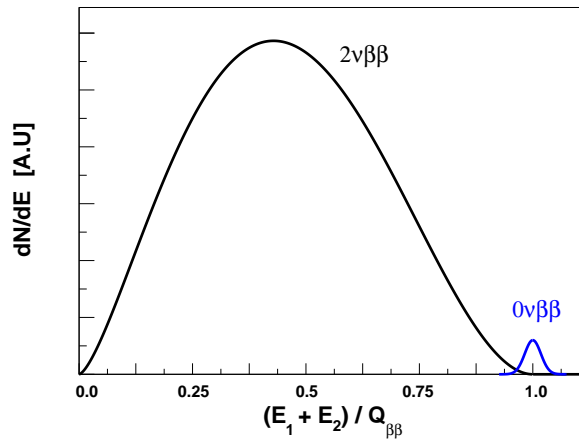


Figure 2.6: Distribution of the sum of electron energies in case of $2\nu\beta\beta$ and $0\nu\beta\beta$. Here the assumption is that $T_{1/2}^{2\nu}$ is 1 % of $T_{1/2}^{0\nu}$.

2.3.2 Other mechanisms

It also exists many other mechanisms which can induce $0\nu\beta\beta$ decay. All these mechanisms imply new interactions or/and new particles beyond the SM. The most common and quoted in the literature are the right-handed current and Majoron emission modes. Other processes as R-parity violating super-symmetry, extra dimensions or squark^a mixing have also been proposed.

Right-handed Current

In the SM, all the experimental observations show that parity is maximally violated in weak interactions [13, 69]. As a consequence, only left-handed W boson (W_L) are allowed to interact weakly in the SM. To restore this asymmetry, Left-Right Symmetric models have been proposed and postulate the existence of a new W_R gauge boson. In these new models $V + A$ vertices are allowed and can lead to $0\nu\beta\beta$ without a helicity flip. A Feynman diagram for $0\nu\beta\beta$ decay mediated by right handed current is shown in Figure 2.7, where a W_L boson couples to a $\bar{\nu}_R$ at top vertex which is absorbed at the bottom vertex without the need for a helicity change [70].

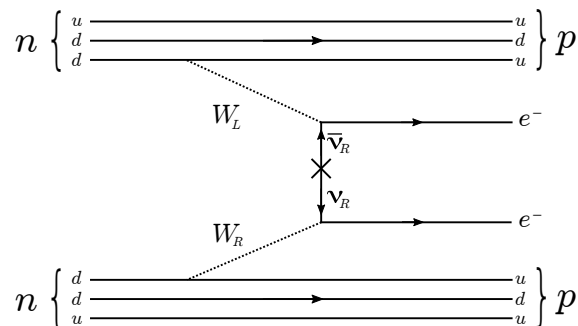


Figure 2.7: Feynman diagram for $0\nu\beta\beta$ decay using a right handed current.

^asuperpartner of quark in supersymmetry models

To describe the physics behind the right handed current two physics parameters are introduced : $\langle \lambda \rangle$ and $\langle \eta \rangle$. The $\langle \lambda \rangle$ parameter assumes a pure W_R and describes the coupling between right handed quarks and right handed leptons. In theory, the mediating gauge boson can be a mixture of W_L and W_R states. In this case, the $\langle \eta \rangle$ parameter is used to describe the coupling between left handed quarks and right handed leptons and so is related to the mixing angle between W_L and W_R . These parameters are related to the decay rate as :

$$(\mathcal{T}_{1/2}^{0\nu\lambda})^{-1} = G_{0\nu} \times |M_{0\nu}|^2 \times \langle \lambda \rangle^2 \quad (2.15)$$

$$(\mathcal{T}_{1/2}^{0\nu\eta})^{-1} = G_{0\nu} \times |M_{0\nu}|^2 \times \langle \eta \rangle^2 \quad (2.16)$$

As there are two electrons in the final state, the total energy is equal to the $Q_{\beta\beta}$ value of the decay as for the neutrino mass mechanism. To distinguish between the two mechanisms other variables must be used. Due to the presence of the W_R state at one vertex, the two electrons are preferentially emitted co-linearly which modifies the energy and angular distributions of the electrons as shown in Figure 2.8. These distributions motivate independent measurements for each electron.

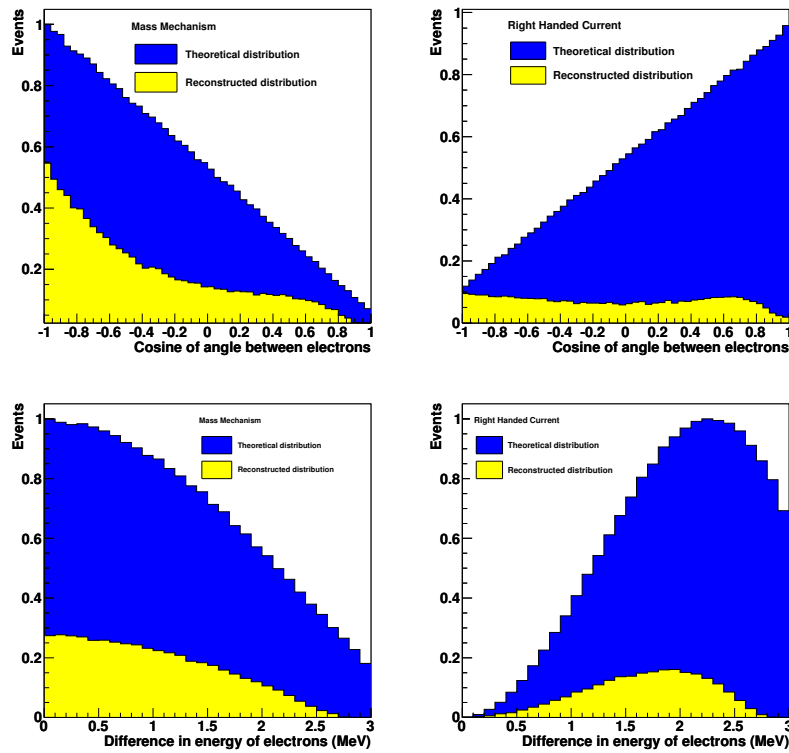


Figure 2.8: Comparison of the angular and energy difference distribution for the mass mechanism and right-handed current mechanisms. The blue distribution shows the theoretical distribution while the yellow distribution shows the expected response of SuperNEMO [71].

Majoron Emission

In many theories beyond SM a new global symmetry is introduced relating the difference between baryon and lepton number ($B-L$). In these theories, processes violating individually the baryon number

and lepton number are allowed as long as the total quantity $B-L$ is preserved [72]. Such extensions to the SM require that $B-L$ symmetry is spontaneously broken generating a massless Goldstone boson referred to as Majoron (χ^0) which could provide a mechanism for $0\nu\beta\beta$. Different models with singlet, doublet and triplet have been developed including couplings to the Z^0 boson [73–75]. Since the doublet and triplet models predict additional coupling to the Z^0 and increase the Z^0 width by the equivalent of half or two extra neutrinos respectively, these models have been excluded by the LEP measurement on the width of the Z^0 boson [12]. The singlet model is still viable even if it requires an important fine tuning of the neutrino-majoron coupling in order to preserve the current constraints on neutrino mass.

In the 1990s, new models have been proposed to avoid this significant fine tuning. In some of these models the Majoron is massive, carries a lepton number and do not require to be Goldstone boson [76]. They also provide mechanisms leading to $0\nu\beta\beta$ decay such as :

$$\begin{aligned} (A, Z) &\rightarrow (A, Z+2) + 2e^- + \chi^0 \quad (\text{singlet}) \\ (A, Z) &\rightarrow (A, Z+2) + 2e^- + 2\chi^0 \quad (\text{doublet}) \end{aligned} \quad (2.17)$$

The Feynman diagrams of two Majoron decays are presented in Figure 2.9, the singlet on the left (a) and the doublet on the right (b). In case of doublet, a new hypothetical mediating particle is introduced referred to as zino (\tilde{Z}). This particle comes from the supersymmetry model in which a symmetry between fermions and bosons is predicted [77]. \tilde{Z} is the supersymmetric fermion partner to the Z boson.

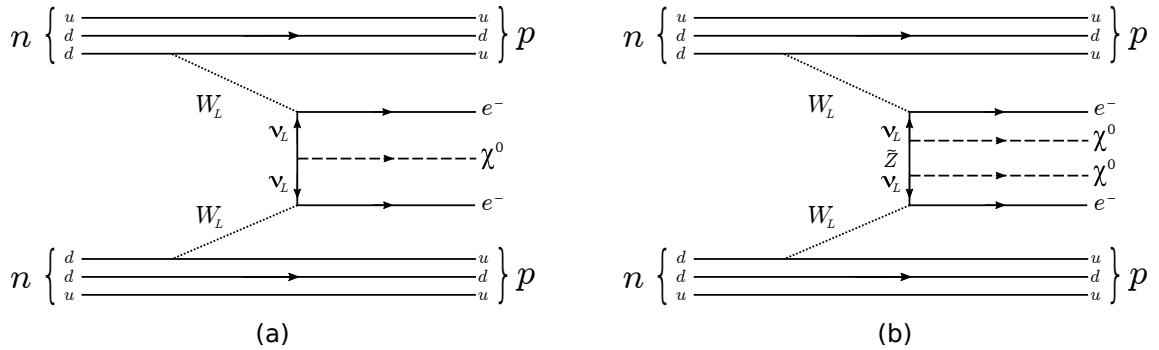


Figure 2.9: Feynman diagram for $0\nu\beta\beta$ decay mediated by Majoron emission with spectral indices $n = 1$ (a) and $n = 2$ (b).

Ten different Majoron models exists which can provide a mechanism for $0\nu\beta\beta$ decays [76]. Some of them conserve the lepton number while others violate it. To differentiate between these models the total energy of the electrons can be used. As extra particles are emitted the energy spectrum is not a monochromatic line but a continuous spectrum. The shape of this spectrum is affected in different ways according to the Majoron model. This spectrum modification is governed by the spectral index, n , describing the dependance of the phase space factor on the Majoron(s) energy :

$$G_{0\nu\chi^0} \propto (Q_{\beta\beta} - E_{e1} - E_{e2})^n \quad (2.18)$$

where E_{e1} and E_{e2} are the energy of the emitted electrons, $Q_{\beta\beta}$ the nuclear transition energy and $G_{0\nu\chi^0}$ the space phase factor. The electron energy distribution for n equal 1, 2, 3 and 7 are given in Figure 2.10.

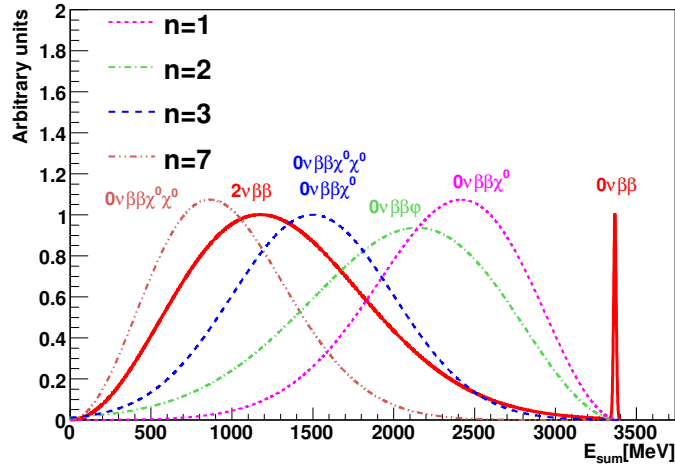


Figure 2.10: Distribution of the sum of electron energies for $2\nu\beta\beta$ and $0\nu\beta\beta$ according to different Majoron decay modes with spectral indices 1,2,3 and 7 [78].

2.3.3 Nuclear Matrix Element

In order to set a value or a limit on the physics parameter η of the Equation 2.12 from the experimentally measured $T_{1/2}^{0\nu}$, the phase space factor and the nuclear matrix element (NME) must be evaluated. The phase space factors which include the kinematics of the decay can be calculated with good precision. Due to the many-body nature of the problem, the computations of the NME are not trivial and different assumptions have to be made to facilitate them which led to the development of different models. The NME of the $0\nu\beta\beta$ decay can be expressed as :

$$|M_{0\nu}| = |M_{GT}^{0\nu} - \frac{g_{Av}^2}{g_V^2} M_F^{0\nu} + M_T^{0\nu}| \quad (2.19)$$

where g_{Av} and g_V are the axial-vector and vector coupling constants of the weak interaction and $M_{GT}^{0\nu}$, $M_F^{0\nu}$ and $M_T^{0\nu}$ are the Gamov-Teller, Fermi and tensor parts of the NME. $M_T^{0\nu}$ is neglected in most of the calculations due to its small contribution.

All the methods which have been implemented for the calculation of NME involve two different stages. In a first step, the interactions between nucleons, the nuclear physics informations and the physical mechanism behind $0\nu\beta\beta$ are incorporated via a many-body Hamiltonian. The second step consists in the introduction of a mean field to take into account the nuclear structure and residual interactions. It is in this second step that the models tend to differ by introducing different approximations and/or simplifying assumptions. This section briefly describes the different models and the difference between them.

Interacting shell model

The interacting shell model (ISM) handles a limited number of nuclear orbitals close to the Fermi level^b [79–82]. This model considers all the possible correlations between nucleons, proton-proton,

^bThe Fermi level is a thermodynamic quantity corresponding to the total chemical potential for the electrons. Its meaning is the thermodynamic work required to add one electron to the body.

neutron-neutron and proton-neutron, such that both proton and neutron numbers are conserved. It is accepted that this model works well for light nuclei such as ^{48}Ca , ^{76}Ge and ^{82}Se but is not appropriate for calculations involving heavy or deformed nuclei such as ^{150}Nd where orbitals far from the Fermi level must be taken into account.

Quasiparticle random phase approximation

Contrary to ISM, the quasiparticle random phase approximation model (QRPA) considers a high number of nuclear orbitals with reduced interactions between the nucleons [83–85]. The NME are calculated by assuming that the initial and final nuclear states are connected via many virtual intermediate collective states. As the proton-proton and neutron-neutron interactions are treated separately the proton and neutron numbers are not necessarily conserved in this model. It is accepted that the QRPA model gives more reliable results for heavy nuclei but this model can also be used to compute NME of lighter nuclei. Deformations in the initial and final state wave functions can be introduced in the calculations.

Interacting boson model

The interacting boson model (IBM) is a model in which protons and neutrons pair up and act as a single particle having boson properties [86]. Two versions of the model exist depending if protons and neutrons are treated in the same way (IBM-1) or separately (IBM-2). Due to the pairing, only the even-even nuclei are taken into account by the IBM model, which is not a problem since only even-even nuclei can undergo $0\nu\beta\beta$ decay as seen before. The IBM is, in form, quite similar to ISM.

Other methods

Other methods exist to compute the NME such as projected Hartree-Fock-Bogoliubov (PHFB) [87, 88] and energy density function (EDF) [89–91]. The PHFB method has been successful in the study of $2\nu\beta\beta$ but may suffer from a certain degree of oversimplification. The EDF method is an improvement of the PHFB method which takes into account the inter-nucleon interactions.

Comparison of the NME calculations

In order to understand the consequences of the assumptions made by the different models it is interesting to compare the NME results given by each method. This comparison has to be done carefully since different values are used in the calculations. Mostly for historical reasons, the ratio of the vector and axial-vector couplings, g_A , is set at either 1.0 or 1.25. Moreover, the value which parameterizes the size of the atomic radius, r_0 is either 1.1 fm or 1.2 fm ^c. The results of the NME calculations with the values $g_A = 1.25$ and $r_0 = 1.2$ fm are shown in Figure 2.11. The results obtained by Tübingen-Bratislava-Caltech and Jyväskylä groups using QRPA method are referred to as QRPA (T) and QRPA (J) respectively. Depending on the isotopes, the results differ to factor of 2-3. The ISM method tends to overestimate the correlations between the nuclear orbitals reducing the values of the NME and making the nucleus more stable.

Except for the ISM model, the results for ^{130}Te and ^{136}Xe are in good agreement. Moreover the QRPA (T) and IBM methods agree across all isotopes. The disparities between the two QRPA methods, and more particularly for ^{82}Se , ^{96}Zr and ^{100}Mo are still unexplained.

^cThe atomic radius R_A is commonly parametrised as $r_0A^{1/3}$ [92]

It is not possible to measure $M^{0\nu}$ independently from measuring the $0\nu\beta\beta$ half-life. The large range of $M^{0\nu}$ translates into a large uncertainty on the limits for $0\nu\beta\beta$ processes. Different ways are explored to succeed in reducing uncertainties. Recently, thanks to the measurements of β and $\beta\beta$ -decay half-lives for different isotopes, QRPA calculations of $M_{GT}^{0\nu}$ can be more constrained leading to a reduction of the $M^{0\nu}$ uncertainties. Moreover, the different models used to compute the NME values are also used to predict some observables of nuclear structure such as valence nucleon occupancies or nucleon pairing correlations. A dedicated program has been created to measure these observables in order to compare them with the theoretical predictions [93]. These results could also be used to tune the models. Finally, the decay via the excited state of the daughter nucleus can bring additional informations on the nuclear structure and help for the NME calculations.

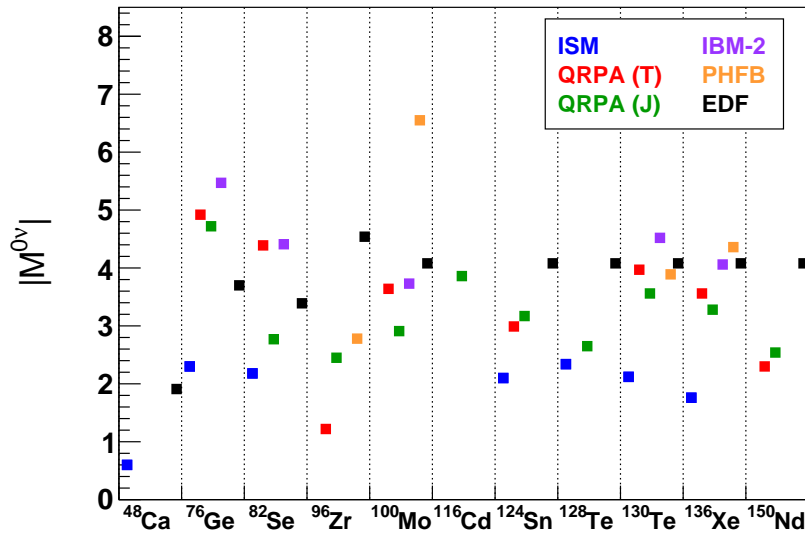


Figure 2.11: Summary of $0\nu\beta\beta$ Nuclear Matrix Element (NME) computations, calculated for 11 isotopes, using different approaches. These results are extracted from [94], conversion for $g_A = 1.25$ and $r_0 = 1.2$ fm have been made when necessary.

2.4 Experimental search for $\beta\beta$ decays

Despite that the $2\nu\beta\beta$ decay is very rare and very challenging to observe, its observation is a confirmation of the SM at the second order which provides additional information on the nuclear structure. Concerning the $0\nu\beta\beta$ decay its detection would confirm the Majorana nature of the neutrino and could give access to their mass scale. It is for these reasons that many experiments searching for $\beta\beta$ decays have been built around the world. This section presents the general considerations to design a $\beta\beta$ experiment in order to reach the best sensitivity on the $\beta\beta$ processes.

2.4.1 Half-life sensitivity for $0\nu\beta\beta$

The expected half-life sensitivity that an experiment can reach for the $0\nu\beta\beta$ decay can be approximately parametrised with the following expression [95] :

$$T_{1/2}^{0\nu}(n_\sigma) = \frac{4.16 \times 10^{26} \text{ y}}{n_\sigma} \left(\frac{\epsilon a}{W} \right) \sqrt{\frac{MT}{b\Delta E}} \quad (2.20)$$

where $T_{1/2}^{0\nu}$ is the half-life sensitivity to $0\nu\beta\beta$ in years, n_σ is the number of standard deviations for a given confidence level (90% CL corresponds to $n_\sigma = 1.64$), ϵ is the detection and identification efficiency, a is the isotopic abundance of the $0\nu\beta\beta$ source isotope of the source mass, W is the weight of the source isotope, M is the total mass of the source in [kg], T is the live time of the experiment in [y], b is the background rate in [keV kg y^{-1}], and ΔE is the energy resolution in [keV] at the $Q_{\beta\beta}$ value of the isotope.

Equation 2.20 demonstrates that to obtain the best sensitivity value, an experiment has to investigate a huge amount of isotope mass during the longest possible time with a very good detection efficiency, a very good energy resolution and with the lowest background possible. Generally, to maximise the sensitivity of an experiment, the highest signal efficiency and the lowest level of background is sought.

2.4.2 Maximising signal

To maximise the chance to observe a $\beta\beta$ decay, an experiment should study a large number of atoms of isotopes for as long as possible. Furthermore, even if a decay occurs, the detector must not miss it, thus the experiment must have a high detection efficiency to maximise the sensitivity.

The choice of the $\beta\beta$ isotope is also important when looking to maximise the signal. Indeed, as shown in Eq. 2.10 and 2.12 the phase space factors and the NME are related to the decay rate. Isotopes with high phase space factor and NME have a shorter half-life compared to the others. As a result, in the same amount of time, more decays can occur, which makes their detection more likely.

The molar mass of the isotope also plays a role in the maximization of the signal since it influences the total number of atoms in the sample. This parameter is generally not considered since there is a factor around 5 between the lighter and the heavier isotopes (^{46}Ca and ^{238}U) which is negligible compared to the $G^{0\nu}$ which can vary over a factor around $2 \cdot 10^4$ depending on the isotope (^{80}Se and ^{150}Nd).

The natural abundance and the ability to enrich an isotope must be taken into account. To reach a considerable mass of $\beta\beta$ isotope, it is simpler and cheaper if the isotope is already present in large quantities in nature. Depending on the isotope, different enrichment techniques exist having different yields and prices. The majority of the isotopes can be enriched via centrifugation method which is relatively cheap and allows the enrichment up to large mass. For some isotopes, such as ^{48}Ca , only electromagnetic separation is available, which only allows the enrichment of smaller quantities.

2.4.3 Minimising background

By looking at the Equation 2.20 which assumes a gaussian background it makes sense that an ideal $0\nu\beta\beta$ experiment should minimize the $b \times \Delta E$ term to increase the half-life sensitivity. As seen before, $\beta\beta$ decays is a very rare process, in which two electrons are emitted with a typical energy of a few MeV (2.0 - 4.3 MeV depending on the isotope). The main background in the search for $\beta\beta$ decay is the natural radioactivity in which particles with similar energies are emitted. The two main isotopes contributing to the background are the radioactive elements ^{214}Bi and ^{208}Tl , which are naturally present in small quantities in the materials from the ^{238}U and ^{232}Th decay chains shown in Figure 2.12. The electrons and photons emitted during the decays can by different processes such as Bremsstrahlung,

possible without also increasing the level of background. As a result, many experiments have been developed in order to optimize the sensitivity to $0\nu\beta\beta$ decay in different ways. This section presents the different experiments with their advantages and disadvantages. A summary of recent results of each experiment is also given.

2.5.1 Semiconductor experiments

Some semiconductors such as germanium have some isotopes which undergoes $\beta\beta$ decays, and can be used both as $\beta\beta$ decay source and detector. The $\beta\beta$ isotope, usually ^{76}Ge , is placed between two electrodes. Ionizing radiation creates electron-hole pairs in the material. The electrons are drifted towards the electrodes and produce signals which are proportional to the total energy of the decay. Due to their homogeneous design, semiconductor experiments have a very high acceptance and detection efficiency. These detectors typically work at cryogenic temperatures, to suppress the Intrinsic detector noise. This has also the advantage of obtaining a very good energy resolution, $\sim 0.3\%$ FWHM at the $Q_{\beta\beta}$ value of ^{76}Ge [96]. These detectors have only access to the total energy deposit and can not measure the full topology of the two electrons being emitted. Five old and recent semiconductor experiments are described in the following section.

Heidelberg-Moscow

The Heidelberg-Moscow (H-M) experiment operated in Laboratori Nazionali del Gran Sasso (LNGS), from 1990 to 2003, with five HPGe detectors enriched to 86 % in ^{76}Ge . With a total exposure of 35.5 kg y, H-M experiment set a limit of $T_{1/2}^{0\nu} > 1.9 \times 10^{25}$ y corresponding to $\langle m_{\beta\beta} \rangle < 250 - 500$ meV [97].

In 2001, a part of the collaboration claimed that the peak at 2039 keV present in the energy spectrum, shown in Figure 2.13 corresponds to a $0\nu\beta\beta$ decay signal [98]. For an exposure of 71.7 kg y, the half-life has been measured to be $T_{1/2}^{0\nu} = 1.19^{+2.99}_{-0.50} \times 10^{25}$ y which corresponds to $\langle m_{\beta\beta} \rangle < 100 - 900$ meV [98].

This claim is controversial because of the presence of an unidentified peak at 2030 keV and also because the ratios of the ^{214}Bi peaks are incorrect [99]. The background and the systematic uncertainties of the experiment were also probably underestimated [99]. Moreover, results obtained by recent experiments searching for $0\nu\beta\beta$ decay in ^{76}Ge strongly disfavour this claim.

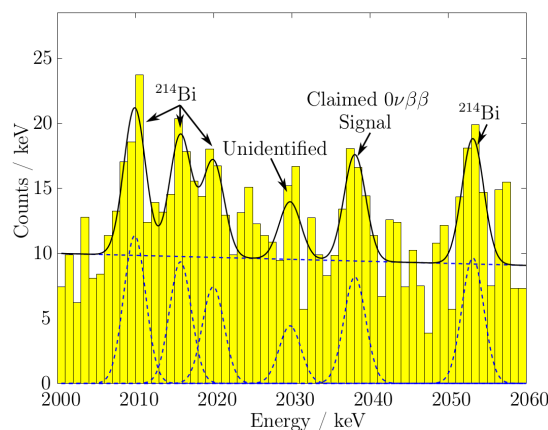


Figure 2.13: Total energy spectrum from the H-M experiment [97]. The peak at 2039 keV was claimed as a discovery of $0\nu\beta\beta$ decay.

IGEX

The International GErmanium eXperiment (IGEX) was a similar experiment to H-M using 2.0 kg of ^{76}Ge enriched to 86 % distributed in six detectors. With an exposure of 8.9 kg y of data, a limit on the half-life has been set to $T_{1/2}^{0\nu} > 1.57 \times 10^{25}$ y which corresponds to $\langle m_{\beta\beta} \rangle < 280 - 550$ meV [100].

GERDA

The GERmanium Detector Array experiment (GERDA) uses a serie of HPGe detectors including 8 from the H-M and IGEX experiments with the intention of testing the claim of $0\nu\beta\beta$ decay observation. 17.7 kg, along with 3.6 kg of new Broad Energy Ge (BEGe) detectors was immersed in a 64 m³ cryostat filled with liquid argon acting as a coolant and as a shielding. 3 m of water Cerenkov is added around to veto cosmic muons [101].

Installed at LNGS, GERDA took data, in a first phase, from November 2011 to May 2013 for a total exposure of 23.6 kg y. No $0\nu\beta\beta$ signal has been observed, and a limit of $T_{1/2}^{0\nu} > 2.1 \times 10^{25}$ y has been set which corresponds to $\langle m_{\beta\beta} \rangle < 240 - 480$ meV [101]. In a second phase, 20 kg of enriched ^{76}Ge have be added. GERDA collects data since December 2015 and no hint of $0\nu\beta\beta$ signal has been found in the combined data as shown in Figure 2.14. A limit has been set to $T_{1/2}^{0\nu} > 5.3 \times 10^{25}$ y at 90% C.L. corresponding to $\langle m_{\beta\beta} \rangle < 150 - 330$ meV.

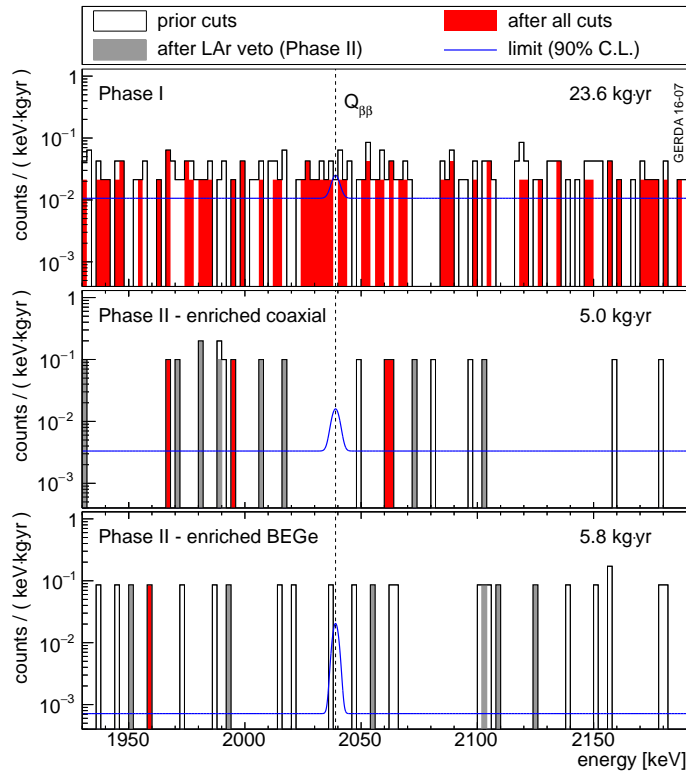


Figure 2.14: Combined Phase I data (top), Phase II coaxial (middle) and BEGe detector spectra (bottom) in the analysis window. The red histogram is the final spectrum, the filled grey one without pulse shape discrimination and the open one in addition without argon veto cut. The blue line is the fitted spectrum together with a hypothetical signal corresponding to the 90% C.L. limit of $T_{1/2}^{0\nu} > 5.3 \times 10^{25}$ y [102].

MAJORANA

The MAJORANA experiment will also search for $0\nu\beta\beta$ decays with enriched ^{76}Ge crystals. This experiment expects to surpass the sensitivity of H-M and IGEX by improving the radiopurity of the detector materials, by using more effective shieldings and by increasing the background-signal discrimination. Their aims are to achieve an energy resolution better than 3 keV and a very low background rate of 1 count/tonne/y in the ROI. A demonstrator module (MJD) is currently operating at the Sanford Underground Research Facility to show that the background levels can be achieved and extended to a tonne-scale experiment. If the desired background levels are achieved with the demonstrator, a sensitivity of $\langle m_{\beta\beta} \rangle < 80 - 160$ meV can be reached after 2.5 y of data taking [103].

The GERDA and MAJORANA collaborations are strongly connected. Depending on their results, there is a possibility of merging the two projects to build an experiment called LEGEND [104] containing 1 tonne of ^{76}Ge to reach a sensitivity of $\langle m_{\beta\beta} \rangle < \sim 10$ meV [105].

COBRA

Most of the semiconductor experiments use germanium detectors but other semiconductor technologies can provide competitive results. The COBRA experiment (Cadmium Zinc Telluride 0-neutrino double-Beta Research Apparatus) runs at LNGS and searches for $0\nu\beta\beta$ decays among 5 $\beta\beta$ isotopes (^{70}Zn , ^{114}Cd , ^{116}Cd , ^{128}Te and ^{130}Te) with an array of CdZnTe semiconductors. The energy resolution of this semiconductor is not as good as with HPGe experiments (~ 30 keV at 2800 keV) but it operates at room temperature. Thanks to the pixellated array, the tracking and identification of the particles are possible which reduces the background level (~ 1 count/keV/kg/y at 2800 keV is expected). In its demonstrator phase, COBRA comprises 64 CdZnTe coplanar-grid semiconductor detectors arranged in 4×4 detectors. After an exposure of 234.7 kg.d no signal of $0\nu\beta\beta$ has been found. The limits set on the five isotopes are reported in Table 2.1 such as their $Q_{\beta\beta}$ value and the measured background for the different R.O.I. [106].

Isotope	$Q_{\beta\beta}$ [keV]	b [cts./keV/kg/yr]	$T_{1/2}^{0\nu}$ [$\times 10^{21}$ y] at 90% C.L.
^{70}Zn	997	$4.51^{+0.6}_{-1.0}$	6.8×10^{-3}
^{114}Cd	543	$219.9^{+1.0}_{-1.7}$	1.6
^{116}Cd	2814	$2.7^{+0.1}_{-0.2}$	1.1
^{128}Te	867	$65.5^{+0.5}_{-1.6}$	1.9
^{130}Te	2528	$3.6^{+0.1}_{-0.3}$	6.1

Table 2.1: Results on the $0\nu\beta\beta$ half-life decay rate of the COBRA in its demonstrator phase.

2.5.2 Scintillation experiments

Scintillation experiment consists of scintillating materials doped with $\beta\beta$ isotopes. It can be either in an organic crystal form or in large volume of liquid scintillator. The particles emitted during a decay excite the scintillating medium which re-emits the absorbed energy as scintillation light. This light is then usually detected by an array of PMTs. This kind of detector have the advantages to be relatively inexpensive and have a high degree of radiopurity.

ELEGANT VI

Operating in Kamioka, the ELEGANT VI experiment searched for $0\nu\beta\beta$ decay in 23 $\text{CaF}_2(\text{Eu})$ crystal scintillators with 7.6 g of enriched ^{48}Ca . With an exposure of 0.015 kg y, the experiment sets a limit on the half-life to be $T_{1/2}^{0\nu} > 5.8 \times 10^{22}$ y corresponding to $\langle m_{\beta\beta} \rangle < 3.2 - 22$ eV [107].

CANDLESIII

The CANDLES experiment operates in Kamioka and consists of 305 CaF_2 crystals, for a total mass of 305 kg, placed in a liquid scintillator surrounded by PMTs. The experiment is currently taking data and a sensitivity of $\langle m_{\beta\beta} \rangle \sim 500$ eV is expected [108].

Aurora

The Aurora experiment investigates the double beta decay of ^{116}Cd using 1.162 kg of Cadmium Tungstate crystal scintillators enriched in ^{116}Cd to 82%. The experiment is installed in the low DAMA/R&D setup operated at the LNGS in Italy. In its last configuration, the CdWO_4 crystal scintillators are fixed in polytetrafluoroethylene containers filled with ultrapure liquid scintillator in order to improve the light collection and acting as an anti-coincidence veto counter. The energy resolution of the detector is 5% (FWHM) at 2.6 MeV. The Aurora experiment measured the $2\nu\beta\beta$ half-life of ^{116}Cd to be $2.62 \pm 0.14 \times 10^{19}$ y with a signal to background ratio of 2.6/1 in the energy interval (1.1 - 2.8) MeV. The Aurora experiment also performs the search for the $0\nu\beta\beta$. No signal has been found and limit of the half life has been set to 1.9×10^{23} y corresponding to $\langle m_{\beta\beta} \rangle < (1.2 - 1.8)$ eV [109].

KamLAND-Zen

KamLAND-Zen is an experiment that uses the KamLAND detector which was built to study the neutrino oscillation. The experiment searches for the $0\nu\beta\beta$ decay in ^{136}Xe , with 13 tonnes of liquid scintillator doped with ^{136}Xe suspended in a nylon balloon at the center of the KamLAND detector. This inner balloon is surrounded by an outer balloon containing 1000 tonnes of liquid scintillator which is used as an active shield against external sources of γ -rays. Around the two balloons a stainless steel tank is instrumented with ~ 2000 PMTs to detect the scintillation light.

In a first phase the experiment identified an unexpected background contributions in the $0\nu\beta\beta$ ROI coming from the surface of the inner balloon. These backgrounds are attributed to the radioactive fallout from the Fukushima accident. The experiment decided to halt in order to purify the inner balloon. The experiment restarted after the balloon purification for a second phase, and reaches by combining the two phases a limit for the $0\nu\beta\beta$ decay half-life of $T_{1/2}^{0\nu} > 1.06 \times 10^{26}$ y corresponding to $\langle m_{\beta\beta} \rangle < 61 - 165$ meV which is the strongest single constraint on $\langle m_{\beta\beta} \rangle$ for any isotope [110]. In a future phase of the experiment, the detector will be upgraded to contain 1 tonne of ^{136}Xe with an improvement of the light collection. The expected sensitivity is $\langle m_{\beta\beta} \rangle \sim 20$ meV [111].

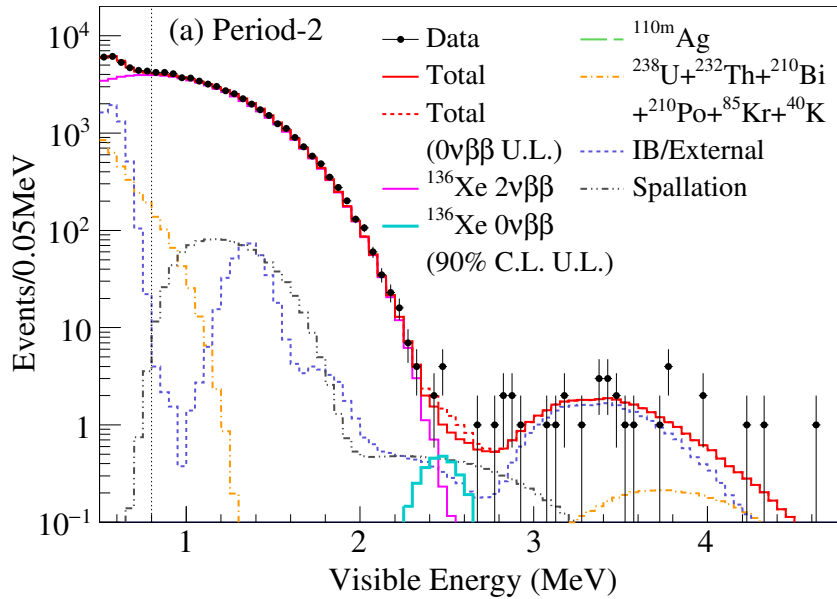


Figure 2.15: Energy spectrum of the selected $\beta\beta$ candidates [110].

SNO+

The SNO+ experiment follows the same principle as KamLAND-Zen. The experiment will operate in SNOlab and will reuse the acrylic sphere used in the SNO experiment. In a first phase, 800 kg of ^{130}Te , will be dissolved in 780 tonnes of liquid scintillator and introduced in the 12 m diameter sphere. Approximately 9500 PMTs will be used to read out the scintillation light. With 5 y of data taking, SNO+ will reach a sensitivity of $\langle m_{\beta\beta} \rangle < 55 - 133$ meV. In a second phase, the mass of ^{130}Te could be increased by a factor 10 and provide sensitivity up to $\langle m_{\beta\beta} \rangle < 19 - 46$ meV [112].

2.5.3 Bolometer experiments

The bolometer experiments detect the ionizing radiations by measuring small increases in temperature of a material. The increase of the temperature changes the electrical properties of the medium which can be measured and related to the ionizing particle energy. These detectors operate at very low temperature, of the order of mK, to obtain very good energy resolution. They measure only the total energy deposited by the particle and do not have good particle identification capabilities making difficult the background identification.

CUORE

The CUORICINO experiment was a prototype of the CUORE experiment (Cryogenic Underground Observatory for Rare Events). It ran at LNGS between 2003 and 2008, and searched for $0\nu\beta\beta$ decay in 507 g of ^{130}Te . The experiment consisted of a tower array of 62 TeO_2 crystals placed in a cryostat. With a total of 19.75 kg y, a limit has been set to $T_{1/2}^{0\nu} > 2.8 \times 10^{24}$ y corresponding to $\langle m_{\beta\beta} \rangle < 300 - 700$ meV [113].

CUORE is the next generation experiment extending the CUORICINO concept to a larger array of bolometers. The full CUORE detector contains 988 TeO_2 crystals (204 kg of ^{130}Te) to reach an expected sensitivity of $T_{1/2}^{0\nu} > 2.1 \times 10^{26}$ y corresponding to $\langle m_{\beta\beta} \rangle < 35 - 82$ meV. A demonstrator module,

CUORE-0, consisting of 52 crystals and 10.7 kg of ^{130}Te is currently running. A first limit has been set to $T_{1/2}^{0\nu} > 8 \times 10^{24}$ y which corresponds to $\langle m_{\beta\beta} \rangle < 270 - 760$ meV [114].

2.5.4 Scintillating bolometer experiments

New detectors will implement scintillating bolometers that simultaneously detect temperature changes and scintillation light. The combination of these two observables can be used for particle identification and to allow a better background rejection.

LUCIFER

LUCIFER (Low background Underground Cryogenics Installation for Elusive Rates) is an experiment which uses ZnSe crystals that act as both a bolometer and a scintillator. The combination of temperature and scintillation light measurements can be used for particle identification and allow a better background rejection. The crystals will contain ~ 18 kg of ^{82}Se to reach a sensitivity of $\langle m_{\beta\beta} \rangle \sim 60$ meV [115]. This detector will serve as a prototype for the CUPID experiment (Cuore Upgrade with Particle IDentification) which is in the early phases of R&D.

LUMINEU

The Luminescent Underground Molybdenum Investigation for NEUtrino mass and nature (LUMINEU) is a French R&D program to search for $0\nu\beta\beta$ decay of ^{100}Mo by using scintillating bolometer technique [116]. The LUMINEU project aims to develop high-quality radiopure ZnMoO_4 crystal scintillators of large mass (300 - 500 g) and test them as low-temperature detectors. The main aim of the project is to demonstrate feasibility of ZnMoO_4 based cryogenic scintillating bolometers for the future $0\nu\beta\beta$ generation experiment. The LUMINEU project could lead to an experiment containing approximately 10 kg of ^{100}Mo . Such experiment could reach a sensitivity on the $0\nu\beta\beta$ half-life on the level of the best current experiments. By scaling up to the 100-1000 kg experiment could entirely cover the inverted ordering region [116].

2.5.5 Time projection chamber experiments

The time projection chamber (TPC) experiments are a type of detector using gaseous or liquid medium combined with an electric field. By crossing the detector, charged particles ionize the medium and produce free electrons. These free electrons are drifted towards segmented collection planes called anodes. The generated current at the anode is proportional to the energy of the initial radiation. Since the anode is segmented, the position can be reconstructed in two-dimensions. The measurement of the arrival times on the anode plane provide information which can be translated into a third position coordinate. As a result, TPC detectors can reconstruct the particle track in three-dimensions which is used to search for common vertex from two electrons.

The most common isotope for $\beta\beta$ decay studies with TPC is ^{136}Xe , which also has the advantage of providing both ionization and scintillation signals. This scintillation light can be used to perform more accurate energy measurement than what is possible with the ionization signal alone.

EXO

The Enriched Xenon Observatory (EXO) experiment is a liquid xenon TPC looking for $0\nu\beta\beta$ decay in ^{136}Xe . The experiment is housed in the Waste Isolation Pilot Plant (WIPP) located at New Mexico, USA. The first prototype, EXO-200, is a cylindrical homogeneous TPC filled with liquid xenon, including

80 kg of ^{136}Xe , which is currently running. The detector uses the scintillation and ionization signals to reconstruct event topologies. It is symmetric around a central cathode plane. The two end caps are instrumented with wire anode grids and avalanche photodiodes to respectively read out the ionization and scintillation signals. The TPC is surrounded by a cryostat, a lead shielding and a plastic scintillator array to reject cosmic rays. After having recorded an exposure of 100 kg y, no signal of $0\nu\beta\beta$ decay has been found. A limit of $T_{1/2}^{0\nu} > 1.1 \times 10^{25}$ y, corresponding to $\langle m_{\beta\beta} \rangle < 190 - 450$ meV have been set [117].

In the future, the EXO experiment could be scaled up to the tonne scale. A new technique to tag the ^{136}Ba ions, daughter of the ^{136}Xe , is investigated to reduce the background level. With a tonne scale experiment, a sensitivity of $T_{1/2}^{0\nu} > 2 \times 10^{27}$ y, corresponding to $\langle m_{\beta\beta} \rangle < 15 - 32$ meV could be achieved.

NEXT

The Neutrino Experiment with a Xenon TPC experiment (NEXT) is an experiment which is under construction in the Canfranc Underground Laboratory in Spain, looking for $0\nu\beta\beta$ decays in ^{136}Xe . It consists of a cylindrical TPC using gaseous xenon at high pressure. The detector will detect both scintillation and ionization signals. The scintillation light will be detected by PMTs at one end cap while the ionization signal will be amplified and produce electroluminescence that can be read out by silicon PM. This second signal provides tracking information and allows improvement of the energy resolution. A prototype detector, NEXT-100, with 100 kg of ^{136}Xe is currently operating, a sensitivity of $T_{1/2}^{0\nu} > 1.9 \times 10^{25}$ y is expected corresponding to $\langle m_{\beta\beta} \rangle < 70 - 150$ meV [118]. The advantage of NEXT-100 is that it is readily scalable. If the prototype is successful, it is possible to enlarge it to contain a tonne of material to reach a sensitivity of $\langle m_{\beta\beta} \rangle < 15 - 32$ meV.

2.5.6 Tracker-calorimeter experiments

The tracker-calorimeter experiments separate the $\beta\beta$ isotope from the detection device which allows to investigate the $\beta\beta$ decay for many candidate isotope. The track of the two electrons and their energies are measured by two distinct detectors. This technique allows to reconstruct the full topology and kinematics of individual particles within an event, which results in excellent background rejection and also gives the possibility to distinguish the mechanism behind the $0\nu\beta\beta$ decay. However, the tracker-calorimeter experiments, due to the separation of the isotope from the rest of the detector, generally suffer from lower energy resolution and detection efficiency compared to the other type of $\beta\beta$ detectors. The most renowned experiments using tracker-calorimeter technique are the NEMO-3 experiment and its successor SuperNEMO. They will be described in more details in Chapter 3.

2.6 Summary and status of the $\beta\beta$ researches

Today, the direct measurement of the $2\nu\beta\beta$ decay has been made for nine isotopes. The most accurate measurements to date are presented in Table 2.2. Due to its ability to measure different isotopes, NEMO-3 is often quoted. ^{76}Ge and ^{136}Xe have been measured by GERDA-I and EXO-200 respectively.

No evidence of $0\nu\beta\beta$ decay has been observed whatever the isotope. The best half-life limits are given in Table 2.3. The best limit on $\langle m_{\beta\beta} \rangle$ has been set by the KamLAND-Zen experiment.

When different experiments investigate the same isotope, their results can be combined to obtain a stronger half-life limit. For example, by combining the GERDA results with H-M and IGEX, a limit of

$T_{1/2}^{0\nu} > 3.0 \times 10^{25}$ y corresponding to $\langle m_{\beta\beta} \rangle < 0.20 - 0.40$ eV can be set [101]. By combining the results on ^{136}Xe from EXO-200 and KamLAND-Zen, the sensitivity is set to $T_{1/2}^{0\nu} > 3.4 \times 10^{25}$ y which corresponds to $\langle m_{\beta\beta} \rangle < 0.12 - 0.25$ eV [119]. These results can be summarised in a plot showing the sensitivity on ^{76}Ge versus the sensitivity of ^{136}Xe for different NME calculations as shown in Figure 2.16. Both results strongly disfavor the H-M claim. The results obtained on the effective neutrino mass for the different isotopes are represented in Figure 2.17. To date the best limit on the effective neutrino mass has been obtained with the ^{136}Xe by KamLAND-Zen experiment.

Today, several new experiments are planned to search for $0\nu\beta\beta$ process as listed in Table 2.4. Some of them are currently running while others are finishing their R&D phase or are in construction stage. These new experiments are expected to approach the parameter space for the inverted hierarchy. Many of them plan to scale up to larger mass to fully explore the inverted hierarchy parameter space at $\langle m_{\beta\beta} \rangle \sim 10$ meV. In a scenario in which nature has chosen the inverted hierarchy for neutrino masses, these experiments will either discover or exclude the $0\nu\beta\beta$ decay.

Isotope	Experiment	$T_{1/2}^{2\nu} [\times 10^{19}\text{y}]$	Ref.
^{48}Ca	NEMO-3	$6.4^{+0.6}_{-0.7} \text{ } ^{+1.2}_{-0.9}$	[120]
^{76}Ge	GERDA-I	$192.6^{+2.5}_{-2.2} \pm 9.2$	[121]
^{82}Se	NEMO-3	$9.93 \pm 0.14 \pm 0.72$	[122]
^{96}Zr	NEMO-3	$2.35 \pm 0.14 \pm 0.16$	[123]
^{100}Mo	NEMO-3	$0.711 \pm 0.002 \pm 0.054$	[124]
^{116}Cd	Aurora	2.62 ± 0.14	[109]
^{130}Te	NEMO-3	$70 \pm 9 \pm 11$	[125]
^{136}Xe	EXO-200	$216.5 \pm 1.6 \pm 5.9$	[126]
^{150}Nd	NEMO-3	$0.934 \pm 0.022^{+0.060}_{-0.059}$	[127]

Table 2.2: Most accurate measurements of the $2\nu\beta\beta$ half-life. The first error corresponds to the statistical and the second is systematic

Isotope	Experiment	Exposure [kg.y]	$T_{1/2}^{0\nu}$ [y]	$\langle m_{\beta\beta} \rangle$ [eV]	Ref.
^{48}Ca	ELEGANT VI	0.015	5.8×10^{22}	3.5 - 22	[107]
^{76}Ge	GERDA-I	16.4	2.1×10^{25}	0.24 - 0.48	[101]
^{82}Se	NEMO-3	4.90	2.2×10^{23}	1.0 - 2.8	[122]
^{96}Zr	NEMO-3	0.031	9.2×10^{21}	7.2 - 19.5	[123]
^{100}Mo	NEMO-3	34.5	1.1×10^{24}	0.33 - 0.62	[128]
^{116}Cd	Aurora	1.31	1.9×10^{23}	1.2 - 1.8	[109]
^{130}Te	CUORICINO/CUORE	19.75	4.0×10^{24}	0.27 - 0.76	[129]
^{136}Xe	KamLAND-Zen	504	1.9×10^{26}	0.061 - 0.165	[110]
^{150}Nd	NEMO-3	0.19	2.0×10^{22}	1.6 - 5.3	[127]

Table 2.3: Best half-life limits obtained from individual experiments from different $0\nu\beta\beta$ isotopes. All the limits are given at 90% CL.

Experiment	Isotope	Mass [kg]	Type	$\langle m_{\beta\beta} \rangle$ [meV]	Ref
GERDA-II	^{76}Ge	40	Semiconductor	50 - 100	[101]
MAJORANA	^{76}Ge	40	Semiconductor	80 - 160	[103]
CANDLES III	^{48}Ca	0.3	Scintillator	500	[108]
KamLAND-Zen	^{136}Xe	640	Liquid Scint.	40 - 85	[111]
SNO+ (0.3%)	^{130}Te	800	Liquid Scint.	50 - 100	
CUORE-0	^{130}Te	10.7	Bolometer	180 - 420	[114]
EXO-200	^{136}Xe	80	Scint. TPC	85 - 180	[117]
NEXT-100	^{136}Xe	90	Scint. TPC	70 - 150	[118]
SuperNEMO	^{82}Se	100	Tracker-Calo	50 - 100	
1ton Ge	^{76}Ge	1000	Semiconductor	10	-
COBRA	^{116}Cd	420	Semiconductor	50 - 70	[130]
CANDLES	^{48}Ca	3	Scintillator	50	[108]
KamLAND2-Zen	^{136}Xe	1000	Liquid Scint.	20	[111]
SNO+ (3.0%)	^{130}Te	8000	Liquid Scint.	20 - 40	-
CUORE	^{130}Te	204	Bolometer	35 - 82	[114]
LUCIFER	^{82}Se	18	Scint. Bolom.	60	[115]
EXO	^{136}Xe	1000	Scint. TPC	15 - 62	[117]
NEXT	^{136}Xe	1000	Scint. TPC	15 - 62	[118]

Table 2.4: Summary of future $\beta\beta$ experiments. The top panel presents the experiments which are either running or under construction. The bottom panel shows experiments that have been proposed as successors to the current generation.

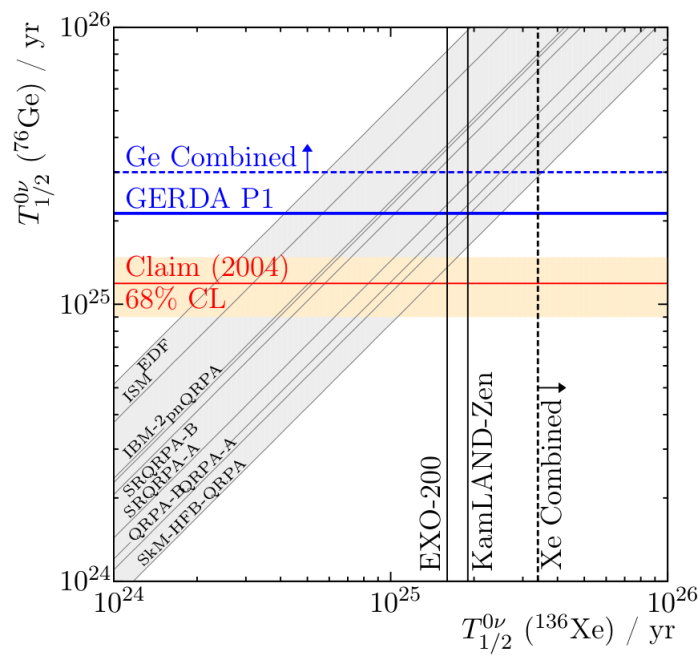


Figure 2.16: Limits on $T_{1/2}^{2\nu}$ for ^{76}Ge from GERDA-I and ^{136}Xe from EXO-200 and KamLAND-Zen compared with the claim of $0\nu\beta\beta$ from H-M experiment [119].

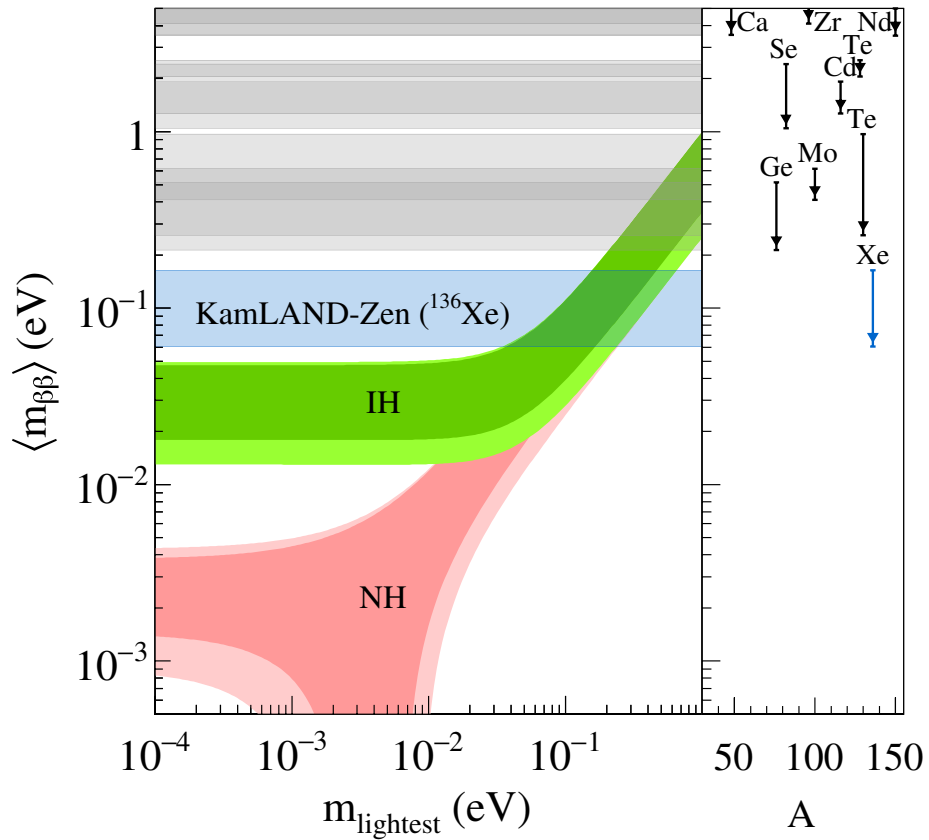


Figure 2.17: Effective neutrino mass ($|\langle m_\nu \rangle| = m_{\text{eff}}$) as a function of the lowest mass eigenstate (m_0). The blue band represents the new limits set by KamLAND-Zen with ^{136}Xe which is close to the inverted ordering region. The grey bands represent the old limit or the limit obtained on the other isotopes. The side-panel shows the corresponding limits for each nucleus as a function of the mass number.

Transition	$Q_{\beta\beta}$ [keV]	η [%]	$G^{2\nu}$ [y^{-1}]	$G^{0\nu}$ [y^{-1}]
$^{46}\text{Ca} \rightarrow ^{46}\text{Ti}$	987 ± 4	0.035	1.148×10^{-22}	1.397×10^{-27}
$^{48}\text{Ca} \rightarrow ^{48}\text{Ti}^\dagger$	4267.98 ± 0.34	0.187	3.968×10^{-17}	2.439×10^{-25}
$^{70}\text{Zn} \rightarrow ^{70}\text{Ge}$	1001 ± 3	0.62	3.155×10^{-22}	2.342×10^{-27}
$^{76}\text{Ge} \rightarrow ^{76}\text{Se}$	2039.6 ± 0.9	7.61	1.305×10^{-19}	2.445×10^{-26}
$^{80}\text{Se} \rightarrow ^{80}\text{Kr}$	130 ± 9	49.8	1.220×10^{-28}	4.274×10^{-29}
$^{82}\text{Se} \rightarrow ^{82}\text{Kr}^\dagger$	2997.9 ± 0.3	8.73	4.348×10^{-18}	1.079×10^{-25}
$^{86}\text{Kr} \rightarrow ^{86}\text{Sr}$	1256 ± 5	17.3	3.333×10^{-21}	6.369×10^{-27}
$^{94}\text{Zr} \rightarrow ^{94}\text{Mo}$	1145.3 ± 2.5	17.4	2.304×10^{-21}	6.369×10^{-27}
$^{96}\text{Zr} \rightarrow ^{96}\text{Mo}^\dagger$	3350.0 ± 3.5	2.8	1.927×10^{-17}	2.242×10^{-25}
$^{98}\text{Mo} \rightarrow ^{98}\text{Ru}$	112 ± 7	24.1	9.709×10^{-29}	6.711×10^{-29}
$^{100}\text{Mo} \rightarrow ^{100}\text{Ru}^\dagger$	3034.40 ± 0.17	9.63	9.434×10^{-18}	1.754×10^{-25}
$^{104}\text{Ru} \rightarrow ^{104}\text{Pd}$	1299 ± 4	18.7	9.174×10^{-21}	1.202×10^{-26}
$^{110}\text{Pd} \rightarrow ^{110}\text{Cd}$	2013 ± 19	11.8	3.984×10^{-19}	5.376×10^{-26}
$^{114}\text{Cd} \rightarrow ^{114}\text{Sn}$	534 ± 4	28.7	1.443×10^{-23}	1.639×10^{-27}
$^{116}\text{Cd} \rightarrow ^{116}\text{Sn}^\dagger$	2813.50 ± 0.13	7.49	8.000×10^{-18}	1.894×10^{-25}
$^{122}\text{Sn} \rightarrow ^{122}\text{Te}$	364 ± 4	4.56	1.047×10^{-24}	8.621×10^{-28}
$^{124}\text{Sn} \rightarrow ^{124}\text{Te}$	2288 ± 1.6	5.64	1.686×10^{-18}	1.055×10^{-25}
$^{128}\text{Te} \rightarrow ^{128}\text{Xe}$	868 ± 4	31.7	8.475×10^{-22}	6.993×10^{-27}
$^{130}\text{Te} \rightarrow ^{130}\text{Xe}^\dagger$	2528.9 ± 2.1	2.1	4.808×10^{-18}	1.698×10^{-25}
$^{134}\text{Xe} \rightarrow ^{134}\text{Ba}$	847 ± 10	10.4	8.621×10^{-22}	7.692×10^{-27}
$^{136}\text{Xe} \rightarrow ^{136}\text{Ba}$	2479 ± 8	8.9	4.831×10^{-18}	1.812×10^{-25}
$^{142}\text{Ce} \rightarrow ^{142}\text{Nd}$	1417.6 ± 2.5	11.1	7.246×10^{-20}	1.812×10^{-26}
$^{146}\text{Nd} \rightarrow ^{146}\text{Sm}$	56 ± 5	17.2	4.854×10^{-30}	1.418×10^{-28}
$^{148}\text{Nd} \rightarrow ^{148}\text{Sm}$	1928.3 ± 1.9	5.7	1.070×10^{-18}	1.276×10^{-25}
$^{150}\text{Nd} \rightarrow ^{150}\text{Sm}^\dagger$	3371.38 ± 0.2	5.6	1.189×10^{-16}	8.000×10^{-25}
$^{154}\text{Sm} \rightarrow ^{154}\text{Gd}$	1251.9 ± 1.5	22.6	4.098×10^{-20}	4.202×10^{-26}
$^{160}\text{Gd} \rightarrow ^{160}\text{Dy}$	1729.5 ± 1.4	21.8	6.623×10^{-19}	1.252×10^{-25}
$^{170}\text{Gr} \rightarrow ^{170}\text{Yd}$	653.9 ± 1.6	14.9	5.495×10^{-22}	1.445×10^{-26}
$^{176}\text{Yb} \rightarrow ^{176}\text{Hf}$	1078.8 ± 2.7	12.6	3.067×10^{-20}	5.714×10^{-26}
$^{186}\text{W} \rightarrow ^{186}\text{Os}$	490.3 ± 2.2	28.6	1.302×10^{-22}	1.439×10^{-26}
$^{192}\text{Os} \rightarrow ^{192}\text{Pj}$	417 ± 4	41.0	5.051×10^{-23}	1.299×10^{-26}
$^{198}\text{Pt} \rightarrow ^{198}\text{Hg}$	1048 ± 4	7.2	6.135×10^{-20}	1.144×10^{-25}
$^{204}\text{Hg} \rightarrow ^{204}\text{Pb}$	416.5 ± 1.9	6.9	8.130×10^{-23}	1.976×10^{-26}
$^{232}\text{Th} \rightarrow ^{232}\text{U}$	858 ± 6	100	5.952×10^{-20}	2.519×10^{-25}
$^{238}\text{U} \rightarrow ^{238}\text{Pu}$	1145.8 ± 1.7	99.275	6.803×10^{-19}	5.952×10^{-25}

Table 2.5: Transition energy, natural abundance and space phase factors of the 35 β^- isotopes from [131] except the values marked by a \dagger where $Q_{\beta\beta}$ uncertainties have been updated.

Chapter 3

NEMO detectors

Initiated in the late 1980s, the main goals of the NEMO project are the search for $0\nu\beta\beta$ and the measurement of $2\nu\beta\beta$ decays. The strategy adopted by the collaboration is the direct detection of the two emitted electrons, by separating the $\beta\beta$ emitters from the rest of the detector. This technique also allows to investigate many $\beta\beta$ isotopes with a powerful background discrimination. The Modane Underground Laboratory (LSM), which hosted all the NEMO prototypes and detectors, is described in Section 3.1. The NEMO-3 detector is presented in Section 3.2. The data taken by this detector will be analysed in Chapter 6 to perform the search for the $\beta\beta$ decays of ^{116}Cd via the excited states of ^{116}Sn . Finally, the SuperNEMO detector is introduced in Section 3.3.

3.1 Modane underground laboratory

Inaugurated in 1982, the Modane Underground Laboratory (LSM) ^a is located in the Frejus tunnel at the border between France and Italy as shown in Figure 3.1.

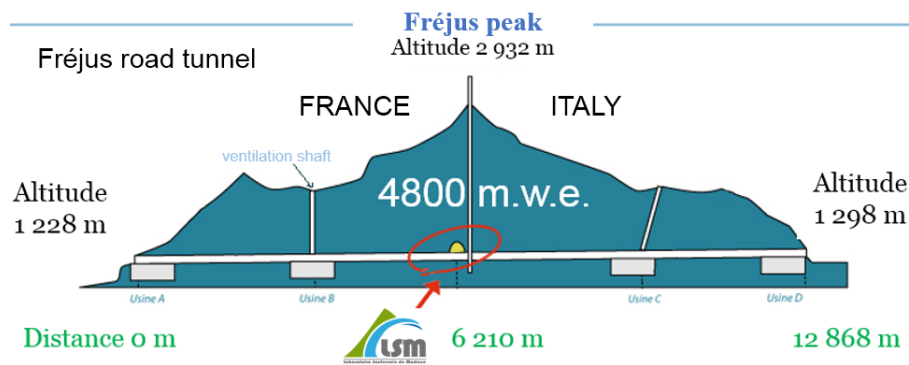


Figure 3.1: Schematic view of the Modane underground laboratory location in the Frejus tunnel.

The laboratory is sheltered from cosmic rays under 1700 m of rocks (4200 m.w.e) ^b which makes it the deepest underground laboratory in Europe and the third one in the world. The cosmic ray flux inside the laboratory has been measured to be 4 muons/m²/day [132], which is a reduction by a factor of one million from the one at sea level. The total muon flux for different underground laboratories is presented in Figure 3.2.

^aLSM : Laboratoire Souterrain de Modane in french

^bm.w.e : meter water equivalent

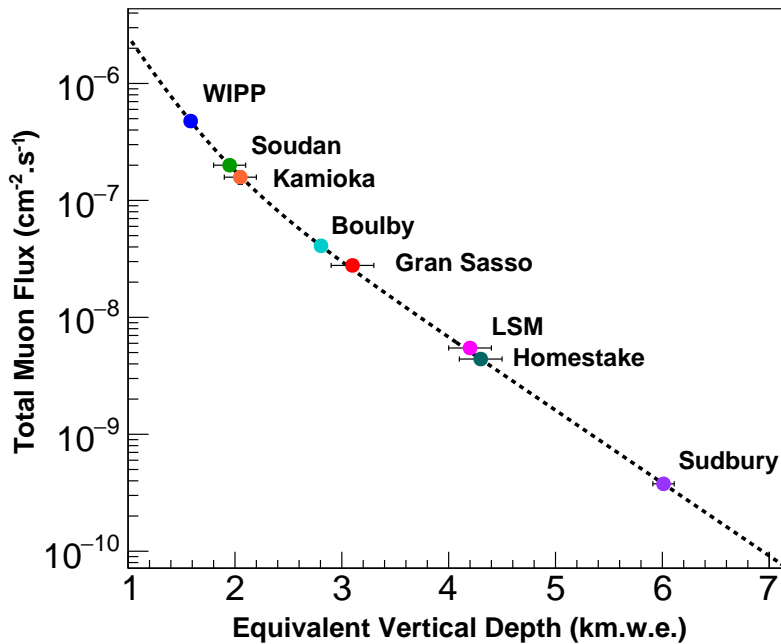


Figure 3.2: Total muon flux measured for various underground sites as a function of the equivalent vertical depth [133].

The protected environment of the laboratory is very favorable to the searches of rare processes which require very low backgrounds. Initially, the laboratory hosted an experiment searching for the proton decay. Later, the laboratory diversified its activities, including astrophysics, biology, geology, electronics and environmental researches. The laboratory also has several High Purity Germanium detectors (HPGe) to measure very low radioactivity.

The first prototypes, NEMO-1 [134] and NEMO-2 [135] were installed at LSM in the late 1980s and early 1990s. Then the laboratory hosted NEMO-3 in early 2000. Today NEMO-3 has been replaced by SuperNEMO demonstrator which is currently under construction and commissioning.

3.2 NEMO-3

The NEMO-3 detector ran from February 2003 to January 2011 and searched for $\beta\beta$ decays among seven different isotopes. NEMO-3, shown in Figure 3.3, was shaped as a cylinder of 5 m in diameter and 3 m high. The detector was divided into 20 identical parts referred to as sectors, a picture of one of them is shown in Figure 3.5. For the direct detection of two electrons, thin foils of $\beta\beta$ emitters were vertically disposed at a fixed radius, as shown in Figure 3.4. Placed on each side of the source foils, wire tracking chambers were used to measure the trajectory of charged particles. The tracker was immersed in a magnetic field of 25 Gauss for charge identification. A calorimeter surrounded the tracking volume on all sides providing both energy and timing measurements of particles. Passive shieldings of iron, paraffin, borated water and wood were installed around the detector against cosmic rays and neutron interactions. This section provides an overview of each detector components based on [136].

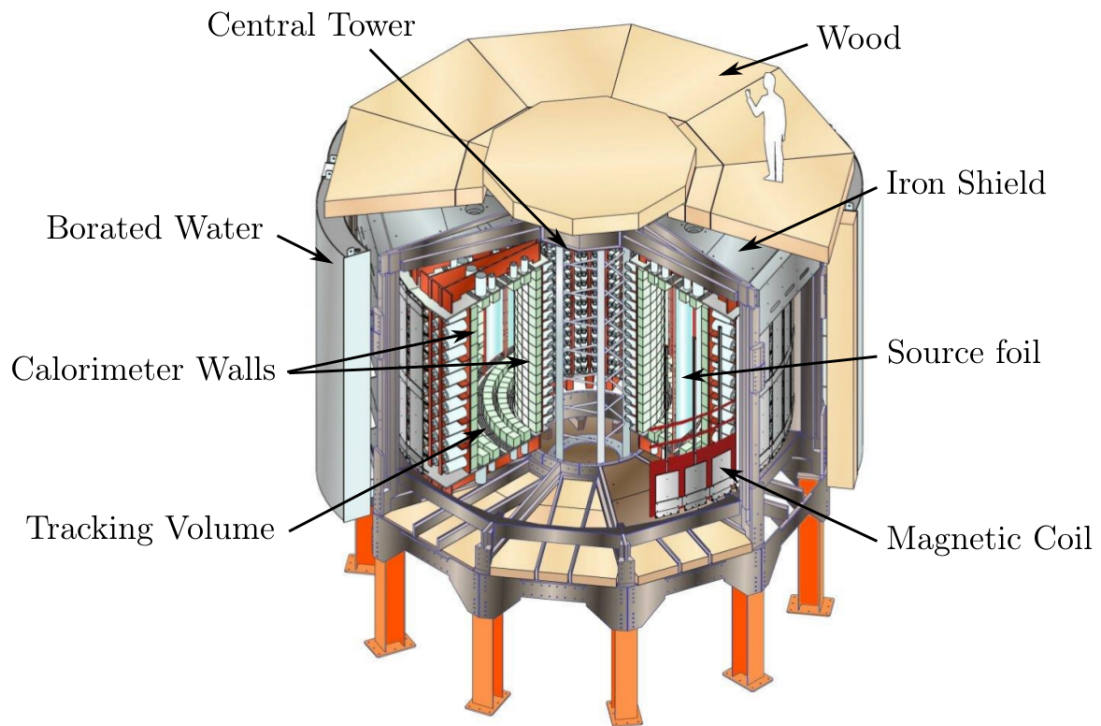


Figure 3.3: Exploded view of the NEMO-3 detector.

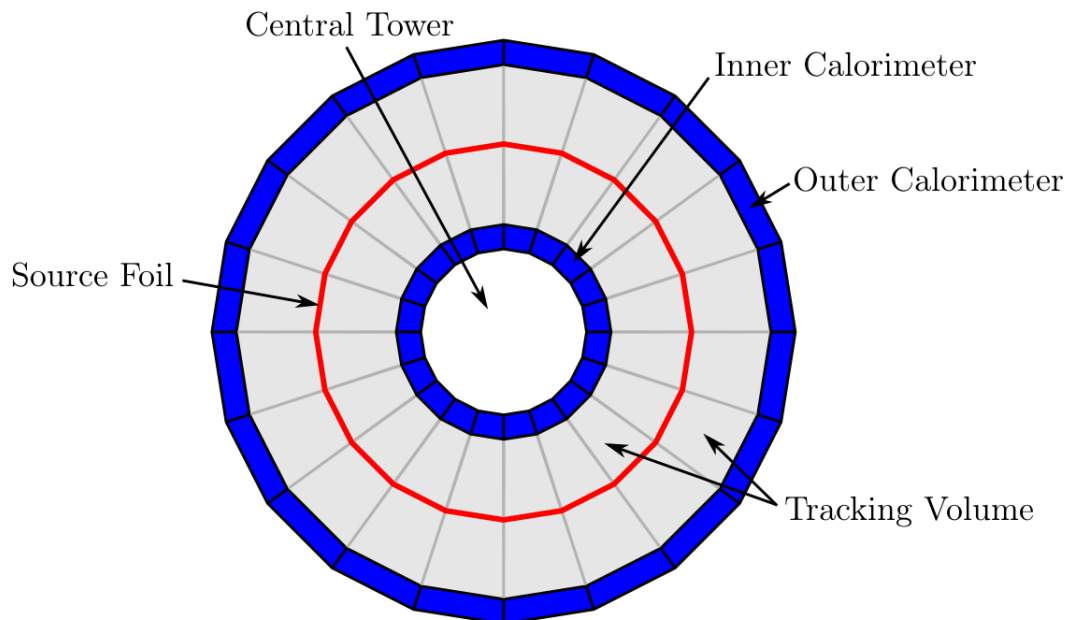


Figure 3.4: Top view of the NEMO-3 detector geometry. The $\beta\beta$ source foils are represented in red, the tracker volume in grey and the calorimeter in blue. The cylinder is divided into 20 sectors.

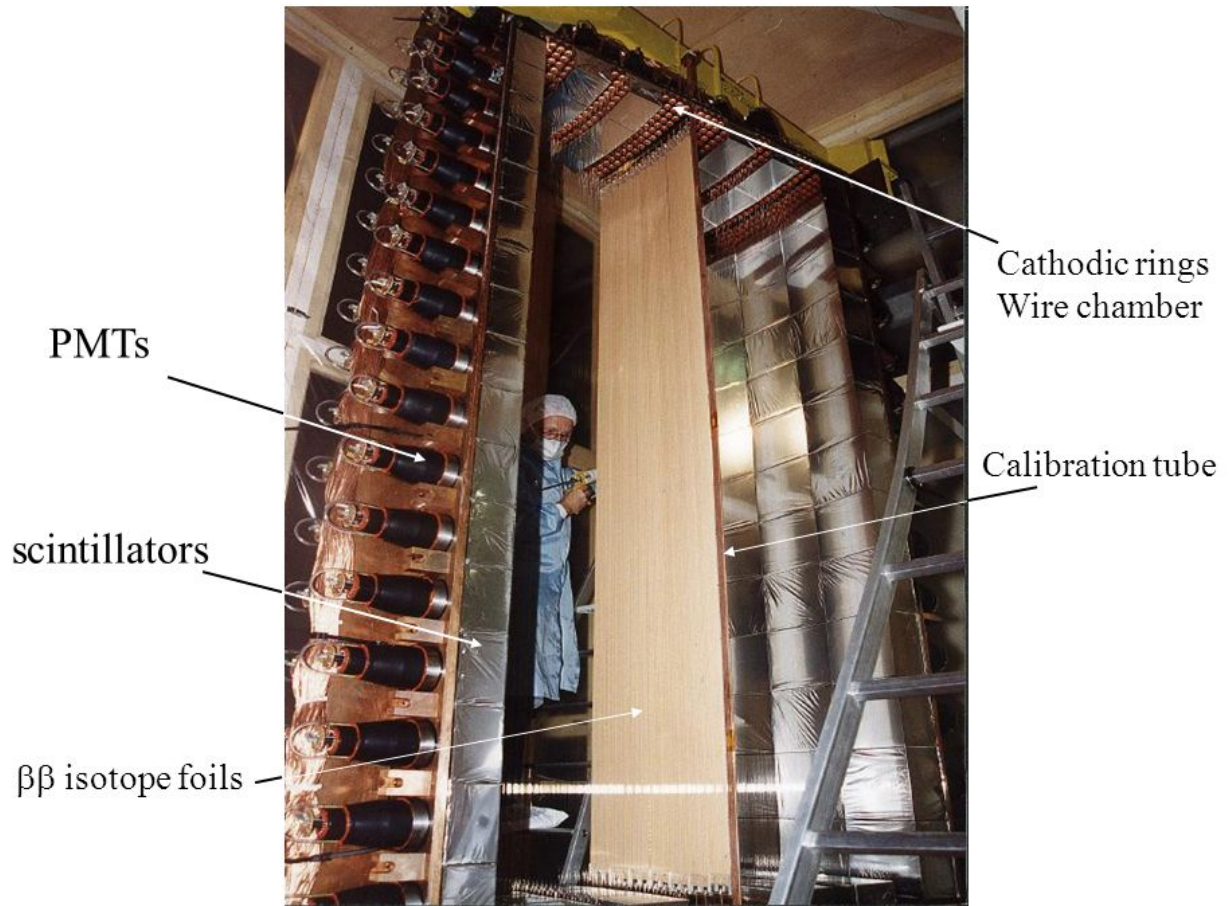


Figure 3.5: Picture of a NEMO-3 sector. A source foil is vertically placed at the center and surrounded by the wire chamber and the calorimeter.

3.2.1 Source foils

The separation of the source foils from the rest of the detector allows the investigation of various $\beta\beta$ emitters. Seven isotopes for a total of 8.8 kg have been introduced in the detector. ^{100}Mo and ^{82}Se were the isotopes with the largest mass with 6.91 kg and 0.93 kg respectively. These two isotopes provide the best sensitivity to search for $0\nu\beta\beta$ decays. Smaller quantities have been included to investigate $0\nu\beta\beta$ and measure the $2\nu\beta\beta$ decay rate, including 0.45 kg of ^{130}Te , 0.40 kg of ^{116}Cd , 36.6 g of ^{150}Nd , 9.43 g of ^{96}Zr , and 6.99 g of ^{48}Ca . Alongside the enriched foils, 0.6 kg of very pure natural tellurium and 0.6 kg of ultra-pure copper foils were installed to control and validate the background measurements. The distribution of the isotopes around the 20 sectors are shown in Figure 3.6. The masses, $Q_{\beta\beta}$ values, and natural abundances (η) for each of these $\beta\beta$ isotopes are given in Table 3.1.

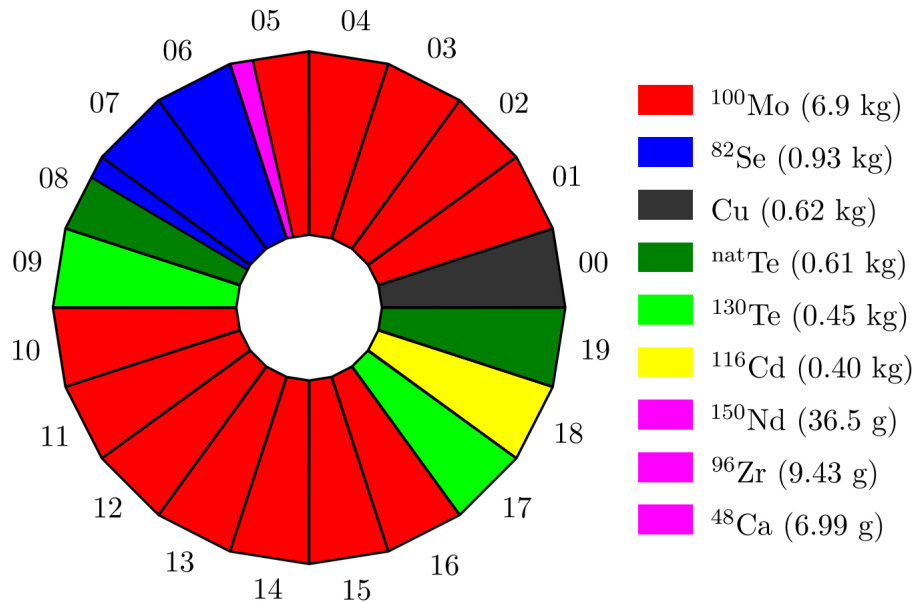


Figure 3.6: Schematic view of the seven different $\beta\beta$ sources location inside the NEMO-3 detector. The main isotopes was ^{100}Mo (6.9 kg) and ^{82}Se (0.9 kg).

Each sector supports a source frame with seven strips of $\beta\beta$ emitter 248 cm long. The five central strips were 6.5 cm wide, while the two strips on the edge were 6.3 cm wide. The surface density of the strips are in the range 30 - 60 mg/cm^2 , which is a compromise to maximise the isotope mass while maintaining the foil thin enough to reduce the electron multiple scatterings through the foil bulk, and to not degrade the energy resolution.

Two different sorts of sources were in NEMO-3 : metallic and composite. The metallic sources are metallic foils having a density of approximately $10 \text{ g}/\text{cm}^3$, corresponding to a thickness of 60 μm . The ^{116}Cd , part of ^{100}Mo and the copper foils were metallic. Note that the ^{116}Cd foils were wrapped into a plastic film to avoid them to creep. The composite foils are a mixture of source powder and organic glue. The density of the composite foil were approximately five times lower than the metallic foils, allowing thickness up to 300 μm . The composite foils were surrounded by two mylar films to provide mechanical strength. To ensure a good bond with the glue and facilitate evaporation, the mylar sheets have a large number of microscopic holes. The ^{82}Se , ^{130}Te , ^{96}Zr , ^{150}Nd and ^{48}Ca and a part of ^{100}Mo foils were composite.

Isotopes	Mass [g]	$Q_{\beta\beta}$ [keV]	η [%]
^{100}Mo	$6\,914 \pm 22$	3034.40 ± 0.17	9.63
^{82}Se	932 ± 5	2997.9 ± 0.3	8.73
^{130}Te	454 ± 2	2528.9 ± 2.1	33.8
^{116}Cd	410 ± 1	2813.50 ± 0.13	7.49
^{150}Nd	37 ± 0.1	3371.38 ± 0.20	5.6
^{96}Zr	9.4 ± 0.2	3350.0 ± 3.5	2.8
^{48}Ca	6.99 ± 0.05	4267.98 ± 0.32	0.19

Table 3.1: Mass, $Q_{\beta\beta}$, $T_{1/2}^{2\nu}$ and natural abundance of the different isotopes introduced in NEMO-3.

3.2.2 The ^{116}Cd source foil

A total mass of 440 g of cadmium was placed in sector 18. The average enrichment of ^{116}Cd was $(93.2 \pm 0.2)\%$ [136] which represents an effective mass of (410 ± 1) g of ^{116}Cd . The enrichment has been realized by the centrifugation separation method. Despite the good yield of this technique, smaller amounts of other cadmium isotopes are still present in the sample, see Table 3.2. Part of the sample (152 g) was previously measured with the NEMO-2 prototype [137].

The cadmium has been divided in seven strips of 2423 cm long and ~ 6.5 cm wide. Each strip was made of one or more smaller pieces which were glued together with Araldite AW 106 and a hardener HV953V. Two 12- μm mylar films surrounded the entire strip to provide mechanical strength. The mylar films were glued using Araldite 2020/A XW 3961 and Araldite 2020/B XW 3972.

Isotope	Mass fraction	Mass (g)
116	0.932	410.08
114	0.03228	14.20
113	0.00885	3.90
112	0.01544	6.79
111	0.00535	2.35
110	0.00468	2.06
108	0.00032	0.14
106	0.00038	0.17
Total	0.999	439.69

Table 3.2: Isotopes present in the 440 g of Cd sample placed in NEMO-3 detector. The total mass of ^{116}Cd is (410 ± 1) g which takes into account the error on the enrichment yield of 0.2%.

To ensure a good bond with the glue, the mylar sheets were perforated of microscopic holes of around 0.4 μm in diameter. The perforation has been realized at the Joint Institute for Nuclear Research (JINR, Dubna, Russia) by irradiating the mylar with a ^{84}Kr ion beam of 3 MeV/nucleon at a luminosity of 5×10^{11} ions/s. The mylar was chemically etched with NaOH at 70° C, washed with water and 1 % of acetic acid. Finally, the film was dried with hot air. All the materials entering in the process of

the backing film have been selected for their radio-purity and have been measured with High Purity Germanium detectors at LSM.

Each strip was connected to its neighboring strips with glue (Araldite AW106). A schematic view of the seven cadmium foils in sector 18 is shown in Figure 3.7. After the installation, some gaps ranging from 2 mm to 4 mm between some parts of the strips have been observed. The source shape is not strictly cylindrical as shown in the top section of Figure 3.7. It was also found that straining of the strips was small due to the softness of the cadmium metal [138].

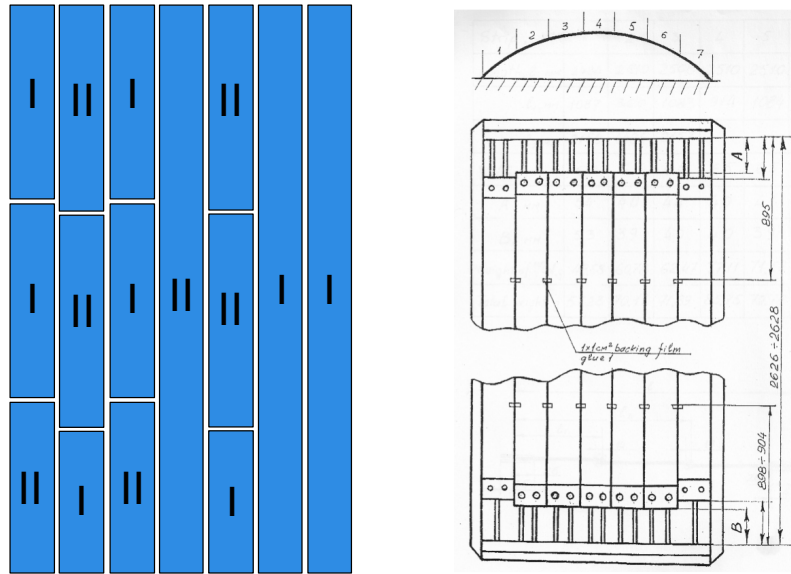


Figure 3.7: Left : Schematic view of the sector 18. The seven cadmium foils are divided in smaller pieces and glued together. The labels I and II correspond to the different ^{116}Cd productions. Right : Drawing of the strips of cadmium showing the plexiglass clips that attach the foil to the support structure. Small pieces of backing film were used to join the individual strips to one another.

Before being introduced in the detector, the radioactive contaminations of the cadmium foils have been measured thanks to High Purity Germanium detector (HPGe). The results of the different contaminations are summarized in Table 3.3.

Source	Mass [g]	Exposure [h]	Activity [mBq/kg]					
			^{40}K	^{235}U	^{234}Th	^{214}Bi	^{228}Ac	^{208}Tl
Type I	257	778	< 13	< 0.5	< 12	< 1.5	< 2	< 0.5
Type II	299	368	< 20	< 1	< 56	< 1.7	< 4	< 0.83

Table 3.3: Measurements of the cadmium source foils (including mylar support) realized with HPGe detector.

3.2.3 Tracker

The NEMO-3 tracker provides three-dimensional tracking of charged particles to measure the decay properties of $\beta\beta$ events. It is composed of 6180 vertical drift cells operating in Geiger mode, which

surround the source foils on both sides. The cells are arranged into nine different layers and divided into a 4-2-3 configuration, as shown in Figure 3.8. The four layers close to the source allow a good reconstruction of the $\beta\beta$ vertex location to the source foil, the two middle layers provide the measurement of the track curvature and the three final layers are used to determine the interaction point with the calorimeter block. The gaps between the layers correspond to the location of calorimeter modules on top and bottom, which increase the coverage of the detector.

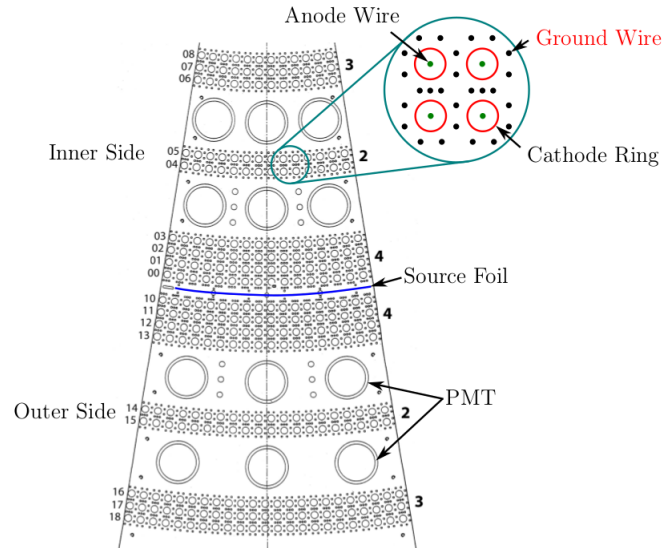


Figure 3.8: Left : The 4-2-3 configuration of the Geiger cells in a NEMO-3 sector. The 12 large rings represent the location of the light guides installed in the support structure to couple the scintillators to the PMTs. Right : Geiger wiring of four elementary Geiger cells.

An elementary cell, shown in Figure 3.9, is 2.7 m long and 3 cm in diameter, consisting of a central anode wire surrounded by eight ground wires. Four of these cathode wires are shared between the neighbouring cells, as shown in Figure 3.8. This is an advantage from a radiopurity point of view because it reduces the amount of material in the tracker volume. It also minimizes the scattering inside the tracker. An extra ground wire has been added between the layers to avoid electrostatic cross talk. The wires are made of stainless steel, 2.7 m long and 50 μm in diameter. Copper cathode rings located at the top and bottom of the anode wires collect signals. These rings are 3 cm long and 2.3 cm in diameter.

The gas inside the tracker volume is a mixture of 95 % of helium, 4 % of ethanol, 1 % of argon and 0.1 % of water held at 10 mbar above atmospheric pressure. Helium is used as basis of the tracking gas, since it is a noble gas with a low atomic number, which minimises multiple scatterings. When traversing the tracker, an electron from $\beta\beta$ decay loses only approximately 30 keV. Small quantities of ethanol are used to quench the photoionisation process, by absorbing UV photons. The performance of the tracker is then improved by reducing the re-firing effect of one cell to another. Some argon is also introduced to the mixture to stabilize the plasma propagation. Finally, in the final year of the detector, very small amounts of water vapour have been added in order to rejuvenate the ageing cells.

When a charged particle crosses the tracking volume, the gas is ionized, producing He^+ ions and electrons. By applying a potential difference of about 1600 V between anode and cathode wires, these electrons drift towards the central anode and are accelerated, ionising more atoms. This creates an

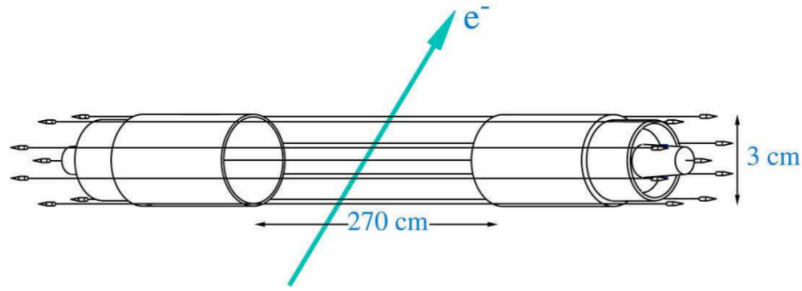


Figure 3.9: Representation of an elementary Geiger cell in NEMO-3. The central anode wire of 270 cm length is surrounded by 8 ground wires. The cathode rings are shown at each end of the cell, 3 cm of diameter.

avalanche that arrives at the anode wire and produces a signal. In this operating mode, a crossing charged particle creates ~ 6 electrons/cm. The drift speed is ~ 2.3 cm/ μ s, close to the anode, and ~ 1 cm/ μ s near the ground wires. The radial position of a particle can be reconstructed using the drift time and the global trigger (see Section 3.2.5). During the electron avalanche, induced UV photons create a plasma that propagates along the length of the wire at a speed of ~ 6 to 7 cm/ μ s. The detection of this plasma by the cathode rings on both sides gives information on the longitudinal position of a crossing particle. For 1 MeV electron, the average hit resolution of a cell has been measured to be 0.5 mm on the transversal plane and 8.0 mm on the longitudinal axis.

3.2.4 Calorimeter

The role of the NEMO-3 calorimeter is to measure the energy of the incident particles, to provide timing information of particles in an event, and to provide a fast trigger signal. The calorimeter surrounds the tracking chambers on all sides. It consists of 1940 separated optical modules. Each optical module is made of a scintillator block, two light guides and a PMT. A schematic view of a NEMO-3 optical module is presented in Figure 3.10.

The scintillator blocks are made of a polystyrene, ($C_6H_5CH=CH_2$), doped with a scintillating agent, p-Terphenyl (PTP), and a wavelength shifter 1.4-di-(5-phenyl-2-oxazolyl) benzene (POPOP). By entering a block, charged particles lose their energy through ionization and excite molecules with an energy proportional to the deposited energy. During its de-excitation, PTP translates energy into scintillation light. This light is then shifted by POPOP into a wavelength matching to the PMT sensitivity. The scintillation light is carried to the PMT via 60 mm thick light guides made of polymethyl methacrylate (PMMA). The light transmission through the guides is approximately 98 %. These light guides also provide a protection for the PMT against the helium of the tracker gas, which would damage the PMTs. The four lateral sides of the scintillator block are wrapped with 350 μ m of polytetrafluoroethylene (PTFE) in order to diffuse scintillation light and increase overall collection. A 12 μ m layer of aluminised Mylar covers the blocks to increase light collection and protect the scintillator from UV photons produced inside the tracker.

To fit the cylindrical geometry of NEMO-3, there are seven different block types referred to as IN, EE, EC, and L1-L4. The location of these blocks is shown in Figure 3.11. The EE and EC blocks are located on the outer calorimeter wall and are coupled to 5" PTMs. The IN blocks corresponds to the blocks located on the inner calorimeter wall and are coupled to 3" PMTs. The L1, L2, L3 and L4

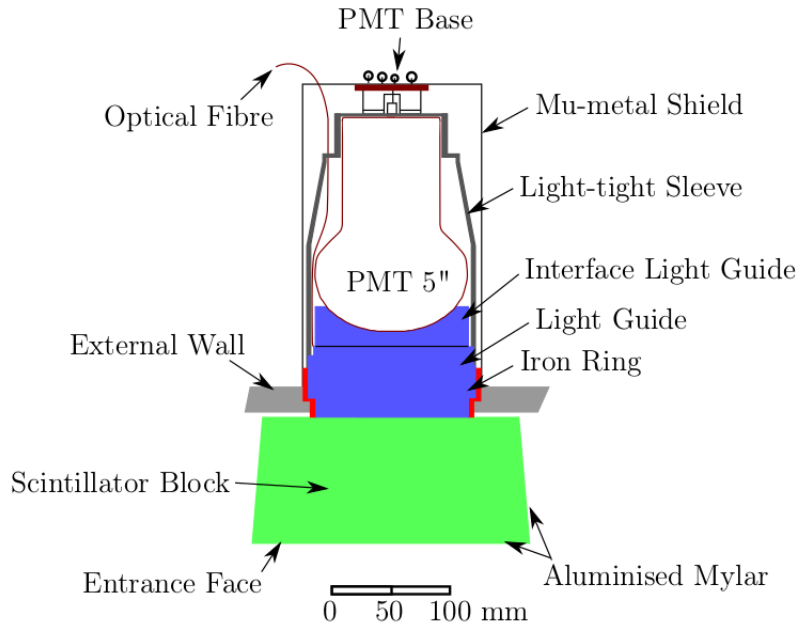


Figure 3.10: Schematic of a single NEMO-3 calorimeter module.

blocks are called petal blocks. They are located on the top and bottom of the detector, L1 being the blocks closest to the inner wall and L4 being the blocks closest to the outer wall. They are coupled to 3\"/>

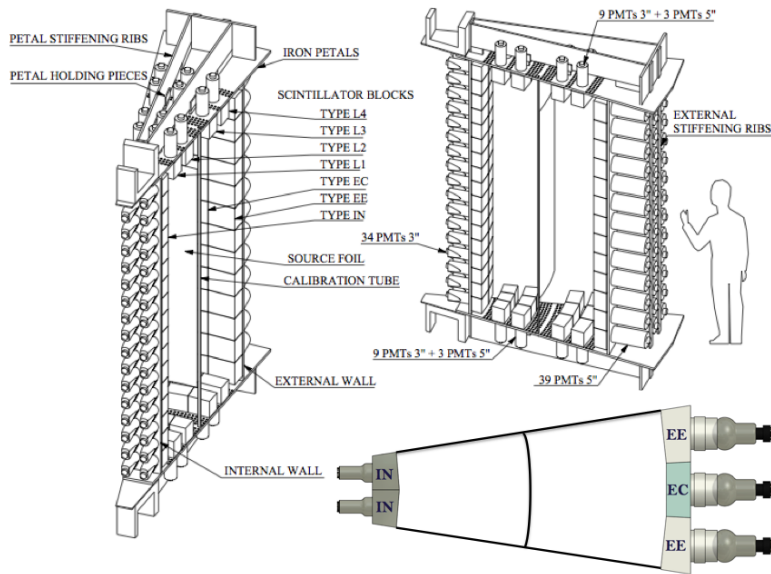


Figure 3.11: One sector of NEMO 3 with details on the source foil, scintillator blocks and photomultipliers location.

The composition and the size of the scintillator blocks are not the same, depending on their position in the detector. The IN, EE and EC blocks are made of 98.49 % of polystyrene, 1.5 % of PTP, and 0.01 % of POPOP. The IN blocks are the smallest with a front face size of 153×154 mm. The EE and EC are the largest with a front face sizes of 200×218 mm. All the petal blocks are made of 98.75 % of polystyrene, 1.2 % of PTP, and 0.05 % of POPOP. The L1 blocks have a similar size to the IN

blocks and L4 have similar size to the EE blocks.

The Hamamatsu company was chosen to produce the 3" and 5" PMTs. The 3" PMTs (R6091) possess twelve dynodes and a flat photocathode, while the 5" (R6594) have ten dynodes and hemispherical photocathode. The radiopurity of the PMT glass has been measured by HPGe detector. The contamination in ^{40}K , ^{214}Bi and ^{208}Tl have been found to be 0.34 Bq/PMT, 0.083 Bq/PMT and 5×10^{-3} Bq/PMT, respectively, for the 3" PMTs, and 0.53 Bq/PMT, 0.24 Bq/PMT and 0.014 Bq/PMT for the 5" PMTs.

3.2.5 Trigger and DAQ

The NEMO-3 detector has independent tracker and calorimeter electronics and data acquisition systems. This separation allows individual or interdependent triggering and data readout to operate in different configurations.

The 1940 PMTs of the calorimeters were supplied at 1800 V (3") and 1350 V (5") with three CAEN power supplies. Each power supply is able to provide 240 HV channels. The anode wires of the NEMO-3 tracker were supplied at a level of 1620-1650 V with two CAEN power supplies.

Trigger system

The trigger system of NEMO-3 has three separate levels referred to as T1, T2 and T3. T1 is based on information given by the calorimeter. Low and high thresholds are set in the electronic boards which read-out data from the PMTs. In case a PMT exceeds the lower threshold, which is set at 7 mV (or 23 keV equivalent), a TDC measurement and charge integration window of 80 ns opens. If a PMT exceeds the high threshold, which is set at 48 mV (150 keV), a signal is sent to the trigger logic. As a consequence, a STOP-PMT signal is sent to all calorimeter channels that stops TDC measurements and stores the integrated charge recorded in each PMT. This STOP-PMT signal is used as the time reference for the event.

T2 is based on information given by the tracker. After the STOP-PMT signal, the read-out electronics for Geiger cells is activated during $6.14 \mu\text{s}$. If an anode pulse coming from a single cell occurs within this time window, this cell is labelled as prompt hit and initiates the TDC measurements for this cell. In the same time, a HIT-GG signal is sent for all Geiger cells in its layer. The stop signal for TDC is provided when the Geiger plasma reaches the cathode rings. To meet the T2 requirements, at least three of the nine Geiger layers must be hit within a half-sector, and two of the hits must be in neighbouring layers.

The event read-out is initiated if both T1 and T2 requirements are met. The digitized time and signal for the triggered PMT channels are read out with two 14-bit analog-to-digital converters (ADCs). After the STOP-PMT signal, the Geiger cells which are not triggered within the $6.14 \mu\text{s}$ window continue the data collection up to $710 \mu\text{s}$. The TDC information of the delayed Geiger hits arriving in this time window is read out and stored. This information are then used to identify the Bi-Po cascade events.

T3 is only used during the calibration runs. It combines information from T2 with information from the calorimeter to select events likely to come from radioactive sources.

3.2.6 Energy and time calibration

As the electron energy is one of the most effective means to discriminate $0\nu\beta\beta$ signal from background, the calorimeter performance variations must be monitored over the life time of the experiment. The

absolute energy and time calibration was performed every ~ 40 days in dedicated runs. The stability of the detector between these runs was ensured by daily laser surveys.

Calibration sources

To calibrate the absolute energy, ^{207}Bi sources were introduced into the detector via copper calibration tubes located at the boundaries between each sector, and at the same radius as the source foil. Each calibration tube was equipped with three pairs of kapton windows, faced towards the inner and outer calorimeter walls, to allow for calibration source products to exit the tubes with minimal scattering. The vertical positions of the windows were at $z = -90, 0$ and $+90$ cm in order to maximise the illumination uniformity of the scintillator blocks. The decay of ^{207}Bi produces two conversion electrons with energies of 482 keV and 976 keV. The comparison between the ADC response from each of the PMTs and these known electron energies provide two-point energy calibration reliable up to 1.5 MeV. To calibrate up to 3 MeV, a ^{90}Sr calibration source was used. The end-point of the β -decay spectrum of its daughter, ^{90}Y , is at 2.28 MeV. The matching of ADC values to this end-point provide a third data point to calibrate the energy.

Tests during the assembly of the optical module observed a dependance of the energy response according to the impact point on the scintillator block. The effect observed may be as large as 10 % for the 5" PMTs. By combining multiple ^{207}Bi runs it is possible to apply corrections to the energy response based on the impact point with the scintillator.

The ^{207}Bi sources are also used to derive the calorimeter energy resolution. By fitting the two conversion electron peaks with multiple Gaussian functions, the energy resolution is extracted from the FWHM. For 1 MeV electrons, the FWHM is found to be 14-17 %.

To calibrate the time response of the calorimeter, ^{60}Co sources were used. This isotope decays via simultaneous emissions of two γ -rays with energies of 1173 keV and 1332 keV [139]. Knowing the distance between each calorimeter blocks and the source position, the difference in arrival time between the two γ -rays is used to measure the relative time shifts between each channel. The ^{60}Co sources are moved to several different positions to cover entirely the detector and all possible combinaisons of PMTs.

To determine the timing resolution, for 1 MeV electrons, the difference in arrival time between the two electrons from ^{207}Bi is used. It has been found to be $\sigma_t = 250$ ps [136].

Laser survey

To monitor the stability of the calorimeter between absolute calibration runs, a laser calibration system has been developed. A di-azote laser (N_2) with a wavelength of 337 ± 15 nm is used. The light beam is divided into two parts. The first is directly sent to a photocathode to monitor the laser light intensity. The second beam is shifted to 420 nm using a small spherical scintillator to mimic an electron signal. This signal is sent to the NEMO-3 calorimeter blocks via optical fibers. The light is also sent to six reference PMTs equipped with ^{207}Bi , allowing to monitor the laser intensity by measuring energies of both the laser and the 976 keV conversion electrons.

After each absolute calibration run, a laser survey is immediately conducted, and constitutes a reference position for the laser light peak ($C_{\text{laser}}^{\text{t}_0}$) in the reference PMTs and calorimeter PMTs. A second reference point is determined for the reference PMT, by comparing $C_{\text{laser}}^{\text{t}_0}$ to the 976 keV electron from

the ^{207}Bi source ($C_{\text{Bi}}^{\text{t}_0}$). The shift of the laser peak over the time ($C_{\text{laser}}^{\text{t}}$) is monitored for all PMTs. Any changes in $C_{\text{laser}}^{\text{t}}$ reflects both a change in the NEMO-3 PMT performances and changes in the laser light itself. By comparing $C_{\text{laser}}^{\text{t}}$ to $C_{\text{Bi}}^{\text{t}_0}$, the consequences from a change in the laser light are calibrated out, leaving only the gain variation in the PMTs to account for.

In case a PMT fluctuates too much over time, it is removed from the analysis for the periods of instability. It has been found that there is no instability for 87 % of the PMTs, with a further 7 % being unstable in a brief period.

3.2.7 Magnetic coil and shielding

Despite the fact that NEMO-3 was located at LSM under 4800 m.w.e, which highly reduces the cosmic muon flux, the detector must be protected from different background sources. Neutrons produced from (α , n) reactions, cosmic muon spallation or spontaneous fission of uranium undergo neutron capture and produce high energy γ -rays. As seen in Section 2.4.3, these γ -rays are able to reproduce the $\beta\beta$ decay signal. Layers of passive shielding were installed around the detector to protect against the external neutron and γ -ray flux. A magnetic field allowing for positron/electron discrimination helps the identification of remaining external decay products.

The magnetic coil

A solenoid magnet surrounding entirely the calorimeter produces a magnetic field of 25 Gauss parallel to the axis of the cylinder. The field is generated by running a current of ~ 30 A through a 5 tons copper coil of 5320 mm in diameter, 2713 mm high. Fans were used to cool the coil and the PMTs. A μ -metal shielding is used to protect the PMTs from the magnetic field.

The magnetic field allows discrimination between $\beta\beta$ decay events and electron-positron (e^+e^-) pair from interactions of high energy γ -rays in the source foil. The rejection efficiency of e^+e^- pair is ~ 95 % at 1 MeV [136].

The shieldings

To suppress the neutron flux inside NEMO-3, a neutron shielding surrounds the detector. This shield consists of 20 cm of paraffin located below the central tower (not shown in Figure 3.3), 35 cm of borated water placed in tanks and 28 cm of wood above and below the detector end caps. Neutrons are thermalized by the paraffin, wood or water, and captured on boron.

To stop the γ -ray emitted in the neutron capture, a second shield made of iron is placed between the detector and the first shielding. This shield is made of 177 tonnes of iron, selected for its radiopurity, and is 20 cm thick.

The anti-radon facility

Despite precautions taken to isolate the detector from the laboratory air with radon-tight seals, an excess of radon has been discovered after one year of data-taking. This high level of radon was due to leaks through the joints of the external shielding and calorimeter walls.

To fix this problem, an anti-radon facility has been installed at the end of 2004. The facility is made of an hermetic polyethylene tent surrounding the entire detector, filled with radon-free air. The air of the

laboratory was purified thanks to a radon trapping system using porous charcoal. When the air passes through the charcoal, the radon is trapped for a period of time allowing its decay. The output air is three orders in magnitude poorer in radon than the incoming air.

After the installation of the anti-radon facility, the level of radon inside NEMO-3 decreased by a factor ~ 6 [140], see Figure 3.12. This reduction is much lower than the expected reduction, which is not completely explained. The two main hypotheses are that there is a higher radon level inside the tent than at the facility output, or a significant level of radon may be emanating from detector components. The two periods before and after the installation of the anti-radon facility are referred to as Phase 1 (February 2003 to September 2004) and Phase 2 (October 2004 to January 2011) respectively.

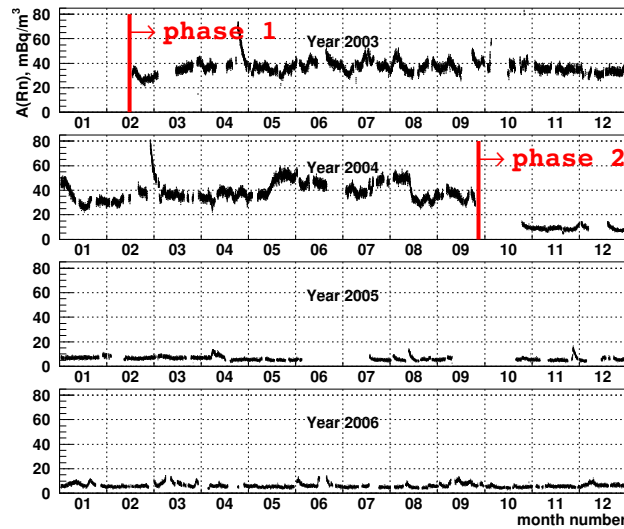


Figure 3.12: Radon activity measured in the NEMO-3 detector. The level of radon is reduced by a factor ~ 6 . The time periods preceding and following the anti-radon facility are respectively referenced as Phase 1 and Phase 2.

3.2.8 Results and measurements

After seven years of data taking, NEMO-3 has been stopped and disassembled. The strongest limit produced for $0\nu\beta\beta$ comes from ^{100}Mo , with a measurement of $T_{1/2}^{0\nu} > 1.1 \times 10^{24}$ y corresponding to $\langle m_{\beta\beta} \rangle < 0.3 - 0.8$ eV [128].

The results on the searches for $2\nu\beta\beta$ and $0\nu\beta\beta$ are gathered in Table 3.4. Most of these decays have been measured for the first time by NEMO-3 and some of them constitute the world's best measurements or limits. All the results concerning the $2\nu\beta\beta$ decay are world's most accurate. The fifth column of Table 3.4 presents the limit set on $m_{\beta\beta}$ in case of the $0\nu\beta\beta$ is induced by the exchange of a light Majorana neutrino. These results have also been interpreted in the context of other models and limits have been set on different mechanisms such as the exchange of R-parity violating supersymmetric particles, right-handed currents and majoron emission [120, 127, 128, 141].

Thanks to the ability of NEMO-3 to fully reconstruct the events topology, more exotic searches can also be performed. Studies of the decays via the excited states and search for quadruple beta decay ($0\nu 4\beta$) are ongoing [143]. Chapter 6 presents the analysis done for this thesis concerning the search for the $\beta\beta$ decays of ^{116}Cd via the excited states of ^{116}Sn .

Isotopes	Exp. [y]	$T_{1/2}^{2\nu}$ [y] 90 % C.L.	$T_{1/2}^{0\nu}$ [y] 90 % C.L.	$m_{\beta\beta}$ [eV]	ref
^{100}Mo	4.96	$[7.1 \pm 0.5] \times 10^{18}$	$> 1.1 \times 10^{24}$	$< [0.33 - 0.62]$	[128]
^{82}Se	5.25	$[10.07 \pm 0.14 \pm 0.54] \times 10^{19}$	$> 2.5 \times 10^{23}$	$< [1.2 - 3.0]$	[142]
^{130}Te	3.49	$[7.0 \pm 0.9 \pm 1.1] \times 10^{20}$	$> 1.3 \times 10^{23}$	-	[125]
^{116}Cd	5.26	$[2.74 \pm 0.04 \pm 0.18] \times 10^{19}$	$> 1.0 \times 10^{23}$	$< [1.4 - 2.5]$	[141]
^{150}Nd	5.25	$[9.34 \pm 0.22 \pm {}^{+0.62}_{-0.60}] \times 10^{18}$	$> 2.0 \times 10^{22}$	[1.6 - 5.3]	[127]
^{96}Zr	3.35	$[2.35 \pm 0.14 \pm 0.16] \times 10^{19}$	$> 9.2 \times 10^{21}$	-	[123]
^{48}Ca	5.25	$[6.4 \times {}^{+0.7}_{-0.6} {}^{+1.2}_{-0.9}] \times 10^{19}$	$> 2.0 \times 10^{22}$	$< [6.0 - 26]$	[120]

Table 3.4: Summary of the different half-lives measured for isotopes introduced in NEMO-3.

3.3 The SuperNEMO demonstrator module

Based on the success of NEMO-3, a new detector with higher sensitivity, SuperNEMO, has been proposed. The goal of the SuperNEMO experiment is the search for the $0\nu\beta\beta$ decays with a sensitivity of 10^{26} y corresponding to $m_{\beta\beta} < 0.04 - 0.1$ eV. The construction of a first SuperNEMO module called demonstrator is ongoing at LSM. It consists of a central frame supporting thin $\beta\beta$ foils surrounded by two trackers enclosed by a calorimeter as shown in Figure 3.13. The module is 4 m high, 6 m long and 2 m wide.

An extended R&D program has been performed in order to improve the detector design and its radiopurity to increase detector performance. This module will be used to validate all the design upgrades and verify that a very low level of background is achievable (10^{-4} events/keV/kg/y in the region of interest) with such a large mass of detector and source foils. It will contain 7 kg of ^{82}Se to reach a half-life sensitivity of $\sim 6 \times 10^{24}$ years, after 2.5 years of data-taking, in the best case scenario.

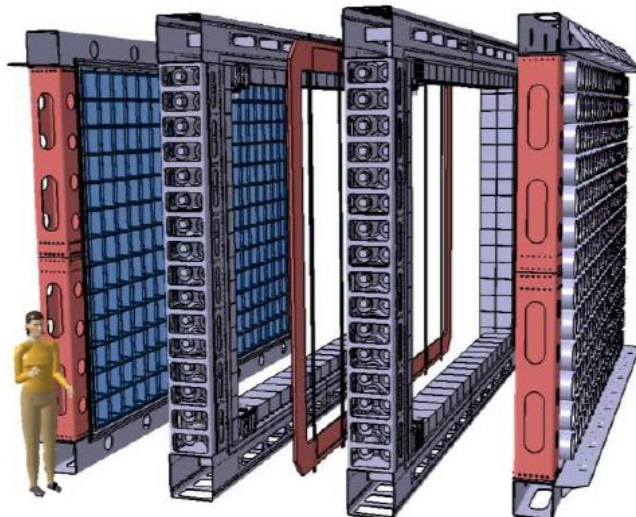


Figure 3.13: Exploded view of one module of SuperNEMO. Thin source foils of ^{82}Se are placed at the center of the detector. Two tracker modules made of 2034 Geiger cells reconstruct the electron tracks. Two calorimeter walls measure the energy of the electrons.

3.3.1 Source foils

The demonstrator module will contain 7 kg of enriched ^{82}Se . The choice of this isotope has been mainly motivated because none of its characteristics, phase space, NME, $2\nu\beta\beta$ half-life and isotopic abundance, is an obstacle to the search for $0\nu\beta\beta$. Furthermore its high end-point is far away from most of the background coming from radioactivity. To reach a sensitivity of $\sim 10^{26}$ y in $500 \text{ kg} \times \text{y}$ of exposure with ^{82}Se the radio-purity level of the source foil in ^{208}Tl and ^{214}Bi must be better than $2 \mu\text{Bq/kg}$ and $10 \mu\text{Bq/kg}$ respectively [144].

The source is divided into 36 foils of 2.7 m long as shown in Figure 3.14. The 34 central foils are 13.55 cm wide, and the 2 border foils are 12.5 cm wide.

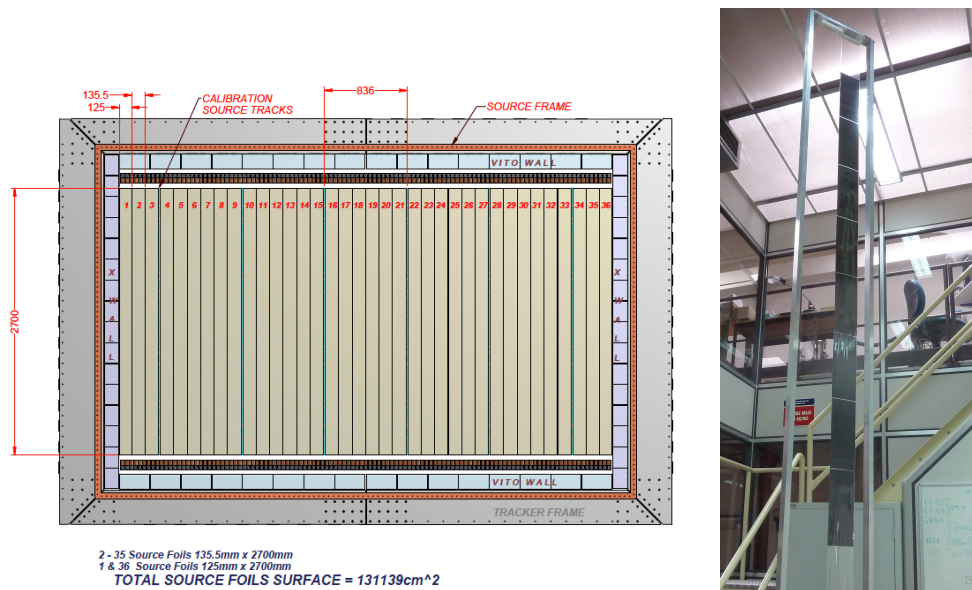


Figure 3.14: Left : Source plane design. It is divided in 36 foils (34 with 13.55 cm width and 2 with 12.5 cm width). Right : Picture of one strip.

They are composite foils with a surface densities of $40 - 60 \text{ mg/cm}^2$. The selenium is under a powder form which is mixed with a radiopure glue (PolyVinyl Alcohol : PVA) and ultrapure water to obtain a liquid paste. This paste is then spread out between two backing films made of $12 \mu\text{m}$ thick mylar sheets. However, the fabrication technique applied for NEMO-3 used perforated mylar backing film (section 3.2.2). The process to produce these holes can contaminate the source foil. It is for that reason that a new foil fabrication procedure has been proposed and studied. The new method consists of un moulding the selenium foil and cut it into pads. These pads are then inserted into two raw mylar foils without micro-holes, joined with a weld as shown in Figure 3.14. Chapter 4 presents the work done for this thesis concerning the design optimisation of the SuperNEMO source foil.

To measure the very high purity of the foils ($2\mu\text{Bq/kg}$ and $10\mu\text{Bq/kg}$ in ^{208}Tl and ^{214}Bi respectively), the NEMO collaboration decided to develop and build a dedicated detector called BiPo [145]. The concept of the BiPo detector is the identification of the so-called Bi-Po events which corresponds to the detection of an electron followed by a delayed α particle. For example, as shown in Figure 3.15, in uranium decay chain, ^{214}Bi is a β emitter decaying to ^{214}Po , which is itself an α emitter with a characteristic half-life of $164 \mu\text{s}$. The BiPo technique consists in installing the material of interest between two thin ultra pure plastic scintillators. The ^{208}Tl and ^{214}Bi contaminations are measured by

detecting the β -decay as an energy deposition in one scintillator and no coincidence signal from the opposite side, and the delayed α particle as a delayed signal in the second opposite scintillator without a coincidence in the first one.

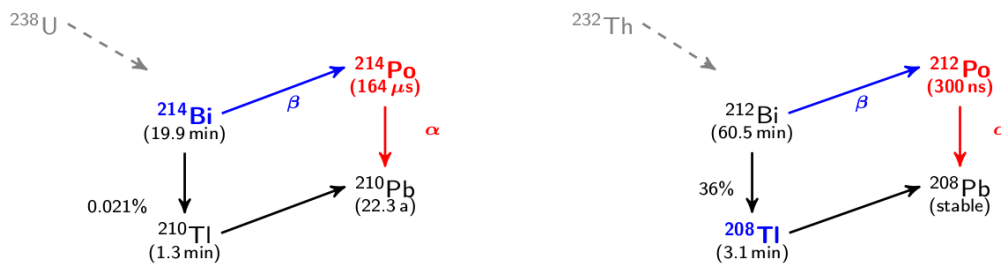


Figure 3.15: The ^{214}Bi / ^{214}Po and ^{212}Bi / ^{212}Po cascades used to measure the ^{214}Bi and ^{208}Tl contaminations.

The BiPo detector has been installed in 2012 at Canfranc Underground Laboratory in Spain. It is made of 2 identical modules, each of them containing 40 scintillator blocks (coupled with 5" PMTs). Each optical module covers an area of $30 \times 30 \text{ cm}^2$, as presented in Figure 3.16. This segmentation allows detection of possible hot spots on the foil. In a first step, the detector took data without any foils to measure its own level of background. The results of $0.16 \mu\text{Bq}/\text{m}^2$ in ^{214}Bi and $1.28 \mu\text{Bq}/\text{m}^2$ in ^{208}Tl allow to reach the expected sensitivity of 10 and $2 \mu\text{Bq}/\text{kg}$ in ^{214}Bi and ^{208}Tl , after a few months of data taking [145]. BiPo detector also measured different source foil components like the PVA or the Mylar film. The results of these measurements will be given in Chapter 4. F

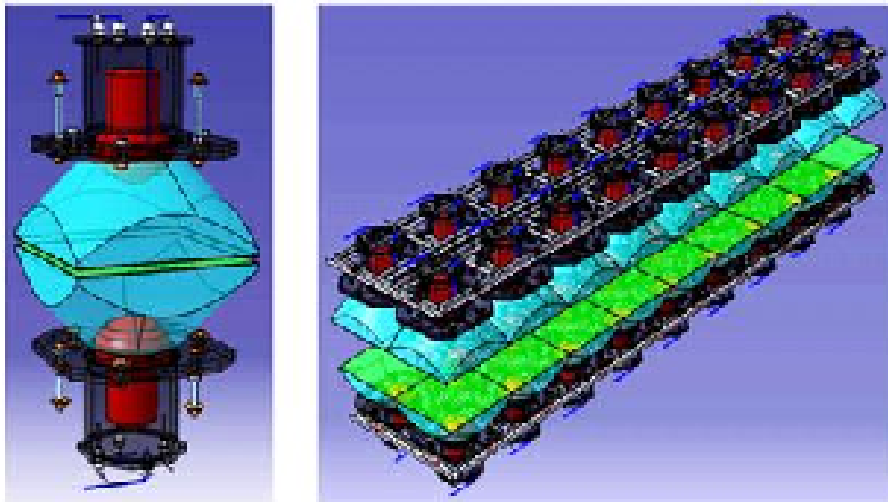


Figure 3.16: Left : Pair of sub-modules coupled face to face. The green part represents the thin scintillators. The optical guides appear in blue and the PMTs in red. Right : assembly of the 40 optical sub-modules.

3.3.2 Tracker

The SuperNEMO tracker is similar in conception to the one of NEMO-3. It contains 2034 Geiger cells arranged in 9 layers parallel to the foil within a gas mixture of He (95 %), ethyl alcohol (4 %),

Ar (1 %) [146]. Each cell is made of a 40 μm stainless steel central anode surrounded by 12 field wire of 50 μm (with neighboring wires in common). To maintain the tracking properties of the detector, the mixture ratio of the gas must be kept constant. A gas system has been developed to ensure its mixture, purification, and flowing into the detector. The SuperNEMO tracker consists of an assembly of four parts called C-sections due to their C-shape.

In order to reduce the risk of contamination of the wires, a wiring robot has been designed and built to automate the manufacturing process. A great care has also been taken concerning the radiopurity of the materials (copper, steel, duracon). Each of them has been tested in germanium detector. The construction of the basic units called cassettes and their assembly in the C frame took place under clean room conditions. To validate both the mechanical processes and the choice of the materials, radon emanation measurements of three of the four C-sections have been realized. The last C-section has not been measured considering no changes in its material and production process. The results of these measurements are summarized in Table 3.5. Extrapolated to the full demonstrator, a value of 0.21 mBq/m^3 can be obtained at nominal flowrate. The value of 0.12 mBq/m^3 can be achieved when the flush rate is at $2\text{m}^3/\text{hr}$.

C-section	Radon emanation
C0	$11.37 \pm 1.44 \text{ mBq}$
C1	$15.26^{+2.5}_{-4.0} \text{ mBq}$
C2	$3.28 \pm 1.39 \text{ mBq}$

Table 3.5: Summary of the radon emanation measurements of the different C-sections. The C3 has not been measured.

The commissioning of the first C-section has been realized using cosmic muon events. Scintillator planes below the tracker volume were acting as a trigger. A picture of a C-section and cosmic muon event is shown in Figure 3.17. Finally all the 2034 cells have been tested, 23 cells are considered as dead due to their triggering or a bad plasma propagation. The proportion of fully operational or recoverable channels is 99 % over the first three tracker sections.

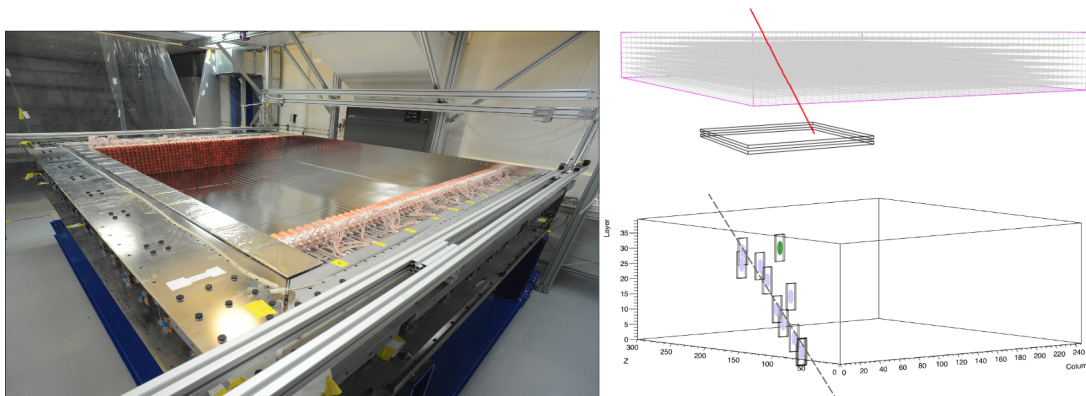


Figure 3.17: Left : picture of one of the four C-sections fully assembled. It is set horizontally, later in the SuperNEMO demonstrator, the Geiger cells will be vertical, parallel to the source foil. The copper parts are the end-caps supporting the wires. Top right : simulation of a cosmic muon crossing through the tracker. Bottom right : real cosmic muon event crossing the tracker.

In order to improve the impermeability of the seals closing the tracking volume, especially to avoid radon diffusion coming from PMTs, the wire chamber will be isolated from the rest of the detector with a nylon radon-tight film. Furthermore, the entire detector will be inside a radon clean tent.

3.3.3 Calorimeter

The goals of the SuperNEMO calorimeter are the same than the NEMO-3 calorimeter, measure the energy and arrival time of particles and provide a fast trigger. The calorimeter of the SuperNEMO demonstrator is composed of 712 optical modules distributed in six walls [147].

The two main walls are located on opposite sides of the source foil faces. Each main wall contains 260 polystyrene cubic scintillator blocks of $256 \text{ mm} \times 256 \text{ mm} \times 194 \text{ mm}$, coupled to 8" low radioactive PMT (R5912-03). The main difference with the NEMO-3 blocks is that the PMT is directly coupled to the scintillator block as shown in Figure 3.18. Furthermore, some polystyrene scintillators used in NEMO-3 have been replaced with poly-vinyl toluene (PVT). Thanks to this new design the energy resolution has been improved by a factor two, the FWHM has been measured to be 8 % at 1 MeV as shown in Figure 3.19 [147].



Figure 3.18: Optical module composing the calorimeter before being wrapped into teflon and mylar. The scintillator block is directly coupled to the PMT.

The calorimeter is completed with two γ -veto capping the top and the bottom of the detector containing 64 plastic scintillator blocks of $210 \text{ mm} \times 200 \text{ mm} \times 145 \text{ mm}$. These blocks are coupled to 5" PMTs (R6594). Finally, two x-walls cover the sides of the detector. They are made of 32 plastic scintillator blocks ($290 \text{ mm} \times 304 \text{ mm} \times 145 \text{ mm}$) also coupled to 5" PMT. Note that the first and last rows of the main wall are coupled with 5" PMTs since these blocks are partially covered by the γ -veto and will probably not be used for the analysis.

To improve the light collection, all the block sides are wrapped into teflon film while the entry face is covered by two aluminized mylar layers of $6 \mu\text{m}$. Figure 3.20 is a picture of the SuperNEMO main wall during its construction at LSM.

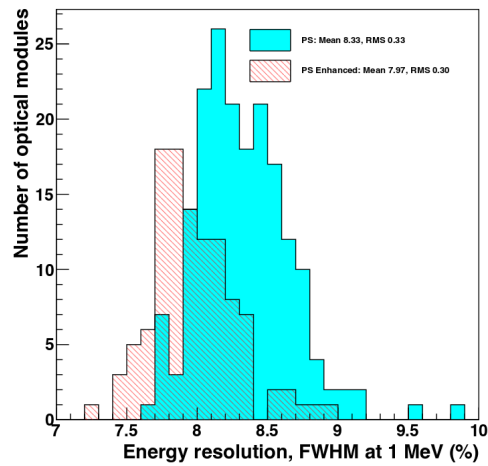


Figure 3.19: Energy resolution of the optical modules.



Figure 3.20: Front view of one main wall during its assembly at LSM. The wall is built by assembling the bricks (8 by 8).

3.3.4 Calibration system

The strategy to calibrate both energy and time is the same as that used in NEMO-3. Monthly, during dedicated runs, ^{207}Bi sources will be introduced in the detector to calibrate the absolute energy scale. Between these runs, the response and the linearity will be monitored daily.

An improvement in the calibration system consists of the removal of the calibration tubes in which the sources were introduced. In this new automated system, the ^{207}Bi sources are guided into position

thanks to a system of weights and stepper motors. In this way, no material will remain in the detector outside the calibration runs.

To monitor the response of the optical modules a light injection system has been developed. The idea is exactly the same as it was with the NEMO-3 laser survey using LEDs instead of lasers. A schematic view of the light injection system is presented in Figure 3.21. 20 UV LEDs will inject pulsed LED light into each scintillator blocks via optical fibers. A reference optical module is used to monitor the light level against a ^{241}Am source.

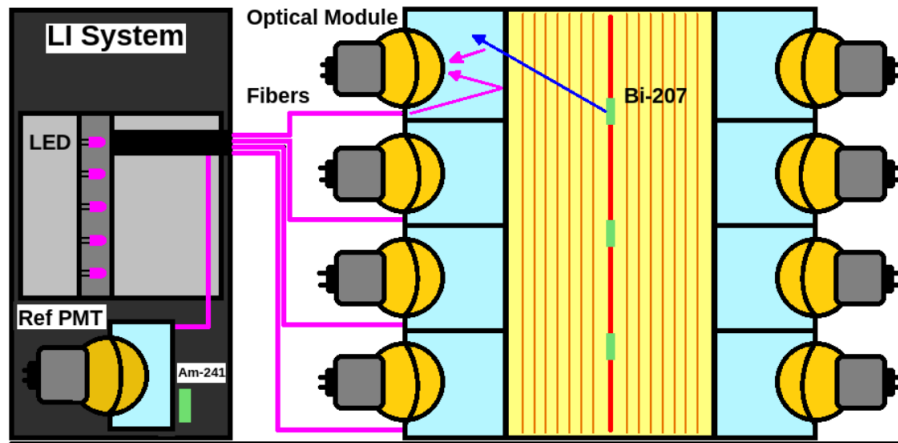


Figure 3.21: Schematic representation of the light injection system. Installed in an independent rack, a pulser will send into each optical module UV light via optical fibers. A reference PMT coupled to an americium-241 source is used to control the light level.

3.3.5 Shieldings

The strategy to protect the detector against the neutron and γ -ray fluxes is similar to the NEMO-3 strategy. Multilayer shields made of iron (20 cm), paraffin (20 cm), borated water (20 cm) and wood (30 cm) will surround the detector to reduce photon and neutron fluxes coming from the rocks of the laboratory. Finally, to minimise radon diffusion an anti-radon tent will surround the detector and will be constantly flushed with filtered air.

3.3.6 Prospects

The construction of the demonstrator began with most of the different components already manufactured and present at LSM. The first and second calorimeter walls were built between the end of 2016 and the beginning of 2017. Two C-sections have been assembled and coupled to the first calorimeter wall to form a half-detector. The installation of the source foils is planned by autumn of 2017.

In case the demonstrator module is successful, other SuperNEMO like modules could be deployed. The goal would be to investigate $0\nu\beta\beta$ with 100 kg of ^{82}Se to reach a half-life sensitivity of 10^{26} years, corresponding to an effective neutrino mass of 50 - 100 meV. The 100 kg of ^{82}Se could be divided between 20 identical and independent modules, in a way to provide flexibility in the modules location as they can be arranged to maximise the available space in underground laboratories. As the source is decoupled from the detector, other isotopes as ^{150}Nd and ^{48}Ca could also be introduced.

Table 3.6 summaries key experimental achievements of NEMO-3 and the target levels for SuperNEMO to reach the sensitivity of 10^{26} years.

	NEMO-3	SuperNEMO
Mass [kg] (main isotopes)	7 (^{100}Mo)	100 (^{82}Se) (7 kg demonstrator)
$T_{1/2}^{2\nu}$ [y]	7.2×10^{18}	9.9×10^{19}
Energy resolution		
FWHM at 1 MeV	15 %	8 %
FWHM at 3 MeV	8 %	4 %
Source radiopurity		
A(^{208}Tl)	$\sim 100 \mu\text{Bq/kg}$	$< 2 \mu\text{Bq/kg}$
A(^{214}Bi)	$< 300 \mu\text{Bq/kg}$	$< 10 \mu\text{Bq/kg}$
Level of radon A(^{222}Rn)	$\sim 5.0 \text{ mBq/m}^3$	$< 0.15 \text{ mBq/m}^3$
Sensitivity after 5 y of data taking	$T_{1/2}^{0\nu} > 10^{24}$	$T_{1/2}^{0\nu} > 10^{26} \text{ y}$

Table 3.6: Summary of the key experimental achievements of NEMO-3 and the target levels for SuperNEMO.

Chapter 4

Source foil design optimisation

Sensitivity studies of the SuperNEMO experiment have shown that to reach a sensitivity of $\sim 10^{26}$ y in $500 \text{ kg} \times \text{y}$ of exposure with ^{82}Se , the radio-purity level of the source foil in ^{208}Tl and ^{214}Bi must be better than respectively $2 \mu\text{Bq/kg}$ and $10 \mu\text{Bq/kg}$ [144]. In order to measure these very low contaminations, the collaboration built the BiPo detector as explained in Section 3.3.1. The LAPP team is involved in the fabrication of half of the source foils for the SuperNEMO demonstrator module and proposed alternative source foil designs to the composite foil adopted in NEMO-3 in order to reach the level of radio-purity. The two main designs explored are a NEMO-3-like foils made of ^{82}Se , glue and two mylar backing films, and a design made of ^{82}Se , glue and a central nylon mesh. These two different concepts could induce different performances such as the level of background or the sensitivity to the $0\nu\beta\beta$ half-life.

This chapter summarizes the work realized on the optimisation of the source foil design of the SuperNEMO demonstrator module. Section 4.1 presents the results of the radio-purity measurements of the different materials entering in the fabrication of the different source foils designs. The description of these designs is also provided in this section. The simulation of the events coming from the source foil, the reconstruction of the detector response and the selection of the $2e$ events are presented in Section 4.2. Section 4.3 describes the calculation and the validation of the sensitivity. The detector performances with the different designs of the ^{82}Se source foil are presented in Section 4.4. The conclusion of the work is given in Section 4.5.

4.1 Source foil design

The source of double-beta decay is made of enriched ^{82}Se powder shaped in thin foils to minimise the energy loss of the out-coming particles and placed in the middle of the detector as discussed in Section 3.3.1.

To eliminate background events due to impurities in the source foil, the required radio-purity levels for ^{208}Tl and ^{214}Bi are very challenging. In order to shape the $\beta\beta$ emitter in thin foils, the ^{82}Se powder is mixed with a polyvinyl-alcohol (PVA) glue to produce a solid and uniform thin foil. A mechanical support is required to provide enough strength over a 3 m long foil. Different material can be considered as mechanical support for the foil as well as different amount of PVA could be used. However the choice of the best materials and the design of the foil must be performed taking into account different aspect which are the radio-purity level in ^{208}Tl and ^{214}Bi , the mass of a given material w.r.t ^{82}Se mass and the thickness of the foil.

Section 4.1.1 recalls the source foil geometry of the SuperNEMO demonstrator module. The foil composition and the radiopurity of the materials are respectively described in Section 4.1.2 and Section 4.1.3. The different designs under consideration are introduced in Section 4.1.5. Some final considerations are discussed in Section 4.1.6.

4.1.1 Foil geometry

As described in Section 3.3.1, the source foil of the SuperNEMO demonstrator module consists of 36 strips 270 cm long for a total surface of about 14 m² which will contain 7 kg of ⁸²Se, with a surface density of about 50 mg/cm². A drawing of the source foil is shown in Figure 3.14. The total mass of ⁸²Se is fixed but the mass of the other materials, especially for the mechanical strength of the foil, will depend on the source design.

4.1.2 Foil composition

Depending on the design under consideration, different materials can enter in the composition of the source foils, they are described below.

Selenium

Six natural selenium isotopes exist : ⁷⁴Se, ⁷⁶Se, ⁷⁷Se, ⁷⁸Se, ⁸⁰Se and ⁸²Se. Selenium is a nonmetal element discovered in 1817 by the Swedish chemist Jacob Berzelius. All these isotopes are stable, except ⁸²Se which decay via double beta decays to ⁸²Kr with a very long half-life of 1.0×10^{20} y [124]. Selenium is rarely found as a pure ore and its salts are toxic in large amounts. Selenium can appear red, grey or black depending on the molecular structure of the salt. In its black form, selenium is irregular and complex, and consists of polymeric rings with up to 1000 atoms per ring.

Polyvinyl alcohol

Polyvinyl alcohol (PVOH, PVA, or PVAL) is a water-soluble synthetic polymer. It has the idealised formula $[\text{CH}_2\text{CH}(\text{OH})]_n$. It is used in paper-making, textiles, and a variety of coatings. It is colourless and odourless. It is sometimes supplied as beads or as solutions in water.

Mylar

BoPET (Biaxially-oriented polyethylene terephthalate) is a polyester film made from stretched polyethylene terephthalate (PET) and used for its high tensile strength, chemical and dimensional stability, transparency, reflectivity, gas and aroma barrier properties, and electrical insulation.

Nylon6-6

Polyamide from nylon class, made of hexamethylenediamine and adipic acid, which gives nylon 6-6 a total of 12 carbon atoms in each repeating unit, and its name. Nylon 6-6 is frequently used when high mechanical strength, great rigidity, and good stability under heat is required.

4.1.3 Material radiopurity

The level of contamination in ²⁰⁸Tl and ²¹⁴Bi of the materials under consideration for the foil production have been measured in BiPo [145]. The activities in ²⁰⁸Tl and ²¹⁴Bi at 90% C.L. are summarised in Table 4.1.

Material	Density [g/cm ³]	A (²¹⁴ Bi) [μBq/kg]	A (²⁰⁸ Tl) [μBq/kg]
PVA	1.30	[532;1094] ± 77	< 65
Nylon6-6 (tulle)	1.08	[275;681] ± 48	[222;407] ± 32
Mylar backing film	1.40	[618;1637] ± 106	[64;229] ± 14

Table 4.1: Material densities and radio-purities, as measured by BiPo. The values represent the 90% C.L. intervals. The systematic uncertainties on the interval limits are also reported.

4.1.4 Foil parameters

In this section, several useful parameters characterising the different foil compositions are defined. The mass fraction f_i of a given component is defined as the ratio between its mass M_i and the total mass of the compound M_T :

$$f_i = \frac{M_i}{M_T} \quad (4.1)$$

The density ρ of the compound is defined as the average of the density of each ingredient ρ_i weighted on their mass fraction :

$$\rho = \sum_i f_i \rho_i \quad (4.2)$$

If the compound is uniformly spread over a flat surface S , as in our case with the source foil, its surface density is defined as :

$$a = \sum_i a_i = \frac{\sum_i M_i}{S} \quad (4.3)$$

and the thickness of the foil as :

$$t = \frac{a}{\rho} \quad (4.4)$$

By taking the definitions given in Equations 4.1, 4.2, 4.3, Equation 4.4 can be rewritten as :

$$t = \frac{M_T}{S \times \rho} \quad (4.5)$$

As shown by the Equation 4.5, for a given surface, the thickness of the foil increases linearly with the mass of the components, and decreases linearly with the total density of the compound. A last parameter to define is the total expected activity in ²⁰⁸Tl and ²¹⁴Bi, defined as :

$$A = \sum_i \frac{f_i}{f_{Se}} \times A_i \quad (4.6)$$

where A_i are the activities measured by BiPo for the different components summarised in Table 4.1.

4.1.5 Designs under consideration

The main designs under consideration for the source foil of the SuperNEMO demonstrator module are described in this section.

IDEAL

The IDEAL design is a design in which the source foil is made of ^{82}Se mixed with a small fraction of PVA ($< 5\%$). This design is referred to ideal because it is not realistic. From the technical point of view, this design is very hard to produce and handle as there is no mechanical support. Nevertheless, this design is not without interest since it represents the simpler design which can be considered at this stage. Due to the absence of a mechanical support and the small amount of PVA, the IDEAL design is expected to provide thinner foils with smaller contamination in ^{208}Tl and ^{214}Bi .

MYLAR

The MYLAR design is based on the design developed for the source foil of NEMO-3. In this design, ^{82}Se and PVA are mixed together in a paste which is spread as uniform as possible within two mylar films of $12\mu\text{m}$ thick and $\sim 2.5\text{ mg/cm}^2$ of surface density. The evaporation of the water contained in the paste and the drying of the foil is favored by the presence of micro holes in the mylar film. Note that adding the mylar film, which provides a mechanical support, brings additional contamination with respect to the IDEAL case. A schematic view of the foil design is shown in Figure 4.1.

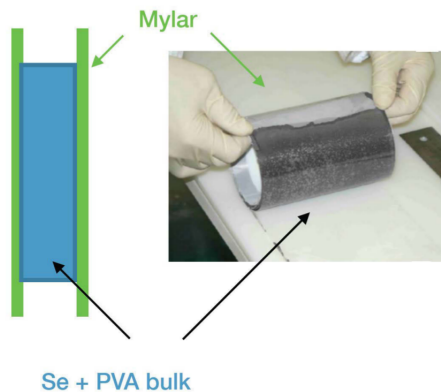


Figure 4.1: Schematic side view of the mylar design.

TULLE

The TULLE design is a new design for the source foils in which the ^{82}Se and the PVA paste is spread as uniform as possible over a thin layer of bobbinet tulle made of nylon6-6 providing a light and resistant mechanical support. A schematic view of the foil design is shown in Figure 4.2. The bobbinet tulle is constructed by warp and weft yarns in which the weft yarn is looped diagonally around the vertical warp yarn to form a hexagonal mesh which is regular and clearly defined.

To minimise the contamination in ^{208}Tl and ^{214}Bi coming from the tulle, the lightest fabric available on the market has been chosen, corresponding to a weight of 0.7 mg/cm^2 and was not treated with resins nor paint after weaving. The tulle is lighter than the mylar backing film and gives the advantage of introducing a smaller contamination of ^{208}Tl and ^{214}Bi which will translate in lower background levels. Nevertheless, in this design, due to the lack of external protection the source foil is directly in contact with the gas in the tracker and is exposed to the risk of ^{82}Se losses. In order to avoid this problem the amount of PVA can be increased to improve the foil strength. An increase of the amount of PVA will translate into a higher contamination and a higher thickness of the source foil.

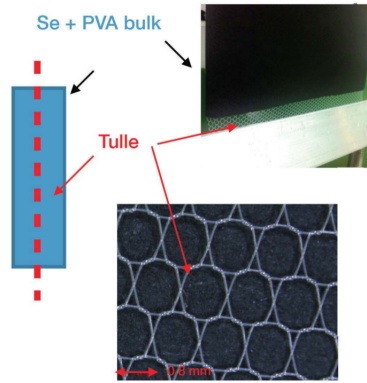


Figure 4.2: Schematic side view of the tulle design.

4.1.6 Discussion

The parameters used for the modelisation of the source foils for the different designs are summarized in Table 4.2 and 4.3. The case of the MYLAR foil, which is considered as an IDEAL foil with two external backing films, the parameters are shown separately for the bulk (b) and the film (f). The TULLE foil is modelled as an IDEAL foil with the nylon mesh uniformly distributed in the foil.

As shown in Table 4.3, from the radio-purity point of view, the TULLE design is very promising. Compared to the MYLAR design, even if more PVA is used, it allows to obtain a total activity in ^{214}Bi and ^{208}Tl which is respectively 18% and 29% lower.

Design	f_{Se} [-]	f_{PVA} [-]	f_{Support} [-]	a [mg/cm^2]	ρ [g/cm^3]	t [μm]
IDEAL	0.95	0.05	0.00	52.5	3.11	169
TULLE	0.888	0.10	0.012	56.3	2.98	189
MYLAR	0.95	0.05	-	$52.5_{\text{b}} + 3.2_{\text{f}}$	$3.11_{\text{b}} + 1.4_{\text{f}}$	$169_{\text{b}} + 24_{\text{f}}$

Table 4.2: Summary of the foil parameters for the source foil designs under consideration. The MYLAR design is considered as IDEAL with two external backing films. The parameters in this case are then shown separately for the bulk (b) and the film (f).

Design	$f_{\text{Se}}/f_{\text{Se}}$ [-]	$f_{\text{PVA}}/f_{\text{Se}}$ [-]	$f_{\text{Support}}/f_{\text{Se}}$ [-]	$A (^{214}\text{Bi})$ [$\mu\text{Bq}/\text{kg}$]	$A (^{208}\text{Tl})$ [$\mu\text{Bq}/\text{kg}$]
IDEAL	1	0.053	0.000	62.0	3.4
TULLE	1	0.113	0.014	142.5	13.5
MYLAR	1	0.053	0.068	$62.0_{\text{b}} + 111.6_{\text{f}}$	$3.4_{\text{b}} + 15.6_{\text{f}}$

Table 4.3: Expected ^{208}Tl and ^{214}Bi activities computed from Equation 4.6. The values do not include the activity of the ^{82}Se which is not known at this stage.

4.2 Monte-Carlo simulations

The study performed in this work is based on the event simulation performed through the software developed by the collaboration. The propagation of the particles through the detector is performed by a GEANT4 based module which simulates all relevant processes, such as multiple scattering, ionisation, Compton scattering, Bremsstrahlung. The detector response is then obtained by smearing the true information provided by GEANT4 with respect to the calorimeter and the tracker resolution. Dedicated reconstruction and selection modules allow to select events in a specific channel for dedicated analysis.

4.2.1 Source foils modelisation

The modelisation of the source foils is realized through rectangular boxes made of ^{82}Se , PVA, nylon or mylar depending on the design under consideration. The composition of the different designs introduced in Section 4.1.5 are used with the parameters summarised in Table 4.2. The implementation of the material composition is performed by defining the fraction mass for each element, mainly ^{82}Se , $^{\text{Nat}}\text{Se}$, O, C and N which is found in the nylon mesh.

4.2.2 Event generation

The generation of the events is performed uniformly from the source foil. They are generated for the $0\nu\beta\beta$, $2\nu\beta\beta$ and the internal background coming from contamination in ^{208}Tl and ^{214}Bi . For the MYLAR design, to take into account the contamination coming from the backing film, events of ^{208}Tl and ^{214}Bi are also generated in the mylar film. Table 4.4 shows the statistics generated for each event type.

Design	$0\nu\beta\beta$	$2\nu\beta\beta$	^{208}Tl	^{214}Bi
IDEAL	10^6	10^7	10^7	10^7
TULLE	10^6	10^7	10^7	10^7
MYLAR				
(bulk)	10^6	10^7	10^7	10^7
(film)			10^7	10^7

Table 4.4: Generated statistics for each event type and source foil design.

Since the event generation has been performed with many different configurations of the source foil, the statistics has been optimised to contain the event production within reasonable processing time (24 hours). This current production allows to keep the statistical uncertainty on the number of events selected in the relevant energy region within 0.2% for the $0\nu\beta\beta$ and the $2\nu\beta\beta$ events and within 5% for the ^{208}Tl and ^{214}Bi events which is already a factor 2 lower than the systematic uncertainties observed for the internal background in NEMO-3 (10%). As these systematics are expected to be similar in SuperNEMO, we consider that the statistics of the MC samples is enough in this context.

4.2.3 Energy distribution

The reconstruction of the events and the selection of the 2e channel is then performed. Only the events having two negative tracks hitting two calorimeter blocks with a total energy deposition $E_{\beta\beta} > 2 \text{ MeV}$ are selected. The energy distributions for the signal and the backgrounds are shown in Figure 4.3. These p.d.f will be used thereafter to compare among different designs of the source foil. The IDEAL design

is shown in black, the TULLE design in red and the MYLAR design in blue. From these distributions it can be seen that the shape of the energy distribution does not depend heavily on the considered design even if a small overall decrease of the event selection efficiency is observed for the TULLE and MYLAR design compared to the IDEAL case. This decrease is more important for the $0\nu\beta\beta$ and $2\nu\beta\beta$ while it is not significant for the ^{208}Tl and ^{214}Bi . The effect is due to the increased thickness of the source foil in the TULLE and the MYLAR designs compared to the IDEAL case, which slightly shifts the p.d.f to the lower energies due to an increased energy loss in the foil. The selection efficiency for the signal and the background obtained in the [2000; 3200] keV energy window are shown in Table 4.5.

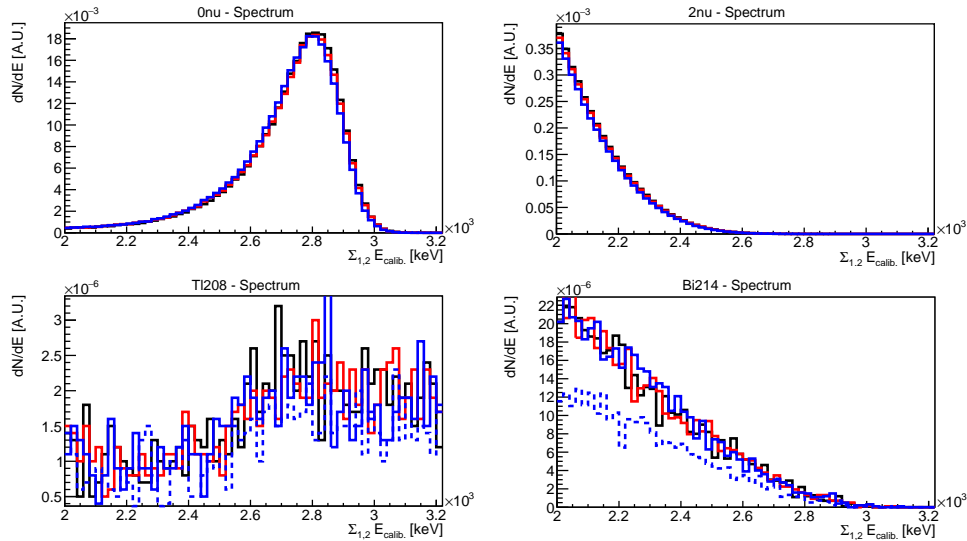


Figure 4.3: Comparison of the 2e energy distribution for signal and background channels for different source foil designs. Black IDEAL. Red : TULLE. Blue : MYLAR. Top left : $0\nu\beta\beta$, top right : $2\nu\beta\beta$, bottom left : ^{208}Tl , bottom right : ^{214}Bi . The dashed blue histogram in the bottom plots represent the expected energy for events generated in the mylar backing film.

Design	$\epsilon_{0\nu}$ [%]	$\epsilon_{2\nu}$ $\times 10^{-2}$ [%]	ϵ_{Tl} $\times 10^{-2}$ [%]	ϵ_{Bi} $\times 10^{-2}$ [%]
IDEAL	29.01 ± 0.05	33.64 ± 0.04	0.99 ± 0.03	4.3 ± 0.1
TULLE	28.84 ± 0.04	33.05 ± 0.04	0.95 ± 0.03	4.4 ± 0.1
MYLAR				
(bulk)	28.86 ± 0.04	31.75 ± 0.04	0.92 ± 0.03	4.5 ± 0.1
(film)			0.73 ± 0.03	2.7 ± 0.1

Table 4.5: Event selection efficiency in the 2e channel in [2000; 3200] keV.

4.3 Sensitivity study

In order to define the sensitivity to a phenomenon not yet observed, we assume the experiment does not observe any signal. In this worse case scenario, we study which portion of the allowed parameter phase space the experiment can exclude. The p.d.fs obtained in the previous section with the IDEAL design are used in the following as example of sensitivity computation. Here the backgrounds are normalised to $2 \mu\text{Bq/kg}$ and $10 \mu\text{Bq/kg}$ for the ^{208}Tl and the ^{214}Bi internal background respectively (i.e. the target

radio-purity level of SuperNEMO). The $2\nu\beta\beta$ background is normalised to 9×10^{19} y as measured in NEMO-3 [140]. This configuration is referred in the text as IDEAL*.

4.3.1 R.O.I method

As defined in Section 2.4, the sensitivity on the $0\nu\beta\beta$ decay half-life is given by :

$$T_{1/2}^{0\nu} > \frac{N_A \ln 2}{W} \times \frac{\epsilon \times M \times T}{S(b)} \quad (4.7)$$

where N_A is the Avogadro number, W the atomic mass of the $\beta\beta$ isotope under study, ϵ is the signal selection efficiency and $M \times T$ the total experimental exposure. The $S(b)$ term represents the average upper limit on the number of signal events that would be obtained by an ensemble of identical replicas of such experiments, each one with the same mean expected background and no true signal. The Feldman & Cousins unified approach for the definition of the confidence level is adopted [148]. This method optimises the region of interest (R.O.I.) with respect to the sensitivity to the $T_{1/2}^{0\nu}$. This optimisation is achieved by maximising the $\epsilon/S(b)$ ratio for a given exposure $M \times T$.

4.3.2 Selection efficiency

The signal and the background selection efficiencies in the 2e channel are obtained by integrating the respective p.d.f. in the R.O.I. defined by the energy window (E_{low} , E_{up}) :

$$\epsilon_i(E_{low}; E_{up}) = \frac{1}{N} \int_{E_{low}}^{E_{up}} \frac{dN}{dE} dE \quad (4.8)$$

Figure 4.4 shows the value of efficiency for the $0\nu\beta\beta$ signal (red) and background ($2\nu\beta\beta$ in blue, ^{214}Bi in orange and ^{208}Tl in green) when the upper edge of the R.O.I. is kept fixed at 4500 keV while the lower edge is moved from 2000 keV up to 3500 keV. These efficiencies are then used to estimate the expected background level for a given exposure $M \times T$ following :

$$N_{2\nu} = \frac{N_A \ln 2}{W} \times \frac{\epsilon_{2\nu} \times M \times T}{T_{1/2}^{2\nu}} \quad (4.9)$$

$$N(^{214}\text{Bi}) = A(^{214}\text{Bi}) \times \epsilon(^{214}\text{Bi}) \times M \times T \quad (4.10)$$

$$N(^{208}\text{Tl}) = A(^{208}\text{Tl}) \times \epsilon(^{208}\text{Tl}) \times M \times T \quad (4.11)$$

Where $T_{1/2}^{2\nu}$ is the measured half-life for the $2\nu\beta\beta$ decay, and $A(^{214}\text{Bi})$ and $A(^{208}\text{Tl})$ are the expected activity level of ^{214}Bi and ^{208}Tl contamination of the foil source. The expected number of background events as a function of the low energy edge of the R.O.I is provided by the renormalisation of the histogram given in Figure 4.4 through the Equations 4.9, 4.10 and 4.11 and is shown in Figure 4.5.

Instead of fixing the value of E_{up} when computing the integral of Equation 4.8, both edges of the R.O.I can be changed to obtain a 2D scan of the selection efficiencies. The same renormalisation through Equations 4.9, 4.10 and 4.11 provides the 2D scan of the expected number of background events w.r.t. the edges of the R.O.I. as shown in Figure 4.6.

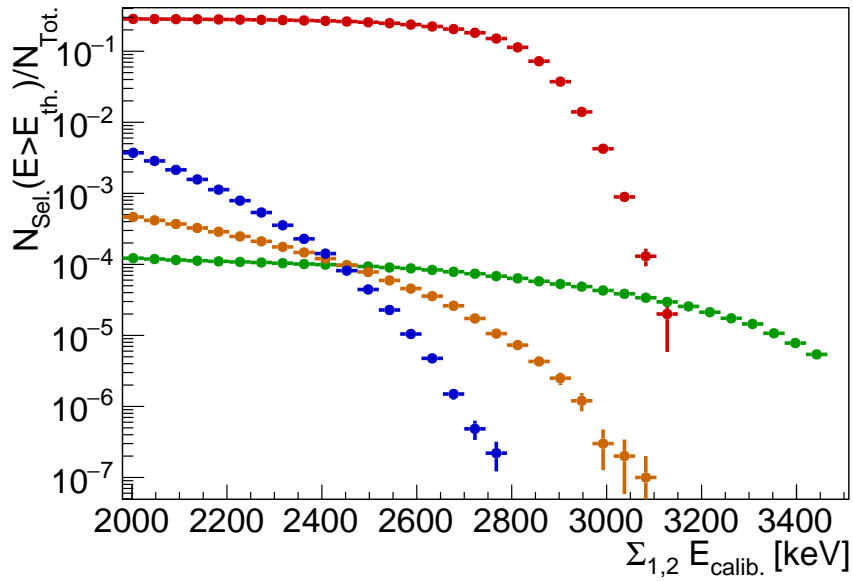


Figure 4.4: Selection efficiency for the ^{82}Se $0\nu\beta\beta$ signal (red) and the different backgrounds ($2\nu\beta\beta$ in blue, ^{214}Bi in orange and ^{208}Tl in green). The upper edge of the R.O.I is kept fixed at 4500 keV while the lower edge is moved from 2000 keV up to 3500 keV.

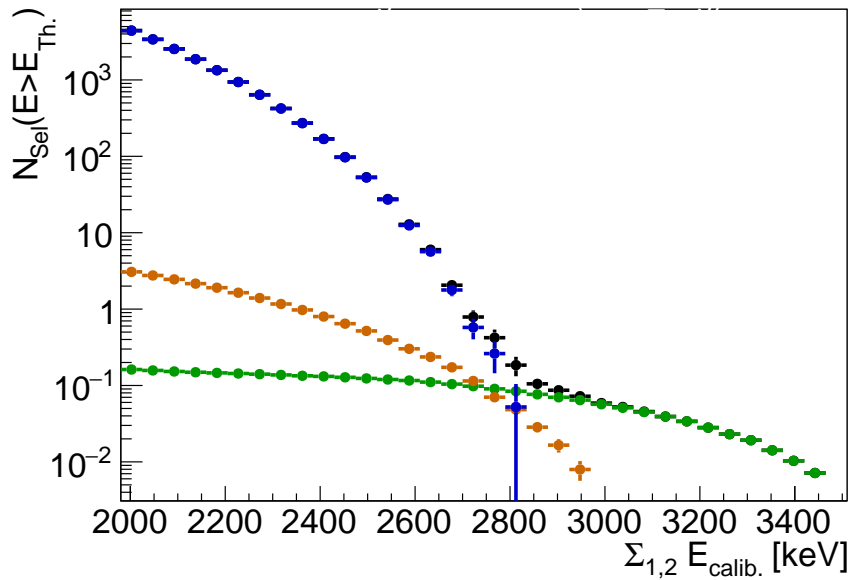


Figure 4.5: Expected number of background events ($2\nu\beta\beta$ in blue, ^{214}Bi in orange and ^{208}Tl in green) as a function of the low energy edge of the R.O.I. The black points show the sum of all background contributions.

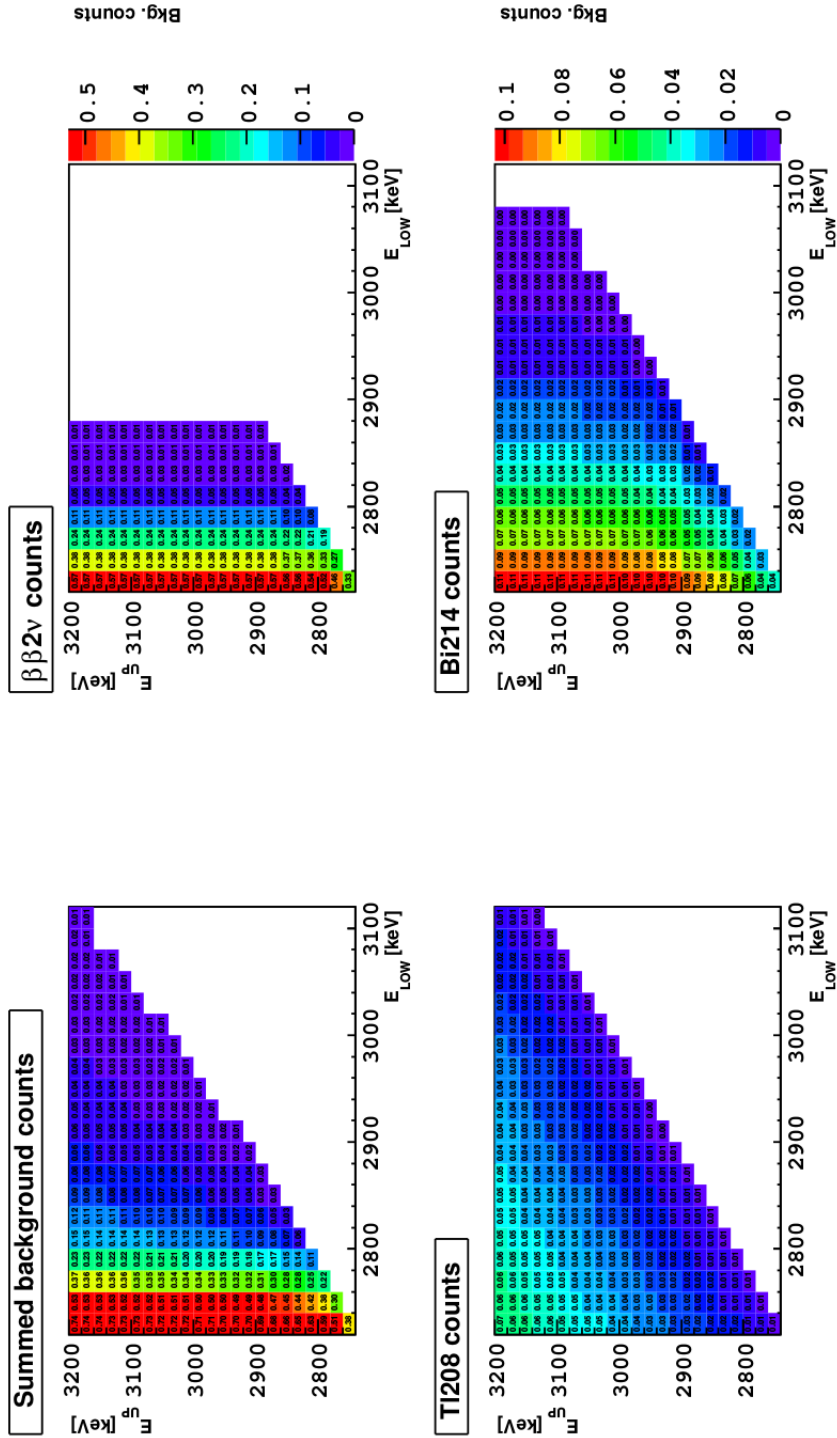


Figure 4.6: Expected background counts as a function of the edges of the R.O.I..

4.3.3 The Feldman & Cousins 90% C.L.

The $\mathcal{S}(b)$ term of Equation 4.7 is defined following the Feldman & Cousins prescription for the definition of confidence interval of a small signal [148]. Defining $U(n|b)$ as the function yielding the (unified approach) upper limit (at the desired C.L.) for a given observation n and a mean predicted background level b . Given that the variable n follows a Poisson p.d.f., $P(n|b) = P(n; b)$, then $\mathcal{S}(b)$ is given by :

$$\mathcal{S}(b) = E[U(n|b)] = \sum_{n=0}^{\infty} \mathcal{P}(n; b) \times U(n|b) \quad (4.12)$$

The sensitivity $\mathcal{S}(b)$ of an experiment expecting b events of background and no true signal is obtained by averaging the upper limits obtained using the unified approach $U(n|b)$ with the likelihood of the individual observations $P(n|b)$. Figure 4.7 shows the 90% C.L. curve for a background level spanning in $[0; 40]$ c.t.s. Note that in the large background approximation, the sensitivity curve as a function of b follows the expected classical limit obtained through the Neyman construction of the confidence belt, with $a = 1.64$ (1.96) at 90% (95%) C.L. : $\mathcal{S}(b) \propto a \times \sqrt{b}$, for large b .

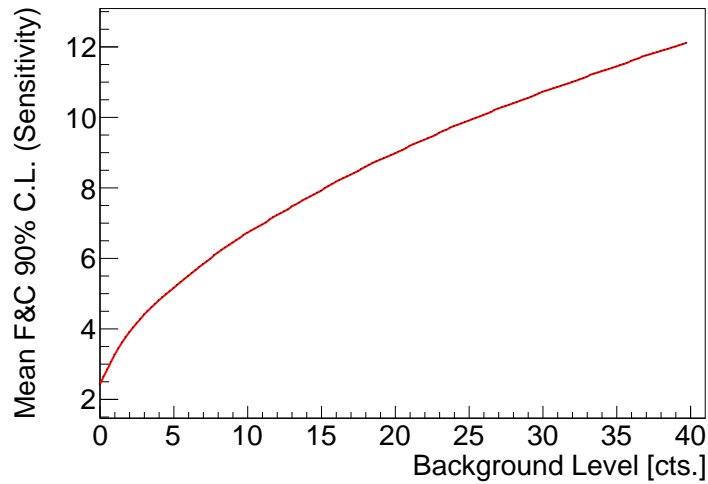


Figure 4.7: The 90% C.L. sensitivity curve as a function of the number of background events.

4.3.4 1d vs 2d R.O.I. optimisation

By using Equation 4.7, the sensitivity is computed as a function of the R.O.I for a given experimental exposure. Figure 4.8 shows the 1d sensitivity scan as a function of the low energy edge of the R.O.I. for an exposure of $21 \text{ kg}\times\text{y}$. The best sensitivity is found to be $6.1 \times 10^{24} \text{ y}$ in the energy window of $[2720; 3200]$ keV. The expected total background contamination in the region is of 0.74 ± 0.06 cts. The same strategy is applied for the 2d optimisation of the R.O.I, except both edges simultaneously vary to optimise the R.O.I.. The best sensitivity of $6.12 \times 10^{24} \text{ y}$ is found in $[2720; 3060]$ keV, with an expected total background contamination of 0.72 ± 0.06 cts. No major reduction of the background is observed, the results are found to be compatible within the statistical uncertainties.

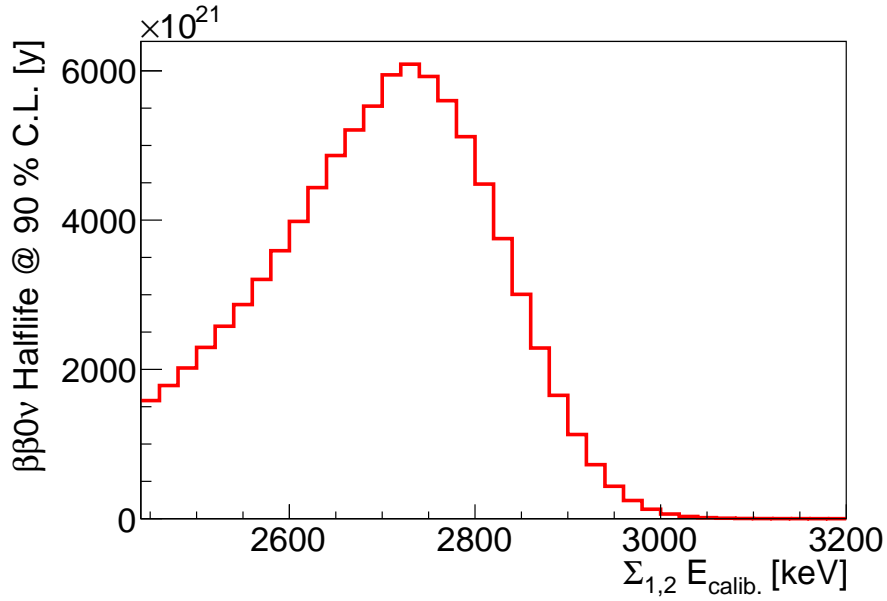


Figure 4.8: The 1d sensitivity scan as a function of the low energy edge of the R.O.I.. The high energy edge is kept fixed at 3200 keV. The best sensitivity of 6.1×10^{24} y is found in [2720; 3200] keV after 21 kg \times y exposure, with an expected total background contamination of 0.74 ± 0.06 cts.

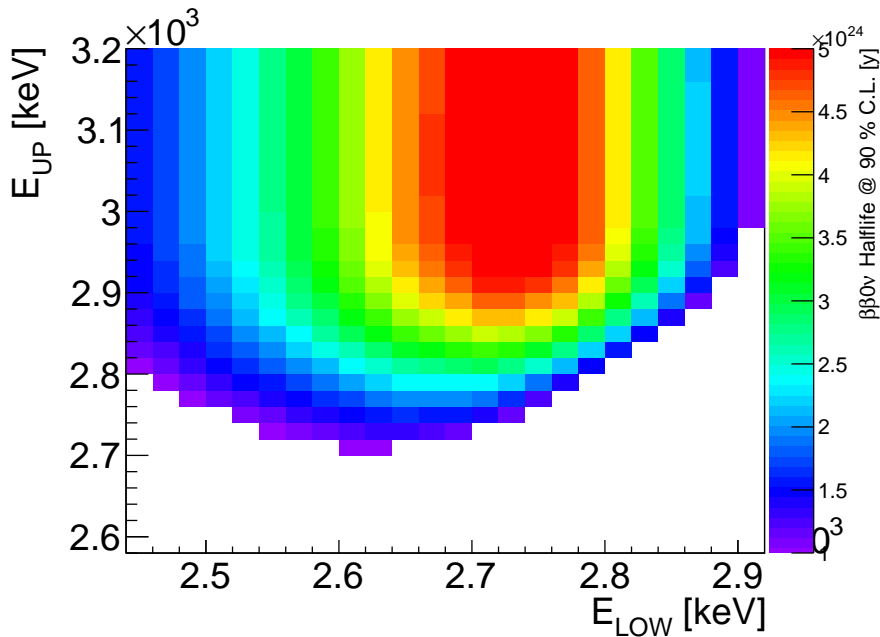


Figure 4.9: The 2d sensitivity scan as a function of the energy edges of the R.O.I.. The best sensitivity of 6.12×10^{24} y is found in [2720; 3060] keV after 21 kg \times y exposure, with an expected total background contamination of 0.72 ± 0.06 cts.

4.3.5 Validation of the background level

The NEMO-3 results on the ^{100}Mo [128] can be used to crosscheck the background level obtained in Section 4.3.1. The background measured in NEMO-3 for ^{214}Bi and ^{208}Tl can be incorporated in Equations 4.9, 4.10 and 4.11 which are normalised to the exposure of the SuperNEMO demonstrator.

Table 4.6 shows the internal ^{208}Tl and ^{214}Bi activities measured in NEMO-3, the measured background level in [2.8; 3.2] MeV and its extrapolation to the activities and exposure expected for the SuperNEMO demonstrator. The expected background levels extracted from Figure 4.6, considering the same R.O.I. as NEMO-3, is presented in the last column.

A difference of 33% and 42% is observed for the ^{208}Tl and the ^{214}Bi respectively. Note that a direct comparison could not be applied since NEMO-3 and SuperNEMO are not the same detector. SuperNEMO has a better energy resolution (8% FWHM at 1 MeV w.r.t. the 14% FWHM of NEMO-3) and a higher detection efficiency due to an optimised design of the tracker and the calorimeter. NEMO-3 has a $0\nu\beta\beta$ detection efficiency of 4.7% in [2.8; 3.2] MeV, for SuperNEMO this value is 11%, as obtained from the simulation performed in this work. Neglecting the different energy resolutions (^{208}Tl and the ^{214}Bi spectra are rather flat in the R.O.I.) the values of Table 4.6 agree within 20% when considering that the $0\nu\beta\beta$ selection efficiency of SuperNEMO is $\times 2.3$ higher than NEMO-3.

	NEMO-3 ^{100}Mo results		Extrapolation to SuperNEMO		Expectation (simulation)
	Activities [$\mu\text{Bq/kg}$]	Events in 22 kg \times y	Activities [$\mu\text{Bq/kg}$]	Events in 21 kg \times y	Events in 21 kg \times y
^{208}Tl	128 ± 3	2.39 ± 0.22	< 2	0.036 ± 0.004	0.054 ± 0.003
^{214}Bi	380 ± 40	0.92 ± 0.13	< 10	0.028 ± 0.004	0.048 ± 0.006

Table 4.6: The internal ^{208}Tl and ^{214}Bi activities measured in NEMO-3, the measured background level in [2.8; 3.2] MeV and its extrapolation to the activities and exposure expected for the SuperNEMO demonstrator. The last column shows the expected background level obtained from the calculation of sec. 4.1, considering the same R.O.I. as NEMO-3.

4.3.6 Estimation of the systematic uncertainty

In NEMO-3, the following uncertainties have been estimated : $\pm 10\%$ on the $0\nu\beta\beta$ selection efficiency, $\pm 0.7\%$ on the $2\nu\beta\beta$ background and $\pm 10\%$ for both ^{214}Bi and ^{208}Tl background [128]. Taking into account these values in the sensitivity calculation with the R.O.I. method, an uncertainty of about $\pm 11\%$ is obtained on the half-life limit. To estimate roughly the systematic uncertainties in the sensitivity calculation the same errors are considered. For simplicity, we assume that the signal selection efficiency and the backgrounds fluctuate in opposite directions. Table 4.7 summarises the results of the sensitivity scan taking into account the NEMO-3 systematic uncertainties.

Syst. effect		R.O.I	Bkg.	$T_{1/2}^{0\nu}$
$\epsilon_{0\nu}$	Bkg.	[keV]	[c.t.s]	[$\times 10^{24}$ y]
-10%	+10%	[2720;3060]	0.74 ± 0.06	5.54
none		[2720;3060]	0.72 ± 0.06	6.12
+10%	-10%	[2720;3060]	0.71 ± 0.06	6.83

Table 4.7: Sensitivity scan taking into account the NEMO-3 systematic uncertainties [6]: $\pm 10\%$ on the $0\nu\beta\beta$ selection efficiency, $\pm 0.7\%$ on the $2\nu\beta\beta$ background and $\pm 10\%$ for both ^{214}Bi and ^{208}Tl .

Table 4.8 summarises the results obtained in the case of the IDEAL* design taking into account the systematic uncertainties.

Method	R.O.I [keV]	Bkg. [c.t.s]	$T_{1/2}^{0\nu}$ [$\times 10^{24}$ y]
R.O.I 1d	[2720 - 3200]	0.74 ± 0.06	6.09
R.O.I 2d	[2720 - 3060]	0.72 ± 0.06	6.12

Table 4.8: Sensitivity calculation methods applied to the IDEAL* design.

4.4 Source foil design and detector performance

The events simulated and the method developed in Section 4.3 to compute the sensitivity are used in the following sections to study the performance of the SuperNEMO detector. The background level and the sensitivity achievable with the different source foil designs introduced in Section 4.1 are compared in Section 4.4.1 and Section 4.4.2 respectively. The amount of PVA glue to mix with ^{82}Se during the production of the TULLE design is optimised in order to provide a competitive performance with respect to the alternative MYLAR design in Section 4.4.3. Finally the effects of a non uniform thickness of the source foil is evaluated in Section 4.4.4 providing a target value for the foil production.

4.4.1 Radio-purity vs background level

As shown in Table 4.5 the event selection efficiencies in the 2e channel are different according to the designs. These differences translate into a different background level for a given internal contamination and a given exposure. Assuming an exposure of 21 kg \times y the expected level of background in the optimised R.O.I. is computed changing the ^{208}Tl and the ^{214}Bi activity from 0 $\mu\text{Bq/kg}$ to 15 $\mu\text{Bq/kg}$. The resulting histograms are shown in Figure 4.10. Note that for the MYLAR design, each value of activity is equally shared among the p.d.f. of the bulk and the backing film. If all the activity is given to the bulk p.d.f. only, the background increases by 10. At the target radio-purity level of 2 $\mu\text{Bq/kg}$ in ^{208}Tl and 10 $\mu\text{Bq/kg}$ in ^{214}Bi the expected background coming from the internal contamination is 0.15 counts for TULLE and MYLAR designs. Figure 4.11 shows the expected number adding the contribution of the $2\nu\beta\beta$. Compatible background levels are found as a function of the ^{208}Tl and the ^{214}Bi activities among the source foil designs.

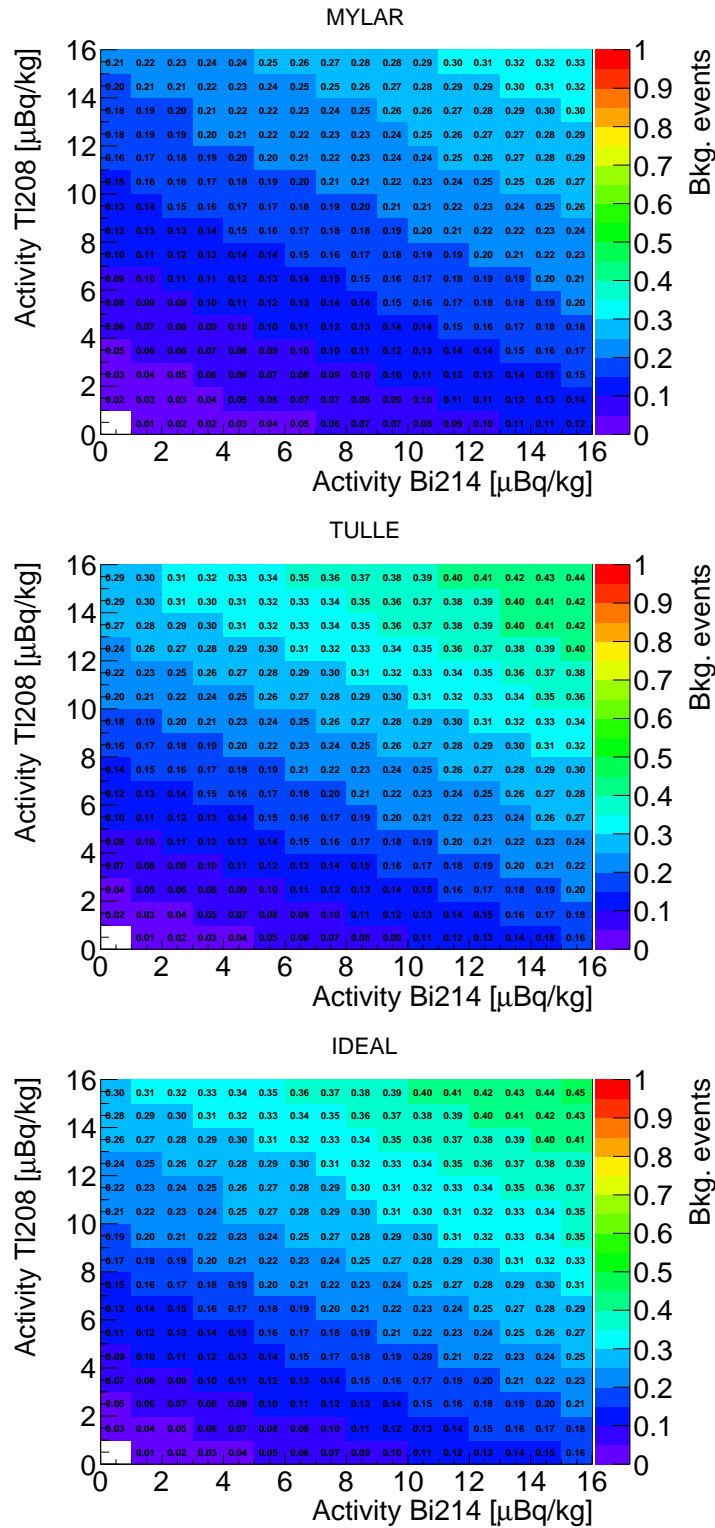


Figure 4.10: Expected number of ^{208}Tl and ^{214}Bi background events as a function of their activity in the source foil for an exposure of $21 \text{ kg} \times y$ as expected for the SuperNEMO demonstrator. Top: MYLAR. Center: TULLE. Bottom: IDEAL

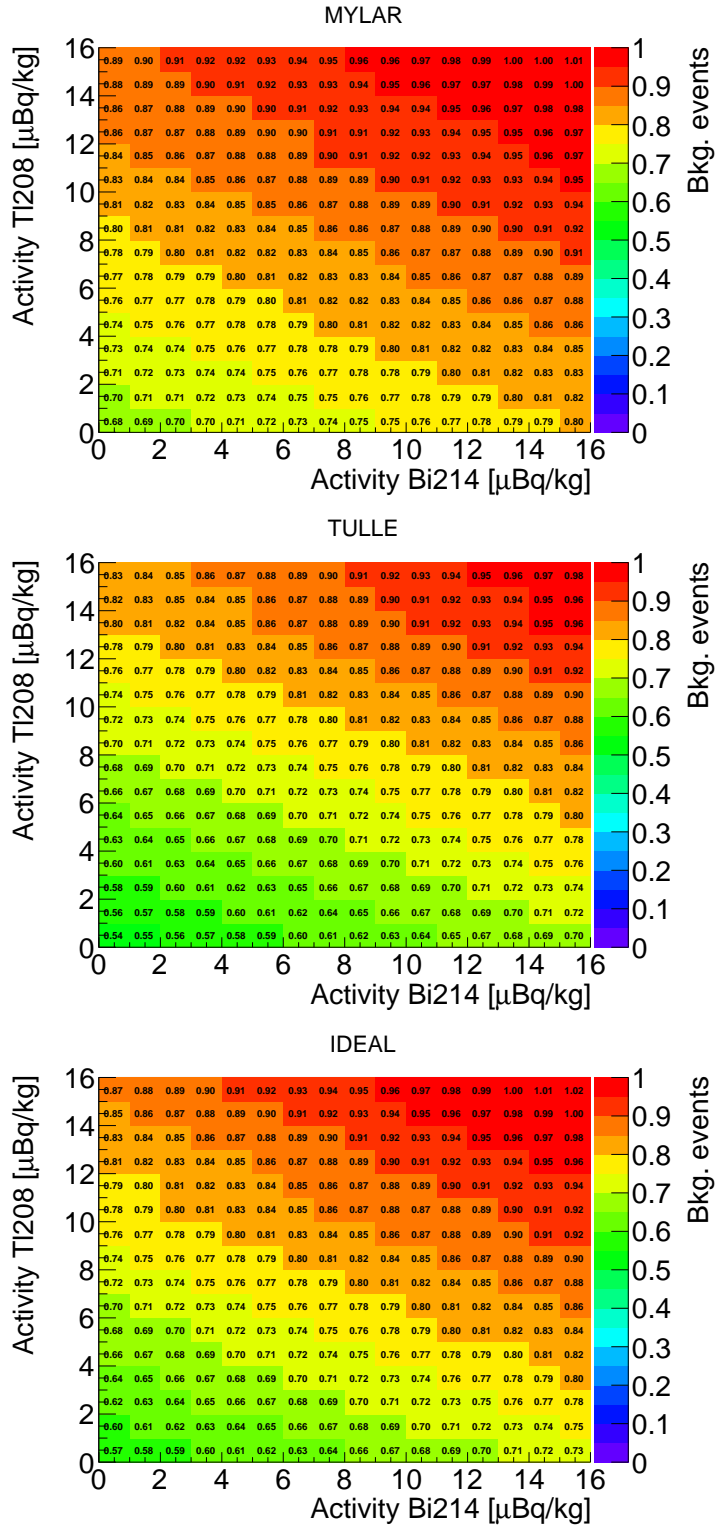


Figure 4.11: Expected number of total ($2\nu\beta\beta + {}^{208}\text{Tl} + {}^{214}\text{Bi}$) background events as a function of the ^{208}Tl and the ^{214}Bi activity in the source foil for an exposure of 21 kg \times y. Top: MYLAR. Center: TULLE. Bottom: IDEAL

4.4.2 Sensitivity vs. foil designs

Table 4.9 summarises the performances achievable with the SuperNEMO demonstrator module with respect to the source foil design, considering an exposure of $21 \text{ kg}\times\text{y}$. The signal and background p.d.f obtained in Section 4.2.3 have been normalised to the ^{208}Tl and the ^{214}Bi activities measured by BiPo and summarised in Table 4.1. The label IDEAL* refers to IDEAL design case in which the background p.d.f. are normalised to the target radio-purity level of SuperNEMO. Figure 4.13 shows the result of the sensitivity scan w.r.t. the energy edges of the R.O.I.

Design	R.O.I [keV]	$\epsilon_{0\nu}$ [%]	bkg. [cts.]	$T_{1/2}^{0\nu} [\times 10^{24} \text{ y}]$
IDEAL*	[2720 ; 3060]	17.44 ± 0.04	0.7 ± 0.1	6.12
IDEAL	[2720 ; 3060]	17.44 ± 0.04	1.3 ± 0.1	5.34
TULLE	[2720 ; 3020]	16.98 ± 0.04	2.3 ± 0.1	4.47
MYLAR	[2720 ; 3000]	16.44 ± 0.04	2.1 ± 0.1	4.50

Table 4.9: SuperNEMO demonstrator performance for different source foil designs.

As discussed in Section 4.2.3 the design of the source foil does not have a strong impact on the shape of the signal and background energy distributions. Nevertheless, the different activities of the material considered for the foil production and their mass fraction with respect to the ^{82}Se affect in a non negligible way the performance of SuperNEMO. The performances obtained with the TULLE and MYLAR designs are compatible within 3% but decreases by approximately 16% compared to the IDEAL design. Figure 4.12 shows the extrapolation of the SuperNEMO sensitivity beyond the exposure expected for the demonstrator module, up to $1000 \text{ kg}\times\text{y}$.

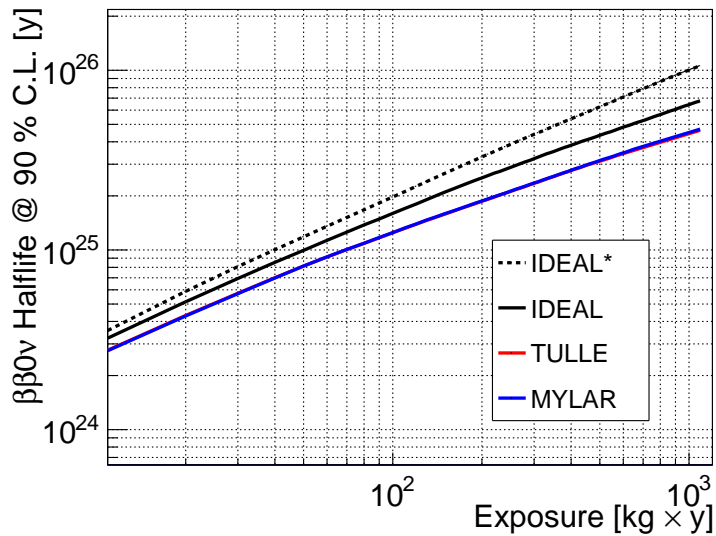


Figure 4.12: SuperNEMO $0\nu\beta\beta$ half-life limit at 90% C.L. as a function of the exposure for the different source foil designs. The dotted line refers to the IDEAL design of the foil in which the backgrounds are normalised to the target radio-purity level of SuperNEMO.

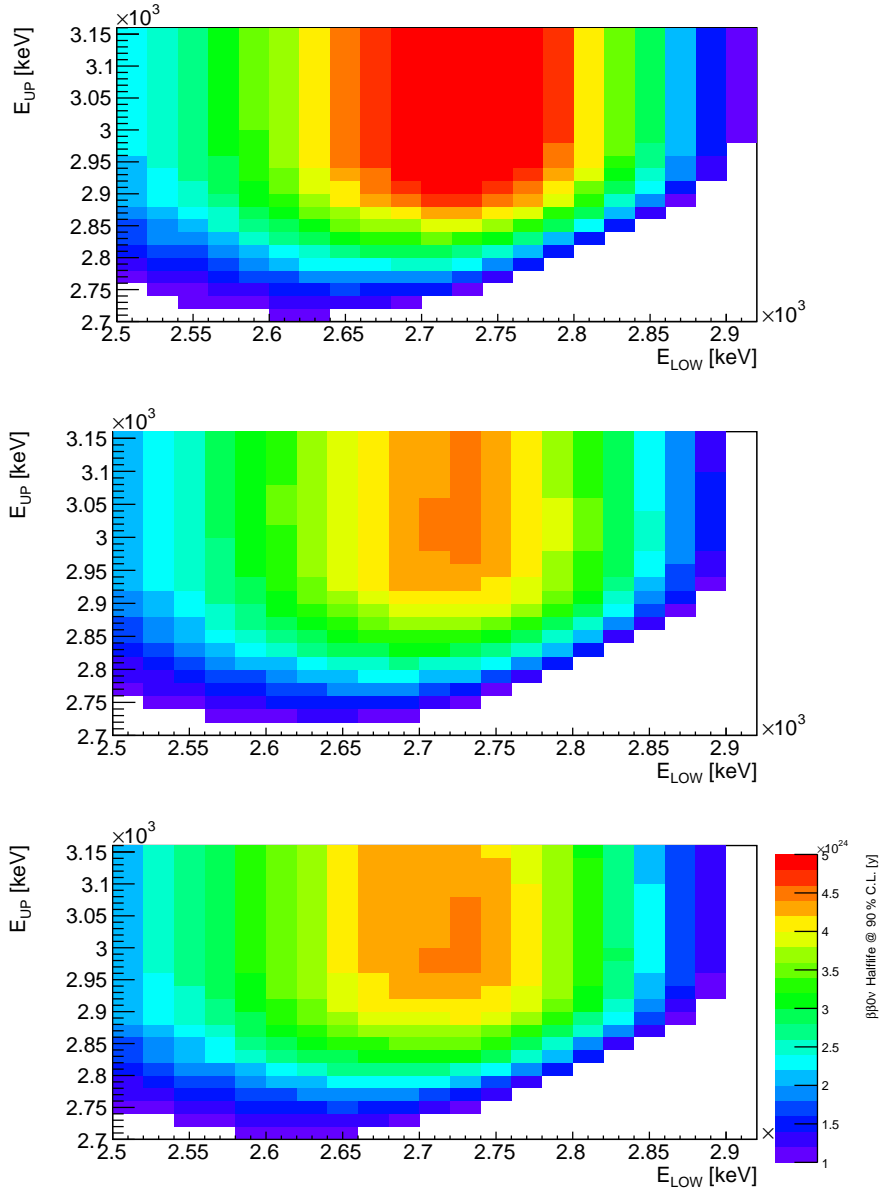


Figure 4.13: SuperNEMO demonstrator sensitivity for different source foil designs. Top: IDEAL. Center: TULLE. Bottom: MYLAR

4.4.3 Optimising the amount of PVA

The amount of PVA introduced in the foil during its fabrication has an impact on the its thickness and its density as shown in Figure 4.10. The amount of PVA also modifies the shape of the signal and background p.d.f as shown in Figure 4.14 as well as the background level. Table 4.11 summarizes the results of the performance study as a function of the amount of PVA for the TULLE design. Best performances are obtained without PVA, but this scenario is not technically feasible since the ^{82}Se foil will not be resistant enough. A TULLE foil containing 5% of PVA would still be compatible with the IDEAL design within 10%, but it would be very hard to produce, as observed during the R&D tests at LAPP. From the technical point of view, a fraction of 10-15% of PVA seems more reasonable and would allow of achieving performance compatible with the MYLAR design within 10%.

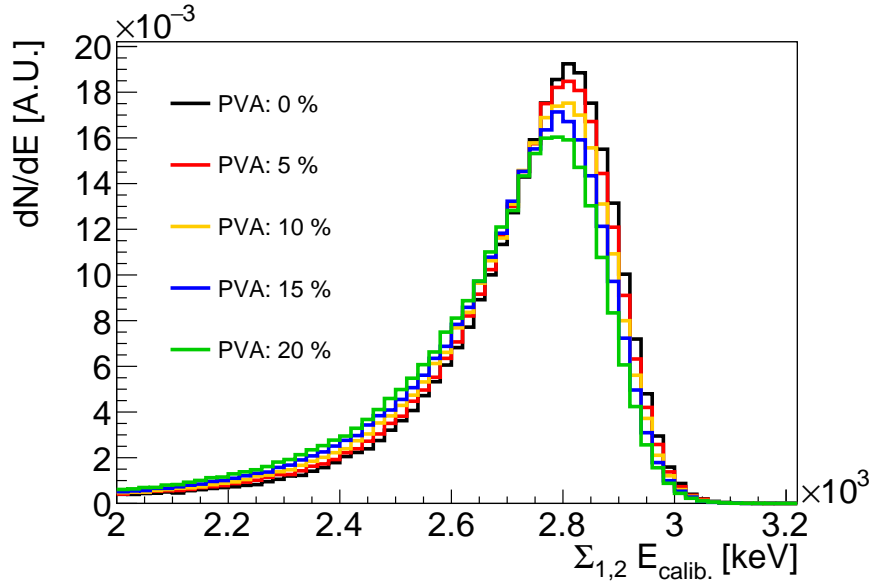


Figure 4.14: $0\nu\beta\beta$ p.d.f. with TULLE foils containing different amounts of PVA. The increased amount of PVA shifts the p.d.f. toward lower energies, due to an increased e energy loss in a thicker foil.

f_{Se} [-]	f_{PVA} [-]	f_{Support} [-]	a [mg/cm ²]	ρ [g/cm ³]	t [μm]	A (²¹⁴ Bi) [μBq]	A (²⁰⁸ Tl) [μBq]
0.986	0.00	0.014	50.7	3.17	160	10.2	6.1
0.937	0.05	0.013	53.4	3.08	173	72.7	9.6
0.888	0.10	0.012	56.3	2.98	189	142.0	13.5
0.838	0.15	0.012	59.6	2.89	206	219.8	17.8
0.789	0.20	0.011	63.4	2.80	227	306.9	22.6

Table 4.10: Parameters of TULLE foils containing different amounts of PVA.

f_{PVA}	R.O.I [keV]	$\epsilon_{0\nu}$ [%]	bkg. [cts.]	$T_{1/2}^{0\nu}$ [$\times 10^{24}$ y]
0.00	[2720 ; 3040]	17.84 ± 0.04	0.9 ± 0.1	6.03
0.05	[2700 ; 3020]	18.31 ± 0.04	2.0 ± 0.1	5.01
0.10	[2720 ; 3020]	16.98 ± 0.04	2.3 ± 0.1	4.47
0.15	[2700 ; 2980]	16.27 ± 0.04	3.3 ± 0.2	3.85
0.20	[2680 ; 3020]	16.51 ± 0.04	5.7 ± 0.3	3.26

Table 4.11: SuperNEMO performances with TULLE foils containing different amounts of PVA.

4.4.4 Foil uniformity

The thickness of the source foil impacts the energy losses of the out-coming particles worsening the resolution on the energy measurement. For similar reasons, the thickness also impacts the probability of observing 2e events from the beta decay of ²⁰⁸Tl and ²¹⁴Bi. During the production of the source foil, the ⁸²Se and the PVA paste is poured on a dedicated support and spread uniformly over the surface. Since the process is performed manually, a non uniform deposition of the paste may happen. This

t	Density	$\epsilon_{0\nu}$	$\epsilon_{2\nu}$	ϵ_{TI}	ϵ_{TI}
$[\mu\text{m}]$	$[\text{mg}/\text{cm}^2]$	$[\%]$	$\times 10^{-5}[\%]$	$\times 10^{-3}[\%]$	$\times 10^{-3}[\%]$
150	44.7	19.58 ± 0.04	8.84 ± 0.05	3.2 ± 0.2	2.1 ± 0.1
170	50.7	18.37 ± 0.04	7.92 ± 0.05	2.8 ± 0.2	1.9 ± 0.1
190	56.6	17.25 ± 0.04	6.29 ± 0.05	3.0 ± 0.2	1.6 ± 0.1
210	62.6	16.07 ± 0.04	5.59 ± 0.04	2.9 ± 0.2	1.6 ± 0.1
230	68.5	14.95 ± 0.04	4.00 ± 0.04	3.1 ± 0.2	1.4 ± 0.1

 Table 4.12: Signal and background efficiencies for $E_{\beta\beta}$ in [2700; 3000] keV.

t $[\mu\text{m}]$	Bkg. [cts.]	$T_{1/2}^{0\nu} [\times 10^{24} \text{ y}]$
150	3.3 ± 0.2	4.63
170	3.0 ± 0.2	4.46
190	2.5 ± 0.1	4.41
210	2.4 ± 0.1	4.15
230	2.1 ± 0.1	4.01

Table 4.13: Background level and best sensitivity for E in [2700; 3000] keV.

will cause a non uniform thickness over the foil length affecting the performance of the SuperNEMO demonstrator in terms of background level and sensitivity. For this reason it is important to study such effects in order to define the acceptable level of uniformity of the source foil.

Signal and background vs foil thickness

Signal and background events have been simulated considering a TULLE foil design containing 90% of ^{82}Se and 10% of PVA. The reference thickness of 190 μm has been varied by $\pm 10\%$ and $\pm 20\%$. For each foil thickness, the simulated sample consists of 10^6 $0\nu\beta\beta$ events and 10^7 events for each background channel, $2\nu\beta\beta$, ^{208}Tl and ^{214}Bi . The expected energy spectra of the 2e channel are shown in Figure 4.15 for the different thicknesses. It appears clearly from the $0\nu\beta\beta$ (top left) and the $2\nu\beta\beta$ (top right) spectra of Figure 4.15 that the overall effect is a worsening of the energy resolution (increasing of the $0\nu\beta\beta$ peak width) and a shift of the events towards lower energies due to an increase of the energy lost within the foil. Table 4.12 summarises the impact of the source foil thickness on the selection efficiency for the signal and the backgrounds. The selection efficiency being defined as the fraction of events satisfying the simple selection criteria of two reconstructed negative tracks hitting two calo blocks with a total energy deposition in [2700; 3000] MeV, defined as the ROI maximising the sensitivity to $T_{1/2}$. The total background level and the best sensitivity obtained in the ROI are summarised in Table 4.13.

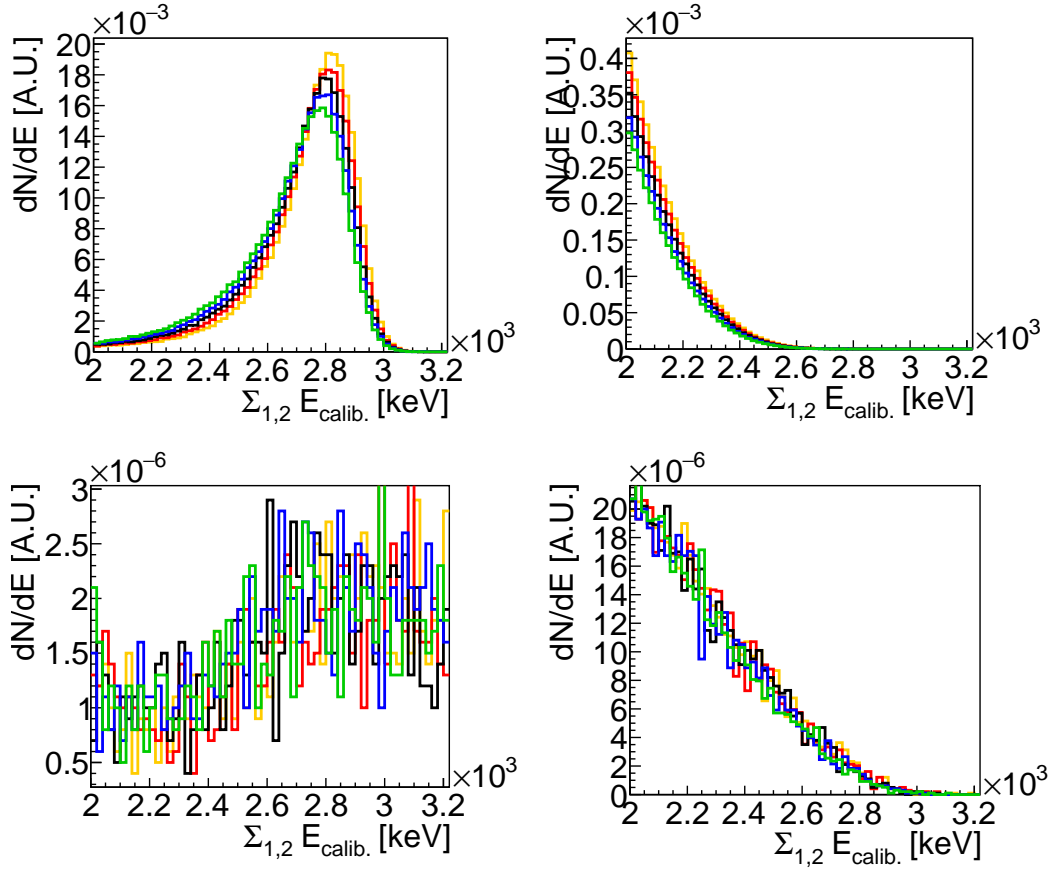


Figure 4.15: Signal and background p.d.f. generated with different source foil thickness : 150 μm (yellow), 170 μm (red), 190 μm (black), 210 μm (blue), 220 μm (green). Top left : $0\nu\beta\beta$, top right : $2\nu\beta\beta$, bottom left : ^{208}Tl and ^{214}Bi .

Effects of the foil uniformity

To mimic the effect of a non uniform foil thickness, we consider a case in which half of the foil is, for example, +10% thicker and the other half is -10% thinner than the nominal value. The average thickness of such a foil is still the nominal value and the amount of ^{82}Se + PVA paste required to produce it would be unchanged. The overall effect of such a non uniformity on a generic observable x is then obtained by averaging the same observable x_+ and x_- obtained for the thicker and the thinner foil respectively. The relative comparison against the same observable obtained with the nominal thickness allows to obtain the systematic effect σ due to the non uniformity :

$$\langle x \rangle = x_+ \left(\frac{t_+}{t_+ + t_-} \right) + x_- \left(\frac{t_-}{t_+ + t_-} \right) \quad (4.13)$$

$$\sigma_x = \frac{|\langle x \rangle - x|}{x} \quad (4.14)$$

The red and the blue histograms in Figure 4.16 show the averaged spectra obtained varying the foil thickness by $\pm 10\%$ and $\pm 20\%$ respectively. The black histogram shows the expected spectra at the nominal thickness of 190 μm . Table 4.14 shows the systematic effects on the signal and background selection efficiencies induced by a foil non uniformity for $E_{\beta\beta}$ in [2700; 3000] keV, where the best sensitivity is found.

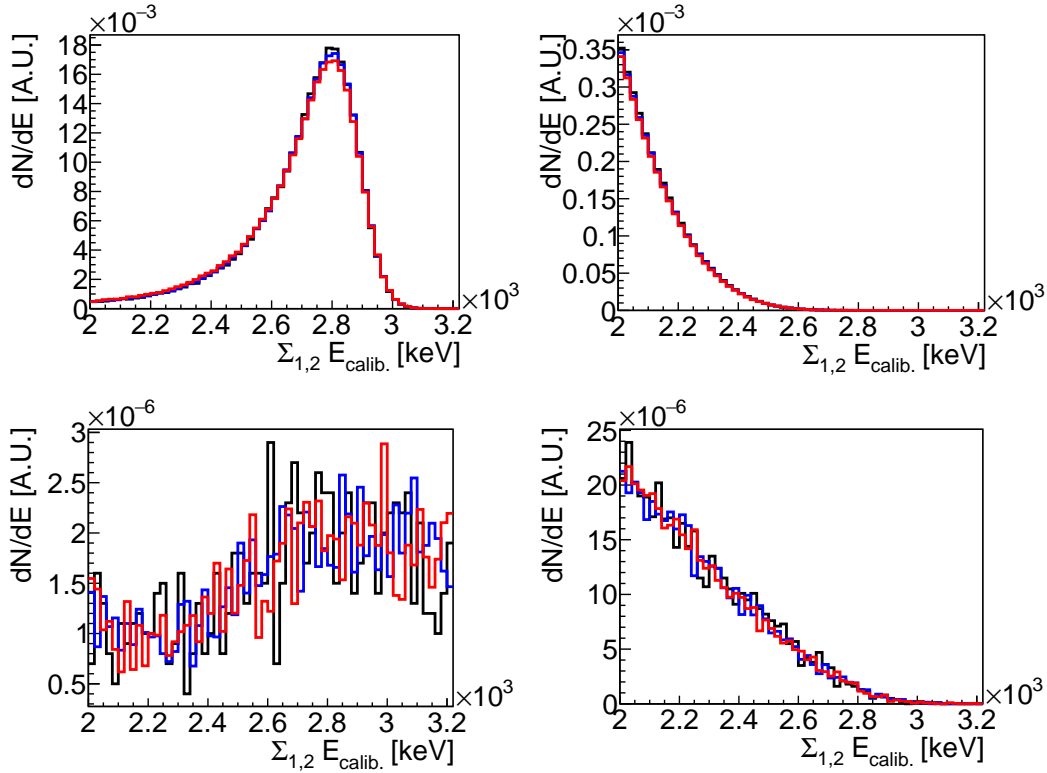


Figure 4.16: The red and the blue histograms show the expected spectra by varying the foil thickness by $\pm 10\%$ and $\pm 20\%$ respectively. The black histogram shows the expected spectra at the nominal thickness of $190 \mu\text{m}$.

Uniformity	$\sigma_{\epsilon 0\nu}$ [%]	$\sigma_{\epsilon 2\nu}$ [%]	$\sigma_{\epsilon Tl}$ [%]	$\sigma_{\epsilon Bi}$ [%]	$\sigma_{T1/2}$ [%]
$\pm 10\%$	0.9	5.4	5.2	8.4	2.8
$\pm 20\%$	2.8	6.0	3.4	4.2	3.3

Table 4.14: Systematic effect on signal and background efficiencies induced by non-uniformity of the source foil thickness for E in $[2700; 3000]$ keV.

The effect of the thickness uniformity on the $0\nu\beta\beta$ sample is $< 3\%$ while for $2\nu\beta\beta$ it increases up to 6% . For the other internal backgrounds, the effect is $< 8\%$. The overall effect on the sensitivity is $< 3\%$. Assuming the systematic uncertainty on the signal and background efficiencies of 7% and 10% respectively [128] as the upper limit for the SuperNEMO demonstrator module, it is recommendable to aim for an uniformity $< 20\%$ over the whole foil surface. The effect of a $\pm 20\%$ uniformity remains in fact within the expected systematic uncertainties.

4.5 Conclusion

This study shows that the different activities of ^{208}Tl and ^{214}Bi in the materials considered for the foil production and their mass fraction with respect to the ^{82}Se affect in a non negligible way the performance of SuperNEMO. With respect to the IDEAL design, the performance decreases by about 17% and 22% for the TULLE and the MYLAR design respectively. The TULLE and the MYLAR

designs are compatible within 3%. The differences among the designs decrease as the activities in ^{208}Tl and ^{214}Bi increase, making the choice of the source foil design rather equivalent in case of a high contamination coming, for example, from the ^{82}Se . The effect of a non uniformity on the thickness of the source foil has also been studied. The result of the sensitivity calculation performed for different thicknesses of the foil recommends a uniformity $<20\%$ over the whole foil surface.

After a R&D program and despite its good performances in terms of radiopurity, the TULLE design has been abandoned. As in this design the $^{82}\text{Se} + \text{PVA}$ is not protected with a mylar film, the foil will be directly in contact with the tracker gas. Ageing tests have been realized at LAPP and have shown a deterioration of the foil when placing it in a similar environment to the tracker. Based on the experience of the R&D program, an alternative design has been proposed consisting of spreading the $^{82}\text{Se} + \text{PVA}$ paste on a delrin mold. Once the preparation is dry, the stand alone foil is inserted into a raw mylar pocket which is then welded. The raw mylar film has the advantage to provide a protection against the tracker gas, and has a better radiopurity compared to the mylar backing film, since no holes have been made in the film. The sensitivity reachable with this new design is compared to the IDEAL and MYLAR (MYLAR backing film) as shown in Figure 4.17. This design has a slightly better performance than the design using a mylar backing film. Note that the previous results on foil optimisation and uniformity stay valid for this design. It has been chosen for producing half of the foils for the demonstrator.

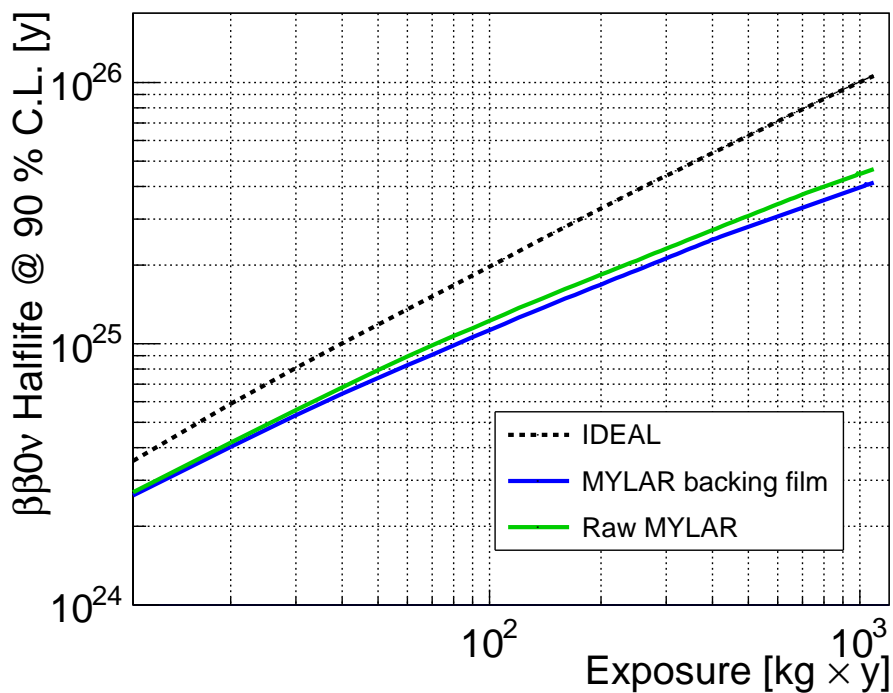


Figure 4.17: SuperNEMO $0\nu\beta\beta$ half-life limit at 90% C.L. as a function of the exposure for the IDEAL, MYLAR backing film and raw MYLAR designs.

Chapter 5

Radon in SuperNEMO

As discussed in Chapter 3, the $\beta\beta$ process is very rare and its study requires a very low background environment. The detectors searching for $\beta\beta$ decays are installed in underground laboratories and protected with different shields to be sheltered against the cosmic ray and the photon/neutron fluxes coming from the laboratory.

Despite these precautions, some backgrounds can still be present and bother the $\beta\beta$ searches. One of the main background is induced by radon. Radon (^{222}Rn) is a highly diffusive gas emanating from the rocks surrounding the underground laboratory. At LSM, its activity in the surrounding air has been measured to be $10\text{Bq}/\text{m}^3$ [149]. The descendants of the ^{222}Rn , mainly the ^{218}Po , could deposit themselves on the tracker wires or on the surface of the source foil. As shown in Figure 5.1, ^{222}Rn reaches during its decay chain, the ^{214}Bi isotope which is one of the main backgrounds in the NEMO experiments due to the emitted electron up to 3.27 MeV. Figure 5.2 shows how the decay of ^{214}Bi can by different processes (Möller scattering or Compton effect) mimic the $\beta\beta$ signal.

From the NEMO-3 to the SuperNEMO experiments, the aim is to reduce the ^{222}Rn contamination inside the tracker by a factor 50. The following techniques will be employed :

- Improve the radiopurity of each components avoiding ^{222}Rn emanation coming from the detector itself.
- Install an anti-radon system made of a clean tent which surrounds the entire detector hermetically and filters the air inside the tent with a radon trap.

Despite the good radiopurity of the components and the anti-radon system, some residual contamination of ^{222}Rn is expected in the tracker volume. In order to identify and suppress these remaining events, analysis tools have been implemented. The strategy is to use the fact that ^{214}Po , the daughter nucleus of ^{214}Bi , is not stable. The ^{214}Po nucleus decays to ^{210}Pb by emitting an alpha particle with a half-life of $164.6 \pm 0.3 \mu\text{s}$ [150] as shown in Figure 5.3. The reconstruction of these events, called BiPo events, with the characteristic coincidence time among the prompt electron and the delayed alpha provides a very clean and sensitive way to measure the $^{214}\text{Bi}/^{222}\text{Rn}$ contamination in the detector.

The number of expected events coming from ^{214}Bi , can be estimated, for each part i of the detector by using :

$$(N_{1e1\alpha})_i = (\epsilon_{1e1\alpha})_i \times A_i \times T \quad (5.1)$$

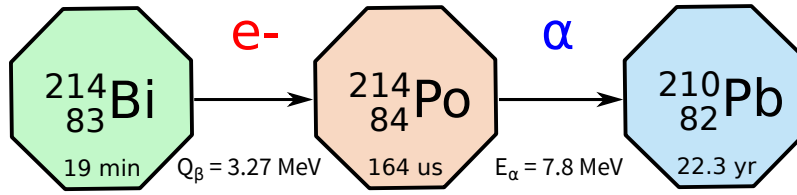


Figure 5.3: The ^{214}Bi decay chain. The first decay emits an electron with $Q_\beta = 3.27$ MeV. The daughter ^{214}Po then decays by emitting a monoenergetic alpha particle, $E_\alpha = 7.8$ MeV. The half-life of ^{214}Po is $164.6 \pm 0.3\mu\text{s}$.

used in this study. Section 5.3 presents the algorithm developed in this work to identify and reconstruct the alpha particles. The selection and the efficiency of reconstruction of the $1e1\alpha$ channel are presented in Section 5.4. Section 5.5 explains the strategy used to estimate the level of background induced by ^{222}Rn and with what precision it can be measured. Section 5.6 presents the results of this work.

5.1 Computation of the expected activity

By knowing the ^{214}Bi contamination of the different detector components and their mass or volume, the activity of ^{214}Bi can be evaluated for each of these parts. Sections 5.1.1 and 5.1.2 respectively present the activity computations for the contamination coming from the source foil and from the tracker.

5.1.1 Activity source the foil

^{214}Bi contamination expected from the source foil has been measured in the BiPo detector. Results presented in [151, 152] put an upper limit on the total activity of 2200×10^{-6} Bq/kg for the ^{82}Se and 210×10^{-6} Bq/kg for the raw mylar.

Thanks to these measurements, the radiopurity of each component used in the source foil fabrication is known. By assuming that the bulk of the foil is only made up of ^{82}Se and the surface of the foil is made up of only raw mylar, the total activity can be computed in each part of the detector :

- the bulk of the foil :

$$A_{\text{bulk}} = 2200 \times 10^{-6} \text{ Bq/kg} \times 7 \text{ kg} = 15.4 \text{ mBq} \quad (5.2)$$

- the surface of the foil :

$$M_{\text{surface}} = 2 \text{ sides} \times \rho \times V = 2 \times 1.40\text{g/cm}^3 \times 314.7\text{cm}^3 = 0.88 \text{ kg} \quad (5.3)$$

$$A_{\text{surface}} = 210 \times 10^{-6} \text{ Bq/kg} \times 0.88 \text{ kg} = 0.18 \text{ mBq} \quad (5.4)$$

where A_{bulk} and A_{surface} are the bulk and surface activities of the source foil, M_{surface} is the mass of the mylar computed as the product of its density ρ and its volume V .

5.1.2 Activity from the tracker

The intrinsic tracker activity has been measured using a Radon Concentration Line (RnCL) at MSSL [153]. By assuming that the air is not flushing and that the contamination is 4 times the contamination of the C0 section measured at 11.37 mBq, the activity of the tracker is evaluated to be :

$$A_{\text{tracker}} = 4 \times 11.37 = 45.5 \text{ mBq} \quad (5.5)$$

This value of 45.5 mBq for the tracker activity is probably an overestimation since C1 and C2 sections have been measured respectively at 15.2 mBq and 3.28 mBq as reported in Table 3.5. Calculating the mean value of these measurements gives 10 mBq/C-section corresponding to a total expected activity of 40 mBq for the tracker. Furthermore, the fact that a certain amount of ^{222}Rn present in the tracker contaminates the surface of the foil is not taken into account, which would decrease the tracker activity. In addition, the activity inside the tracker can be reduced by flushing the air inside the tracker chamber. Despite this approximation, the value of 45.5 mBq is chosen for this study since it is probably not so far from the real value (C3 has not been measured) and that we want to test the measurement method. The total activities of each part of the detector (source and tracker) are summarized in the Table 5.1.

	Bulk	Surface	Tracker
Activity [mBq]	15.4	0.18	45.5

Table 5.1: Summary of the total activity, in different parts of the detector, computed from the radiopurity measurements.

5.2 Simulation and Reconstruction

The simulation and reconstruction tools used in this work are available in the software package developed by the collaboration called Falaise (version 1.0.0). The simulations of the events is done by GENBB and presented in Section 5.2.1. The propagation of the particle inside the SuperNEMO detector is done by GEANT4 and introduced in Section 5.2.2. For the reconstruction, each event is processed through a pipeline consisting of a sequence of software modules as discussed in Section 5.2.3. Each module is responsible for the elaboration of additional information stored in dedicated banks. An additional tool giving interesting variables on standard ROOT trees is developed for an easier access to the simulated and reconstructed information.

5.2.1 Generation of the ^{214}Bi events

The first step is the generation of ^{214}Bi events with the simulation software. In this chapter, the events are generated at the surface of the source foil, in the bulk of the source foil and in the tracker volume. The event generation is done by GENBB and the propagation of the particles into the SuperNEMO detector is realized by GEANT4 [154].

GENBB is a Monte-Carlo event generator for double beta processes and the decay of radioactive nuclei. It can generate the decay (α , β^\pm , electron conversion) of all known isotopes by taking into account the information of the decays (decay mode, energy release, transition probability, half-life...). Transitions to the ground state as well as to excited levels of daughter nuclei are allowed. GENBB generates the energy, the time of decay and the direction of emitted particles.

In this work, the generation is performed in agreement with the decay scheme of ^{214}Bi . Since GENBB also simulates secondary nuclear effects such as internal conversion or decay via the excited state, the consequence is the generation of different topologies :

- The $1e1\alpha$ topology, which represents 18.2% of all the simulated topologies, corresponds to the standard (BiPo) decay. The ^{214}Bi decays to the ground state of ^{214}Po .
- The $1e1\alpha\gamma$ topologies, which represent 79.1% of all the simulated topologies, correspond to the BiPo decay accompanied by a gamma emission. In this case, the ^{214}Bi decays to an excited state of ^{214}Po and a gamma or a cascade of gammas is then produced.
- The $2e1\alpha\gamma$, $3e1\alpha\gamma$, $4e1\alpha\gamma$ topologies, which represent 2.58% of all the simulated topologies, correspond to a BiPo event with an internal conversion (IC). An excited ^{214}Bi nucleus can directly transfer its energy to an orbital electron. This electron is expelled from the atom with a discrete energy. The direct consequence is the generation of more than one electron in the event, which could mimic $2e^-$ event from $\beta\beta$ decay.

In any case, whatever the topology, an alpha is always present. This justifies its search and why the $1e1\alpha$ channel is an appropriate channel to detect the ^{214}Bi .

A way to quantitatively ensure that these electrons really come from internal conversions is to analyze the energy spectrum of all the simulated electrons as shown in Figure 5.4. The shape of the energy spectrum of the emitted electrons from ^{214}Bi beta decay is well recognizable with a Q_β at 3.27 MeV. The sharp overlapping peaks correspond to the monoenergetic electrons emitted from internal conversions.

By removing the contribution of the electrons coming from the β decay, only the electrons coming from internal conversions are kept. Figure 5.4 shows the energy spectrum of these electrons normalized to the number of total events. The four main peaks observed at 0.516, 0.592, 1.027 and 1.322 MeV correspond to the internal conversion of ^{214}Bi . Table 5.2 shows the intensity comparison between the published values [150] and the values obtained in this study which agree rather well.

The above channels are the predominant ones in the decay of the ^{214}Bi . Alongside these there are also a few much less probable final states such as α -decay of ^{214}Bi (1α , $1\alpha1\gamma$,...) or other channels with positron emissions ($2e1\alpha1p$). Table 5.3 summarizes all the topologies created by GENBB during the simulation of the ^{214}Bi decay.

Electron energy [MeV]	published values [150]	this study
0.516	0.676 ± 0.010 %	0.688 ± 0.015 %
0.592	0.189 ± 0.003 %	0.210 ± 0.008 %
1.027	0.186 ± 0.003 %	0.198 ± 0.008 %
1.322	0.480	0.493 ± 0.013 %

Table 5.2: Comparison of the intensities of the four main peaks due to internal conversion electrons.

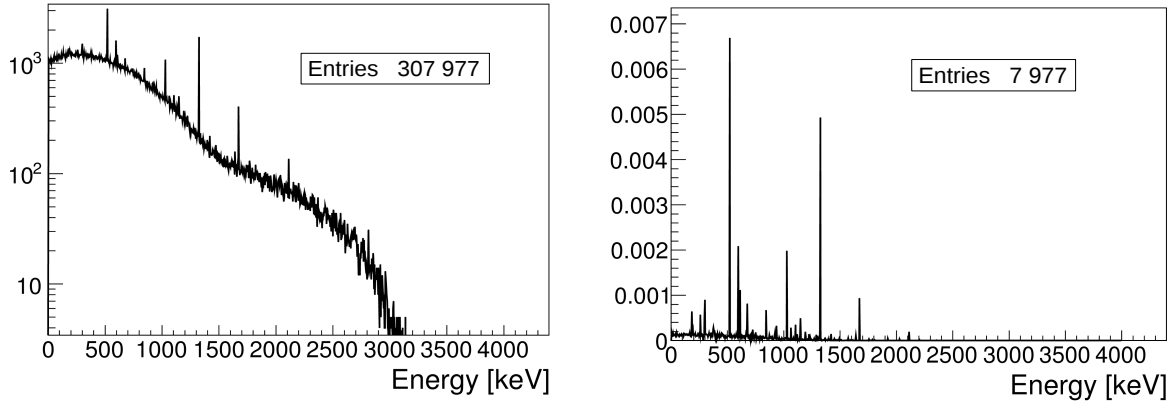


Figure 5.4: Left : Energy spectrum of all simulated electrons. The shape of the energy spectrum of the ^{214}Bi beta decay is well recognizable with a Q_β of 3.27 MeV. The sharp peaks correspond to the monoenergetic electrons emitted from internal conversions. Right : Energy spectrum of the electrons emitted in internal conversions normalized to the number of total simulated events.

	Simulated topology	300 000	100 %
^{214}Bi α - decay	1α	21	0.007 %
	$1\alpha 1\gamma$	9	0.001 %
	$1\alpha 2\gamma$	2	0.0006 %
BiPo decay ground and excited states	$1e1\alpha$	54 592	18.2 %
	$1e1\alpha 1\gamma$	101 304	33.8 %
	$1e1\alpha 2\gamma$	122 765	40.9 %
	$1e1\alpha 3\gamma$	12 994	4.3 %
	$1e1\alpha 4\gamma$	426	0.14 %
	$1e1\alpha 5\gamma$	1	0.0003%
BiPo with IC	$2e1\alpha 1\gamma$	1266	0.4 %
	$2e1\alpha 2\gamma$	5052	1.7 %
	$2e1\alpha 3\gamma$	1313	0.4 %
	$2e1\alpha 4\gamma$	107	0.04 %
	$3e1\alpha 2\gamma$	91	0.03 %
	$3e1\alpha 3\gamma$	30	0.01 %
	$3e1\alpha 4\gamma$	2	0.0006 %
	$4e1\alpha 3\gamma$	2	0.0006 %
others	$2e1\alpha 1p$	17	0.006 %
	$2e1\alpha 1p 1\gamma$	6	0.002 %

Table 5.3: The topology of the events simulated during the decay of ^{214}Bi

5.2.2 Detector response simulation

The second step is the GEANT4 simulation of the detector response. A brief reminder of the SuperNEMO geometry useful to this work are presented here. The response of the tracker and the calorimeter is done within the Calibration module.

The tracker, that sandwiches the source foil, is composed of 2034 Geiger cells (9 layers and 113 rows). Each Geiger cell is composed of an anodic wire and 12 cathodic wires for a total of 12948 wires (cathodic wires are shared between neighboring cells). The distance between each Geiger cell is 4.4 cm.

The calorimeter is composed of 6 walls : 2 main walls on opposite sides of the source foil, 2 γ -vetos and 2 x-walls to cap the sides, the top and the bottom of the detector. Each main wall has 260 optical modules made of Polystyrene scintillator blocks directly coupled to a 8-inch low radioactivity PMT. The mean energy resolution of the optical modules, at 1MeV, is $\sim 8\%$ FWHM. The distance between the source foil and the main wall is 45 cm.

The response of the calorimeter is simulated through a Gaussian smearing of the true energy taking into account the energy resolution of the calorimeter. The transverse drift radius of the Geiger cells is simulated according to the relation between the drift time and radius plotted in Figure 5.5 [155]. This module creates and fills the Calibrated Data (CD) bank.

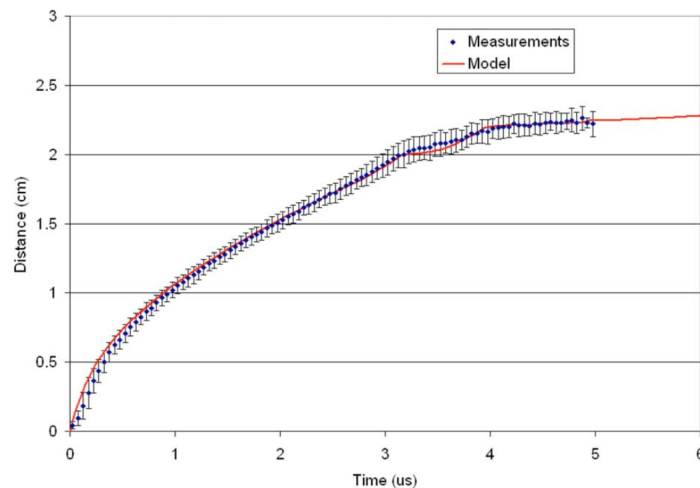


Figure 5.5: The relation between the transverse drift time and drift radius

5.2.3 Reconstruction of the simulated events

The third and last step is the reconstruction of the simulated events. The list of modules processed in the pipeline used in this study are given below :

- **Cellular Automaton Tracker (CAT)** : this module clusters the calibrated Geiger hits. It creates and fills the Tracker Clustering Data (TCD) bank. The TCD bank contains all the cluster information. The clusterisation runs in two steps. The first step is to perform a pre-clusterisation. CAT sorts the Geiger hits according to the drift time. If the drift time is smaller than $10 \mu\text{s}$ from the time of the first particle emission, the cluster is considered as prompt, otherwise it is considered as delayed. The two samples of Geiger hits are then treated separately. The second

step is the clusterisation of the Geiger hits by taking into account their proximity in space through a cellular Automaton Algorithm.

- **TrackFit** : this module fits the clusters found by CAT. It creates and fills the Tracker Trajectory Data (TTD) bank. The TTD bank contains all the track information. The fitting algorithm tries to fit a straight line or a helix to the cluster. If the cluster is better approximated by a straight line fit, the track is defined by 2 parameters : the first and the last points of the line. In case a helical trajectory is fitted, the track is defined by 5 parameters : the center, radius, pitch and first and last angles of the helical segment. Due to the minimum number of degrees of freedom required to fit a straight line, TrackFit considers only clusters containing 3 or more Geiger hits. TrackFit is also able to estimate the alpha emission time which is in practice unknown.
- **Charge Particle Tracking** : this module creates and fills the Particle Track Data (PTD) bank. It computes for each track the charge according to the curvature from the magnetic field. Charged Particle Tracking also extrapolates the track to estimate its vertex. If the layer of the wires nearest to the foil source is triggered, the vertex is extrapolated onto the source foil. In the same way, if a calorimeter hit occurs close to a track and if the layer of wires nearest this calorimeter block have been triggered, the track is extrapolated to the surface of the calorimeter block.

Others modules have been developed and are used for the reconstruction of the different channels. They are briefly described here :

- **Particle Identification module** : this module tags the reconstructed particles according to definitions given by the user. If a particle meets the requirements defined to be an electron the particle is tagged and fills the electron bank.
- **Topology module** : this module creates a new data bank called Topology Data (TD). The particles in an event are associated to form a topology. This module computes some observables of the reconstructed topology :
 - the time of flight from the foil to calorimeter
 - the angle θ between the particles at the emission vertex
 - the difference in vertex positions on the foil
 - The delay time between the electron and the alpha ($\Delta t_{e-\alpha}$)
 - The Y, Z and YZ distances between the two extrapolated vertices on the source foil
 - The X, Y and Z distance between the two nearest Geiger hits to the source foil.
- **Process $1e1\alpha$ topology cut** : specific to this work, this module recognizes the $1e1\alpha$ topology among all the rest.
- **Output module** : this last module is responsible for storing the simulated and reconstructed information in a ROOT tree.

5.3 Reconstruction of the α particle

Because of its high ionization power, the energy loss of an alpha is much larger than that of an electron. The stopping power ($-dE/dx$) for an alpha particle, in a gas made of 100 % of He, is ~ 0.25 MeV/cm. In other words, the typical path length of an alpha with an energy equal to 7.7 MeV does not exceed

40 cm. So an alpha coming from the source foil is not expected to hit the main calorimeter wall. Due to their high mass, alpha particles are not significantly affected by the magnetic field so their tracks will be essentially straight lines. An alpha particle is then identified as a short straight line of Geiger hits delayed in time with respect to the electron. A visualisation of a typical alpha track coming from the source is shown in Figure 5.6.

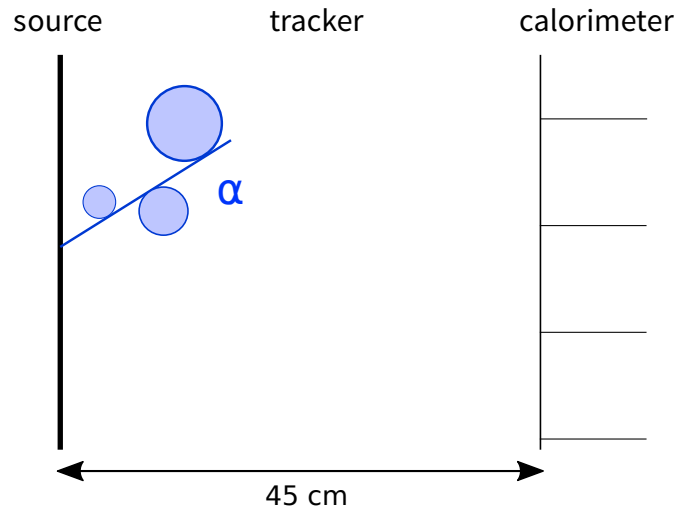


Figure 5.6: Visualisation of a typical alpha track coming from the source. The blue circles represent the Geiger hits and the straight line the fitted track.

5.3.1 The Alpha Finder algorithm

The typical alpha track is a delayed short and straight line. Some alphas can have only 1 or 2 Geiger hits, these alphas could otherwise be lost because they are not fitted by TrackFit. For this reason, an algorithm, called Alpha Finder, was developed. Its goal is to search for delayed non-clustered (single) hits and the delayed non-fitted (double) hits. The algorithm is based on the algorithm developed for NEMO-3 and is described here.

In each event, the presence of a prompt electron track is checked. It is important to verify the presence of a prompt track because, later, during data taking, a window of 1 ms will be opened just after a calorimeter hit triggered by a prompt track. If the event contains a prompt track, the presence of delayed unfitted tracks (a 2 hit cluster) or delayed unclustered Geiger hit (a single hit) is verified.

Once we are sure that the event contains such ignored delayed Geiger hits, their X,Y and Z position and their time are stored. To be accepted, the delayed Geiger hit(s) must fulfill some requirements :

- the delayed time of the delayed Geiger hits has to be greater than a certain time defined by the `minimum_delayed_time`. The CAT algorithm considers a hit as delayed if the delayed time is greater than 10 μ s. The same time has been chosen for the Alpha Finder.
- the distance in XY between the delayed hit(s) and the hits of the prompt track is computed, and must be smaller than a certain distance called `minimal_cluster_xy_search_distance`. The default value has been set at 40 cm.
- the same distance is computed for the Z axis, and must be smaller than `minimal_cluster_z_search_distance`. The default value has been set at 30 cm.

- Finally, the distance between the delayed hit(s) and the vertex of the prompt track is also computed. The distance has to be smaller than a certain distance called `minimal_vertex_distance`. The default value has been set to 30 cm.

If all these different criteria are fulfilled, the delayed cluster (2 hits) or the single hit are added to the alpha bank along with their properties (delayed time, X,Y and Z position...). The delayed time of the alpha corresponds to the delayed time of the Geiger cell which is known with an uncertainty of $4 \mu\text{s}$. $4 \mu\text{s}$ corresponds to a drift radius of 2.2 cm which is a Geiger cell radius.

In the case of just one delayed hit, the length of the alpha track is set by computing the distance between the vertex extrapolation of the prompt track and the center of the delayed cell. In the case of 2 delayed hits, the length of the alpha track is set by computing the distance between the vertex extrapolation of the prompt track and the center of the furthest delayed cell.

To summarise, there are two ways to find the alpha particles. The alpha particles with 3 or more Geiger hits (long alpha) are found by CAT while the alpha particles with 2 or fewer Geiger hits (short alpha) are found by the Alpha Finder. During the reconstruction of the $1e1\alpha$ channel, long and short alpha particles are treated equally, whatever the way they have been found.

5.3.2 The alpha emission time t_0

To find the radius of a Geiger cell, the drift time has to be known. For the prompt tracks it is quite easy to recover the drift time. In an event, the anodic time (t_{Ae}) corresponds to the electron emission time (t_e) plus the drift time (t_d) :

$$t_{Ae} = t_e + t_d$$

The electron emission time corresponds within a few ns to the time when the electron hits the calorimeter wall. The response of the calorimeter is very quick (few ns). The anodic time is given by the tracker. The response of the tracker is slower than the calorimeter. In this way, the drift time can be calculated. The correspondence between drift time and the radius has been measured and is given in Figure 5.5.

For the delayed tracks, it is a little bit different. The anodic time ($t_{A\alpha}$) corresponds to the electron emission time (t_e) plus the alpha emission time (t_α) plus the drift time (t_d).

$$t_{A\alpha} = t_e + t_\alpha + t_d$$

In practice the alpha emission time is unknown. Nevertheless, a solution has been found to estimate this time. The trick is to consider the alpha emission time as a parameter of the fit of the track (done by Trackfit) to the following expression :

$$t_{A\alpha} - t_\alpha = t_e + t_d$$

In Figure 5.7, the difference Δt_0 between the true alpha emission time and the reconstructed alpha emission time is plotted. A picture of the visualisation is also shown in the Figure 5.8. The agreement between the reconstruction and the simulation is correct and accurate enough for the following studies presented in this chapter. The more the number of Geiger hits in the track the better the α emission time is reconstructed. If the number of Geiger hits in a cluster is equal to 2 or less, this calculation is not done because it relies on the fitting of the tracks.

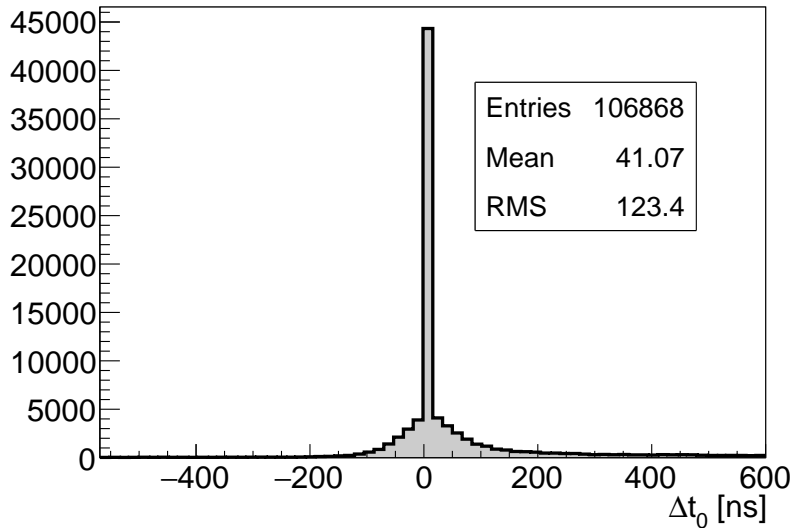


Figure 5.7: The difference between the true alpha emission time and the reconstructed alpha emission time. The distribution is peaked at 0 showing that the reconstruction and the simulation are in good agreement.

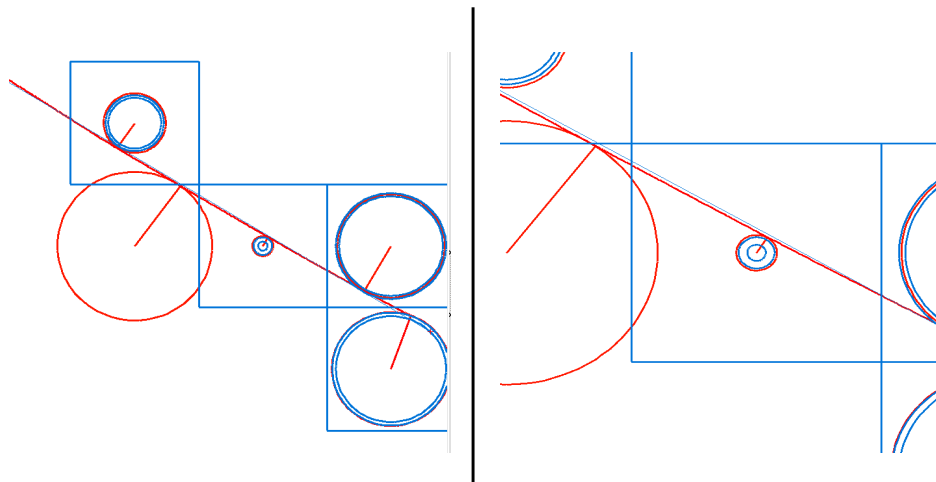


Figure 5.8: Visualisation of simulated (red) and reconstructed (blue) alpha. On the left, a global view is shown, on the right, a zoomed view of the same event is presented. In the simulation, 5 Geiger cells are hit (red circles) whereas only 4 cells are triggered in the reconstruction (blue circles). The blue squares represent the delayed cells found by the reconstruction, the blue circles represent drift radius estimated by TrackFit with the fitting technique. We can see in the right image that the true alpha track and the reconstructed track are very close.

5.4 Selection of the $1e1\alpha$ channel

In the following discussions, the number of simulated events is always 3.10^5 (unless otherwise noted). This number allows one to obtain good statistics in a reasonable time. The $1e1\alpha$ events are generated in the foil (bulk and surface) and uniformly in the tracker at the surface of the wires.

The reconstruction of the $1e1\alpha$ channel is performed by associating, in the same event, an electron and

an alpha according to proximity criteria. Depending on the vertex of the $1e1\alpha$ events, two selections have been introduced :

- source selection : optimized to select the $1e1\alpha$ events coming from the source foil and reject the events coming from the tracker.
- tracker selection : optimized to select the $1e1\alpha$ events coming from the tracker and reject the events coming from the source foil.

5.4.1 $1e1\alpha$ events from the source foil

A picture representing the $1e1\alpha$ selection of the event coming from the source foil is shown in Figure 5.9. Only the events close to the source in which the first layer of wire is hit are selected. They are represented by the green region the Figure 5.9.

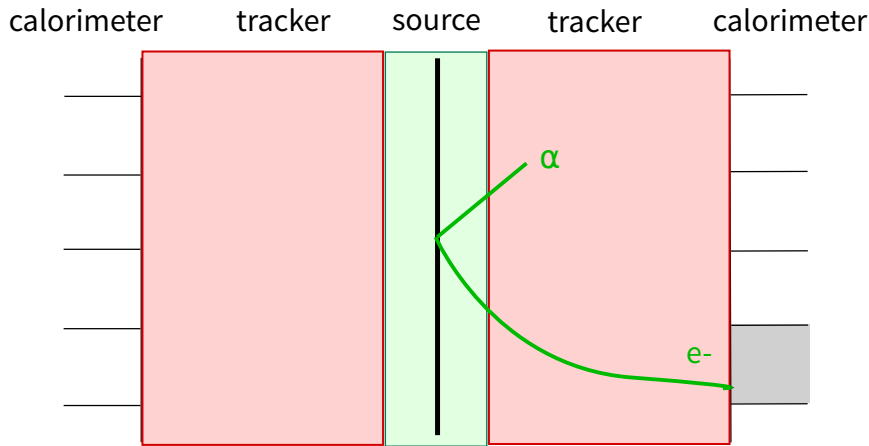


Figure 5.9: Source selection diagram of the source selection. The green part represents the region where the events are selected.

The design of SuperNEMO has been optimized to detect electrons coming from the source foil. The distance between the source foil and the main calorimeter wall is 45 cm. The presence of a magnetic field curves the charged particles and allows for charge separation. An electron emitted from the source foil, can easily cross the 9 layers of the tracker and hit the calorimeter. To be identified as an electron, a particle must come from the source foil, hit the main calorimeter wall, and have a reconstructed track with a negative curvature. The cut flow for selecting the electrons coming from the surface of the foil is summarized in Table 5.4.

	N	ϵ
# of simulated electrons	308 000	
# of reconstructed electrons	353 117	$114.6 \pm 0.2 \%$
# coming from the foil	296 440	$96.2 \pm 0.2 \%$
# hitting the main wall	126 520	$41.1 \pm 0.2 \%$
# having a negative charge	116 325	$37.8 \pm 0.2 \%$

Table 5.4: Cut flow of the electrons coming from the surface of the foil. The efficiencies are computed by dividing by the number of simulated electrons.

The number of reconstructed particles is higher than the number of simulated electrons ($+114.6 \pm 0.2\%$). This is due to some events, where the number of reconstructed particles can be higher than 1. The number of reconstructed particles can reach 4 or 5 in some events. An electron can be scattered by a wire in the tracker or can rebound on a calorimeter wall. The track is broken. In this case, CAT recognizes two clusters. These two clusters are then processed independently by TrackFit which fits two tracks instead of only one. In the future, a specific module could be implemented to merge these events in a single particle.

More than 96 % of the reconstructed particles come from the source foil. $42.2 \pm 0.2\%$ of the particles possess both a vertex on the source foil and a calorimeter impact in the main wall. Finally, by requiring negative charge, selection efficiency drops to $37.8 \pm 0.2\%$. The number of Geiger hits, the length of the track, and the energy of the electrons are shown in Figure 5.10.

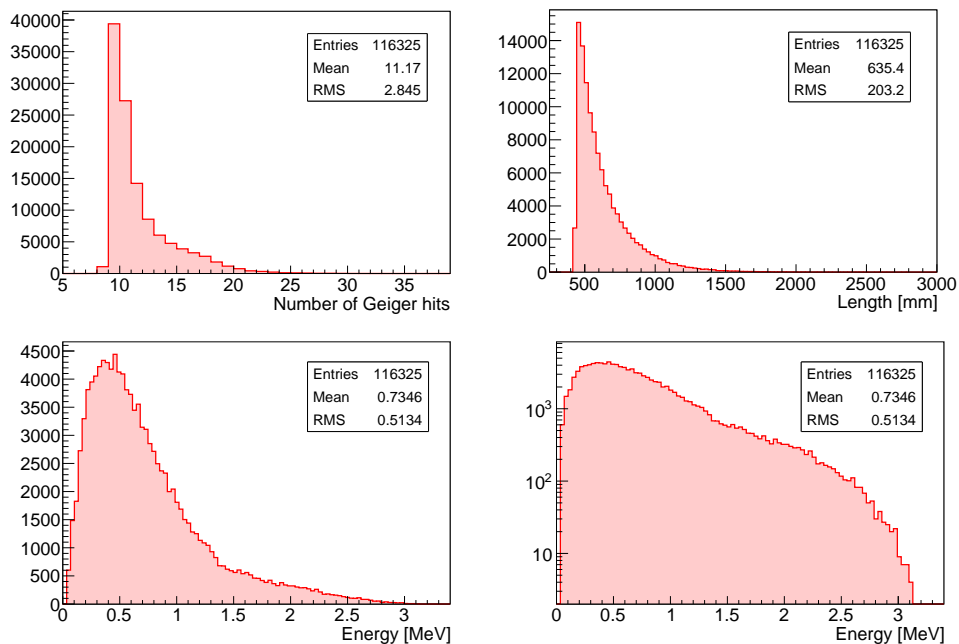


Figure 5.10: Top left : distribution of the number of Geiger hits for the electrons. Top right : length of the selected electron tracks. Bottom left : energy spectrum of the selected electron. Bottom right : energy spectrum in log scale

The number of Geiger hits is always greater than 8. This result makes sense because the tracker has 9 layers of wires between the source foil and the main calorimeter wall and the electron must cross the entire distance. Similarly, the distance between the source foil and the main calorimeter wall is 45 cm, so the minimum length observed cannot be smaller than this distance. The average distance travelled by an electron is 63 cm. The energy spectrum looks like the expected energy spectrum of the ^{214}Bi with the Q-value of 3.27 MeV.

The cut flow of the electrons coming from the bulk of the foil and coming from the tracker are summarized in Table 5.5 and Table 5.6.

With the source selection, $\sim 17\%$ of the electrons generated in the tracker are reconstructed and selected. These electrons correspond to events where the electron is simulated on the first layer close to the source foil. The vertex of these events is extrapolated and is considered to be on the source foil.

	N	ϵ
# of simulated electrons	308 000	
# of reconstructed electrons	320 379	104.0 \pm 0.2 %
# coming from the foil	272 325	88.4 \pm 0.2 %
# hitting the main wall	133 255	43.3 \pm 0.2 %
# having a negative charge	122 170	39.7 \pm 0.2 %

Table 5.5: Cut flow of the electrons coming from the bulk of the foil. The efficiencies are computed by dividing by the number of simulated electrons.

	N	ϵ
# of simulated electrons	308 000	
# of reconstructed electrons	385 176	125.0 \pm 0.2 %
# coming from the foil	210 811	68.4 \pm 0.2 %
# hitting the main wall	60 279	19.6 \pm 0.2 %
# having a negative charge	51 480	16.7 \pm 0.2 %

Table 5.6: Cut flow of the electrons coming from the tracker. The efficiencies are computed by dividing by the number of simulated electrons.

In order to verify the usefulness and the influence of the charge cut, a study is realized. The definition of the charge confusion is introduced as the ratio between the number of true electrons that have been reconstructed with a positive or no charge over the total of true electrons.

$$\text{charge confusion} = \frac{N_e^{\text{wrong}}}{N_e^{\text{tot}}} \quad (5.6)$$

Figure 5.11 (left) shows the electron track length. The black curve represents all the reconstructed electrons coming from the foil and hitting the main wall. The fraction of these electrons reconstructed with a negative charge are shown in red. The electrons reconstructed with a positive or no charge are plotted in blue. Figure 5.11 (right) also shows the charge confusion with respect to the length of the electron track.

For the events coming from the source foil, the charge confusion is $\sim 8\%$ and remains constant as a function of the length of the electron track. This criteria on the charge suppresses the multi-scattering of the electron inside the tracker chamber. For the selection of $1e1\alpha$ events coming from the source foil, this charge cut is used in order to get a high purity electron sample.

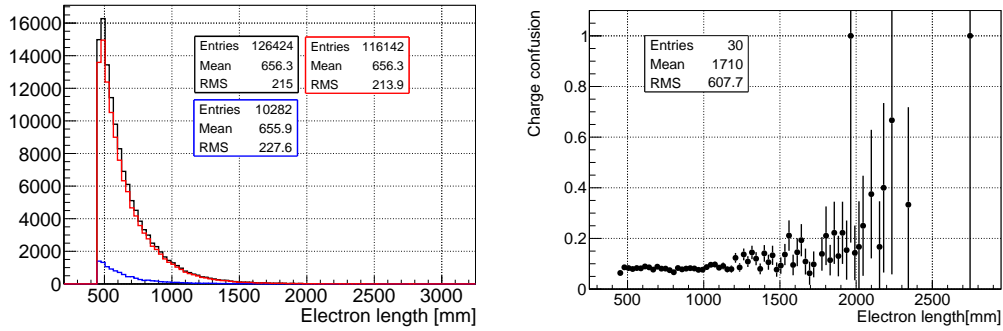


Figure 5.11: On the left : length of the electron track for different charge. The black curve represents all the reconstructed electrons coming from the foil and hitting the main wall. In red, the electrons coming from the source foil and hitting the main wall reconstructed with a negative charge. In blue, the electrons reconstructed with a positive or undefined charge. On the right: the charge confusion vs the length of the electron track.

To be identified as an alpha, the particle must be delayed, coming from the source foil without hitting the calorimeter. The cut flow of the alpha coming from the surface of the source foil is shown in Table 5.7.

	N	ϵ
# of simulated alphas	300 000	
# of reconstructed alpha	104 288	$34.8 \pm 0.2\%$
# being delayed	104 288	$34.8 \pm 0.2\%$
# coming from the foil	87 316	$29.1 \pm 0.2\%$
# not hitting the calorimeter	87 316	$29.1 \pm 0.2\%$

Table 5.7: Cut flow of the alpha coming from the foil surface. The efficiencies are computed by dividing by the number of simulated alphas.

After the simulation, 34.8 % of the alpha particles are reconstructed. Compared to the electron detection efficiency this number is much lower. Due to the high energy losses, events generated towards the source foil will not cross it, and $\sim 50\%$ of the events are lost. The number of alpha particles found by our criteria is $29.2 \pm 0.2\%$ of the simulated particle. The length and the number of Geiger hits of the alpha particles are plotted in Figure 5.12.

As expected the number of Geiger hits is low and does not exceed 9. The average number of Geiger hits for an alpha particle is 4. The average track length of the identified alpha is ~ 22 cm which is consistent with the estimated value in section 4, knowing that the tracker gas is made of 95 % of He. The cut flow of the alphas coming from the bulk of the foil and coming from the tracker are presented in Table 5.8 and Table 5.9 respectively.

The $1e1\alpha$ topology is built by associating, an electron and a delayed alpha. The track length of the alpha and the time between the electrons and the alphas are the main observables of this topology. The track length of the alphas according to the vertex generation (bulk in black, surface in blue, tracker in red) is shown in Figure 5.13.

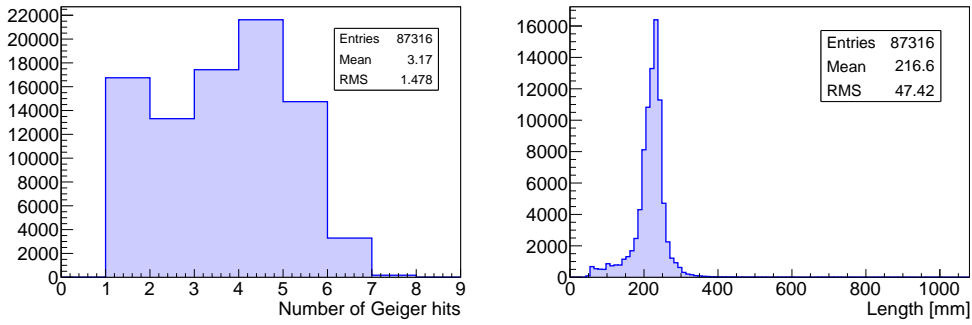


Figure 5.12: (a) On the left, the number of Geiger hits for the alpha particles. On the right the length of the track of the alphas

	N	ϵ
# of simulated alphas	300 000	
# of reconstructed alpha	33 876	$11.3 \pm 0.2\%$
# being delayed	33 876	$11.3 \pm 0.2\%$
# coming from the foil	24 306	$8.1 \pm 0.2\%$
# not hitting the calorimeter	24 301	$8.1 \pm 0.2\%$

Table 5.8: Cut flow of the alpha coming from the foil bulk. The efficiencies are computed by dividing by the number of simulated alphas.

	N	ϵ
# of simulated alphas	300 000	
# of reconstructed alpha	131 596	$43.9 \pm 0.2\%$
# being delayed	131 596	$43.9 \pm 0.2\%$
# coming from the foil	32 737	$10.9 \pm 0.2\%$
# not hitting the calorimeter	32 716	$10.9 \pm 0.2\%$

Table 5.9: Cut flow of the alpha coming from the tracker. The efficiencies are computed by dividing by the number of simulated alphas.

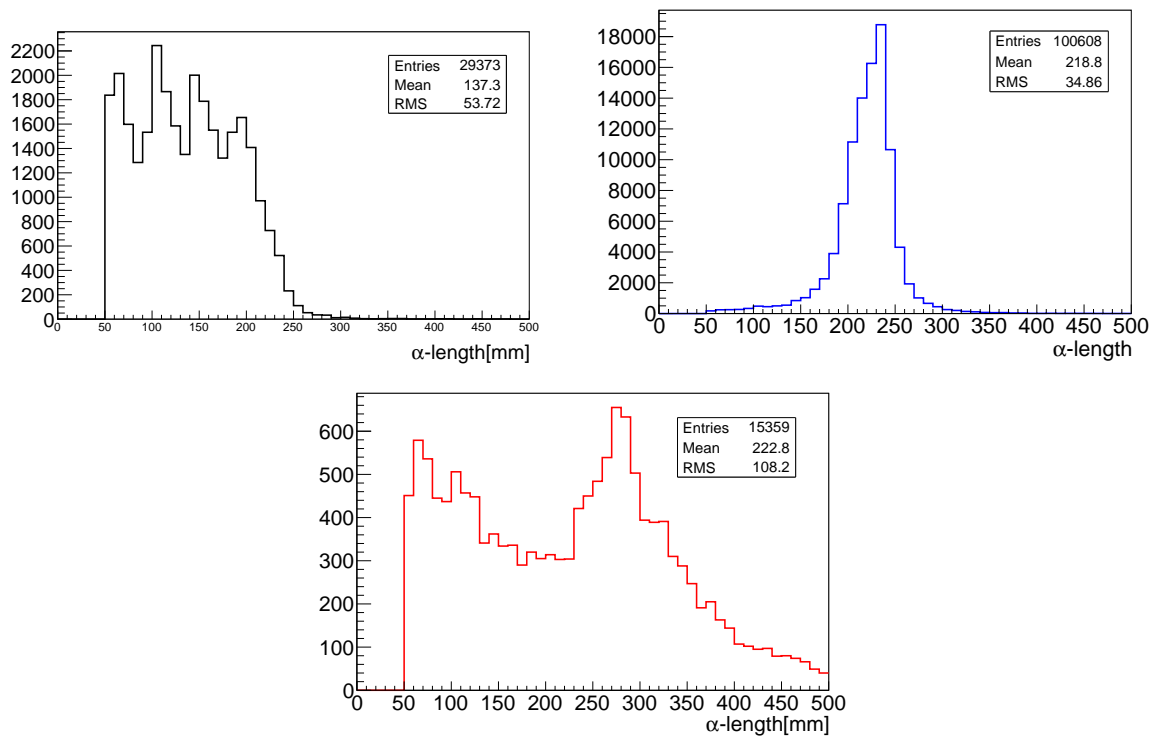


Figure 5.13: Alpha track length in the 1a1 α channel for the three contributions : source bulk (black), source surface (blue) and tracker (red).

Given the high ionisation power of the alpha particles, they lose a lot of energy just by crossing the source foil. Thus, the alpha particles coming from the bulk are expected to have a shorter track length than the alpha particles coming from the surface of the foil. The alpha particles coming from the tracker cross only the helium gas of the detector. Given the energy loss of the alpha in helium, the maximum length of the track will be around 45-50 cm.

The multi-peak distribution of the alpha particles coming from the bulk of the foil can be explained by the tracker configuration. The first peak corresponds to the alpha hitting the first tracker layer. The width of each peak corresponds to all the possible incident angles. The second peak corresponds to the alpha hitting the second layer of the tracker. This distribution is quite different from the distribution observed for the NEMO-3 experiment, due to the larger amount of wires in the tracker chamber which give us a better resolution on the length of the alpha.

The delayed time between the electron and the alpha is plotted in Figure 5.14. The half-life of the process is found to be $t_{1/2} = 162.6 \pm 4.1 \mu s$. This agrees well with the published value of $164.6 \pm 0.3 \mu s$ from [150].

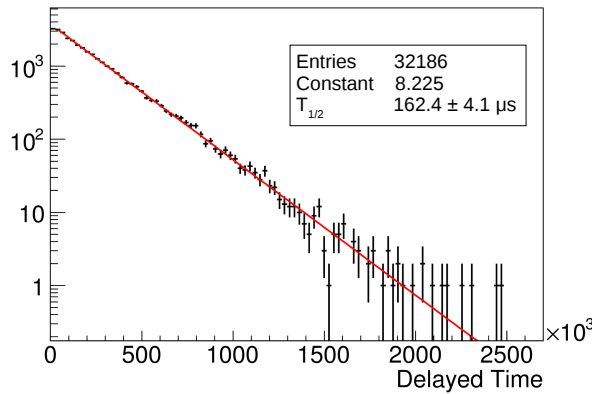


Figure 5.14: Time between the alpha and the electron in the identified $1a1\alpha$ channel with the source selection

A last optimisation on the delay time is done. Indeed, if an electron triggers a very remote cell, the drift time can be greater than $10 \mu s$ thus categorizing the hit as delayed. This Geiger cell will then be mis-identified as an alpha particle by the Alpha Finder algorithm. An example of this kind of event, with a "fake" alpha is shown in Figure 5.15.

The fake alphas lie tangent to the electron track thus the angle between the electron and the alpha ($\theta_{e-\alpha}$) is close to 0. Looking at the $\cos(\theta_{e-\alpha})$ distribution, fake alphas will contribute at $\cos(\theta_{e-\alpha}) \simeq 1$ as shown in Figure 5.16. The time distribution of the events which have $\cos \theta_{e-\alpha}$ in $[0.95 - 1]$ is also plotted in Figure 5.16.

A peak is observed in the time distribution for the events having $\cos(\theta_{e-\alpha}) \simeq [0.95 - 1]$ so, the fake alphas have a different time distribution. The value of Δt can thus be used as discriminating variable to remove the fake alphas. Knowing the true Monte Carlo information, we can check if the cell has

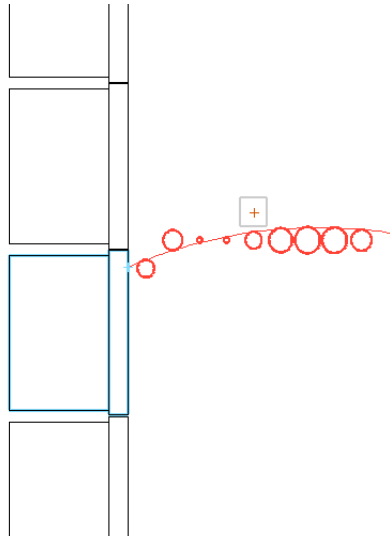


Figure 5.15: Example of a fake alpha : a cell of the electron track (the square) is considered as delayed and identified by the Alpha Finder as an alpha particle.

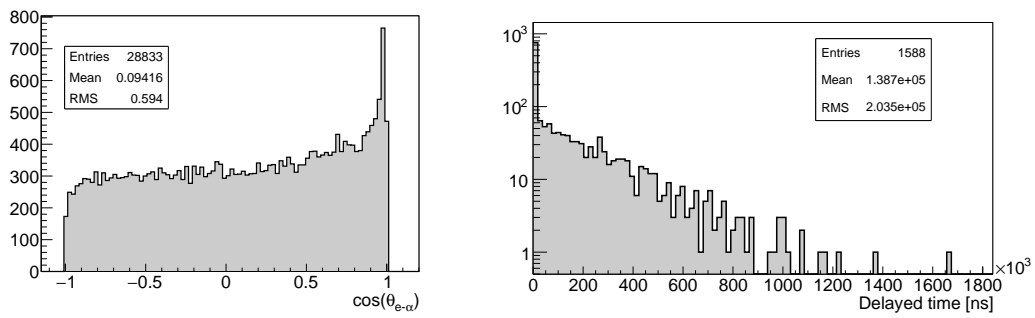


Figure 5.16: On the left : The angular distribution of the $1e1\alpha$ events with the fake alphas. The angle between the electron and the fake alpha is very close to zero, so an excess of events is expected near $\cos(\theta_{e-\alpha}) = 1$. On the right : the time distribution for events with $\cos(\theta_{e-\alpha})$ in $[0.95 - 1]$. An excess of events corresponding to fake alphas is observed for very small Δt .

been triggered by an alpha (true alpha event) or by an electron (fake alpha event) and study the two samples independently.

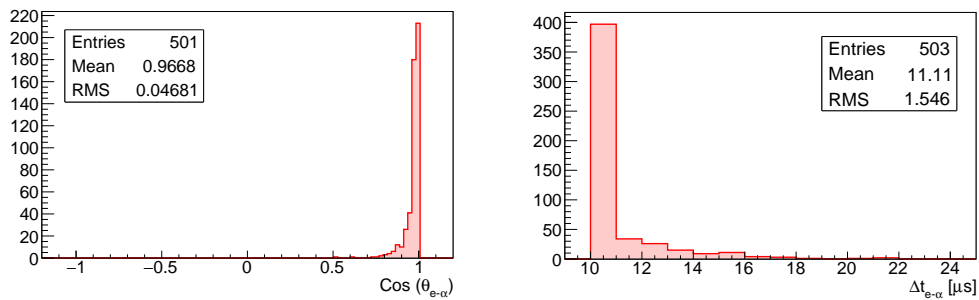


Figure 5.17: On the left : the angular distribution of the fake alpha. On the right : the time distribution of the fake alpha.

The time and angular distribution of the fake alphas are plotted in Figure 5.17. The delay time of the fake alphas never exceeds $25 \mu\text{s}$ and, as expected, the angular distribution is peaked close to $\cos \theta_{e-\alpha} = 1$. The same distributions are plotted in Figure 5.18 for the true alphas.

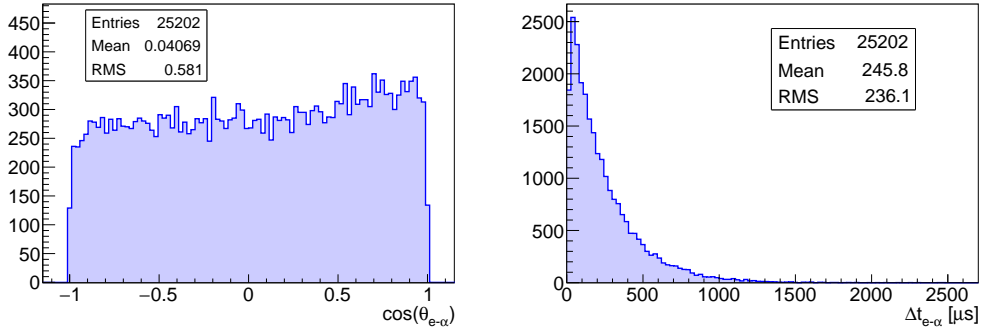


Figure 5.18: On the left : the angular distribution of the true alphas. On the right : the time distribution of the true alphas (note the scale on the abscissa is much larger here).

In order to remove the maximum number of fake alphas but keep the maximum number of true alphas, the cut on Δt has been optimized to maximize the product of the efficiency and purity ($\epsilon \times p$). The efficiency of the cut, is defined by the fraction of fake alphas removed by the cut at Δt :

$$\epsilon = \frac{\int_0^{\Delta t} f(t) dt}{\int_0^{+\infty} f(t) dt} \quad (5.7)$$

where $f(t)$ is the time distribution of the fake alphas. In the same way, the purity is defined as the fraction of the true alphas kept after the cut Δt :

$$p = \frac{\int_{\Delta t}^{+\infty} g(t) dt}{\int_0^{+\infty} g(t) dt} \quad (5.8)$$

where $g(t)$ is the time distribution of the true alphas. The efficiency of the cut (in red) and the purity (in blue) as a function of cut value Δt is shown in Figure 5.19. The product of the efficiency and the purity versus delay time is also plotted in Figure 5.19.

The product is maximized for a cut at $\Delta t_{e-\alpha} = 17.0 \mu\text{s}$. By selecting only events with $\Delta t_{e-\alpha} > 17.0 \mu\text{s}$, 98.6 % of the fake alphas are removed and only 2.9 % of true alphas are lost.

The number of reconstructed $1e1\alpha$ events depending on the vertex is given in the Table 5.10. So, $\sim 10 \%$ of the $1e1\alpha$ events generated on the surface of the foil are reconstructed. The efficiency of reconstruction of the $1e1\alpha$ events coming from the bulk is $\sim 3 \%$. With the source selection, $\sim 1.5 \%$ of the $1e1\alpha$ events coming from the tracker are reconstructed. These events are the events generated on the first layer of tracker wires close to the source foil. By default, the vertex is extrapolated to the source if the first layer of wire is hit.

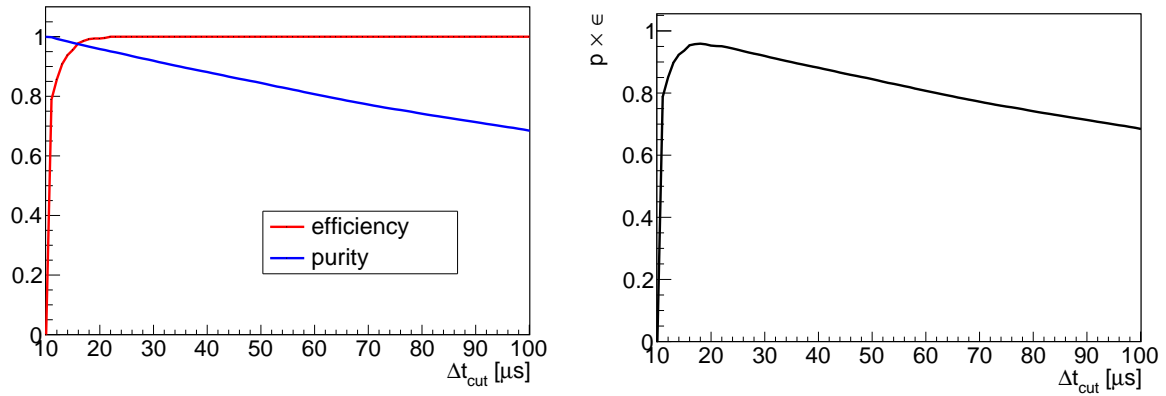


Figure 5.19: Left : the efficiency of the cut for the true alphas in blue and the fake alphas in red. Right : the product of the two efficiencies. This product has a maximum for a cut at $\Delta t_{e-\alpha} = 17.0 \mu s$.

	bulk	surface	tracker
$\epsilon_{1e1\alpha}$ [%]	2.94	10.07	1.59

Table 5.10: Summary of the efficiency, in different parts of the detector, computed with the Monte-Carlo.

5.4.2 $1e1\alpha$ events from the tracker

A picture representing the $1e1\alpha$ selection of the event coming from the tracker is shown in Figure 5.20. Only the events having their vertex in the green region (in the tracker except the first layer of wire close to the source) are selected.

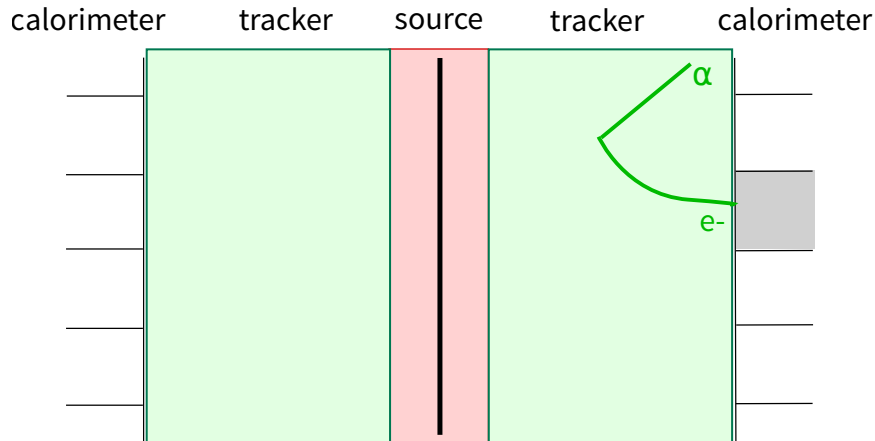


Figure 5.20: Tracker selection diagram of the tracker selection. The green part represents the region where the events are selected.

In this selection, an electron is defined as a prompt particle hitting a calorimeter. To increase the statistics, an electron can also hit the main wall, the γ -veto wall, or the x-wall. Generated in the tracker, some electrons are expected to be simulated very close to a calorimeter block and will not have a long track. In some cases, electron tracks can be only 2-3 Geiger hits even appearing on a straight line. So, the same study about the charge confusion is realized.

The electron length and the charge confusion are plotted in Figure 5.21. The charge confusion is high for the short length and reaches 80 %. The charge confusion decreases with the length of the track and reaches a stable value of 20 % for tracks longer than 50 cm.

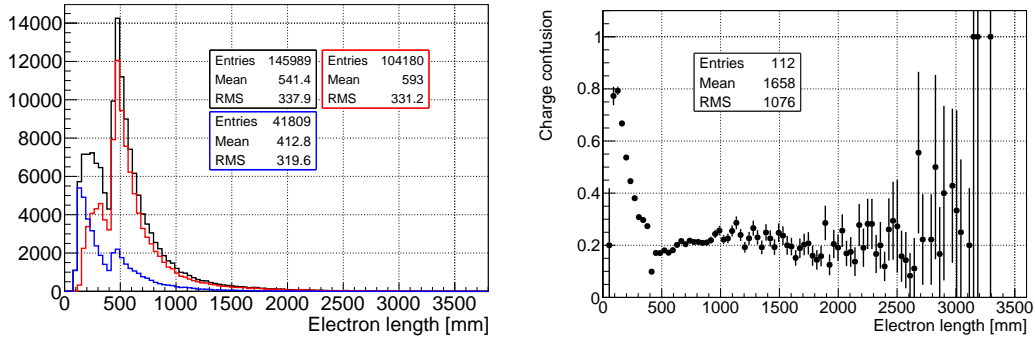


Figure 5.21: On the left : length of the electron vs the charge. The black curve represents all the reconstructed electrons hitting a calorimeter. In red, the electrons hitting a calorimeter reconstructed with a negative charge. In blue, the electrons reconstructed with a positive or undefined charge. On the right : the charge confusion vs the length of the electron track.

If a cut is introduced to select the electrons reconstructed with a negative charge, $\sim 27\%$ of the true electrons are lost. So, in order to avoid losing too many events, no cut on the charge is introduced. The cut flow of the electrons coming from the tracker is summarized in Table 5.11.

	N	ϵ
# of simulated electrons	308 000	
# of reconstructed electrons	385 176	$125.0 \pm 0.2\%$
# coming from the tracker	385 176	$125.0 \pm 0.2\%$
# hitting the main wall	144 187	$46.8 \pm 0.2\%$
# having a negative charge	78 940	$25.6 \pm 0.2\%$

Table 5.11: Cut flow of the electrons coming from the tracker. The efficiencies are computed by dividing by the number of simulated electrons.

By releasing the cut on the charge and allowing an electron to hit the x-wall or the γ veto, the selection of the electron in the tracker is $\sim 25\%$. The cut flow of the electrons coming from the bulk and the surface of the foil are summarized in Table 5.12 and Table 5.13.

As expected, the selection efficiency of the electrons coming from the foil is low, $\sim 6\%$ and $\sim 7\%$. This corresponds to electrons coming from the source foil that did not trigger the first layer of wires of the tracker. The vertex of these events is reconstructed in the tracker even if they come from the source foil.

An alpha is defined as a particle delayed in time hitting no calorimeter and not coming from the source. The cut flow of the alpha of the tracker is summarized in Table 5.14, in Table 5.15 (bulk) and Table 5.16 (surface).

	N	ϵ
# of simulated electrons	308 000	
# of reconstructed electrons	320 379	104.0 \pm 0.2 %
# coming from the tracker	320 379	104.0 \pm 0.2 %
# hitting the main wall	161 308	53.8 \pm 0.2 %
# having a negative charge	17 088	5.4 \pm 0.2 %

Table 5.12: Cut flow of the electrons coming from the bulk. The efficiencies are computed by dividing by the number of simulated electrons.

	N	ϵ
# of simulated electrons	308 000	
# of reconstructed electrons	362 157	117.6 \pm 0.2 %
# coming from the tracker	362 157	117.6 \pm 0.2 %
# hitting the main wall	159 893	51.9 \pm 0.2 %
# having a negative charge	21 567	7.0 \pm 0.2 %

Table 5.13: Cut flow of the electrons coming from the surface. The efficiencies are computed by dividing by the number of simulated electrons.

	N	ϵ
# of simulated alphas	300 000	
# of reconstructed alpha	131 596	43.9 \pm 0.2 %
# being delayed	131 596	43.9 \pm 0.2 %
# coming from the tracker	98 880	33.0 \pm 0.2 %
# hitting no calorimeter	98 859	33.0 \pm 0.2 %

Table 5.14: Cut flow of the alpha coming from the tracker. The efficiencies are computed by dividing by the number of simulated alphas.

	N	ϵ
# of simulated alphas	300 000	
# of reconstructed alpha	33 876	11.3 \pm 0.2 %
# being delayed	33 876	11.3 \pm 0.2 %
# coming from the tracker	9 570	3.19 \pm 0.2 %
# hitting no calorimeter	9 565	3.19 \pm 0.2 %

Table 5.15: Cut flow of the alpha coming from the bulk of the foil. The efficiencies are computed by dividing by the number of simulated alphas.

The $1e1\alpha$ topology is built by associating, an electron and a delayed alpha. The alpha length of the different contributions are plotted in Figure 5.22. The delayed time between the electron and the alpha is shown in Figure 5.23. The optimisation introduced in the previous section on the $\Delta t > 17 \mu s$ is also applied because it does not depend on the vertex position.

	N	ϵ
# of simulated alphas	300 000	
# of reconstructed alpha	104 288	$34.8 \pm 0.2 \%$
# being delayed	104 288	$34.8 \pm 0.2 \%$
# coming from the tracker	16 972	$5.66 \pm 0.2 \%$
# hitting no calorimeter	16 972	$5.66 \pm 0.2 \%$

Table 5.16: Cut flow of the alpha coming from the surface. Cut flow of the alpha coming from the tracker. The efficiencies are computed by dividing by the number of simulated alphas.

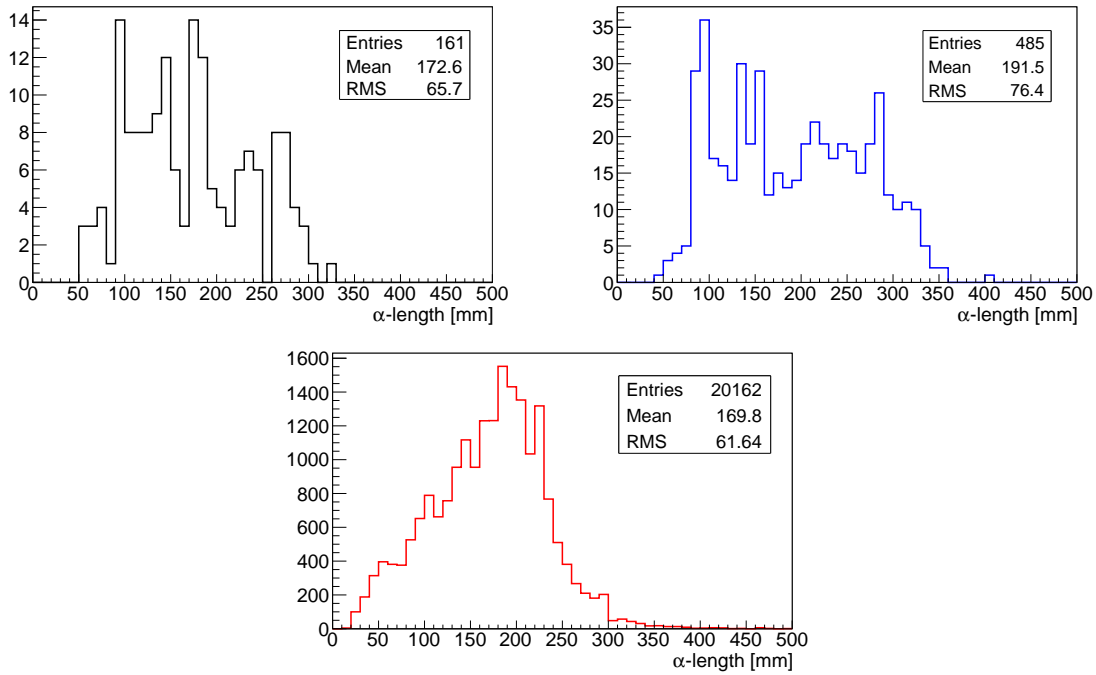


Figure 5.22: Alpha track length for different contributions : source bulk (black), source surface (blue) and tracker (red).

The number of reconstructed $1e1\alpha$ events according to the vertex is given in Table 5.17. So, $\sim 7 \%$ of the $1e1\alpha$ events generated in the tracker are reconstructed. The efficiency of reconstruction of the $1e1\alpha$ events coming from the surface and the bulk is $\sim 0.2 \%$ and $\sim 0.05 \%$. With the tracker selection, the efficiency of reconstruction of the $1e1\alpha$ events coming from the source is very low. These residual events are the events coming from the source foil but not hitting the first layer of wires close to the source foil. The vertex of these events are extrapolated to be in the tracker. Figure 5.23 shows the time between the alpha and the electron in the $1a1\alpha$ channel with the tracker selection. The half-life on the process is found to be $164.01 \pm 4.1 \mu\text{s}$ which is in agreement with the published value [150].

	bulk	surface	tracker
$\epsilon_{1e1\alpha} [\%]$	0.05	0.16	6.72

Table 5.17: Summary of the efficiency, in different parts of the detector, computed with the Monte-Carlo.

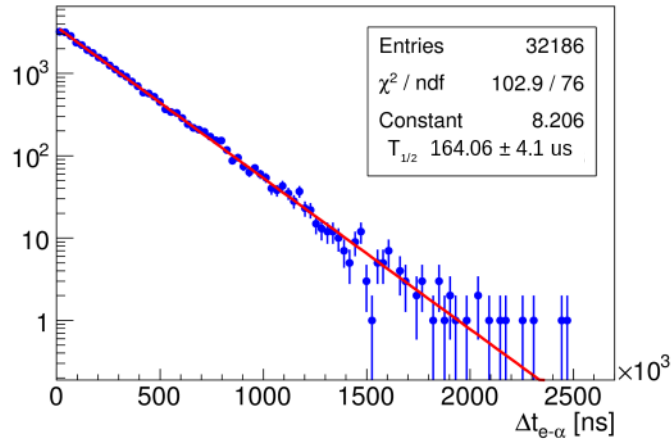


Figure 5.23: Time between the alpha and the electron in the identified $1a1\alpha$ channel with the tracker selection

5.5 Measurement

In order to distinguish the contributions coming from the source foil (bulk and surface) and the tracker, the length of the alpha track is used. The strategy used to compute, for each contribution, the number of expected events and their relative error is described here. As an example, the method is explained using the source selection.

1) Normalization to the activity and sum : The three distributions of the alpha track length given in Figure 5.13 are normalized to their respective activities computed in Section 5.1 and summed. Figure 5.24 shows the summed distribution.

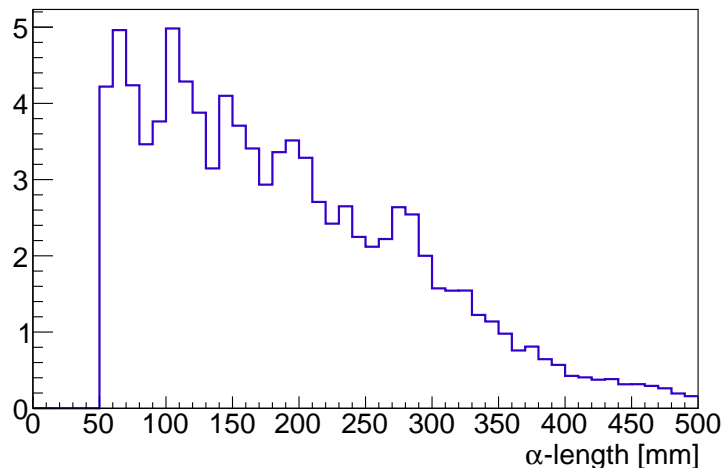


Figure 5.24: Summed and normalized alpha length distribution from the 3 contributions (source bulk, source surface and tracker).

2) Normalization to the exposure : The previous distribution is normalized to a given exposure. The final distribution is obtained.

3) Generation of a pseudo experiment : From this final distribution a pseudo experiment is generated. To mimic the real data, the number of expected events is a random number according to Poissonian law. Figure 5.25 shows a pseudo experiment after an exposure of 60 days.

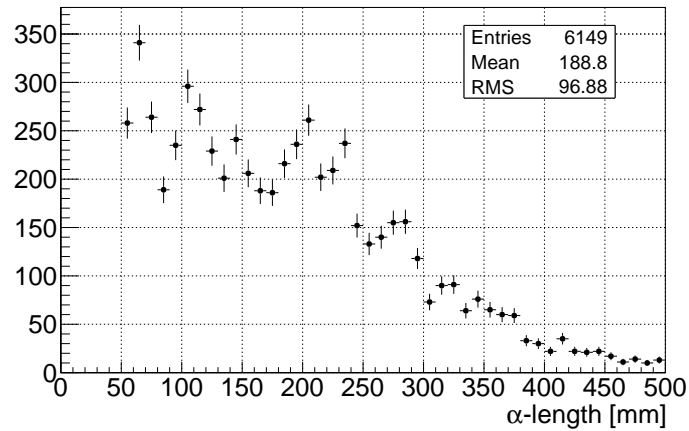


Figure 5.25: Pseudo experiment, length of the α track after an exposure of 60 days.

4) Fit the pseudo-experiment : The pseudo-experiment is fitted with the three distributions presented in Section 5.4. The fit is a likelihood fit (à la NEMO 3) which returns the activity of each component. Figure 5.26 shows the result of the fit.

5) Repeat 3 and 4 : The actions 3 and 4 are repeated 10^5 times. The distribution of the fitted activity of each component is plotted in Figure 5.27. The mean activity (μ) and the sigma (σ) are recovered. The relative error is defined as the ratio : σ / μ .

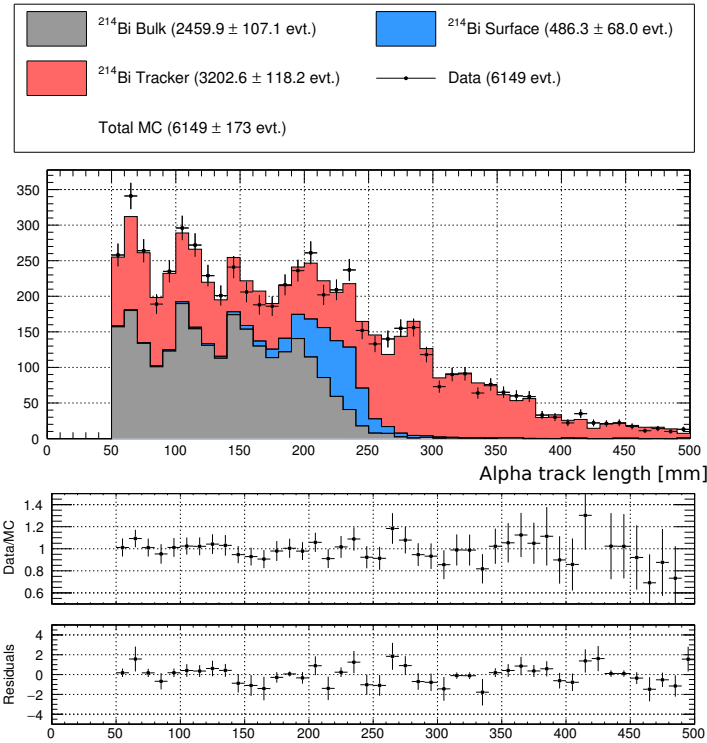


Figure 5.26: Fit of the pseudo-experiment with the three contributions after an exposure of 60 days. In red, the tracker contribution. In blue, the surface contribution. In black, the bulk contribution.

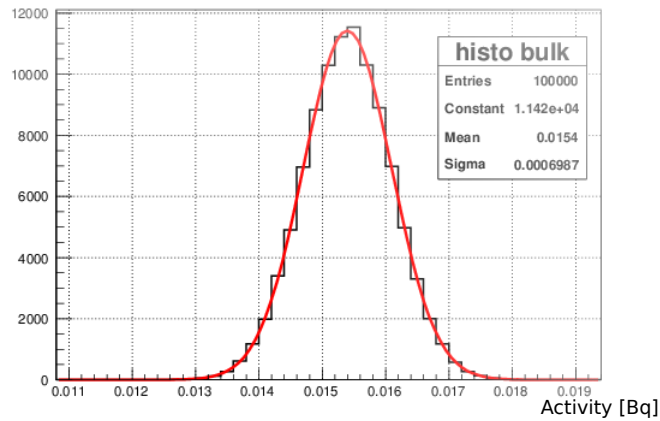


Figure 5.27: Distribution of the fitted activities for the bulk contribution

5.6 Results and Conclusion

The method described in Section 5.5 is generalized to different exposures. For both selections, source and tracker, the number of expected events is computed according to Eq.5.1 and by using the selection efficiency presented in Section 5.4 and the mean activity computed in Section 5.5.

5.6.1 Source selection

Concerning the source selection, the number of events according to the exposure for the different contributions is shown in Figure 5.28. Table 5.18 summarizes the number of expected events after 1 day, 1 week, 2 weeks and 1 month with the source selection. The relative error defined as the ratio σ/μ is computed for different exposures and shown in Figure 5.29. Table 5.19 gives the results at some exposures.

	@ 1 day	@ 1 week	@ 2 weeks	@ 1 month
N_{bulk} [cts.]	~ 40	~ 275	~ 600	~ 1175
N_{surface} [cts.]	~ 2	~ 10	~ 25	~ 50
N_{tracker} [cts.]	~ 60	~ 420	~ 900	~ 1800

Table 5.18: Number of expected events vs the exposure time for the different contributions using the source selection.

	@ 1 day	@ 1 week	@ 2 weeks	@ 1 month
$(\sigma/\mu)_{\text{bulk}}$	24.9 %	9.4 %	6.4 %	4.5 %
$(\sigma/\mu)_{\text{surface}}$	279 %	129 %	88.6 %	63.0 %
$(\sigma/\mu)_{\text{tracker}}$	18.0 %	6.8 %	4.7 %	3.3 %

Table 5.19: Relative errors vs the exposure time for the different contributions using the source selection.

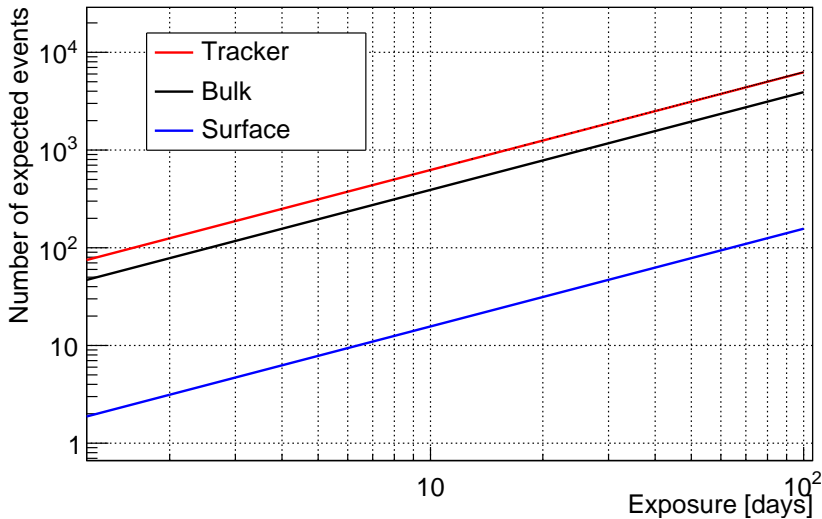


Figure 5.28: Number of expected events vs the exposure time for the different contributions using the source selection.

With the source selection, the level of ^{214}Bi background coming from the source bulk can be known at $\sim 10\%$ after one week of data taking. The level of ^{214}Bi background coming from the surface of the foil, due to its very low activity compared to the other contributions, is expected to be measured with a high uncertainty, $\sim 63\%$ after one month of data taking. Note that this value is a bit pessimistic since

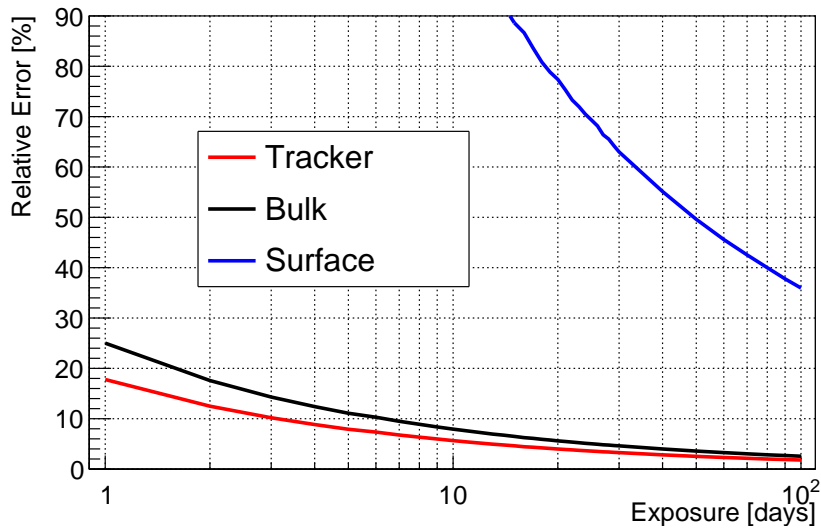


Figure 5.29: Relative errors using the source selection vs the exposure.

this study does not take into account that a fraction of the ^{222}Rn inside the tracker can be transferred to the foil surface. Furthermore, new radon emanation measurements of the tracker show that the activity of the tracker has been a little bit overestimated in this work. Finally, note that even if the source selection is not optimised to measure the background contribution from the tracker, it can be measured at $\sim 7\%$ after one week of data taking.

5.6.2 Tracker selection

For the tracker selection, the number of expected events according to the exposure is plotted in Figure 5.30 and the relative errors are shown in Figure 5.31. Table 5.20 summaries the results for several different exposures. The level of ^{222}Rn inside the tracker can be known at $\sim 8\%$ after one day and can be monitored daily. Moreover, as this selection is not optimised for the events coming from the bulk and the surface of the foil, the selection efficiencies are low and the expected number of events coming from the foil are negligible. The measurement of the level of ^{222}Rn in the tracker volume will be one of the measurements to be performed.

	@ 1 day	@ 1 week	@ 2 weeks	@ 1 month
N_{tracker}	~ 265	~ 1860	~ 4000	~ 8000
$(\sigma/\mu)_{\text{tracker}}$	8.3 %	3.1 %	2.1 %	1.5 %

Table 5.20: Number of expected events and relative errors in tracker vs the exposure time for the tracker selection.

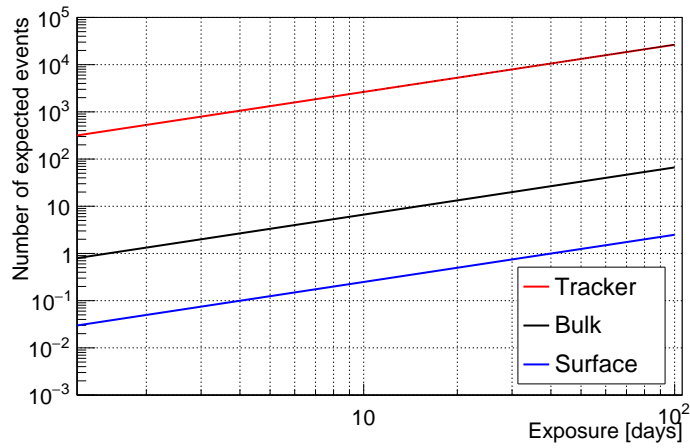


Figure 5.30: Number of expected events vs the exposure time for the different contributions using the tracker selection.

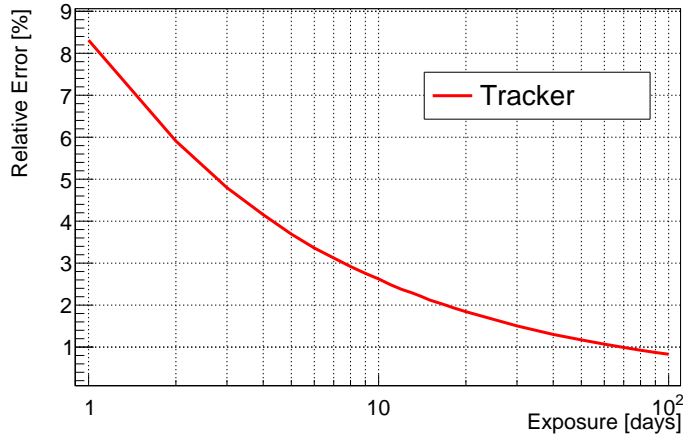


Figure 5.31: Relative errors using the tracker selection vs the exposure.

According to the efficiency of reconstruction of the $1e1\alpha$ channel and the different activities measured by the collaboration, the number of expected events due to the ^{222}Rn can be computed. The level of ^{222}Rn coming from the tracker can be known at $\sim 8\%$ after one day of measurement, so, it can be measured daily. The level of ^{222}Rn coming from the foil bulk can be known at $\sim 10\%$ after one week of measurement.

Chapter 6

Search for $\beta\beta$ decay of ^{116}Cd into the excited states of ^{116}Sn

The investigation of the $\beta\beta$ decays of ^{116}Cd via the excited states of ^{116}Sn is described in this section. These decays are expected to be even rarer than the decays to the ground state but their very clear signature topology, simultaneous emission of two electrons accompanied by one or more photons, allow their searches with a high background suppression.

The two main excited states of ^{116}Sn are introduced in Section 6.1. The analysis technique used to perform the search is described in Section 6.2. The modelisation of the background and the measurement of its different contributions are presented in Section 6.3. The preselection criteria of the events for these decay channels are described in Section 6.4. The optimisation of the cuts using a multivariate approach is presented in Section 6.5. The evaluation of the sources of systematic uncertainties is discussed in Section 6.6. The results of these searches are presented in Section 6.7 and Section 6.8 for the two main excited states respectively in both 2ν and 0ν decay modes. Finally the results are summarised in Section 6.9.

6.1 Excited states of ^{116}Sn

The search for the $2\nu\beta\beta$ and $0\nu\beta\beta$ decays to the ground state have been investigated with the full statistics of NEMO-3 [141]. In theory, the $\beta\beta$ decays can also occur through the excited states of the daughter nucleus. Due to smaller phase spaces these decays to the excited states are even rarer than the decay to the fundamental state but some of them have already been observed for ^{100}Mo and ^{150}Nd nuclei [156]. Concerning the ^{116}Cd , the $\beta\beta$ decays via the excited states have never been observed. The results of this analysis will lead to the first values or limits put on these processes with the NEMO-3 data.

The searches for $\beta\beta$ decays through the excited states is mainly motivated by a better understanding of the nuclear structures. The measurement of the decay rate could bring information on nuclear matrix elements, which are sensitive to nuclear-spin isospin correlations, and provide additional handle for NME calculations. The decays via the excited states are also interesting to investigate the $0\nu\beta\beta$ mechanism by giving us alternative channels to study an hypothetical $0\nu\beta\beta$ signal. Finally, they also offer us the possibility to distinguish between the various $0\nu\beta\beta$ mechanisms since the branching ratios of $0\nu\beta\beta$ decay between the excited states and the ground state could differ according to the model [94].

The simplified diagram of the ^{116}Cd decay to ^{116}Sn is shown in Figure 6.1. Only the 2 first excited

states are considered at 1294 keV (2^+) and at 1757 keV (0^+). These two excited states will be studied in case of $2\nu\beta\beta$ and $0\nu\beta\beta$. The label and the description of each case are given below :

- **(0^+) 2ν** : The signature of this decay is the simultaneous emission of 2 electrons and 2 photons. The $Q_{\beta\beta}$ of the electron energy spectrum is 1048 keV. The photon energy spectrum is very characteristic with two peaks at 463 keV and 1294 keV.
- **(0^+) 0ν** : The signature of this decay is the simultaneous emission of 2 electrons and 2 photons. As no neutrino is emitted, the electron energy sum spectrum is peaked at 1048 keV. The photon energy spectrum is the same as in (0^+) 2ν .
- **(2^+) 2ν** : The signature of this decay is the simultaneous emission of 2 electrons and 1 photon. The $Q_{\beta\beta}$ of the electron energy spectrum is 1511 keV. The gamma energy spectrum is characterized by a peak at 1294 keV.
- **(2^+) 0ν** : The signature of this decay is the simultaneous emission of 2 electrons and 1 photon. The electron energy sum spectrum is characterized by a peak at 1511 keV. The photon energy spectrum is the same as in (2^+) 2ν .

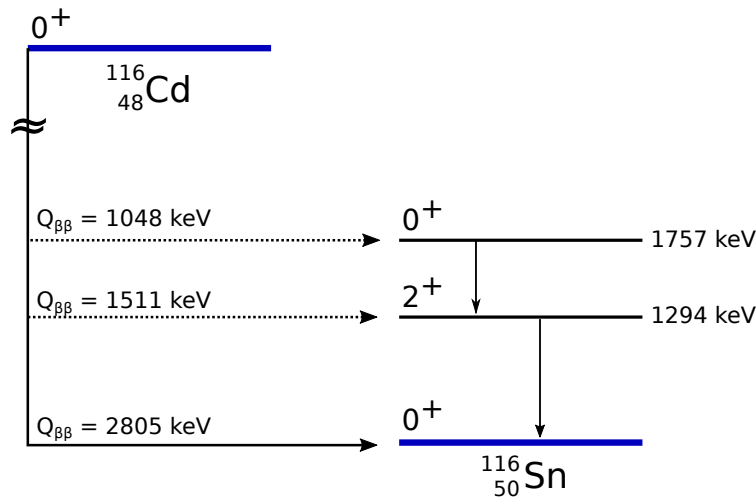


Figure 6.1: Diagram of the two main excited states of ^{116}Sn . The excited state 0^+ (1757 keV) corresponds to the emission of two electrons with a $Q_{\beta\beta} = 1048$ keV and two photons at 1294 keV and 463 keV. The excited state 2^+ (1294 keV) corresponds to the emission of two electrons with a $Q_{\beta\beta} = 1511$ keV and one photon at 1294 keV. In case of $2\nu\beta\beta$ these decays are accompanied by two neutrinos.

Theoretically, the decay probability to the excited states is proportional to $(Q_{\beta\beta} - E^*)^{11}$ in $2\nu\beta\beta$ decay and to $(Q_{\beta\beta} - E^*)^5$ in $0\nu\beta\beta$ decay, where $Q_{\beta\beta}$ is the total available energy and E^* the energy of the excited state. It can be deduced that the decay to the excited state 2^+ is more likely than the decay via 0^+ . Furthermore, as the detection efficiency of the electrons increases with their energy, the decays via the excited state 2^+ seem easier to detect. On the other hand, the presence of two electrons and one photon inside the detector is more reproducible by the background than the presence of two electrons and two photons. In any case, the detection efficiency of the two electrons and one or more photons will be very low. This explains why the search for decays via the excited states is very challenging with the NEMO-3 detector.

Historically, the first observation of the ^{116}Cd $2\nu\beta\beta$ decay was reported in 1995 by three independent experiments : NEMO-2 [156], Elegant-V [157] and at the Solotvina Underground laboratory[109]. NEMO-2 was installed at LSM and took data during ten months with an enriched cadmium source surrounded by tracking chamber and plastic scintillator calorimeter. The half-life of $2\nu\beta\beta$ was measured to be $T_{1/2}^{2\nu} = (2.9 \pm 0.3 \text{ (stat)} \pm 0.2 \text{ (syst)}) \times 10^{19} \text{ y}$. Limit at 90% C.L on the ^{116}Cd half-life of $T_{1/2}^{0\nu} > 5.0 \times 10^{21} \text{ y}$ for $0\nu\beta\beta$ decay was obtained with an exposure of $0.11 \text{ kg}\times\text{y}$. At the same time, ELEGANT-V reported the results of the double beta decay using natural and enriched cadmium foils sandwiched between drift chambers and plastic scintillators. Sodium iodide scintillators were used to enhance background rejection. The half-life has been measured to be $T_{1/2}^{2\nu} = 2.6^{+0.9}_{-0.5} \times 10^{19} \text{ y}$ with an exposure of $0.02 \text{ kg}\times\text{y}$. A lower limit on the $0\nu\beta\beta$ was set to $T_{1/2}^{0\nu} > 2.9 \times 10^{21} \text{ y}$. These measurements are compatible with the results obtained with cadmium tungstate crystal scintillators at the Solotvina Underground Laboratory. The half-life of $2\nu\beta\beta$ was measured to be $T_{1/2}^{2\nu} = 2.7^{+0.5}_{-0.4} \times 10^{19} \text{ y}$. The lower limit on the half-life was set to $T_{1/2}^{0\nu} > 2.9 \times 10^{22} \text{ y}$ at 90% C.L.

More recently the study of the ^{116}Cd decay has continued mainly using CdWO_4 scintillator crystals. The Solotvina experiment reported the results obtained with 330 g of crystals for a total exposure of $0.4 \text{ kg}\times\text{y}$ [158]. The $2\nu\beta\beta$ half-life was measured to be $T_{1/2}^{2\nu} = [2.9 \pm 0.06 \text{ (stat.)}^{+0.4}_{-0.3} \text{ (syst.)}] \times 10^{19} \text{ y}$. Installed at the Gran Sasso Underground Laboratory, the Aurora experiment investigated double beta decay of ^{116}Cd with 1.162 kg of crystal scintillators enriched to 82 % [109]. The half-life of $2\nu\beta\beta$ was measured to be $T_{1/2}^{2\nu} = [2.62 \pm 0.14] \times 10^{19} \text{ y}$ for the ground state. The lower limit on the half-life was set to $T_{1/2}^{0\nu} > 1.7 \times 10^{23} \text{ y}$ at 90% C.L. Aurora also puts new limits concerning the decay of ^{116}Cd via the excited state of ^{116}Sn . The main results obtained for $2\nu\beta\beta$ and $0\nu\beta\beta$ decays to the ground and the excited states are summarised in Table 6.1.

Experiment	Decays	$T_{1/2}$ half-life or limit [y] at 90 % C.L	ref
NEMO-2	2ν (g.s)	$[2.9 \pm 0.3 \text{ (stat.)} \pm 0.2 \text{ (syst.)}] \times 10^{19}$	[156]
	0ν (g.s)	$> 5 \times 10^{22}$	
NEMO-3	2ν (g.s)	$[2.74 \pm 0.04 \text{ (stat.)} \pm 0.18 \text{ (syst.)}] \times 10^{19}$	[141]
	0ν (g.s)	$> 1.0 \times 10^{23}$	
ELEGANT-V	2ν (g.s)	$[2.6^{+0.9}_{-0.5}] \times 10^{19}$	[157]
	0ν (g.s)	$> 2.9 \times 10^{22}$	
Solotvina	2ν (g.s)	$[2.9 \pm 0.06 \text{ (stat.)}^{+0.4}_{-0.3} \text{ (syst.)}] \times 10^{19}$	[158]
	0ν (g.s)	$> 1.9 \times 10^{23}$	
Aurora	2ν (g.s)	$[2.62 \pm 0.06 \text{ (stat.)} \pm 0.14 \text{ (syst.)}] \times 10^{19}$	[109]
	2ν (0^+)	$> 1.0 \times 10^{21}$	
	2ν (2^+)	$> 9.0 \times 10^{20}$	
	0ν (g.s)	$> 1.9 \times 10^{23}$	
	0ν (0^+)	$> 6.3 \times 10^{22}$	
	0ν (2^+)	$> 6.2 \times 10^{22}$	

Table 6.1: Summary of results for the search for $2\nu\beta\beta$ and $0\nu\beta\beta$ decays to the fundamental and excited states.

6.2 Analysis technique

The NEMO-3 analysis technique consists in a comparison of the experimental data obtained by the detector to the Monte-Carlo simulations of physics processes such as double beta decay. The simulated data are then propagated through the NEMO-3 detector by GEANT-3. Section 6.2.1 presents the event generation and their propagation in the detector. Both simulated and real data are then reconstructed with a dedicated software package developed by the collaboration. Section 6.2.2 introduces the event reconstruction which provides the information necessary for building the objects used in particle identification. The particle identification, presented in Section 6.2.3, and the timing information, shown in Section 6.2.4, are then used to identify different independent analysis channels. Section 6.2.6 describes the statistical tools used to measure the background, to set limits or to optimise the selection. Finally, Section 6.2.6 presents the method used to translate decay rates measured with NEMO-3 data into half-lives.

6.2.1 MC simulation

The Monte Carlo simulations for NEMO-3 are generated using the GENBB event generator [160]. This program, which is a particular implementation of DECAY0 used by NEMO-3, provides the initial state of the particles with accurate kinematics, timing and branching ratio. GENBB generates all the necessary information on $2\nu\beta\beta$ and $0\nu\beta\beta$ decay modes and also on the different decays used for the background isotopes.

The transport of the particles generated by GENBB through NEMO-3 is simulated by GEANT-3.21 [161] which uses a full description of the detector. GEANT-3.21 simulates the interactions of the particles in all of the simulated detector components. The simulated data are then digitized in exactly the same format as raw data in a way to use the same reconstruction process.

6.2.2 Event reconstruction

The real and simulated data are reconstructed and calibrated in a same way thanks to a dedicated software package called NEMOR. This program uses the digitized information to produce the physical objects used in the NEMO-3 data analysis.

In order to take into account the different data taking conditions, and ensure that MC events can be directly compared to the real data, all the MC sample events are distributed into several run periods according to the length of the real data runs. This can be performed thanks to the existence of a database containing all the information relative to the real detector running conditions such as the life time of each run. The database also contains the status of each PMT and each Geiger cells during the lifetime of the experiment. All this information such as the dead channel or the real-time calibration coefficients can be used during the reconstruction of the simulated data in order to be as close as possible to the data acquisition conditions.

Track reconstruction

The reconstruction of the particle track inside the tracker is performed in NEMOR software. During the passage of a charged particle in the tracker, the wires close to its passage are triggered and constitute the building blocks for the tracking pattern recognition algorithm. Depending on the transverse and longitudinal hit positions and the timing informations, the hits are clustered together using a cellular automaton tracking algorithm. This algorithm searches for successive hits in the neighbouring layers and

connects them with simple line segments. This process continues until there are no more consecutive hits. When all the segments have been added to the cluster, they are removed from the search and a new one starts until there are no segments available to build a track. After the identification of all the tracks in the events, three helical fits are performed for each track. The first fit, which is global, uses all the hits contained in the track cluster. This fit provides the measurement of the track length. The two other fits are performed using only the hits closest to the source foil and closest to the calorimeter wall to precisely measure the vertex position on the source foil and the impact point on the calorimeter block.

6.2.3 Particle identification

By using the reconstructed information provided by the tracker and calorimeter, NEMO-3 gives us the ability to distinguish between different types of particles. The identifiable particles in NEMO-3 data are electrons, positrons, photons and alpha particles.

Electron identification

Electrons and positrons are identified as curved tracks inside the tracker. The track must intersect the source foil and be associated to a single calorimeter hit. Thanks to the magnetic field, the distinction between electrons and positrons can be performed by looking at their opposite curvature. Figure 6.2.3 shows an event where two electrons have been identified in the NEMO-3 data. In order to properly reconstruct the full energy of the electrons, the neighbouring optical modules, side and diagonally, must not be fired. If neighbouring optical modules have hits, this could be explained by a scattering off of the first optical module to a close one. In this kind of event, the trajectory of the particle is not well reconstructed by the tracking algorithm. These events are associated with a large systematic uncertainty or can be removed from the analysis.

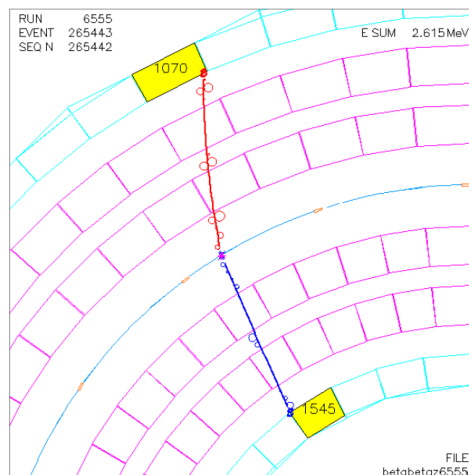


Figure 6.2: Top view of the NEMO-3 detector where two electron candidates have been identified in the NEMO-3 data. The red and blue lines are the reconstructed tracks, the small circles correspond to the Geiger hits. Their sizes depend on the distance between the particle track and the anode wire. The blue boxes are the inner and outer calorimeter walls. The location of the calorimeter hits are colored in yellow. The magenta boxes represent the petal scintillators.

Photon identification

The photons do not leave a track in the tracker volume. Moreover, as the detection efficiency for a photon of 0.5 MeV is 60 %, nothing guarantees that the photon is fully contained in a single or isolated calorimeter hit. Photons are identified as an energy deposit in one or several optical modules without an associated track. During the photon identification, the neighbouring calorimeter hits are clustered and attributed to a single photon. The energy of the photon being equal to the sum of the individual hit energies. Examples of neighbouring calorimeter hits which could be gathered together are shown in Figure 6.2.3. Furthermore, no Geiger cell that is unassociated to tracks should be found within 15 cm radially of calorimeter hits in order to limit the mis-identification from α decay (next section) or scattered electrons as photons.

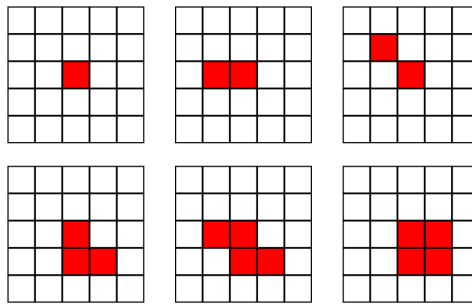


Figure 6.3: Schematic front view of the main wall. The grid represents scintillator blocks. The red squares correspond to optical modules with energy deposits without associated tracks. They could be clustered to form a photon.

Alpha identification

As it was already described in Chapter 5, due to their high ionizing power and to the high mass, the alpha particles are identified as short straight tracks. The alpha particles from radioactive decay are not expected to have tracks longer than 40 cm. The identification of the alpha particle is important to detect the Bi-Po cascades in which a delayed alpha decay with a half-life of $164 \mu\text{s}$ occurs. The BiPo cascade is then identified as the emission of a prompt electron followed by a delayed alpha coming from the same location as shown in Figure 6.4.

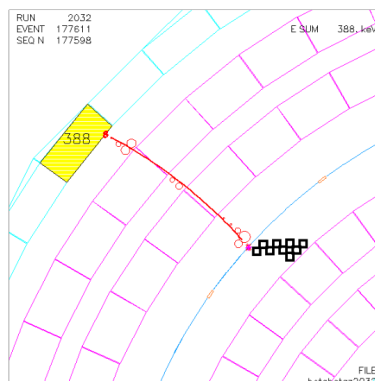


Figure 6.4: Top view of the NEMO-3 detector where a BiPo candidate event has been identified. The red track corresponds to the prompt electron while the black squares represent the delayed Geiger hits of the alpha track.

6.2.4 Time of flight information

The $\beta\beta$ signal is characterized by the emission of two electrons coming from the source foil in coincidence in time. To measure a signal or a background coming from the source it is necessary to reduce as much as possible the contribution of the events from an external origin. To distinguish the origin of the events, internal or external to the source foil, the time of flight information provided by the calorimeter is used. Two different hypotheses, internal and external are introduced which quantify the probability that an event has its origin inside or outside the source foil. These two probabilities are build out of χ^2 distributions using the measured time of particle hits in the calorimeter and the hypothetical time of flight calculated from the estimated speed and the trajectory of the particle between its vertex to the calorimeter. The χ^2 calculations also take into account the uncertainties on the measured and hypothetical times. Next sections present the calculation of the internal and external hypotheses. These hypotheses are calculated between two particles. One of the particles must be an electron with a reconstructed track and vertex. The other particle can be a second electron or a photon. Depending on the type of particle the uncertainties are not computed in the same way as explained at the end of the section.

Internal probability

The internal hypothesis χ_{int} assumes that the two detected particles come from the same decay occurring at a time t_0 inside the source foil :

$$t_1^{\text{mes}} - t_1^{\text{tof}} = t_0 = t_2^{\text{mes}} - t_2^{\text{tof}} \quad (6.1)$$

where t_1^{mes} and t_2^{mes} are the measured time of particle hits 1 and 2 in the calorimeter, and t_1^{tof} and t_2^{tof} are the hypothetical time of arrival of the particle 1 and 2. By taking into account the uncertainties on each of these parameters, the internal pull is defined as :

$$\chi_{\text{int}} = \frac{(t_1^{\text{mes}} - t_1^{\text{tof}}) - (t_2^{\text{mes}} - t_2^{\text{tof}})}{\sqrt{\sigma_{t_1^{\text{mes}}}^2 + \sigma_{t_1^{\text{tof}}}^2 + \sigma_{t_2^{\text{mes}}}^2 + \sigma_{t_2^{\text{tof}}}^2}} \quad (6.2)$$

Then, the internal probability P_{int} is defined from χ_{int} as :

$$P_{\text{int}} = 1 - \frac{2}{\sqrt{\pi}} \int_0^{\chi_{\text{int}}} e^{-x^2} dx \quad (6.3)$$

with x defined as :

$$x = \frac{1}{1 + \sqrt{2\chi_{\text{int}}^2}} \quad (6.4)$$

The internal probability for an internal and an external 2-e event is shown in Figure 6.2.4. For an internal event the distribution is expected to be constant while it is expected to be peaked for an external event.

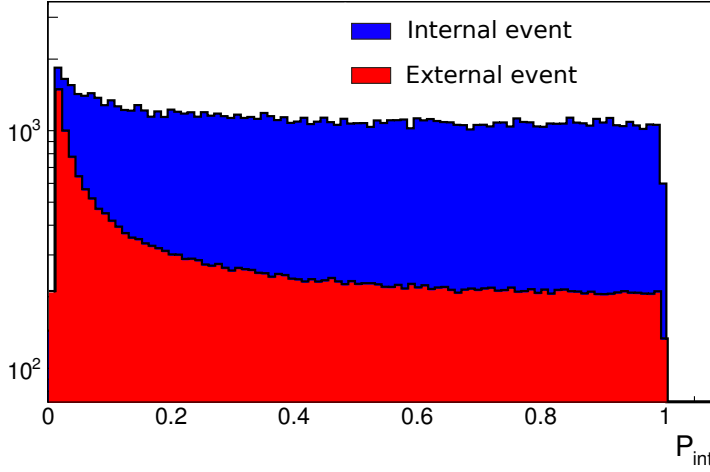


Figure 6.5: Internal probability distribution for an internal 2-e event in blue and for an external event in red.

External probability

The external hypothesis is built like the internal hypothesis except that the vertex of the decay is assumed to be outside the source foil. Figure 6.6 shows two typical external events in which a 2-e event is induced by an external photon. Two different external hypotheses are constructed depending on which particle generates the other :

$$(1 \rightarrow 2) \quad t_1^{\text{mes}} = t_0 = t_2^{\text{mes}} - t_2^{\text{tof}} - t_1^{\text{tof}} \quad (6.5)$$

$$(2 \rightarrow 1) \quad t_2^{\text{mes}} = t_0 = t_1^{\text{mes}} - t_1^{\text{tof}} - t_2^{\text{tof}} \quad (6.6)$$

By considering only the first expression (1 \rightarrow 2), the associated χ_{ext}^2 is defined as :

$$(1 \rightarrow 2) \quad \chi_{\text{ext}}^2 = \frac{(t_2^{\text{mes}} - t_2^{\text{tof}} - t_1^{\text{tof}} - t_1^{\text{mes}})^2}{\sigma_{t_1^{\text{mes}}}^2 + \sigma_{t_1^{\text{tof}}}^2 + \sigma_{t_2^{\text{mes}}}^2 + \sigma_{t_2^{\text{tof}}}^2} \quad (6.7)$$

The χ_{ext}^2 expression for (2 \rightarrow 1) is calculated by modifying the numerator. By using Equation 6.3 the external probabilities, $P_{\text{ext}}(1 \rightarrow 2)$ and $P_{\text{ext}}(2 \rightarrow 2)$ are calculated. For the external event topology the distribution is expected to be uniform except at very low values while the distribution is expected to be very peaked close to zero for the internal events.

Time of flight parameters

The measured time t^{mes} of each particle is given by the calorimeter and their uncertainties are estimated from the timing resolution, gain variations, number of photoelectrons collected and the scintillation light constant of the calorimeter block.

The computation of the hypothetical time of flight t^{tof} and its uncertainties depend on the particle. In case the particle is an electron, the time of flight t_e^{tof} is computed as :

$$t_e^{\text{tof}} = \frac{L_e}{\beta} \quad (6.8)$$

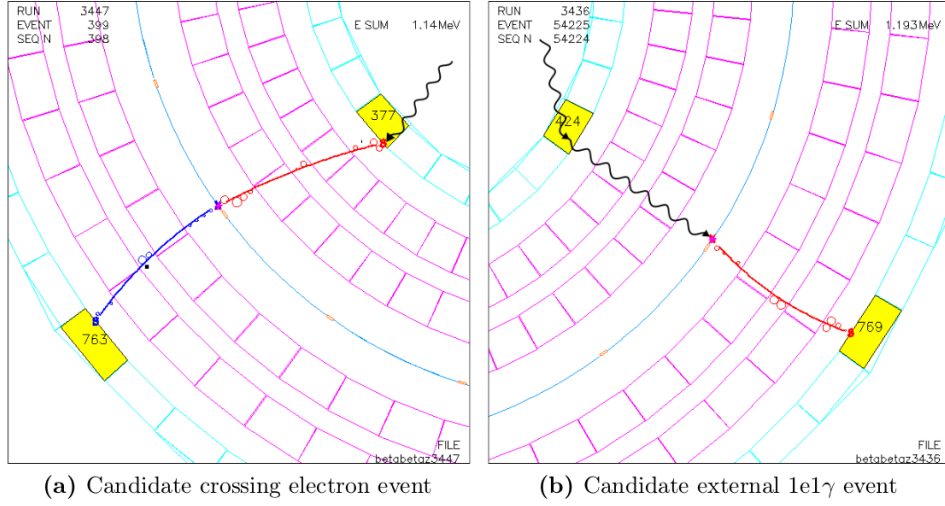


Figure 6.6: Top view of the NEMO-3 detector. (a) external candidate in which a photon creates an electron crossing the detector. (b) external candidate in which a photon interacts with the source foil to create an electron.

where L_e is the length of the reconstructed electron track and β is computed from the electron rest mass m_e and the reconstructed energy E_e :

$$\beta = \frac{\sqrt{E_e(E_e + 2m_e)}}{E_e + m_e} \quad (6.9)$$

To obtain the uncertainties on the hypothetical time $\sigma_{t_{\text{tof}}}^2$, Equation 6.8 is derived :

$$\sigma_{t_{\text{tof}}}^2 = \left(\frac{\partial t_{\text{tof}}}{\partial \beta} \right)^2 \sigma_{\beta}^2 + \left(\frac{\partial t_{\text{tof}}}{\partial L_e} \right)^2 \sigma_{L_e}^2 \quad (6.10)$$

As the uncertainty on the track length is very small compared to the uncertainties on the energy and measured time, the last term is neglected. Finally, the uncertainty on the hypothetical time is written as :

$$\sigma_{t_{\text{tof}}}^2 = \left(\frac{t_{\text{tof}}^2 m_e^2}{E_e(E_e + m_e)(E_e + 2m_e)} \right)^2 \sigma_{E_e}^2 \quad (6.11)$$

In case the particle is a photon, the hypothetical time is calculated as, with c , the speed of light set to 1 :

$$t_{\gamma}^{\text{tof}} = L_{\gamma} + t_{\text{scint}}. \quad (6.12)$$

where L_{γ} is the straight line path from the reconstructed vertex to the center of the front face of the calorimeter block associated with the photon and t_{scint} is an empirical factor which parametrizes the scintillation time. Note that the hypothetical time is more complicated to compute for photons than for electrons since the exact photon path through the detector and the impact point inside the calorimeter block are unknown. The parameter t_{scint} is also present to take into account and correct the simple approximation of a straight line for the photon path. It includes many factors such as the variation of

the interaction depth in the scintillator block and differences between the speed of light in the tracker, calorimeter block and light guides. This factor is energy dependant and has been estimated for the different scintillator blocks composing the calorimeter [162].

The uncertainty on the hypothetical time of flight is defined as :

$$\sigma_{t_{\gamma}^{\text{tof}}}^2 = \sigma_{L_{\gamma}}^2 + \sigma_{t_{\text{scint.}}}^2 \quad (6.13)$$

where $\sigma_{L_{\gamma}}^2$ is the uncertainty on the straight line calculation and $\sigma_{t_{\text{scint.}}}^2$ is the uncertainty of t_{scint} which has been empirically estimated [162].

6.2.5 Data set

For this analysis the full data set available from the NEMO-3 experiment is used. Table 6.2 provides the total run time, dead time, run numbers and corresponding dates for each phase of data taking.

Phase	Date	Runs	Run time [yr]	Dead time
P1	Feb. 2003 - Sep. 2004	1869 - 3395	1.073	1.451 [10^{-2} y]
P2	Oct. 2004 - Jan. 2011	3396 - 9186	4.239	4.471 [10^{-2} y]
P1 + P2	Feb. 2003 - Jan. 2011	1869 - 9186	5.312	5.922 [10^{-2} y]

Table 6.2: Total run time, dead time, run numbers and corresponding dates for Phase 1 and Phase 2. By combining data sets from both phases corresponds to an exposure of 2.15 kg.y for ^{116}Cd .

Phase 1 (P1) corresponds to the period before the installation of the anti-radon facility and therefore has a higher level of radon. The work presented in this thesis takes all the standard analysis runs of the NEMO-3 data set by excluding detector dead time for a total time of 5.25 y corresponding to an exposure of 2.15 kg.y for the ^{116}Cd .

6.2.6 Statistical analysis

This section describes the different statistical analysis tools used to perform the analysis. The fit method to measure the backgrounds is presented in the next sub-section. The optimisation of the cut by a multivariate method is described in the second sub-section. The two last sub-sections present the way to set a limit when no significant signal is observed and the extraction of the half-life value when signal events are observed.

Fitting MC templates to data

To fit the observed data with the different simulated distribution a binned log-likelihood fit is performed. Depending on the analysis channel, different sensitive observables can be used such as the energy of the electrons, photons or the alpha track length. To build the likelihood function we assume that for each bin i , the probability p_i to observe the number of data events d_i is governed by Poisson statistics :

$$p_i = \frac{e^{-(s_i + \sum_j b_{i,j})} (s_i + \sum_j b_{i,j})^{d_i}}{d_i !} \quad (6.14)$$

where s_i is the signal prediction given by the MC and $\sum_j b_{i,j}$ is the sum of all j backgrounds. The likelihood L is defined as the product of all the probabilities from all i bins :

$$L = \prod_i \frac{e^{-(s_i + \sum_j b_{i,j})} (s_i + \sum_j b_{i,j})^{d_i}}{d_i !} \quad (6.15)$$

This expression is valid for a single channel. To take into account the multiple channels in which an isotope can contribute, Equation 6.15 can be rewritten to include all n channels in the fit simultaneously :

$$L = \prod_{i,n} \frac{e^{-(s_{i,n} + \sum_j b_{i,j,n})} (s_{i,n} + \sum_j b_{i,j,n})^{d_{i,n}}}{d_{i,n} !} \quad (6.16)$$

It is generally more convenient to work with the logarithm of the likelihood and the new quantity to maximise is :

$$\ln(L) = \sum_{i,n} \left[-(s_{i,n} + \sum_j b_{i,j,n}) + d_{i,n} \ln \left(s_{i,n} + \sum_j b_{i,j,n} \right) + \ln(d_{i,n}!) \right] \quad (6.17)$$

The quantity is then multiplied by a factor -2 such that the distribution $-2\ln(L)$ follows a χ^2 distribution. The best estimates for signal and background contributions are extracted when $-2\ln(L)$ reaches its global minimum. The TMinuit package and the MIGRAD minimization routine in ROOT [163] are used to minimise the likelihood, calculate the errors and correlation matrices for all parameters.

Some isotopes can be measured in different channels. For these isotopes, the activity can be firstly measured in the most sensitive channel and be constrained when measuring the other channels. Gaussian additional constrains, c_k , can be added to the likelihood with the form :

$$c_k = \exp \left[-\frac{1}{2} \left(\frac{A_k - A_{k_0}}{\sigma_{A_{k_0}}} \right)^2 \right] \left(\frac{1}{2\pi\sigma_{A_{k_0}}} \right) \quad (6.18)$$

where A_{k_0} and $\sigma_{A_{k_0}}$ are the activity and the uncertainties of isotopes k as measured in a different channel or by HPGe detector where the sensitivity to that isotope is much better.

Multivariate analysis

Usually, in the previous NEMO-3 analyses, the search for $0\nu\beta\beta$ decay has been performed by comparing the S+B and B-only hypothesis using only one observable : the total electron energy distribution of the two electrons. Thanks to the ability of NEMO-3 to reconstruct other observables such as energy of photons or timing information, these additional observables can be used to better discriminate between signal and background by multivariate analysis. An optimisation of the cuts can then be performed in order to maximise the background rejection while maintaining the highest signal efficiency. The recent analyses such as the searches for $0\nu\beta\beta$ decay of ^{150}Nd or ^{116}Cd used these techniques, which can, in some cases, improve the sensitivity by 10% [127]. The same strategy is used in this work. Furthermore, this approach can be beneficial as the photon(s) emitted in the decay via the excited state are mono-energetic.

The Toolkit for Multivariate Analysis (TMVA) is used to optimise the cuts. It provides a ROOT-integrated environment for the processing, parallel evaluation and application of multivariate classification

and regression techniques. The package includes rectangular cut optimisation, multi-dimensional likelihood estimation, artificial neural networks, boosted decision trees etc. As the observables are not strongly correlated, the Rectangular Cuts method (RC), is used. It has the advantage of providing direct and explicit interpretation of the cuts on the different observables.

The RC method is the simplest and most common classifier for selecting signal events from a mixed sample of signal and background events. A set of rectangular cuts is applied on discriminating variables to maximise the background rejection at given signal efficiency. A scan over the full range of the latter quantity is performed. The cut classifier only returns a binary response : signal or background. The cut optimisation is performed with the use of multivariate parameter fitters. In RC method, 3 fitters are implemented and can be chosen by the user : Monte-Carlo sampling, Genetic Algorithm and Simulated Annealing. It has been observed that in our case, the Genetic Algorithm gives us satisfying results in a reasonable time, justifying why it has been chosen for this study.

The Genetic Algorithm consists of a technique to find approximate solutions to optimisation or search problems. As its name suggests, this algorithm is inspired by the process of natural selection by relying on bio-refered operators as mutation, cross-over and selection. The underlying concept is that a population (set of individuals with their own properties) faced with a problem evolve toward the better solutions.

From a mathematical point of view, a fitness function is defined. The aim of this fitness function is the evaluation of the goodness of each individual of the population. A value representing the goodness of each individual is returned. The different steps of the algorithms are described below :

- The first step is the **initialisation**. It consists in the creation of the population. This population is a set of individuals created by randomly setting the parameters of the abstract representation (variables). So, each individual represents a point in the solution domain of the initial problem. The size of the population is one of the parameters of the algorithm.
- The second step is the **evaluation**. Each individual is evaluated using the fitness function.
- The third step is the **selection**. Depending on the goodness of the individual to the fitness function, individuals are kept or rejected. Several selection procedures are possible. For example, only the worst performing fraction of the population is rejected. This is the simplest procedure. Another possibility is to assign each individual a survival probability which depends on the goodness of the individual.
- The fourth step is the **reproduction**. The surviving individuals are copied, mutated, crossed-over until the initial population size is reached again.
- The last step is the **termination**. The evaluation, selection and reproduction steps are repeated. It ends when the maximum number of cycles is reached or when an individual satisfies a maximum-fitness function. The solution of the problem is then the best individual.

To optimize the performances of the Genetic Algorithm, the user can tune different parameters. The more intuitive and the more important for enhancing the quality of the results is the size of the population. The calculation time should increase roughly as the population size. During the reproduction step, to generate the next generation, new individuals are created from the survival individuals. In theory they are identical but some mutations can occur. These changes are randomly generated following a Gaussian distribution function. The width of the Gaussian is one of the parameters and simulates the

mutation rate. Finally the user can choose the maximum number of cycles or the maximum-fitness function to decide when to end the algorithm. The list of all the parameters and their influence on the performance of the algorithm can be found in the User Guide of TMVA [164].

Limit setting

If no evidence of a signal over background is observed, an upper limit on the allowed signal strength can be set through a statistical procedure at a given confidence level (CL). In this analysis, the limit calculations are performed with the Collie software package which has the advantage of properly introducing the systematic errors in the computation. This section is mainly based on the Collie documentation provided in [165].

Two hypotheses are constructed and compared to the observed data : the signal and background hypothesis (S+B) and the background only (B) hypothesis. In the scenario where the low signal and background statistics are searched, the likelihood ratio turns out to be the best choice, it is defined as :

$$Q_{s,b,d} = \frac{L(S+B)}{L(B)} \quad (6.19)$$

By using the definition of the likelihood in Equation 6.15 and by binning the observable and treating each bin as an independant channel, the ratio can be written :

$$Q_{s,b,d} = \prod_i^{\text{bins}} \frac{e^{-s_i+b_i} (s_i + b_i)^{d_i} / d_i!}{e^{-b_i} b_i^{d_i} / d_i!} \quad (6.20)$$

$$Q_{s,b,d} = \prod_i^{\text{bins}} e^{-s_i} \left(\frac{s_i + b_i}{b_i} \right)^{d_i} \quad (6.21)$$

where s_i is the signal contribution in bin i , b_i the background contribution and d_i the number of observed data. As before, this expression is transformed in a negative log-likelihood ratio (NLLR) as :

$$\text{NLLR} \equiv -2 \ln (Q) = 2 \sum_i^{\text{bins}} (s_i - d_i \ln(1 + s_i/b_i)) \quad (6.22)$$

which follows a χ^2 distribution. A toy MC is used to generate the distributions of $\chi(d)$ which are then used to calculate the confidence levels. NLLR distributions are generated by replacing each value of d_i by a pseudo-data randomly generated as a Poisson variable with an expectation of $s_i + b_i$. The same procedure is followed for the B-only hypothesis. The two distributions of NLLR are shown in Figure 6.2.6. The systematic errors are taken into account by altering the expected number of events obtained from each pseudo-experiment via a Gaussian smearing.

The NLLR distributions constructed from pseudo-experiments are then compared to the observed NLLR value χ_{obs} calculated from Equation 6.22 with the observed number of data events. The confidence level for excluding the possibility of simultaneous presence of a signal and background is :

$$\text{CL}_{S+B} = P_{S+B}(\chi \geq \chi_{\text{obs}}) = \int_{\chi_{\text{obs}}}^{\infty} \frac{\partial P_{S+B}}{\partial \chi} d\chi \quad (6.23)$$

with a similar confidence level for the B-only hypothesis :

$$\text{CL}_B = P_B(\chi \geq \chi_{\text{obs}}) = \int_{\chi_{\text{obs}}}^{\infty} \frac{\partial P_B}{\partial \chi} d\chi \quad (6.24)$$

The confidence level for the signal is related to the S+B and B-only hypotheses by :

$$\text{CL}_S = \frac{\text{CL}_{S+B}}{\text{CL}_B} \quad (6.25)$$

To find the appropriate limit, the signal strength is increased until $1-\text{CL}_S \geq 0.9$ to reach a confidence level of 90 %.

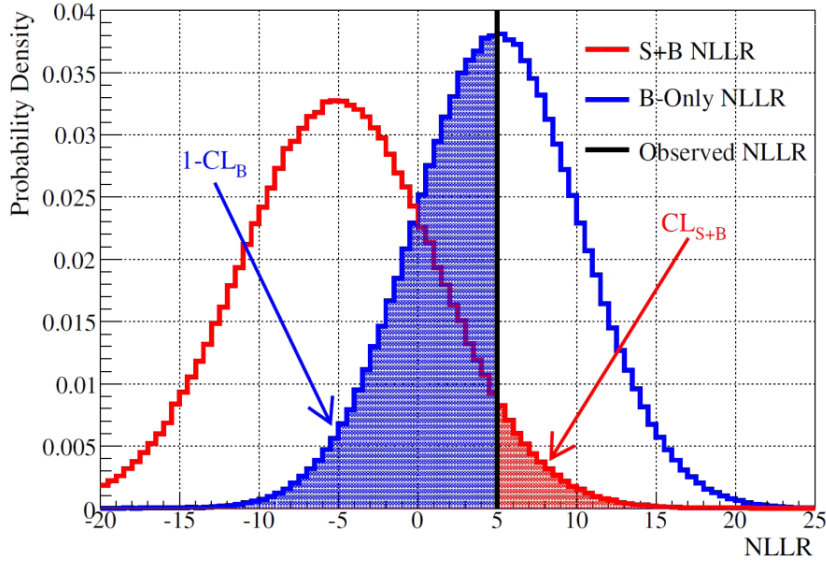


Figure 6.7: NLLR distribution for the S+B (red) and B-only (blue) hypotheses generated from many pseudo-experiments [165].

Usually, in $\beta\beta$ searches, the best observable to set a limit is the sum in energy of the two electrons. In the investigation of the excited states, the energy of the photon could also be used. Collie gives the possibility to use a 2-D distribution to set a limit. In our case, the limit is set using the 2-D distribution (ΣE_e vs E_γ), since more information is used and a higher sensitivity can be reached.

Half-life calculation

In the scenario a signal is observed, the half-life of the source isotope can be deduced. This value can then be compared to values obtained from other experiments.

Let's consider an initial sample containing N_0 unstable atoms of an isotope. The remaining number of atoms after a time t is given by the exponential law :

$$N(t) = N_0 e^{-\lambda t} \quad (6.26)$$

where λ is the decay constant of the isotope which is related to its half-life $T_{1/2}$ as :

$$\lambda = \frac{\ln 2}{T_{1/2}} \quad (6.27)$$

As the half-lives of double beta are very huge compared to the life time of the NEMO-3 experiment, a very good approximation can be done in λt using the Taylor expansion :

$$e^{-\lambda t} \approx (1 - \lambda t) \quad (6.28)$$

and the Equation 6.26 can be written :

$$N(t) \approx N_0 (1 - \lambda t) \quad (6.29)$$

$$N_0 - N(t) = N_0 \lambda t \quad (6.30)$$

where the left-hand side of Equation 6.30 represents the number of observed events N_{obs} with a detection efficiency ϵ . Replacing λ by its expression in Equation 6.27 :

$$\frac{N_{\text{obs}}}{\epsilon} = \frac{N_0 \ln 2 t}{T_{1/2}} \quad (6.31)$$

The number of initial atoms in the sample can be expressed in terms of the isotope mass m and its atomic number A :

$$N_0 = \frac{N_A m}{A} \quad (6.32)$$

where N_A is Avogadro's constant. Equation 6.31 can be re-arranged to provide the final expression for the half-life in terms of measurable quantities :

$$T_{1/2} = \frac{N_A \ln 2}{A} \times m t \times \frac{\epsilon}{N_{\text{obs}}} \quad (6.33)$$

6.3 Background to the search for the excited states

The $\beta\beta$ decays to the excited states present very specific signatures : emission of two electrons accompanied by one or more photons. Moreover, the energies of these photons are very characteristic. Very few isotopes are able to reproduce this kind of signature. In NEMO-3 the backgrounds are divided in two parts according to its origin :

- **Internal background** : the backgrounds having their origin inside the source foil.
- **External background** : the backgrounds not coming from the source foil.

6.3.1 Internal backgrounds

The internal background mainly come from the presence of radioactive isotopes of the ^{238}U and ^{232}Th decay chains inside the source foil. The more troublesome are the isotopes with large Q_β as ^{208}Tl ($Q_\beta = 4.99$ MeV) and ^{214}Bi ($Q_\beta = 3.27$ MeV). During their decay, they can induce 2-e like events through three main processes :

- the electron emitted in β decay can undergo a Möller scattering and create a second electron.

- the β emission can be accompanied by a second electron coming from the internal conversion of the daughter nucleus.
- the β decay is accompanied by a photon coming from the de-excitation of the daughter nucleus. A second electron is produced by Compton scattering of this photon.

These 2-e like events can be accompanied by one or more gamma emission(s) coming from Bremsstrahlung scattering or de-excitation of the daughter nucleus after a decay. As the electron energy is not high (< 2 MeV), the creation of one photon is more likely than the creation of two photons. That is why the $2e1\gamma$ channel is expected to be more polluted by the background than the $2e2\gamma$ channel. The different mechanisms leading to 2-e like events accompanied with two photons at the origin of internal backgrounds are summarized in Figure 6.8. The same mechanisms can also occur and be accompanied by only 1γ .

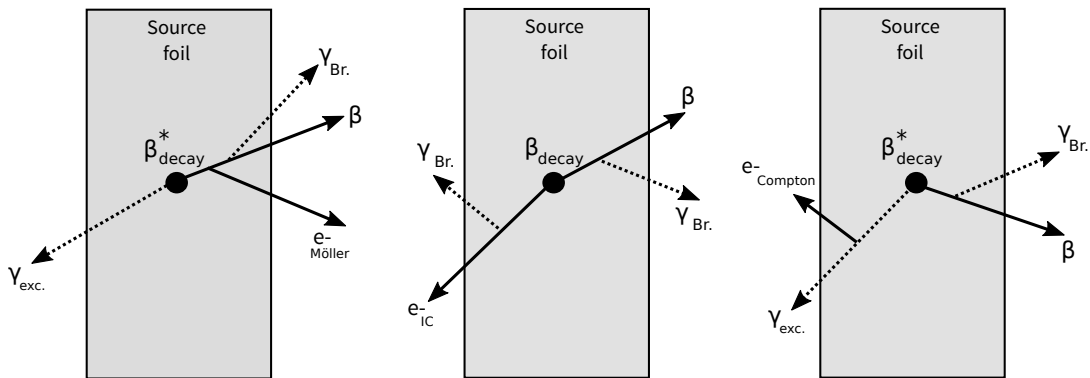


Figure 6.8: The different mechanisms leading to 2-e like events accompanied with 2 photons at the origin of internal backgrounds. Left : a β -decay via excited state is followed by a Moller scattering and Bremsstrahlung. Middle : β -decay with an internal conversion and 2 Bremsstrahlung effects. Right : a β -decay via excited state is followed by a Compton scattering and Bremsstrahlung effect.

The radioactive isotopes of the ^{238}U and ^{232}Th decay chains can be already present inside the initial source powder and not be entirely removed by the purification process. They can also be introduced later during the source foil production, handling and installation. This explains why a great care was taken in the production and purification of the enriched materials, as well as during the source foil production and mounting.

Another background to take into account when searching for the excited state is the $2\nu\beta\beta$ decay to the ground state. Each or both electrons of the $2\nu\beta\beta$ decay can undergo a Bremsstrahlung scattering and mimic $2e1\gamma$ or $2e2\gamma$ events. The $2\nu\beta\beta$ decay also constitutes an irreducible background for the search of $0\nu\beta\beta$ decay. In the region where a signal of $0\nu\beta\beta$ is expected some events of $2\nu\beta\beta$ decay can be present. This contribution strongly depends of the $2\nu\beta\beta$ half-life and the energy resolution of the detector.

6.3.2 External backgrounds

The presence of radioactive elements as radon and thoron inside the detector constitutes one of the main important external background components. These gases are released by the rock walls of the laboratory and are highly diffusive. They can enter inside the detector by tiny gaps between sectors or through gas pipe joints. The decays of these progeny produce photons and electrons. If such a decay occurs close to the source foil it is indistinguishable from a $2e$ events.

The second important contribution of the external background is the interaction of photons with the source foil. These photons come from different origins. Part of them is produced by neutron interactions in the shielding of the detector. They also come from radon in the air surrounding the detector. Another source of photon is the rock walls of the laboratory. The last contribution is the radioactive isotopes present in the detector. For example, despite a drastic selection, some traces of ^{40}K , ^{214}Bi and ^{208}Tl have been found in the glass of the PMTs. The three main mechanisms able to reproduce the $2e$ topology from an external photon are :

- the γ hitting the source foil create a pair (e^+e^-). Due to a bad reconstruction of the track curvature of the e^+ , it is identified as an e^- .
- the γ hitting the source foil undergo a double Compton scattering.
- the γ hitting the source foil undergo a Compton scattering. A second electron is created in a Möller scattering of the emitted electron.

As in internal backgrounds, these mechanisms can be accompanied by one or more photons. Figure 6.9 summarizes the different processes. The ^{210}Bi decay is also a possible source of background.

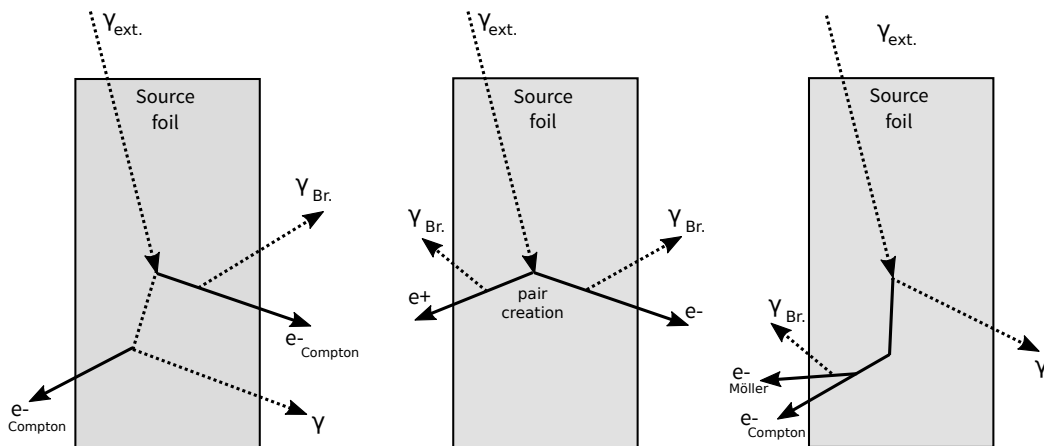


Figure 6.9: Mechanisms leading to $2e$ like events accompanied with 2 photons coming from an external γ . Left : the external γ undergoes a double Compton scattering accompanied by Bremsstrahlung effects. Middle : pair creation from the external γ with Bremsstrahlung effects. The positron is identified as an electron due to a bad reconstruction. Right : Compton scattering of the external γ followed by a Möller diffusion of the electron and a Bremsstrahlung.

One additional external background contribution should be added. It is called OCE (one crossing electron) and corresponds to an electron produced externally and crossing the entire detector.

6.3.3 Background model

The background model used in this analysis have been developed for the analysis of $\beta\beta$ decay of ^{116}Cd to the ground state [141]. The strategy is to benefit from the NEMO-3 ability to reconstruct the topology of the events. The backgrounds can be measured through different channels. The considered channels and the measured contaminations are summarized in Table 6.3. The following is dedicated to the presentation of these different channels. In a first step, the cadmium foil is divided into three different regions according to the activity.

Contaminations	Channels
Externals	OCE and $(\gamma, e)_{\text{Ext}}$
$^{214}\text{Bi}, ^{222}\text{Rn}$	1e1 α
^{208}Tl	1e2 γ and 1e3 γ
$^{40}\text{K}, ^{234\text{m}}\text{Pa}, ^{210}\text{Bi}$	1e
$^{208}\text{Tl}, ^{214}\text{Bi}$	1e1 γ

Table 6.3: Contaminations under consideration and channels in which they can be measured.

Different activity regions in the ^{116}Cd sector

In the 1e channel the vertex distributions shown in Figure 6.10 highlights a non uniformity in the activity of the foil such that three activity regions have been defined :

- an high activity region, where the number of events per bin is greater than 200,
- a medium activity region, where the number of events per bin is between 100 and 200,
- a low activity region, where the number of event per bin is lower than 100.

The high activity region observed for Sector < 18.08 corresponds to the calibration tube. This area is not taken into account in the analysis since no ^{116}Cd foil is present here. The other high activity regions match with the links between the different strips which compose the foil as described in Section 3.2.2 and shown in Figure 3.7. The excess of events observed in the high activity region probably comes from a contamination of single β -emitters. This suggestion is supported by non-observation of any strong excess in 1e1 γ channel as shown in Figure 6.10. The small excess corresponds to the emission of Bremsstrahlung by the single β -emitter. Studies realized by the collaboration highlighted an excess of $^{234\text{m}}\text{Pa}$ with respect to ^{40}K and ^{210}Bi and validated the hypothesis that the single β -emitter is the origin of the high activity region.

The high activity regions are excluded from the analysis with simple rectangular cuts based on the number of events by bin. A total of 12 spots are defined as high activity regions which correspond to around 11% of the ^{116}Cd foil. The location of the removed area are presented in Table 6.4.

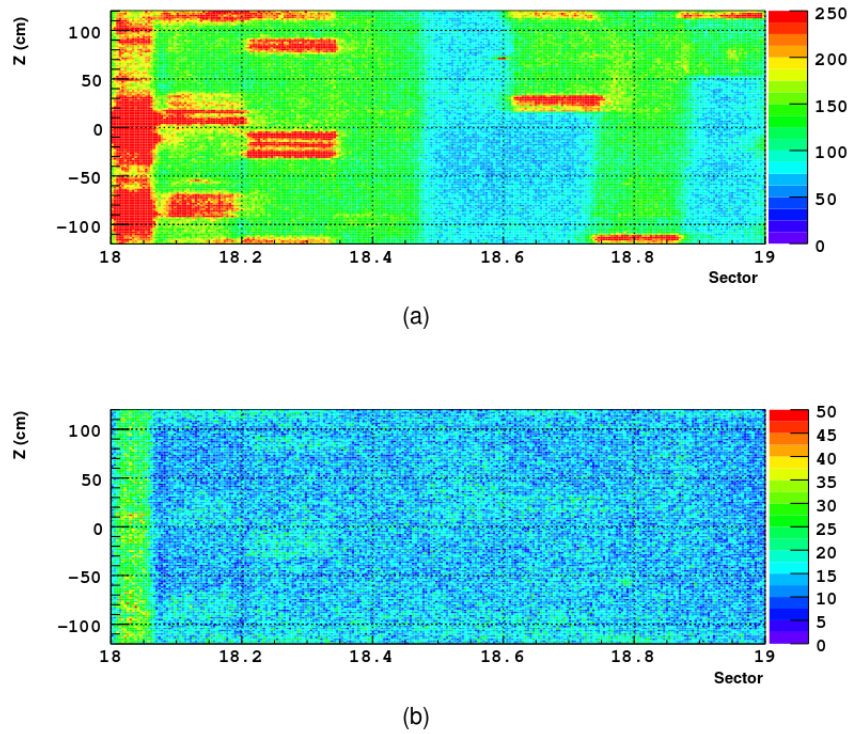


Figure 6.10: (a) ^{116}Cd sector in 1e channel. Blue region corresponds to the low activity region, the green region to medium activity. The high activity regions appear in red, these regions are excluded from the analysis. (b) ^{116}Cd sector in 1e1 γ channel [141].

	Z	Sector
1	[110.00 ; 120.00]	[18.08 - 18.32]
2	[114.00 ; 120.00]	[18.61 - 18.75]
3	[112.00 ; 120.00]	[18.86 - 19.00]
4	[76.00 ; 92.00]	[18.21 - 18.35]
5	[70.00 ; 73.00]	[18.59 - 18.61]
6	[0.00 ; 35.00]	[18.08 - 18.23]
7	[16.00 ; 34.00]	[18.61 - 18.75]
8	[-32.00 ; -3.00]	[18.20 - 18.35]
9	[-58.00 ; -52.00]	[18.12 - 18.16]
10	[-94.00 ; -64.00]	[18.08 - 18.20]
11	[-120.00 ; -112.00]	[18.14 - 18.35]
12	[-120.00 ; -110.00]	[18.74 - 18.88]

Table 6.4: Location of the high activity region on the ^{116}Cd foil in [Sector;Z] units. 12 regions are identified and excluded from the analysis which correspond to about 11 % of the foil.

External background measurement

As explained in Section 6.3.2, the gamma flux coming from the detector or its shielding can create 2-e like events. These events possess a characteristic time sequence which can be reconstructed knowing the hit times into the calorimeter. A variable representing the probability of an event coming from outside can be built. A cut on this variable allows an efficient rejection of the external backgrounds. But, due to the finite calorimeter timing resolution and to the very large number of external backgrounds events, some will pass the cut and will be selected as 2e events. It explains why the total external background rate have to be estimated.

The model developed to estimate the external background is an effective model. Its aim is to provide an accurate description of the total external gamma flux in the detector region near the ^{116}Cd foil. It contains a total of 12 free parameters considering the contaminations coming from the PMTs, scintillator, iron shielding (Fe shield), internal copper tower (Cu tower), PMT μ -metal, radon and thoron in the air. To measure the external backgrounds two channels are used : the one crossing electron channel (OCE) and the external electron- γ ($(\gamma,e)_{\text{Ext}}$) channel.

The OCE-channel contains the events having a single electron travelling across the detector. The signature of these events is two tracks with opposite curvature with a length greater than 30 cm. These two tracks are associated with isolated scintillator hits. The timing of the calorimeter hits must be consistent with the external TOF hypothesis and have $P_{\text{ext}} > 0.04$ and $P_{\text{int}} < 0.01$. The energy of each electron has to be greater than 300 keV.

The $(\gamma,e)_{\text{Ext}}$ channel corresponds to the event in which a high energy γ ray interacts in the calorimeter followed by a Compton scattering in the source foil to produce an electron. These events are identified by a single electron with an energy greater than 300 keV accompanied by a γ ray with an energy of at least 150 keV. The track length of the electron has to be greater than 50 cm. The timing of the particles must be consistent with the external TOF hypothesis ($P_{\text{ext}} > 0.04$ and $P_{\text{int}} < 0.01$).

The total energy distribution is used in both channels to discriminate the different contributions and to perform the likelihood fit. The results obtained are gathered in Table 6.5. Figure 6.11 shows the distribution of the total energy of $(\gamma,e)_{\text{Ext}}$ channel with the ratio Data/MC and the residual computed as $(\text{Data} - \text{MC}) / \sqrt{\text{MC}}$.

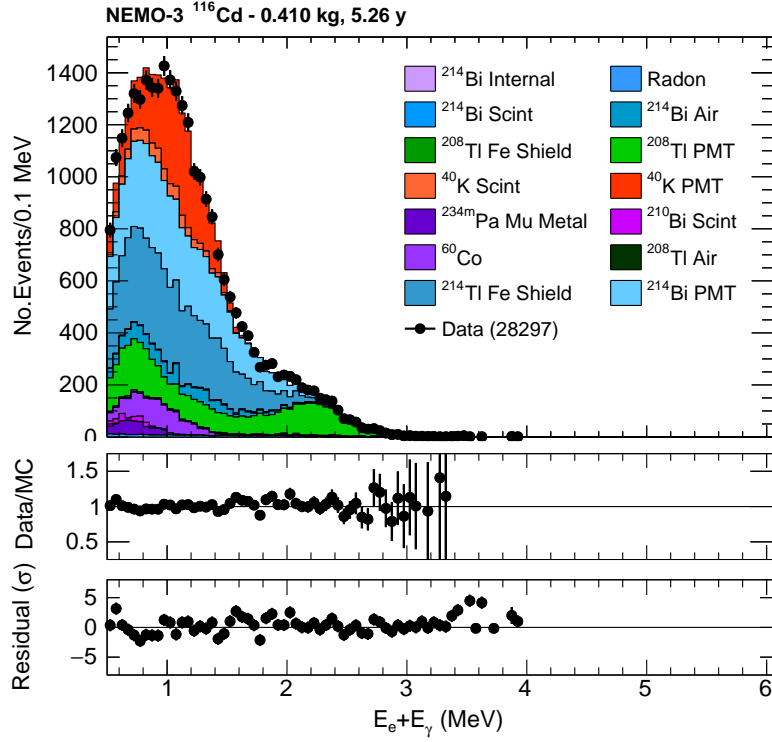


Figure 6.11: Distribution of the total energy of the $(\gamma, e)_{\text{Ext}}$ channel in linear scale [141]. The residual is calculated as $\sigma = (\text{Data} - \text{MC}) / \sqrt{\text{MC}}$.

		Activity (Bq)
^{40}K	PMT	1300 ± 45
	Scintillator	19 ± 1
^{214}Bi	PMT	269 ± 47
	Air LSM (P1)	600 ± 20
	Scintillator	0.25 ± 0.03
^{208}Tl	Fe Shield	10303 ± 2023
	PMT	45.4 ± 1.4
	Air LSM (P1)	14 ± 3
^{210}Bi	Fe Shield	55 ± 50
^{210}Bi	Scintillator	35 ± 4
^{60}Co	Tower + μ -metal	62 ± 13
$^{234\text{m}}\text{Pa}$	μ -metal	2655 ± 1180

Table 6.5: External background activities measured in ^{116}Cd sector.

Internal ^{214}Bi (^{222}Rn) measurement

As explained in Chap. 5, the ^{214}Bi contamination is measured using the $1e1\alpha$ channel. During the first year of running, the level of ^{222}Rn was measured to be relatively high. To reduce the level an anti-radon facility has been installed. The data collected before the installation are referred to Phase 1 and as Phase 2 if the data have been registered after.

The $1e1\alpha$ events are identified by a prompt electron with an energy greater than 300 keV followed by a delayed α . The α track length must be smaller than 40 cm and possesses at least two hits in the tracker. To verify the purity of this selection, the delayed time of the α is used. The time difference between the electron and the α matches with the half-life of ^{214}Po of $164 \mu\text{s}$ as shown in Figure 6.12.

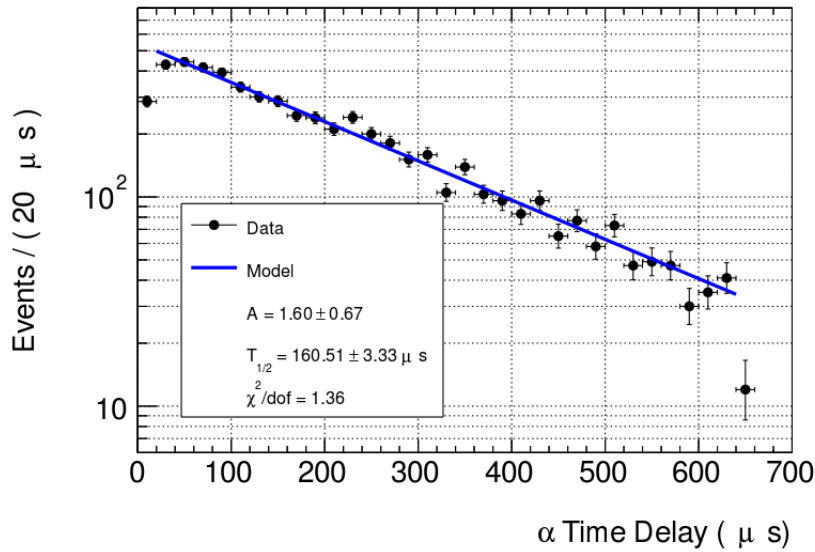
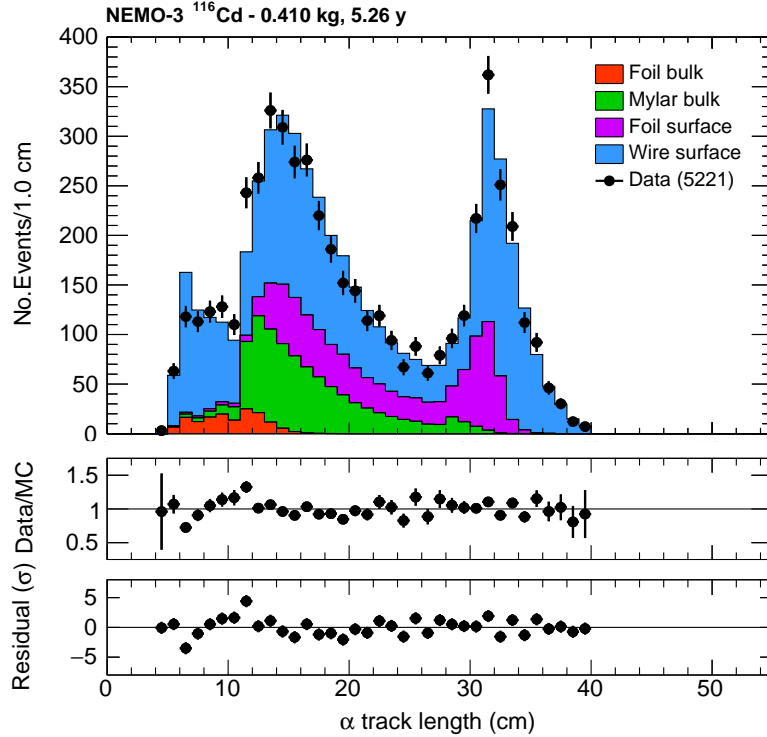


Figure 6.12: Average time delay between the electron and the α candidate Geiger hits in $1e1\alpha$ channel. The blue line is an exponential fit which matches to the ^{214}Bi half-life [141].

The α track length is used to distinguish the different ^{214}Bi contributions and to perform a likelihood fit. A total of 10 parameters is used corresponding to the different locations and phases. To take into account the reduction of the radon level after the installation of the anti-radon system, the ^{214}Bi on the surface of the wires and foil are fitted separately (Phase 1 and Phase 2). The internal and mylar ^{214}Bi contributions are fit over both phases as their activities are not expected to vary during the data taking. The results of the likelihood fit are summarized in Table 6.6. Figure 6.13 shows the distribution of α track length in $1e1\alpha$ channel.


 Figure 6.13: Distribution of the delayed α track length in the $1e1\alpha$ channel [141].

		^{214}Bi Activity (mBq)
P1	Wire surf.	667 ± 27
	Foil surf.	15 ± 1
P2	Wire surf.	91 ± 5
	Foil surf.	1.3 ± 0.3
Mylar (mBq/kg)		2.8 ± 0.2
Internal (mBq/kg)		0.4 ± 0.1

 Table 6.6: ^{214}Bi activity measured in the ^{116}Cd sector

Internal ^{208}Tl (^{220}Rn) measurement

The β -decay of ^{208}Tl is almost always accompanied by a cascade of photons from the excited states of ^{208}Pb as shown in Figure 6.14. To measure the ^{208}Tl activity, one of the most sensitive channels is provided by the $1e2\gamma$ channel.

To select $1e2\gamma$ events coming from the source foil, an event must have a single electron with energy greater than 300 keV accompanied by two γ rays with an energy of at least 200 keV each. The electron track length has to be greater than 50 cm. The timing of each γ has to be in agreement with criteria $P_{\text{int}} > 0.04$ and $P_{\text{ext}} < 0.01$.

The best discriminant variable to distinguish between the ^{208}Tl contribution from the isotopes which contribute to the $1e2\gamma$ channel is given by the sum of the electron and photon energies. Above $E_{\text{Tot}} > 3$ MeV, a pure sample of ^{208}Tl is obtained, this distribution is used to perform the likelihood fit. Due to the high sensitivity of the $1e2\gamma$ channel, the ^{208}Tl activity is the only free parameter. The other contributions as radon inside the tracker volume or from the surface of the foils are constrained to

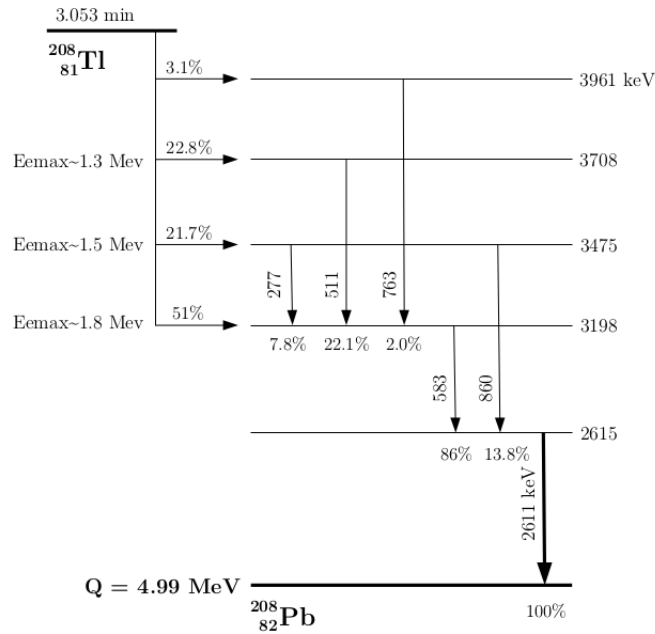


Figure 6.14: Simplified decay diagrams of ^{208}Tl .

the value measured in previous sections. The result is shown in Table 6.7. Figure 6.15 shows the distribution of the energy sum in the $1e2\gamma$ channel.

	Activity [mBq/kg]
^{208}Tl	0.14 ± 0.02

Table 6.7: ^{208}Tl activity measured in the cadmium sector.

The internal ^{208}Tl contribution can also be measured in the $1e3\gamma$ channel. Despite a worse sensitivity, this channel is useful to validate the result obtained in $1e2\gamma$ channel. The $1e3\gamma$ channel is defined as the $1e2\gamma$ channel with an additional γ ray ($E_\gamma > 200$ keV). Unfortunately due to the very low statistics (150 events passing the cuts) the sensitivity is not enough to measure the ^{208}Tl activity. But, by normalizing the MC in the $1e3\gamma$ channel to the activities measured previously, the data and MC are in good agreement which enhances the confidence in the estimation of the ^{208}Tl activity.

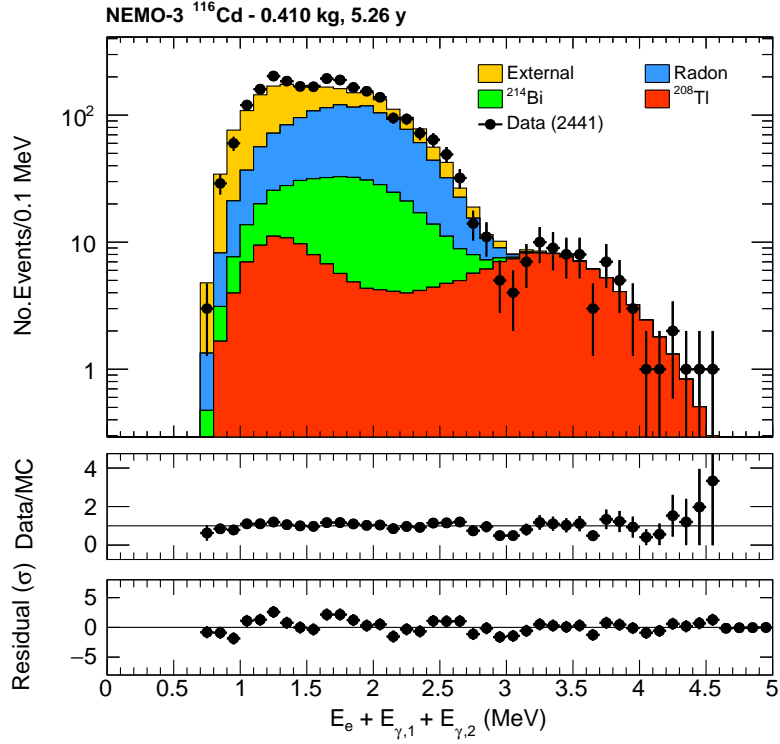


Figure 6.15: Total energy distribution ($E_e + E_{\gamma_1} + E_{\gamma_2}$) in the $1e2\gamma$ channel [141].

Other internal contributions (^{40}K , $^{234\text{m}}\text{Pa}$ and ^{210}Bi)

The activities of the single beta emitter internal contributions (^{40}K , $^{234\text{m}}\text{Pa}$ and ^{210}Bi) can be measured in the $1e$ channel. Other sources contribute to the events observed in the $1e$ channel. The first one is due to the external backgrounds. These backgrounds are constrained to the activity measured previously in the fit. Events from $\beta\beta$ decays of ^{116}Cd can also end up in the $1e$ channel if one of the electrons is not detected.

The single electron energy distribution is used to perform the fit. This distribution is shown in Figure 6.16. The results obtained are summarized in Table 6.8.

	Activity (Bq)
^{40}K	0.0152 ± 0.0001
$^{234\text{m}}\text{Pa}$	0.0037 ± 0.0001
^{210}Bi (surf. foil)	3.91 ± 0.01
^{210}Bi (surf. wire)	2.4 ± 0.1

Table 6.8: Measured activity in the $1e$ channel of the other internal components.

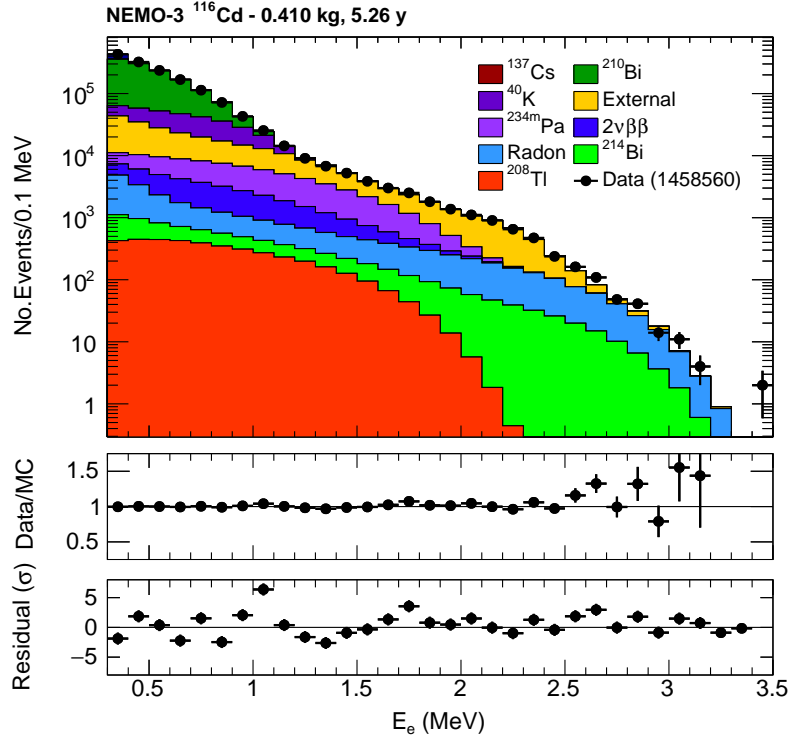


Figure 6.16: Electron energy distribution of the electron in the 1e channel. The three main components are ^{40}K , $^{234\text{m}}\text{Pa}$ and ^{210}Bi [141].

Background model validation

The background model is validated by measuring the activity of ^{208}Tl and ^{214}Bi in the 1e1 γ channel. The results are then compared to the measurement obtained in the 1e1 α channel for ^{214}Bi and the 1e2 γ and the 1e3 γ channels for ^{208}Tl .

The 1e1 γ channel contains the events with a single electron having an energy greater than 300 keV associated to a photon ($E_\gamma > 200$ keV).

The very good agreement ($< 1 \sigma$) of the results validates the background model. The comparison of the values measured in different channels are shown in Table 6.9.

Activity	1e1 γ	1e2 γ	1e1 α	$\Delta A / \sigma$
^{208}Tl [mBq/kg]	0.14 ± 0.02	0.14 ± 0.02	-	0.00
^{214}Bi [mBq/kg]	0.35 ± 0.1	-	0.36 ± 0.1	0.06
Wire surf. P1 [mBq]	696 ± 28	-	667 ± 27	0.8
Wire surf. P2 [mBq]	90 ± 5	-	91 ± 5	0.01
Foil surf. P1 [mBq]	15 ± 2	-	15 ± 1	0.04
Foil surf. P2 [mBq]	1.3 ± 0.2	-	1.3 ± 0.3	0.18

Table 6.9: Comparison of the activity measured in 1e1 α , 1e2 γ and 1e1 γ channels. The last column presents the relative difference among values with respect to their errors.

The summary of all the activities measured in all these different channels is shown in Table 6.10. A total of 26 contributions are taken into account in the background model. The contribution of the $\beta\beta$ decay of ^{116}Cd to the ground state is also added and constitutes the 27th background contribution.

			Activities
Internal Background	^{214}Bi	Wire surface (P1)	$[667 \pm 27]$ mBq
		Foil surface (P1)	$[15 \pm 1]$ mBq
		Wire surface (P2)	$[91 \pm 5]$ mBq
		Foil surface (P2)	$[1.3 \pm 0.3]$ mBq
		Mylar	$[2.8 \pm 0.2]$ mBq/kg
		Internal	$[0.36 \pm 0.1]$ mBq/kg
	^{208}Tl	Internal	$[0.14 \pm 0.02]$ mBq/kg
	^{40}K	Low	$[0.0054 \pm 0.0001]$ Bq
		Medium	$[0.0098 \pm 0.0001]$ Bq
	$^{234\text{m}}\text{Pa}$	Low	$[0.0013 \pm 0.0001]$ Bq
		Medium	$[0.0021 \pm 0.0002]$ Bq
^{210}Bi	Low	$[1.15 \pm 0.01]$ Bq	
	Medium	$[2.76 \pm 0.01]$ Bq	
	Wire Surface	$[2.4 \pm 0.1]$ Bq	
External Background	^{40}K	PMT	$[1300 \pm 45]$ Bq
		Scintillator	$[19 \pm 1]$ Bq
	^{214}Bi	PMT	$[269 \pm 47]$ Bq
		Air LSM (P1)	$[600 \pm 20]$ Bq
		Scintillator	$[0.25 \pm 0.03]$ Bq
	^{208}Tl	Fe Shield	$[10303 \pm 2023]$ Bq
		PMT	$[45.4 \pm 1.4]$ Bq
		Air LSM (P1)	$[14 \pm 3]$ Bq
		Fe Shield	$[55 \pm 50]$ Bq
	^{210}Bi	Scintillator	$[35 \pm 4]$ Bq
^{60}Co	Tower + mu metal	$[62 \pm 13]$ Bq	
$^{234\text{m}}\text{Pa}$	Mu metal	$[2655 \pm 1180]$ Bq	

Table 6.10: Measured activities of each component of the background model in ^{116}Cd [141].

6.4 Event preselection

Before optimizing the selection of each excited state and introducing more specific cuts to search for the decays via the excited state, a preselection of events is introduced to isolate the $2e1\gamma$ and $2e2\gamma$ events. This preselection consists in setting criteria to select the events coming from the ^{116}Cd sector and containing two electrons and one or two photons. The events with an alpha particle are rejected.

An electron is defined as a particle having a negative track with a vertex on the source foil and hitting a calorimeter. The energy of each electron has to be greater than 150 keV and the minimal length of their

track is 50 cm. A photon is defined as a calorimeter hit not associated to a track. To avoid calorimeter noise the energy of the photon has to be greater than 150 keV. An alpha particle is identified as delayed hits inside the tracker volume. Other criteria as the status of the PMT, or the internal probability of the electrons are added. The exhaustive list of the preselection criteria can be found below :

- the run has to be accepted
- the PMTs are good
- no alpha particle in the event
- only 2 electrons in the event
- only 2 tracks in the event
- electron hits a good PMT
- electrons hit different scintillators
- both electrons intersect the foil
- both electrons have fired one hit within 50 cm from the vertex
- both electrons hit the front face of calorimeter block
- the electrons hit isolated blocks
- the 2 electrons originated in the same sector
- the 2 electrons intersect the foil at $|z| < 120$ cm
- $P_{\text{int}} > 0.01$ and $P_{\text{ext}1 \rightarrow 0} < 0.04$ and $P_{\text{ext}1 \rightarrow 0} < 0.04$ for the electrons
- run status = 1 (GOOD RUN)
- coming from the Cd-116 sector (18)
- energy of each electron > 150 keV
- electron track length > 50 cm
- negative electron track sign
- internal probability > 0.01
- external probability < 0.01
- no electron hits petal near the foil
- $|dz_{\text{vtx}}| < 8$ cm and radial distance < 4 cm
- not a hot spot
- $N_{\gamma} > 0$ and ($E_{\gamma} > 150$ keV)

Initially the minimal energy of each electron was fixed to 300 keV. But, in case of decays via the excited state, part of the energy is carried away by the photons and the available energy for the electrons is reduced. This selection criterion has been released to 150 keV in order to increase the signal efficiency of the preselection.

The preselection is applied on all the MC of excited states and all the background components, this is the first step of the selection which is common to all the excited states. Later, other cuts will be added to optimize the background rejection depending on the excited state. The signal efficiency and the number of background events expected after the preselection is calculated for each excited state.

6.4.1 Signal efficiency

From the MC, the signal efficiency of each excited state can be computed by comparing the number of events which passes the preselection to the number of generated events. Depending on the excited state, two preselections are performed by adding a criterion on the number of photons ($N_{\gamma} = 1$ or $N_{\gamma} = 2$). The first one consists in selecting the $2e1\gamma$ events by requiring the presence of only one photon. This preselection is well adapted for the search for the excited state (2^+). The second preselection is exactly the same except that it consists in isolating the $2e2\gamma$ events, by requiring only two photons, to search for the excited state (0^+). The results of the preselection of the events in the $2e1\gamma$ and the $2e2\gamma$ channels are given below.

2e1 γ channel

This channel is dedicated to the search for the excited state (2^+). The results are given in Table 6.11.

Excited state	$N_{\text{generated}}$	$N_{\text{preselected}}$	$\epsilon_{\text{preselection}}$
(2^+) 2ν	10 000 000	13095	$(1.31 \pm 0.01) 10^{-3}$
(2^+) 0ν	5 000 000	91165	$(1.82 \pm 0.01) 10^{-2}$

Table 6.11: Signal efficiency of the preselection 2e1 γ for the excited state (2^+).

The signal efficiencies are small, respectively $\sim 0.13\%$ and $\sim 1.8\%$ for the 2ν and 0ν decay mode. The higher selection efficiency obtained in 0ν is explained by the fact that the two electrons have more available energy in this decay mode. These electrons are less affected by the criterion on their energy ($E_e > 150$ keV) than the electrons emitted in 2ν decays. Moreover, the detection efficiency of the electron is energy dependant and increases with their energy.

2e2 γ channel

This channel is dedicated to the search for the excited state (0^+). The results are given in Table 6.12.

Excited state	$N_{\text{generated}}$	$N_{\text{preselected}}$	$\epsilon_{\text{preselection}}$
(0^+) 2ν	200 000 000	11168	$(5.58 \pm 0.05) 10^{-5}$
(0^+) 0ν	4 999 900	17681	$(3.54 \pm 0.03) 10^{-3}$

Table 6.12: Signal efficiency of the preselection 2e2 γ for the excited state (0^+).

The available energy for the electrons in decays via the excited state (0^+) is even more restrained compared to the (2^+) and the selection efficiencies are very low, respectively $\sim 0.005\%$ and $\sim 0.3\%$. As before, the selection efficiency is higher in 0ν decay mode than the 2ν decay.

6.4.2 Number of expected background

After the preselection, the number of background events can be evaluated in the 2e1 γ and the 2e2 γ channels using :

$$N_{\text{bkg}} = \sum_i N_i = \sum_i \epsilon_i \times A_i \times T \quad (6.34)$$

where ϵ_i is the efficiency of the background component computed as the number of events passing the preselection divided by the number of generated events in MC. A_i is the measured activity of the component, given in Table 6.10, and T the exposure time.

2e1 γ channel

In the 2e1 γ channel, 285 ± 12 events of background are expected. They mainly come from the $\beta\beta$ decay to the ground state (118 ± 1) and external backgrounds (114 ± 11). The other contributions are the radon present in the detector and from ^{214}Bi and ^{208}Tl contained inside the source foil. The

distribution of the background in different observables are given in Figure 6.17. Note that a major part of the background has a photon with a low energy ($E_\gamma < 0.5$ MeV) mainly providing by Bremsstrahlung effect. These background events should not be troublesome since the emitted photon in excited state (2^+) is monoenergetic at 1.3 MeV.

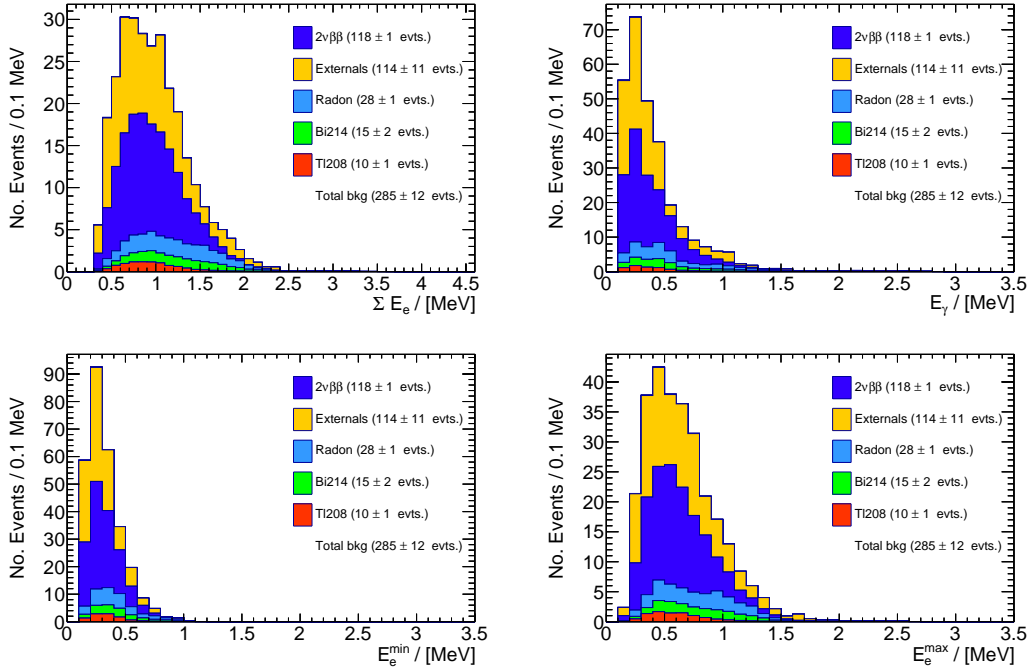


Figure 6.17: Distribution of different observables in the $2e1\gamma$ channel after the preselection. Top left : energy sum of the two electron. Top right : energy of the photon. Bottom left : energy of the less energetic electron. Bottom right : energy of the electron with the higher energy.

$2e2\gamma$ channel

Very few isotopes are able to mimic a signal with two electrons and two photons. The background contribution to this channel is expected to be even lower than in the $2e1\gamma$ channel. After the preselection, only 26 ± 2 background events of background are expected mainly coming from external contribution (16 ± 2). Smaller contributions of radon, ^{214}Bi and ^{208}Tl are also expected. Figure 6.19 and Figure 6.18 respectively show the different observables for the electrons and photons in the $2e2\gamma$ channel.

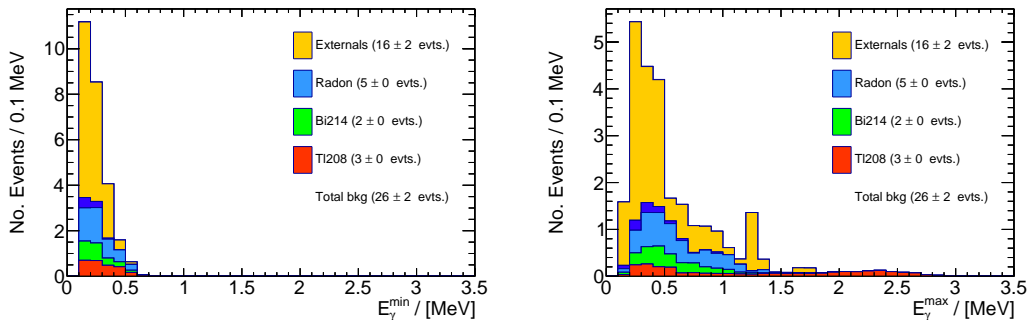


Figure 6.18: Distribution of different observables in the $2e2\gamma$ channel after the preselection. Left : energy of the less energetic photon. Right : energy of the most energetic photon.

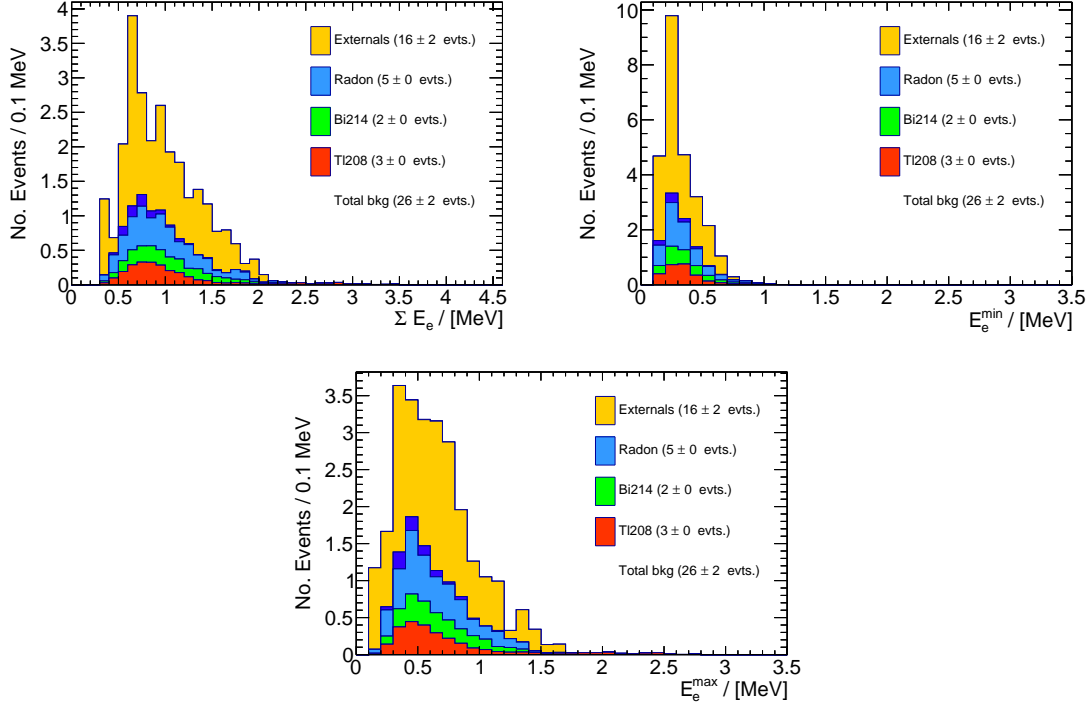


Figure 6.19: Distribution of different observables in the $2e2\gamma$ channel after the preselection. Top left : energy sum of the two electron. Top right : energy of the less energetic electron. Bottom : energy of the electron with the higher energy.

6.5 Cut optimisation using a multivariate approach

Usually, the most important and sensitive observable to detect the $\beta\beta$ decay is the energy sum of the two electrons. For the investigation of the excited state, other observables such as the energy of the photon are used to distinguish the signal from the background by employing a multivariate analysis technique. The list of the discriminating variables is introduced in Section 6.5.1. The selection and the implementation of the rectangular cut method are respectively described in Section 6.5.2 and Section 6.5.3.

6.5.1 Discriminating variables

In $2e1\gamma$ channel, a total of 14 discriminating variables are used, they are listed and defined below :

- the energy of the photon : E_γ
- the minimal and maximal energy of the electrons : E_e^{\min} , E_e^{\max}
- the energy sum of the electron and their subtraction : $\Sigma E_e = E_e^{\min} + E_e^{\max}$, $\Delta E_e = E_e^{\min} - E_e^{\max}$
- the total energy : $E_{\text{tot}} = \Sigma E_e + E_\gamma$
- the 2 internal probabilities of the photons : $P_{\text{int}}^{\gamma-e1}$ and $P_{\text{int}}^{\gamma-e2}$
- the 4 external probabilities : $P_{\text{ext}}^{\gamma \rightarrow e1}$, $P_{\text{ext}}^{\gamma \rightarrow e2}$, $P_{\text{ext}}^{e1 \rightarrow \gamma}$ and $P_{\text{ext}}^{e2 \rightarrow \gamma}$
- the 2 angles of the photon with the electrons : $\cos(\theta_{\gamma-e1})$ and $\cos(\theta_{\gamma-e2})$

These variables are the input of the multivariate method. Their distributions can be found in Figure 6.20 for the (2^+) 2ν . The signal is represented in blue, the sum of all the background is in red. In $2e2\gamma$ channel, the same set of variables is used except the energy of the photon is split into 2 variables : minimal and maximal energy (E_{γ}^{\min} , E_{γ}^{\max}).

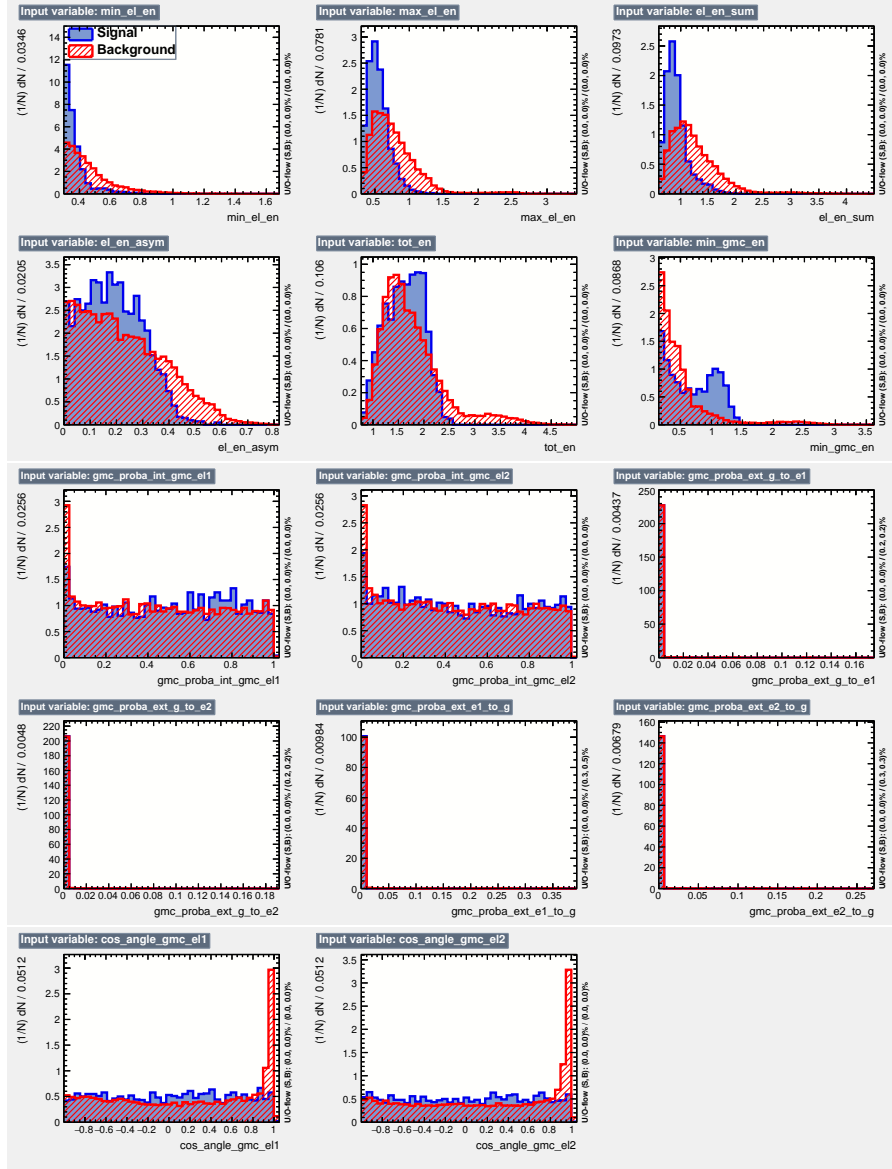


Figure 6.20: Discriminating variables used in the $2e1\gamma$ channel for the 2ν (2^+) case. The signal is represented in blue and the sum of the background in red.

6.5.2 Choice of the rectangular method

As explained in Section 6.2.6, several multivariate methods require general purpose parameter fitting to optimise the value of an estimator. Since the various fitting problems call for dedicated solutions, TMVA has a fitter base class, used by the multivariate methods. The user can choose whatever fitter is deemed suitable and can configure it through the option string of the multivariate method. For the rectangular cut method, three fitters have been implemented : Monte Carlo sampling, Simulated Annealing (SA) and a Genetic Algorithm (GA).

The Monte-Carlo sampling is the simplest and the most straightforward fitting method. It consists in randomly sampling the fit parameters and choosing the set of parameters which optimises the estimator. This method is the less efficient fitting method but it is quite fast.

The simulated annealing algorithm is inspired by the process of annealing which occurs in condensed matter physics. When a metal is heated and slowly cooled, its atoms move to a state of lowest energy. For infinitesimal annealing activity the system will always converge to its global minimum energy [166]. The principle can be translated into an algorithm able to solve a minimisation problem with several discrete or continuous, local or global minima. This fitting method is quite efficient to solve problems with several local minima.

The genetic algorithm is described in Section 6.2.6. It is a technique to find approximate solutions to optimisation or search problems. These three fitting methods have been tested. In our case, the genetic algorithm provides the best performance, at a given efficiency, it always rejects more background than the two other methods as shown in Figure 6.21.

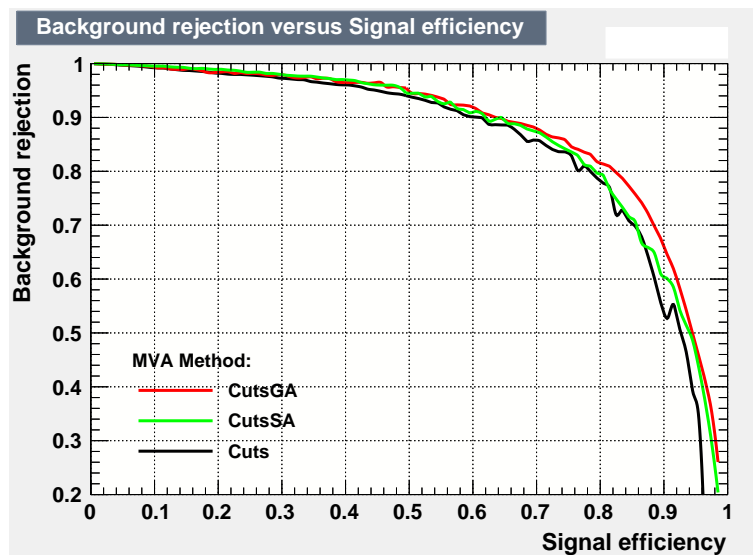


Figure 6.21: Comparison of the different rectangular cut methods. At a given efficiency, the rectangular cut using the genetic algorithm (CutGA in red) always rejects more background than the other methods (Monte Carlo sampling : Cuts in black and Simulated Annealing : CutSA in green).

6.5.3 Reduction of the number of variables

Using too many variables can be difficult to handle for some methods and in particular for the rectangular cut method. To save time, reduce the phase space and avoid convergence to local minima, the number of variables is reduced using correlations. The correlation matrix between the variables in $2e1\gamma$ is shown in Figure 6.22.

It makes sense that the minimum and the maximum energy of the electron are correlated with the energy sum. It is not necessary to have 3 variables. E_e^{\min} and E_e^{\max} are then not used. Also for this reason, the total energy and the asymmetry are not kept. It can be noticed that all the internal and external probabilities are coupled. Only the maximal internal probability and the minimal external probabilities are conserved.

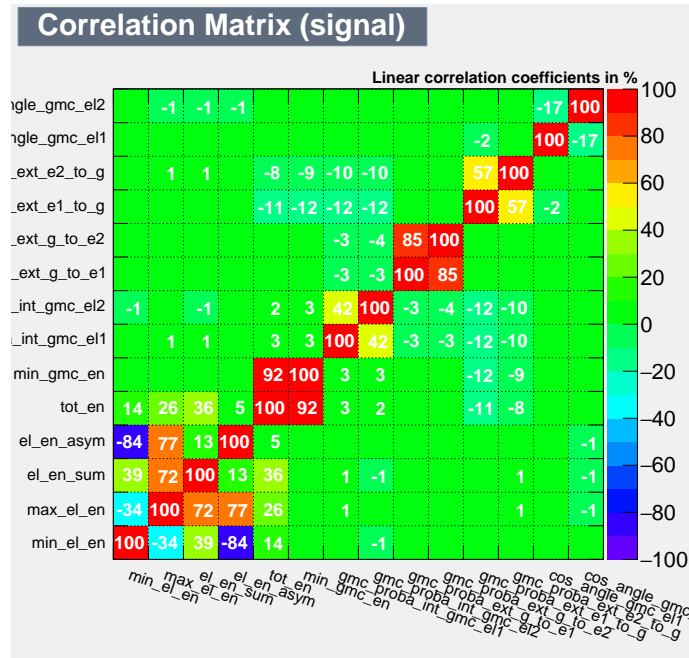


Figure 6.22: Correlation matrix of the signal in 2ν (2^+) case.

Finally, 7 discriminating variables are used in $2e1\gamma$: E_γ , ΣE_e , $P_{\text{int}}^{\gamma-e1}$ max, $P_{\text{ext}}^{\gamma\rightarrow e}$ min, $P_{\text{ext}}^{e\rightarrow\gamma}$ min, $\cos\theta_{\gamma-e1}$ and $\cos\theta_{\gamma-e2}$. In $2e2\gamma$, 8 discriminating variables are used including the same 7 variables defined before and adding the minimal energy of the photon.

The reduction of the number of variables does not affect significantly the performance of the multivariate analysis as shown in Figure 6.23. For a same signal efficiency, the background rejection is equivalent. This result can be explained by the fact that the variables that were removed were strongly correlated with the kept ones. The addition of correlated variables does not add discriminating information.

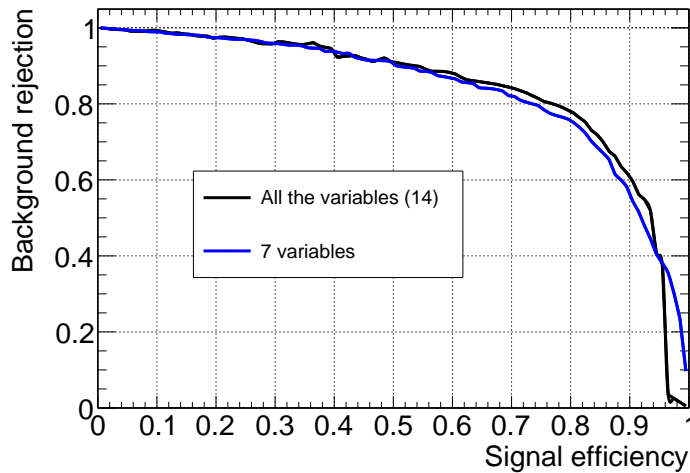


Figure 6.23: Comparison of the background rejection using 14 or 7 variables in the 2ν (2^+) case.

6.6 Sources of systematic uncertainties

The sources of systematic uncertainties which may impact the measurement of the half-lives of the decays to the excited states are presented in this section. Their sources and their values are the same as those evaluated in the decay to the fundamental state [141], they are presented in Section 6.6.1. The systematic uncertainty on the selection efficiency has been re-evaluated for the search of the excited states. Section 6.6.2 presents its evaluation in more detail.

6.6.1 Sources of systematic uncertainties

This part reports the source of systematic uncertainties considered for the search for the $\beta\beta$ decay to the fundamental state. They are evaluated one by one and propagated to the ^{116}Cd $2\nu\beta\beta$ half-life through the likelihood fit to the 2-e channel. Some sources of systematic uncertainties depend on the detector and are common to every isotope such as the energy calibration or the measurement of the ^{208}Tl background. The other sources of systematic uncertainties are dependent of the isotope under consideration. These sources of uncertainties are due to the isotope mass, the geometry, the composition of the source foil, and specific background measured in NEMO-3.

Energy calibration

The systematic uncertainty on the energy calibration is an uncertainty dependent on the detector. As explained in Section 3.2.6, the energy is obtained thanks to a linear fit combining the energy calibration coming from the two ^{207}Bi energy peaks and the end point of the ^{90}Y spectrum :

$$E = \alpha \times \text{ADC} + \beta \quad (6.35)$$

where α is the calibration constant of the calorimeter and β is the extrapolated offset at $\text{ADC} = 0$. Based on the variation on the error on the PMT gains recorded in the NEMO-3 database, α is known at approximately 1 % and $\beta = 33 \pm 3$ keV. Since the uncertainty on the term β is negligible with respect to the uncertainty on the term α , the effect of this systematic uncertainty has been estimated by shifting by ± 1 % the energy scale to simulate the variation of the PMT gain. The effect on the half-lives is +1.20 % and -1.25 %.

Isotope mass

As discussed in Section 3.2.2, 440 g of cadmium enriched at 93.2 ± 0.2 % in ^{116}Cd have been introduced in NEMO-3. By taking into account the uncertainty on the enrichment yield, the total mass of ^{116}Cd is rounded to 410 ± 1 g. The uncertainty on the isotope mass is also rounded to 0.25 % and directly propagated onto the half-lives.

Source foil geometry composition

As described in Section 3.2.2, the cadmium sector is an assembly of thin metallic foils from different cadmium productions glued together. As seen in Figure 6.10, this assembly is at the origin of the different activity regions. The data and MC are then divided into two activity regions, low and medium, according to the vertex position on the foil. The $2\nu\beta\beta$ decay rate is then measured by fitting the two samples. The systematic uncertainty due to MC modelling, geometry and composition of the Cd foils is estimated by comparing the activity measured in these two different regions. The impact on the half-lives is +2.20 % and -3.24 %.

Internal ^{208}Tl background

The uncertainty on the ^{208}Tl activity measurement is estimated by comparing the activities of ^{232}U source with HPGe measurement. The uncertainty is found to be $\pm 14\%$ [167], its effect on the half-lives is $\pm 0.04\%$.

 ^{214}Bi

This uncertainty has been measured by comparing the ^{214}Bi activity measured in the $1e1\alpha$ and in $1e1\gamma$ channels. The agreement is at 2% . The impact on the half-lives is 0.01% .

Rn background

This uncertainty has been estimated by comparing the activities measured in the $1e1\alpha$ and in the $1e1\gamma$ channels to the events coming from tracker and foil surface. The value found is 2.6% . Its impact on the half-lives is 0.02% .

 ^{40}K , $^{234\text{m}}\text{Pa}$, ^{210}Bi backgrounds

This systematic uncertainty is estimated by the relative difference between the activities measured in the $1e$ channel and the one computed in the $2e$ channel. All the contributions are fixed except ^{40}K , $^{234\text{m}}\text{Pa}$ and ^{210}Bi . The total systematic uncertainty on the normalisation of the internal background in the $2e$ channel is then obtained by summing in quadrature the uncertainties on the normalization of each component and is found to be $\pm 35\%$ [141]. This uncertainty is important but its effect on the half-life translate into $\pm 1.07\%$.

External backgrounds

As explained in Section 6.3.3, the model used to estimate the external background is an effective model which provides an accurate description of the total external gamma flux in the detector region near the ^{116}Cd foil. To evaluate the systematic uncertainty on the external background contribution, the results measured in this model are compared to the values obtained of the NEMO-3 background paper [140]. The total systematic uncertainty on the normalisation of external background is obtained by summing in quadrature the uncertainties of each component. The systematic uncertainty is found to be $\pm 15\%$, and its effect on the half-life to be $\pm 0.45\%$.

Summary of common sources of uncertainty

All the systematic uncertainties common to the search for the four excited states are summarized in Table 6.13. The systematic uncertainty on the selection efficiency of the signal is not shown. This uncertainty depends on the excited state under consideration and will be evaluated in the following section.

Origin	Systematic uncertainty [%]	Effect on $T_{1/2}$ [%]
Geometry, composition	+2.20 -3.24	+2.20 -3.24
Energy calibration	± 1.00	+1.20 -1.25
Isotope Mass	± 0.25	± 0.25
^{214}Bi	± 2.0	± 0.01
^{208}Tl	± 14.0	± 0.05
Rn	± 2.6	± 0.02
^{40}K , $^{234\text{m}}\text{Pa}$, ^{210}Bi	± 35	± 1.07
Externals	± 15	± 0.45

Table 6.13: Sources and estimations of the different systematic uncertainties. The last column presents the effect on the ^{116}Cd half-life in %.

6.6.2 Systematic uncertainty on the selection efficiency

The last systematic uncertainty to be evaluated concerns the selection efficiency of the signal. This systematic uncertainty has been estimated by comparing the activities of two ^{232}U sources measured in HPGe detector with the measurements realized with the NEMO-3 detector in the $2e1\gamma$ and the $2e2\gamma$ channels. The measurement of the ^{232}U calibration sources is performed by using the same selections introduced for the excited state analysis. As four specific selections have been implemented, this uncertainty is computed for each selection corresponding to each excited state. The activities measured in HPGe detector are reported in Table 6.14.

Source	HPGe (2012) [Bq]
1	$7.79 \pm 0.04 \pm 0.21$
3	$32.76 \pm 0.17 \pm 0.89$

Table 6.14: Activities of the ^{232}U calibration sources measured in HPGe detector.

HPGe activity measurements are then compared to the activity measured with NEMO-3, calculated using the following expression :

$$A = \frac{N_{\text{fit}}}{\epsilon \times T} \quad (6.36)$$

where A is the activity, N_{fit} is the number of fit events, ϵ is the selection efficiency and T the exposure time. The activities measured for each selection of the source 1 and 3 are respectively given in Table 6.15 and Table 6.16. Figure 6.24 presents the comparison between the activities measured by NEMO-3 and those obtained in HPGe detector. Distribution of photon and electron energy in the $2e1\gamma$ channel for the selection (2^+) 2ν are given in Figure 6.25.

A reduced χ^2 method is used to estimate the systematic uncertainty on the signal efficiency of the $2e1\gamma$ and the $2e2\gamma$ channel denoted σ^{sys} . This method assumes that the spread of the NEMO-3 results around the HPGe central values is due to a Gaussian systematic. The optimal value for σ^{sys} is obtained by numerically solving the following equation :

$$\chi^2 = \sum_{i=1}^2 \frac{(A_i^{\text{NEMO}} - A_i^{\text{HPGe}})^2}{(\sigma_i^{\text{stat}})^2 + (\sigma^{\text{sys}} \times A_i^{\text{HPGe}})^2} = 2 \quad (6.37)$$

Selection	Activity [Bq]	Relative difference w.r.t HPGe [%]
$(0^+) 0\nu$	7.50 ± 1.08	3.7 ± 0.5
$(0^+) 2\nu$	9.07 ± 2.64	16.5 ± 4.8
$(2^+) 0\nu$	6.65 ± 0.71	14.6 ± 1.6
$(2^+) 2\nu$	7.41 ± 0.69	4.9 ± 0.5

Table 6.15: Activity measurement of ^{232}U source number 1 realized in each selection corresponding to each excited state. The last column is the relative difference between the activity measured in these selection and the activity obtained with HPGe detector computed as $(A_{\text{selection}} - A_{\text{HPGe}}) / A_{\text{HPGe}}$.

Selection	Activity [Bq]	Relative difference w.r.t HPGe [%]
$(0^+) 0\nu$	34.02 ± 3.01	3.8 ± 0.3
$(0^+) 2\nu$	45.74 ± 9.2	39.6 ± 8.0
$(2^+) 0\nu$	31.65 ± 1.98	3.4 ± 0.2
$(2^+) 2\nu$	32.54 ± 1.79	0.68 ± 0.04

Table 6.16: Activity measurement of ^{232}U source number 3 realized in each selection corresponding to each excited state. The last column is the relative difference between the activity measured in these selection and the activity obtained with HPGe detector computed as $(A_{\text{selection}} - A_{\text{HPGe}}) / A_{\text{HPGe}}$.

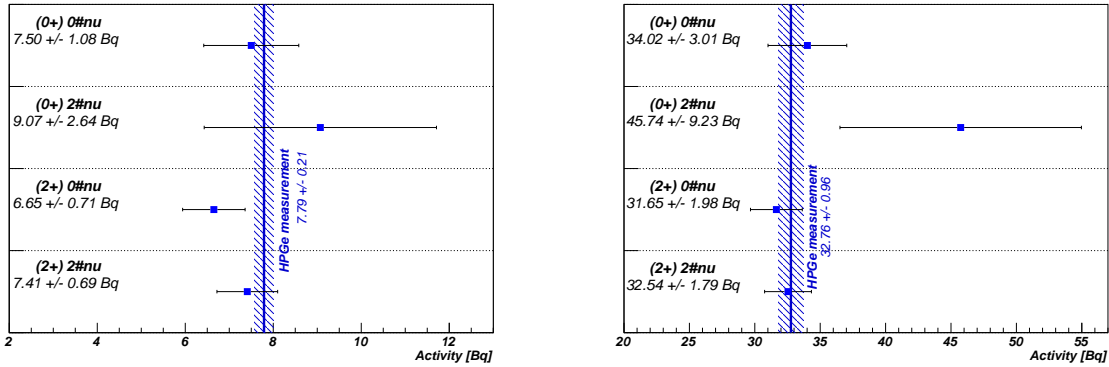


Figure 6.24: Comparison between the HPGe measurements and the activities measured with NEMO-3 for the 4 excited states. Left : source 1. Right : source 3.

where A_i^{NEMO} and σ_i^{stat} are the NEMO-3 activity measurement and their statistical uncertainties, A_i^{HPGe} is the central values of HPGe measurements. Note that, in case the activity and its statistical error measured by NEMO-3 contains the activity and the uncertainty measured by HPGe detector, for both sources, this equation does not have any real solution. It is the case for the $(2^+) 2\nu$ and $(0^+) 0\nu$ selections. For the selection $(2^+) 2\nu$, the higher relative difference is taken as the systematic uncertainty and rounded to 5%. For the $(0^+) 0\nu$ selection, the relative difference with the HPGe measurement is respectively 3.7% and 3.8% for source 1 and 3 which is smaller than 5% systematic uncertainty of HPGe measurement. In this case the systematic uncertainty is set to 4%. Table 6.17 summarizes the systematic uncertainty on the selection efficiency for each selection. These uncertainties are directly translated onto the decay half-life.

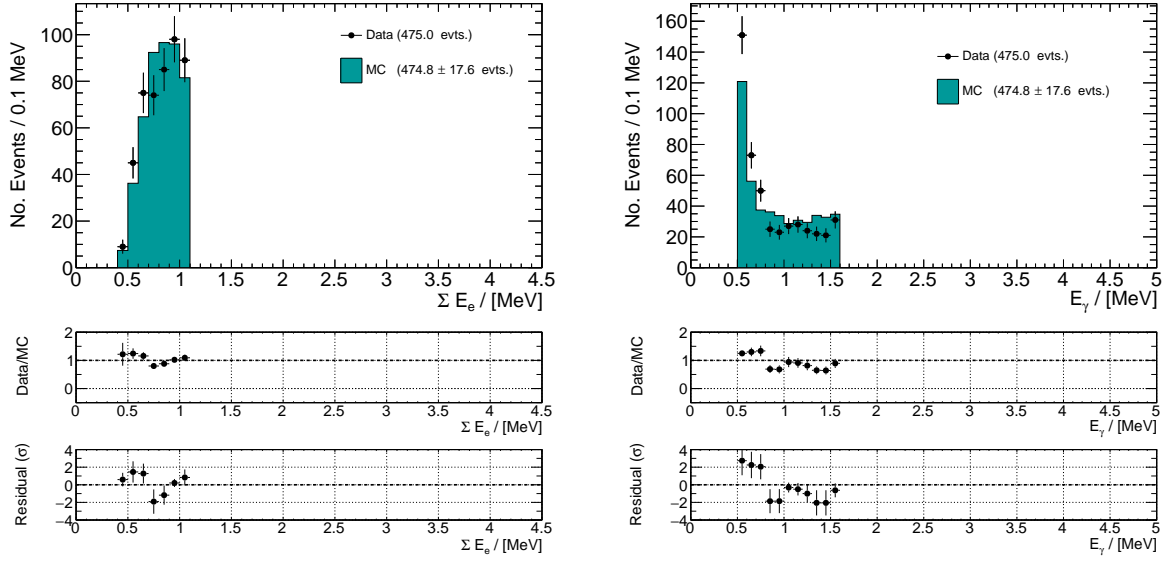


Figure 6.25: Energy distribution in the $2e1\gamma$ channel for the source 3. Left : energy sum of the electrons. Right : photon energy.

		Systematic
(2^+)	2ν	5 %
	0ν	6 %
(0^+)	2ν	10 %
	0ν	4 %

Table 6.17: Systematic uncertainty on the selection efficiency for each selection.

6.7 $\beta\beta$ decay of ^{116}Cd via the excited state (2^+) of ^{116}Sn

After the preselection of the events in the $2e1\gamma$ channel, both decay modes of the excited state (2^+), 2ν and 0ν , are treated individually. First, for each decay mode, the rectangular cut method of TMVA is applied on the remaining events of the preselection. TMVA optimises the set of cuts to reject the maximum of background, for different values of the signal efficiency. Then, for these different signal efficiencies, the sensitivity is computed from the equation :

$$T_{1/2} > \frac{\ln(2)N_A}{W} \times \epsilon_{\text{tot}} \times \frac{M \times T}{N_{\text{exc.}}^{\text{exp.}}} \quad (6.38)$$

where $N_{\text{exc.}}^{\text{exp.}}$ is the expected number of signal events excluded computed by Collie with the 2-D observable ΣE_e versus E_γ , and ϵ_{tot} is the total selection efficiency computed as the product of the preselection efficiency and the signal efficiency remaining after the cut optimisation (called TMVA efficiency). The value of efficiency which maximised the sensitivity is then kept as well as the values of the associated cuts. These cuts are then applied to the real data which are compared to the level of expected background. The results obtained for the 2ν and 0ν decay modes are respectively presented in Section 6.7.1 and 6.7.2.

6.7.1 2ν decay mode

As shown in Figure 6.26 the sensitivity on the half-life is maximised for a TMVA efficiency of 55%. The black points correspond to the expected central value of the sensitivity and the blue points the $\pm 1\sigma$ variations. The associated cuts to obtain this signal efficiency are shown in Table 6.18 and are applied on the signal, backgrounds and data. The cuts reject 93% of the backgrounds. Figures 6.27 and shows the final distribution of the energy sum of the electron, the photon energy and the minimal and maximal energy of the electrons after the application of the TMVA cuts.

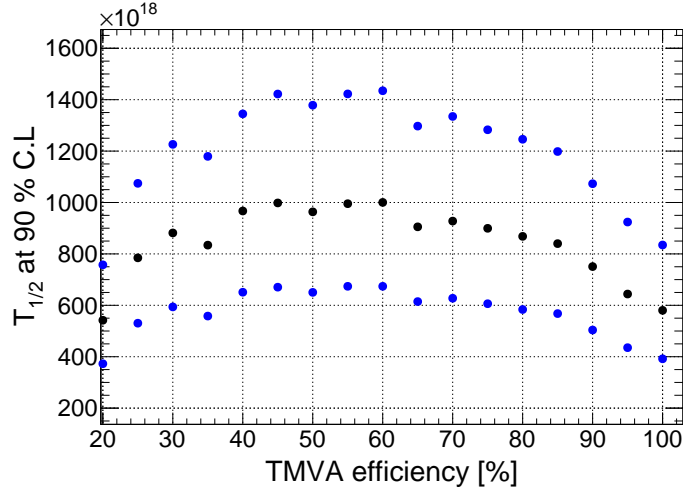


Figure 6.26: Expected sensitivity computed for different values of signal efficiency for the excited state (2^+) 2ν . The black points correspond to the central value.

Variables	Selected value
ΣE_e	[0.30 - 1.13] MeV
E_γ	[0.57 - 1.81] MeV
$P_{\text{int}}^{\text{max}}(e-\gamma)$	[0.012 - 1.000]
$P_{\text{ext}}^{\text{min}}(e \rightarrow \gamma)$	[0.000 - 0.094]
$P_{\text{ext}}^{\text{min}}(\gamma \rightarrow e)$	[0.000 - 0.816]
$\cos(\theta_{e1-\gamma})$	[-0.97 - 0.93]
$\cos(\theta_{e2-\gamma})$	[-1.00 - 0.91]

Table 6.18: Cuts applied on the preselection to optimise the sensitivity on the half-life of the excited state (2^+) 2ν . This selection keeps 55% of the signal and rejects 93% of the background.

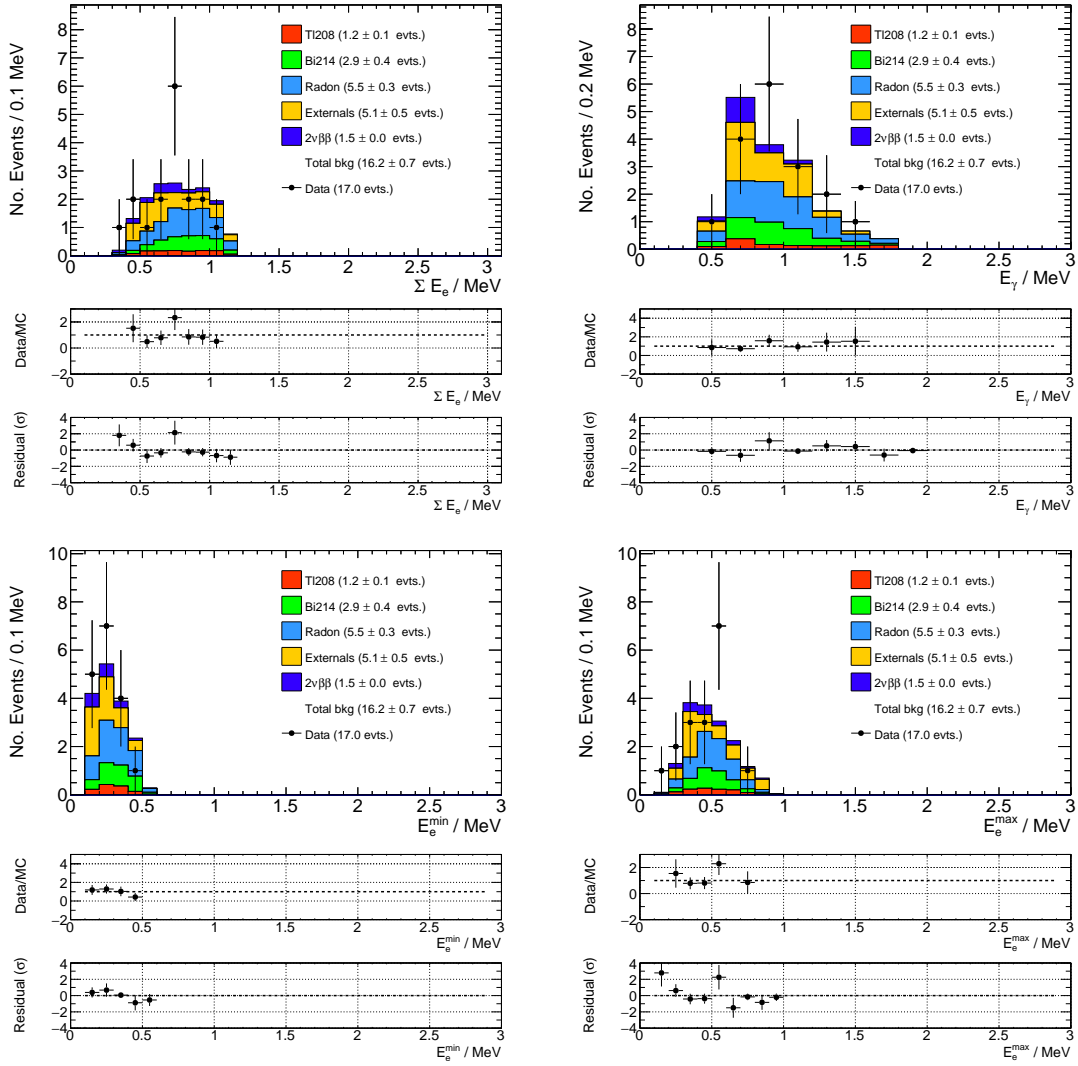


Figure 6.27: Top left : Total electron energy in the $2e1\gamma$ channel. Top right : Photon energy in the $2e1\gamma$ channel. Bottom left : Minimal electron energy in the $2e1\gamma$ channel. Bottom right : Maximal electron energy in the $2e1\gamma$ channel. The minimal energy of each electron is 150 keV

From these distributions, one sees a small excess of events in the region $[0.5 - 0.6]$ MeV for the maximal energy of the electron. This small excess corresponds to the small excess of events observed in the sum of energy of the two electrons (between $[0.7 - 0.8]$ MeV). From the 7 events observed in the bin $0.5 - 0.6$ MeV for the maximal energy of the electron, 4 of them have a very small minimal electron energy lower than 250 keV. As no peaked signal is expected in this bin, this small excess could come from an unknown component of background at low energy which is not taken into account in our background model valid for electron energies greater than 300 keV.

In order to eliminate this possible source of background, the cut on the minimal energy of each electron is increased to 250 keV and the analysis chain is performed again. The sensitivity versus the signal efficiency is shown in Figure 6.28. A plateau is observed for signal efficiency between 40% and 70% and its middle value, at 55%, is chosen. At this signal efficiency 96% of the background is rejected. The cuts corresponding to the 55% signal selection are given in Table 6.19.

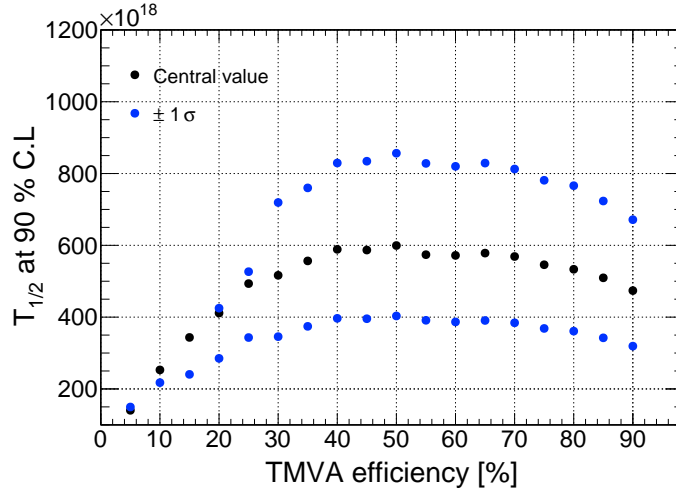


Figure 6.28: Expected sensitivity computed for different values of signal efficiency for the excited state (2^+) 2ν . The black points correspond to the central value.

By looking at Figure 6.20, the cuts can be easily understood. The more relevant cut concerns the photon energy. This cut selects the monoenergetic photon emitted in the decay to the excited state by rejecting the low energy photon coming from Bremsstrahlung and high energy photon from ^{208}Tl isotope. The cut on the sum energy of the two electrons rejects the events with a high energy. Cuts on the internal and external probabilities are introduced to reject a part of the external backgrounds. Finally, to reduce the background coming from $\beta\beta$ decay to the ground state, a slight cut on the angle between the electron and the photon is introduced since the photon is expected to be emitted in the same direction as the electron. By taking into account these cuts and the efficiency of the preselection, the total signal efficiency defined as the product of the TMVA efficiency and of the preselection efficiency, ϵ_{tot} , is $(3.85 \pm 0.06) \times 10^{-4}$.

Variables	Selected value
ΣE_e	[0.49 - 1.12]
E_γ	[0.45 - 1.41]
$P_{\text{int}}^{\text{max}}(e-\gamma)$	[0.024 - 1.000]
$P_{\text{ext}}^{\text{min}}(e \rightarrow \gamma)$	[0.00 - 0.44]
$P_{\text{ext}}^{\text{min}}(\gamma \rightarrow e)$	[0.00 - 0.29]
$\cos(\theta_{e1-\gamma})$	[-1.00 - 0.88]
$\cos(\theta_{e2-\gamma})$	[-0.96 - 0.91]

Table 6.19: Cuts applied on the preselection to optimise the sensitivity on the half-life of the excited state (2^+) 2ν . This selection keeps 55% of the signal and rejects 96% of the background.

As no evidence of signal is observed, an exclusion limit on the signal normalisation is set at 90% C.L. Table 6.20 summarises the expected sensitivity and the observed limit on the signal normalisation as well as the half-life computed from Equation 6.38 and where $N_{\text{exc}}^{\text{exp}}$ is replaced by $N_{\text{exc}}^{\text{obs}}$ for the observed data. The different distributions are shown in Figures 6.29. The observed limit is found to be :

$$T_{1/2}^{2\nu}(^{116}\text{Cd}, 0 \rightarrow 2^+) > 4.2 \times 10^{20} \text{ y at 90\% C.L.}$$

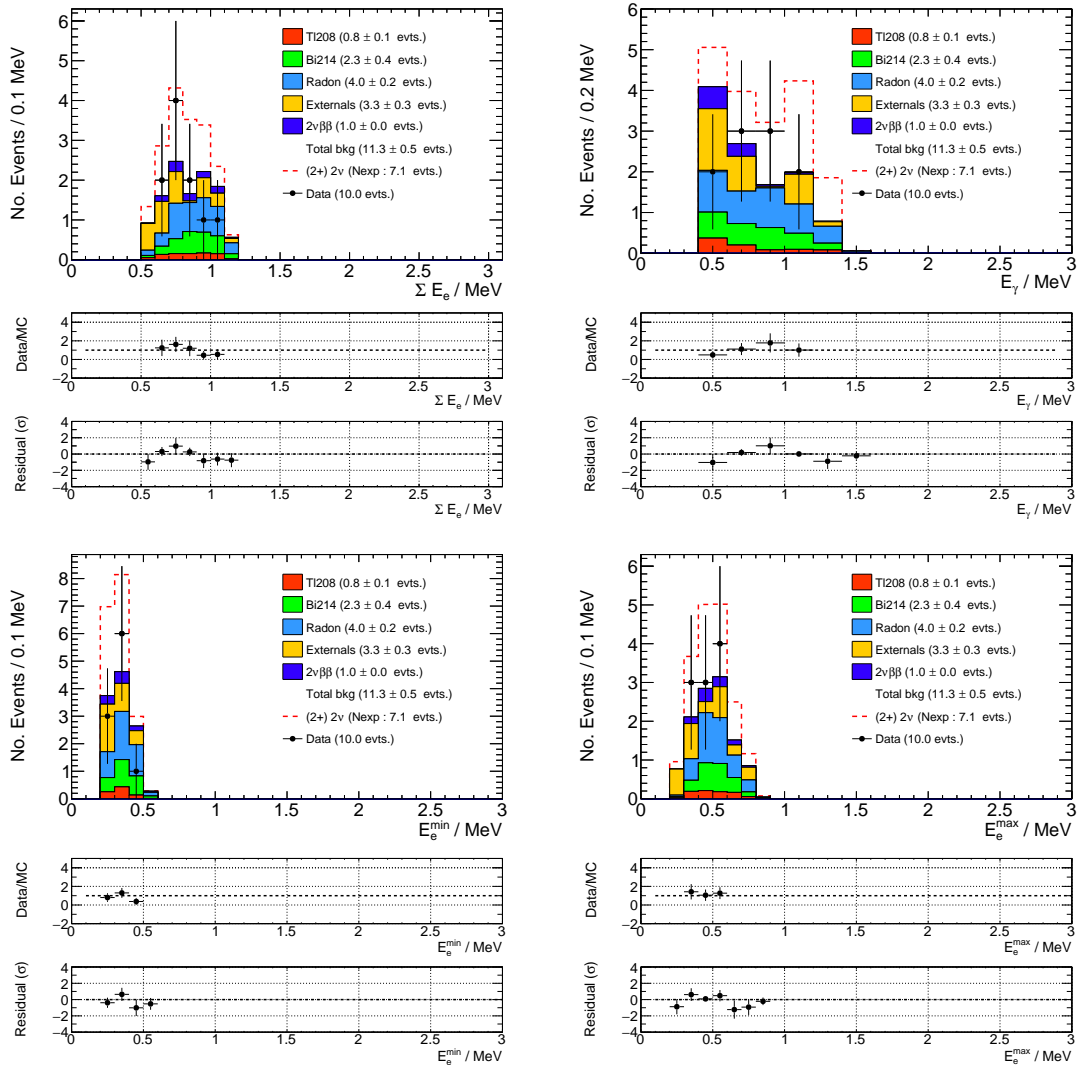


Figure 6.29: Distributions of the backgrounds, the signal normalised to observed limit and the data in the $2e1\gamma$ channel for the excited state $(2^+) 2\nu$. Top left : Total electron energy distribution. Top right : Photon energy. Bottom left : Minimal electron energy. Bottom right : Maximal electron energy. The minimal energy of each electron is 150 keV.

	Expected			Obs.
	-1σ	0	$+1\sigma$	
$N_{exc.}$	3.6	5.2	7.6	7.1
$T_{1/2} \times 10^{20} \text{y}$	8.28	5.74	3.91	4.2

Table 6.20: Expected and observed exclusion limit on the signal normalisation and on the half-life at 90% C.L for the excited state $(2^+) 2\nu$.

6.7.2 0ν decay mode

As it has been done for the 2ν decay mode, the 0ν analysis is performed in several steps. First, rectangular cuts method is applied on the preselection to find the best cuts at each efficiency. Then the sensitivity is computed for each signal efficiency. The value of the efficiency which maximise the sensitivity is kept as well as their associated cuts. The final distributions comparing the data to the expected background are shown in Figure 6.30.

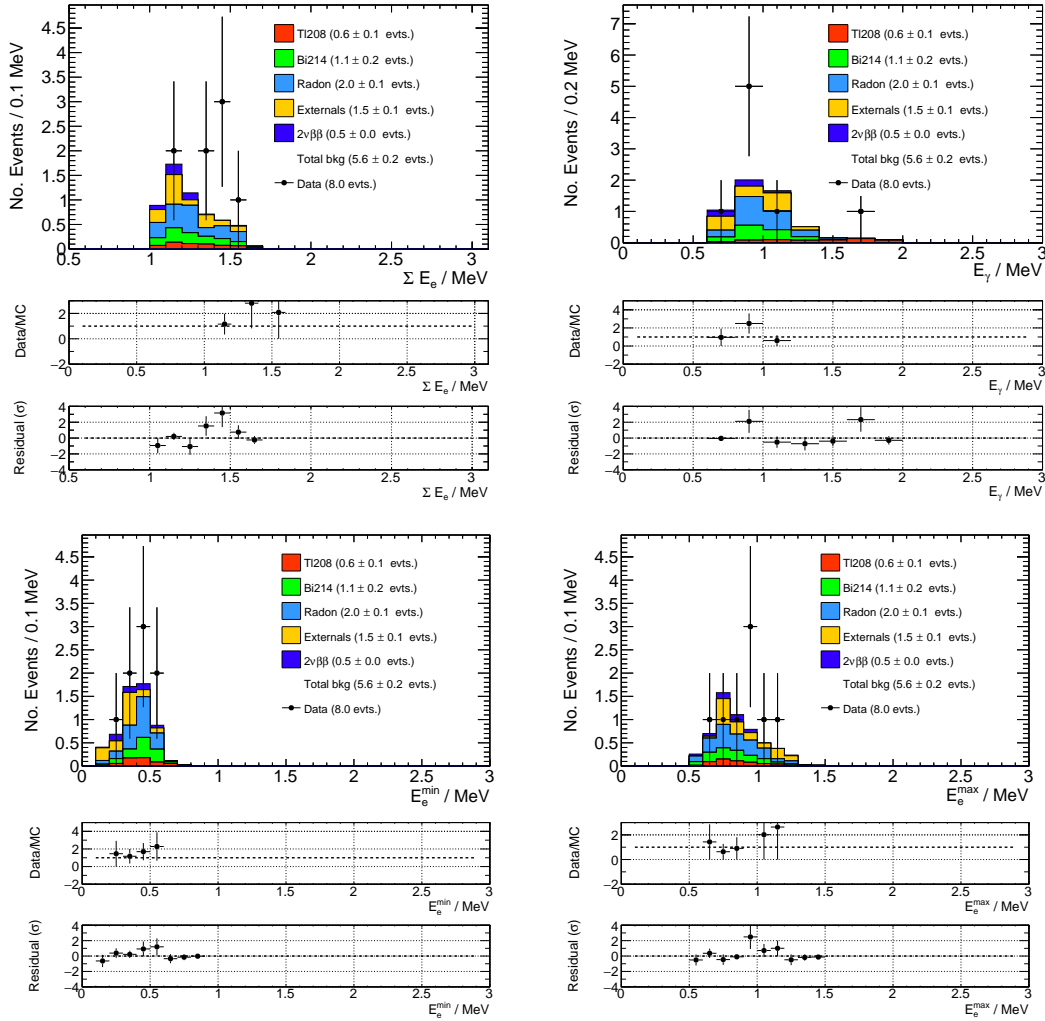


Figure 6.30: Top left : Total electron energy in the $2e1\gamma$ channel. Top right : Photon energy in the $2e1\gamma$ channel. Bottom left : Minimal electron energy in the $2e1\gamma$ channel. Bottom right : Maximal electron energy in the $2e1\gamma$ channel. The minimal energy of each electron is 150 keV.

By looking at the photon energy spectrum, 2 events are in excess. The first event has a high energy photon greater than 1.5 MeV and could be interpreted as events coming from the ^{208}Tl contribution. The second one has internal and external probability which are characteristic of an external event. In order to remove these two events, cuts on the maximal energy photon (< 1.6 MeV) and on the probabilities are introduced ($P_{\text{int}} > 0.1$ and $P_{\text{ext}} < 0.1$) and the cut optimisation is performed again.

The sensitivity versus the signal efficiency is shown in Figure 6.31. A plateau is found between 40% and 80%, the middle value is chosen 60% which corresponds to a total efficiency of $(9.34 \pm 0.04) \times$

10^{-3} and to a background rejection of 96%. The value of the cuts used for this selection is presented in Table 6.21.

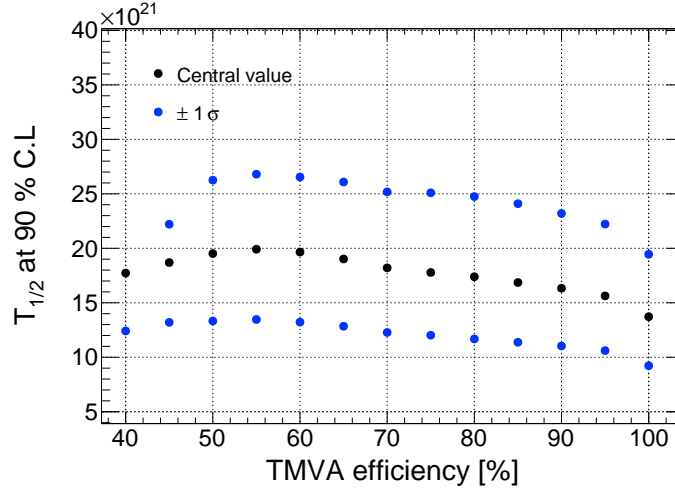


Figure 6.31: Expected sensitivity computed for different values of signal efficiency for the excited state (2^+) 0ν . The black points correspond to the central value.

As in 2ν decay mode, the cut on the photon energy is relevant to select the monoenergetic photon emitted during the decay. The cut on the electron energy is also very important in the 0ν decay mode since the energy sum of the two electrons is expected to be peaked at the $Q_{\beta\beta}$ value. This explains why the value of this cut is higher in the 0ν case than it is in the 2ν case. Additional cuts on the different probabilities are also introduced as well as on the angles.

Variables	Selected value
ΣE_e	[0.99 - 1.55] MeV
E_γ	[0.59 - 1.6] MeV
$P_{\text{int}}^{\text{max}}(e-\gamma)$	[0.01 - 1.00]
$P_{\text{ext}}^{\text{min}}(e \rightarrow \gamma)$	[0.000 - 0.009]
$P_{\text{ext}}^{\text{min}}(\gamma \rightarrow e)$	[0.000 - 0.007]
$\cos(\theta_{e1-\gamma})$	[-1.0 - 0.96]
$\cos(\theta_{e2-\gamma})$	[-1.0 - 0.95]

Table 6.21: Cuts applied on the preselection to optimise the sensitivity on the half-life of the excited state (2^+) 0ν . This selection keeps 60% of the signal and rejects 96% of the background.

After the full selection and optimisation process, 10 events are observed for 6.7 expected as shown in Figure 6.32. In this channel this overall excess is not identified as a clear background contribution and slightly deteriorate the sensitivity.

As no evidence of signal is observed, an exclusion limit on the signal normalisation is set at 90% C.L. Table 6.22 summarises the expected sensitivity and the observed limit on the signal normalisation as well as the half-life. Due to the excess, the limit set on the half-life is below the expected value and is found to be :

$$T_{1/2}^{0\nu}(^{116}\text{Cd}, 0 \rightarrow 2^+) > 7.7 \times 10^{21} \text{ y at 90\% C.L.}$$

	Expected			Obs.
	-1σ	0	$+1\sigma$	
N exc.	2.7	3.7	5.5	9.5
$T_{1/2} \times 10^{22}\text{y}$	2.65	1.97	1.32	0.77

Table 6.22: Expected and observed exclusion limit on the signal normalisation and on the half-life at 90% C.L for the excited state $(2^+) 0\nu$.

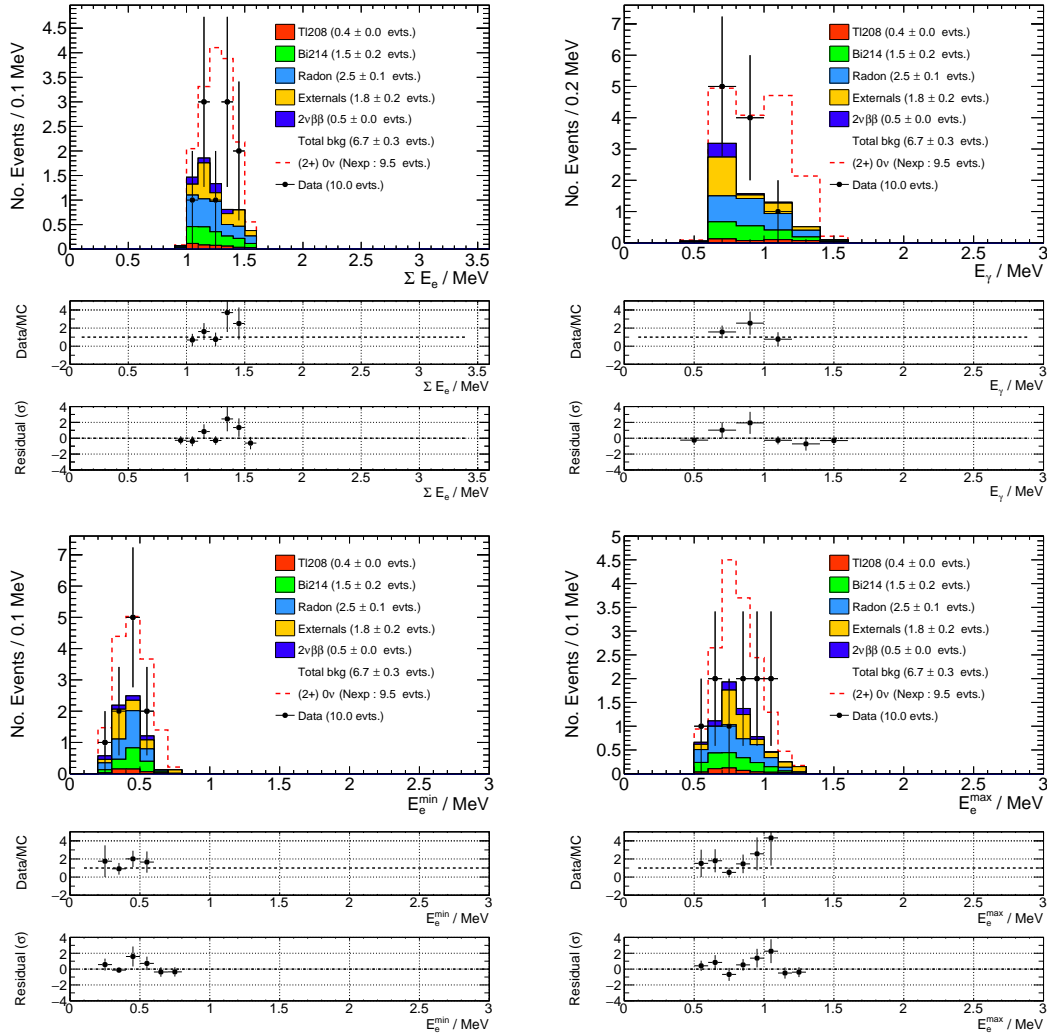


Figure 6.32: Distributions of the backgrounds, the signal normalised to observed limit and the data in the $2e1\gamma$ channel for the excited state $(2^+) 0\nu$. Top left : Total electron energy distribution. Top right : Photon energy. Bottom left : Minimal electron energy. Bottom right : Maximal electron energy. The minimal energy of each electron is 250 keV.

6.8 $\beta\beta$ decay of ^{116}Cd via the excited state (0^+) of ^{116}Sn

This section presents the results obtained in the search for the double beta decay of ^{116}Cd to ^{116}Sn via the excited state (0^+) . The strategy adopted for this investigation is similar to the strategy used for the search for decay via the excited state (2^+) . The only difference is that the optimisation of the cuts

is performed on the events of the $2e2\gamma$ channels. Furthermore, as the energy of the electrons is lower in the (0^+) excited state, the possible additional background at low energy discussed in Section 6.7.1 is expected to contribute more. In order to suppress this contribution the cut on the minimal electron energy ($E_e > 250$ keV) is directly applied. The results of both 2ν and 0ν decay modes are presented in Section 6.8.1 and 6.8.2 respectively.

6.8.1 2ν decay mode

After the optimisation of the selection, it has been found that the sensitivity is maximized for a signal efficiency of 60% from the preselection as shown in Figure 6.33. The cuts corresponding to this selection efficiency are given in Table 6.23. This selection rejects 92% of the background.

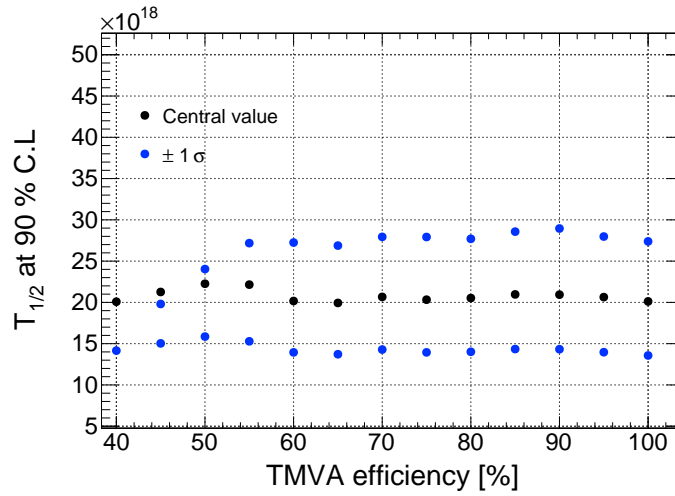


Figure 6.33: Expected sensitivity computed for different values of signal efficiency for the excited state (0^+) 2ν . The black points correspond to the central value.

Variables	Selected value
ΣE_e	[0.50 - 0.89]
E_γ^{\min}	[0.15 - 0.56]
E_γ^{\max}	[0.15 - 1.35]
$P_{\text{int}}^{\max} (e-\gamma)$	[0.13 - 1.00]
$P_{\text{ext}}^{\min} (e \rightarrow \gamma)$	[0.00 - 0.80]
$P_{\text{ext}}^{\min} (\gamma \rightarrow e)$	[0.00 - 0.09]
$\cos(\theta_{e1-\gamma})$	[-0.99 - 0.98]
$\cos(\theta_{e2-\gamma})$	[-1.00 - 0.98]

Table 6.23: Cuts applied on the preselection to optimise the sensitivity on the half-life of the excited state (0^+) 2ν . This selection keeps 60% of the signal and rejects 92% of the background.

The more important cuts concern the energy of the photons. Two monoenergetic photons are emitted at 463 keV and 1294 keV and are kept by the selection. The cut on the electron energy selects the signal spectrum with a $Q_{\beta\beta}$ value at 1048 keV. Additional cuts on the probabilities and angles are introduced to remove external background and events coming from $\beta\beta$ decay to the fundamental state.

	Expected			Obs.
	-1σ	0	$+1\sigma$	
N exc.	2.56	3.5	5.0	3.3
$T_{1/2} \times 10^{19}\text{y}$	2.7	2.0	1.4	2.1

Table 6.24: Expected and observed exclusion limit on the signal normalisation and on the half-life at 90% C.L for the excited state $(0^+) 2\nu$.

The final signal efficiency is then $(8.98 \pm 0.21) \times 10^{-6}$. These cuts are applied on the remaining events of the $2e2\gamma$ preselection. The final distributions are shown in Figures 6.34 and 6.35.

No evidence of signal is observed. An exclusion limit on the signal normalisation is set at 90% C.L. Table 6.24 summarises the expected sensitivity and the observed limit on the signal normalisation as well as the half-life. The observed limit is found to be :

$$T_{1/2}^{2\nu}(^{116}\text{Cd}, 0 \rightarrow 0^+) > 2.1 \times 10^{19} \text{ y at 90\% C.L.}$$

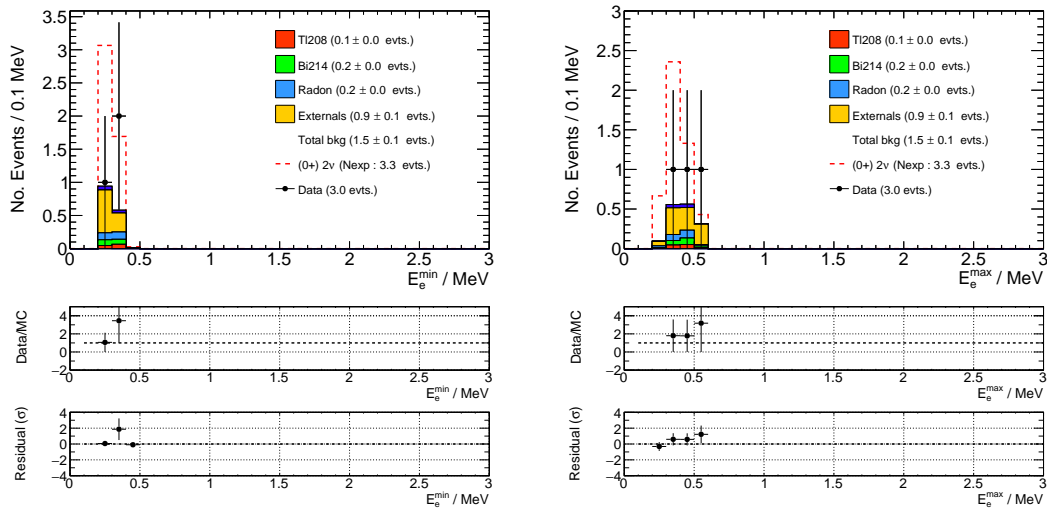


Figure 6.34: Distributions of the backgrounds, the signal normalised to observed limit and the data in the $2e2\gamma$ channel for the excited state $(0^+) 2\nu$. Left : Minimal electron energy distribution. Right : Maximal electron energy distribution. The minimal energy of each electron is 250 keV.

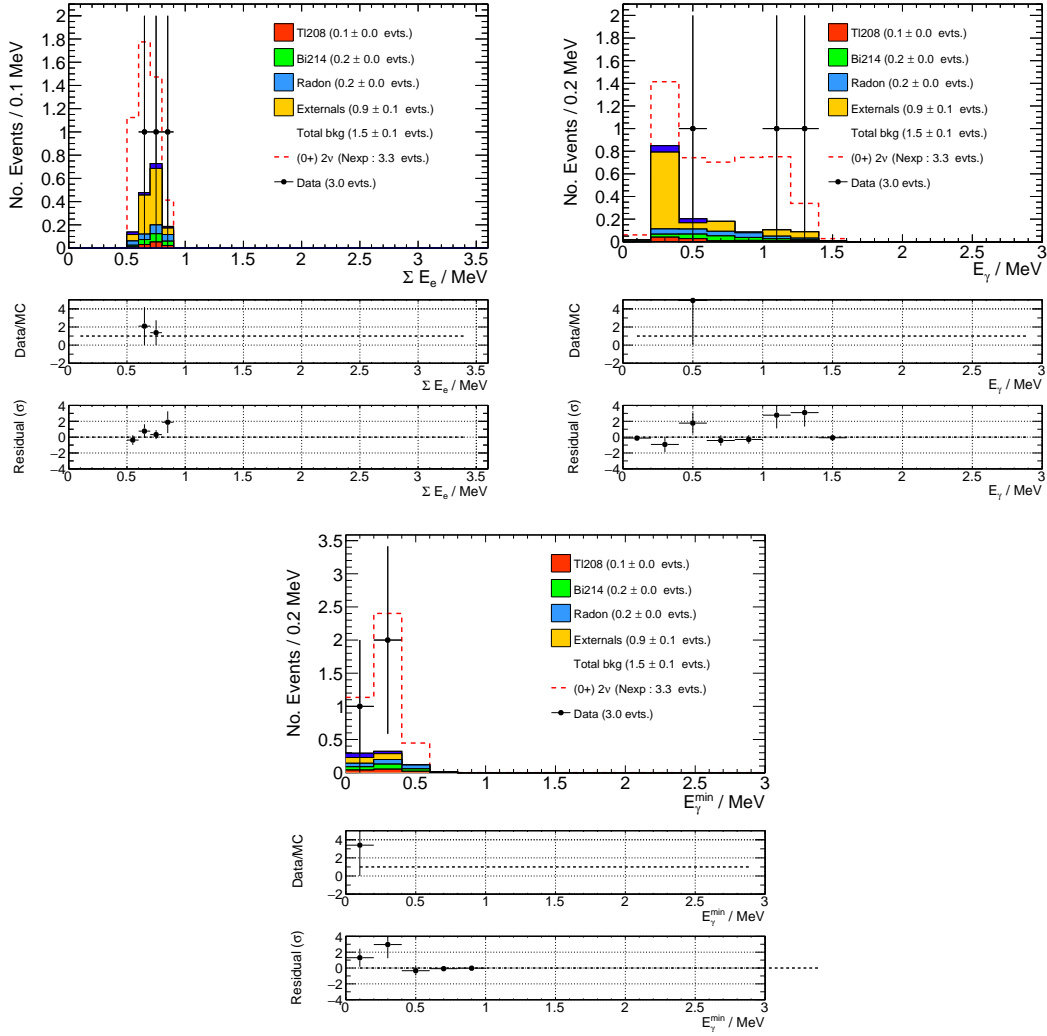


Figure 6.35: Distributions of the backgrounds, the signal normalised to observed limit and the data in the $2e2\gamma$ channel for the excited state $(0^+) 2\nu$. Top left : Total electron energy distribution. Top right : Maximal photon energy. Bottom : Minimal photon energy. The minimal energy of each electron is 250 keV.

6.8.2 0ν decay mode

The analysis of this excited state is performed exactly in the same way as the others. The optimisation of the cuts is realized with TMVA on the preselection of the $2e2\gamma$ channel. The sensitivity against the signal efficiency is shown in Figure 6.36. The value maximising the sensitivity is at 80% for a total efficiency of $(1.96 \pm 0.02) \times 10^{-3}$ and corresponds to a rejection of 89% of the background. The associated cuts are gathered in Table 6.25 and are applied on the events of the $2e2\gamma$ preselection.

No evidence of signal is observed and an exclusion limit is set at 90% C.L. The final distributions are shown in Figures 6.37. Table 6.26 summarises the expected sensitivity and the observed limit on the signal normalisation as well as the half-life. The observed limit is found to be :

$$T_{1/2}^{0\nu}(^{116}\text{Cd}, 0 \rightarrow 0^+) > 3.3 \times 10^{21} \text{ y at 90\% C.L.}$$

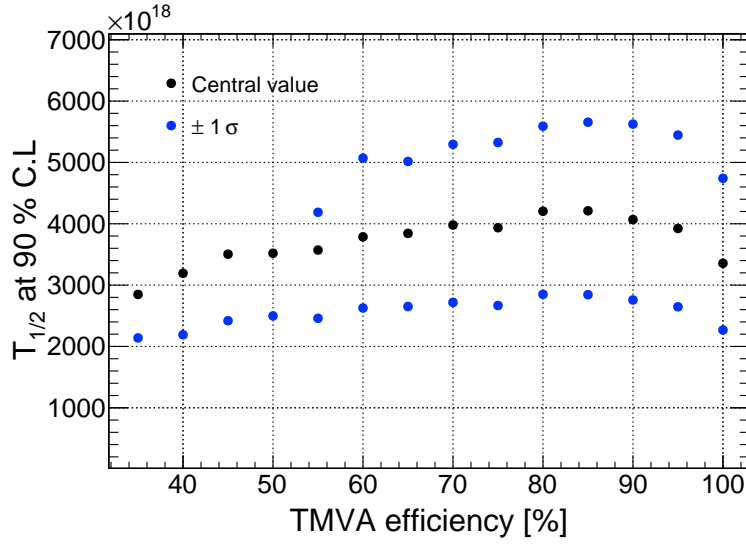


Figure 6.36: Expected sensitivity computed for different values of signal efficiency for the excited state $(0^+) 0\nu$. The black points correspond to the central value.

Variables	Selected value
ΣE_e	[0.53 - 0.97]
E_γ^{\min}	[0.15 - 0.45]
E_γ^{\max}	[0.15 - 1.34]
$P_{\text{int}}^{\max}(e-\gamma)$	[0.1 - 1]
$P_{\text{ext}}^{\min}(e \rightarrow \gamma)$	[0.00 - 0.10]
$P_{\text{ext}}^{\min}(\gamma \rightarrow e)$	[0.00 - 0.08]
$\cos(\theta_{e1-\gamma})$	[-1.00 - 0.95]
$\cos(\theta_{e2-\gamma})$	[-0.98 - 1.00]

Table 6.25: Cuts applied on the preselection to optimise the sensitivity on the half-life of the excited state $(0^+) 0\nu$. This selection keeps 80% of the signal and rejects 88% of the background.

	Expected			Obs.
	-1 σ	0	+1 σ	
N exc.	2.7	3.6	5.3	4.6
$T_{1/2} \times 10^{21}\text{y}$	5.6	4.2	2.9	3.3

Table 6.26: Expected and observed exclusion limit on the signal normalisation and on the half-life at 90% C.L for the excited state $(0^+) 2\nu$.

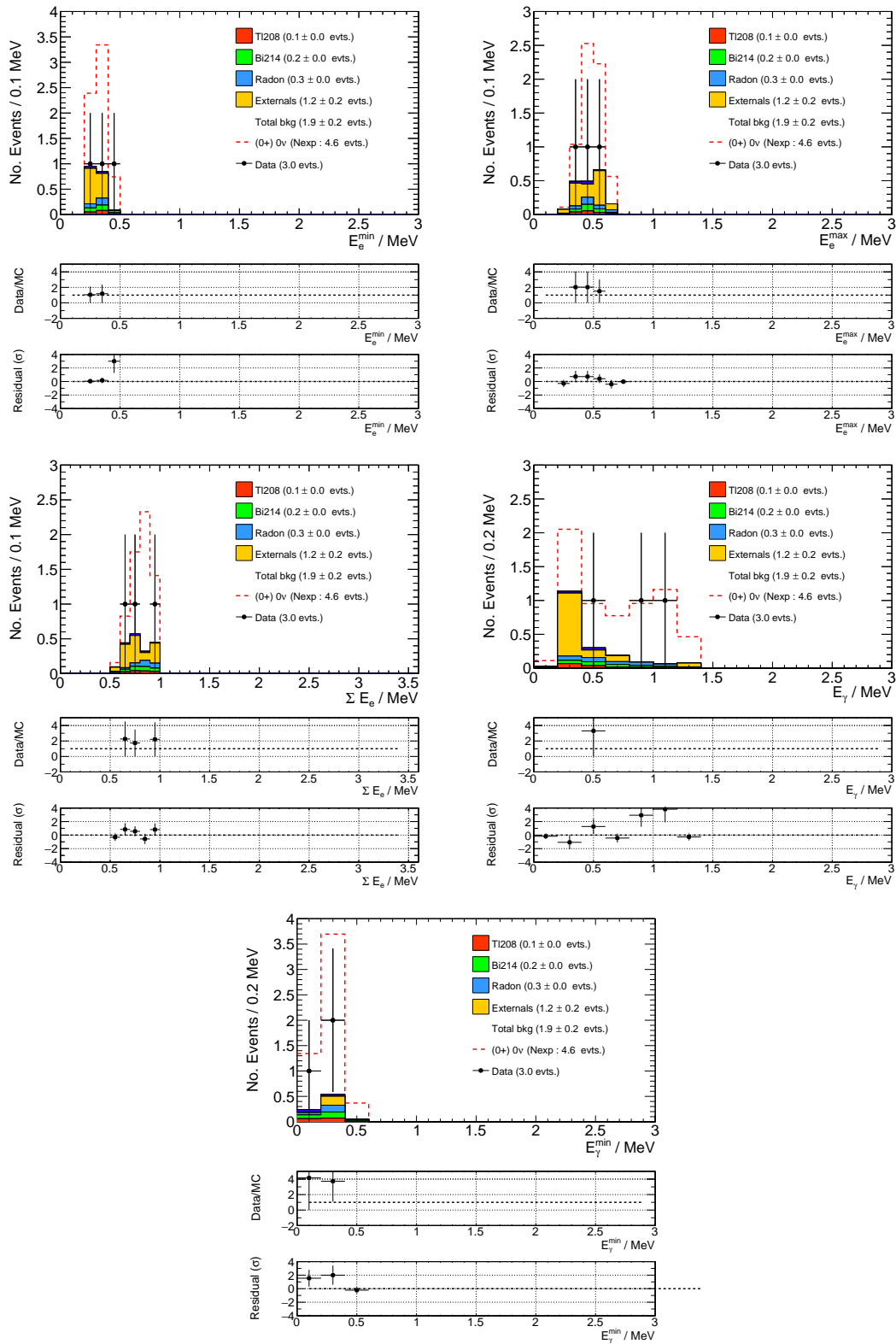


Figure 6.37: Distributions of the backgrounds, the signal normalised to observed limit and the data in the $2e2\gamma$ channel for the excited state $(0^+) 0\nu$. Top left : Minimal electron energy. Top right : Maximal electron energy. Middle left : Total electron energy distribution. Middle right : Maximal photon energy. Bottom : Minimal photon energy. The minimal energy of each electron is 250 keV.

6.9 Summary

The results obtained in this work are compared with the recent results obtained in 2016 by the Aurora experiment [109]. The Aurora experiment investigates double beta decay of ^{116}Cd with the help of 1.162 kg cadmium tungstate crystal scintillators enriched in ^{116}Cd to 82% at LNGS. The Aurora results obtained after 1.37 y are summarised in Table 6.27. The energy resolution is 5 % at 2.6 MeV (FWHM) and the 2e signal efficiency at 98 % which is excellent. The background counting rate of the detector in the energy interval (2.7 - 2.9) MeV has been estimated to be 0.1 cts/yr/kg/keV.

Decay mode	$T_{1/2}$ at 90% C.L.
$(2^+) 2\nu$	$> 9.0 \times 10^{20}$
$(2^+) 0\nu$	$> 6.2 \times 10^{22}$
$(0^+) 2\nu$	$> 1.0 \times 10^{21}$
$(0^+) 0\nu$	$> 6.3 \times 10^{22}$

Table 6.27: Half-life limits given at the 90% C.L. on the $\beta\beta$ decay processes in ^{116}Cd via the excited state of ^{116}Sn from the Aurora experiment. These results have been obtained with CdWO_4 crystal scintillators [109].

The results obtained in this work with the NEMO-3 data are summarised in Table 6.28. Unfortunately, despite a higher exposure, these results obtained in this work are not competitive with the new results from Aurora. This is mainly due to the very low detection efficiency of the NEMO-3 detector compared to the Aurora experiment.

Decay mode	ϵ	$N_{\text{exc.}}^{\text{obs.}}$	$T_{1/2}$ at 90% C.L.
$(2^+) 2\nu$	3.84×10^{-4}	7.1	$> 4.2 \times 10^{20}$
$(2^+) 0\nu$	9.34×10^{-3}	9.5	$> 7.7 \times 10^{21}$
$(0^+) 2\nu$	8.98×10^{-6}	3.3	$> 2.1 \times 10^{19}$
$(0^+) 0\nu$	1.96×10^{-3}	4.6	$> 3.3 \times 10^{21}$

Table 6.28: Efficiency, number of excluded events and half-life limits set on the decays of ^{116}Cd via the 2 main excited states of ^{116}Sn in 2ν and 0ν decay modes.

Conclusion

The search for $\beta\beta$ decays is a very active research topic in neutrino physics. The observation of the $2\nu\beta\beta$ decay to the ground state or the excited states and the measurement of the high half-lives provide useful information on the complex nuclear structure. Moreover the observation of the hypothetical $0\nu\beta\beta$ decay could prove the Majorana nature of the neutrino and also demonstrate that the lepton number is not conserved.

Located at LSM, the NEMO-3 detector investigated $\beta\beta$ decays among 7 different isotopes during 7 years. Its unique technique referred to as tracker-calorimeter allows to search for $\beta\beta$ decays with an excellent background rejection.

In this thesis, the NEMO-3 data of the cadmium sector have been analysed to perform the original searches of $2\nu\beta\beta$ and $0\nu\beta\beta$ decays of ^{116}Cd via the excited state of ^{116}Sn . With 5.25 effective years of data taking with 410 g of ^{116}Cd no signal has been found and the first limits obtained with the NEMO-3 data for these processes have been set to :

$$\begin{aligned} T_{1/2}^{2\nu}(^{116}\text{Cd}, 0 \rightarrow 2^+) &> 4.2 \times 10^{20} \text{ y at 90\% C.L.} & T_{1/2}^{0\nu}(^{116}\text{Cd}, 0 \rightarrow 2^+) &> 7.7 \times 10^{21} \text{ y at 90\% C.L.} \\ T_{1/2}^{2\nu}(^{116}\text{Cd}, 0 \rightarrow 0^+) &> 2.1 \times 10^{19} \text{ y at 90\% C.L.} & T_{1/2}^{0\nu}(^{116}\text{Cd}, 0 \rightarrow 0^+) &> 3.3 \times 10^{21} \text{ y at 90\% C.L.} \end{aligned}$$

Today, the NEMO-3 detector has been disassembled and the construction of the first module of its successor, SuperNEMO, is ongoing at LSM. This first module, called demonstrator, is based on the same NEMO-3 technique and one of its main goals is to demonstrate that the search for $0\nu\beta\beta$ decays can be background-free during 2.5 y of data taking with 7 kg of ^{82}Se . To reach this goal, major efforts have been realised to improve the energy resolution of the calorimeter and the radiopurity of the detector and its source foil. In that context, a new design of source foil, using more radiopure material have been proposed. The optimisation of the SuperNEMO performances with respect to the design of its source foil has been realised in this thesis work. These studies allow to validate that the new design has slightly better performance than the previous one and half of the demonstrator source foils has been made with this new design. Their installation into the detector is planned during autumn 2017.

Always in order to reduce the level of background, the collaboration made important efforts to limit the background induced by the radon such as an improvement of the detector tightness or the installation of an anti-radon system. Despite all these efforts, some residual contaminations of radon are expected inside the tracker. A work performed in this thesis consisted of the implementation and the developement of an algorithm dedicated to search for alpha particles. By exploiting this algorithm, the $1e1\alpha$ events

are efficiently reconstructed allowing a direct measurement of the radon contamination. The results obtained in this thesis have shown that the radon contamination coming from the tracker can be measured daily with a 8% of precision (in the hypothesis the gas is not flushed).

Depending on the results that will be obtained with the demonstrator module, other SuperNEMO like modules could be built in the future. In the hypothesis where 100 kg of ^{82}Se are distributed into 20 different modules, a sensitivity of 10^{26} y could be reached after 5 years of data taking corresponding to an effective neutrino mass of $\langle m_{\beta\beta} \rangle < (0.04 - 0.1)$ eV probing the inverted mass ordering region.

Bibliography

- [1] J. Chadwick., "Intensitätsverteilung im magnetischen Spektrum der β -Strahlen von Radium B + C," *Phys. Ges.*, vol. 16, p. 383, 1914.
- [2] W. Pauli., "Letter to the physical society of tubingen," 1930.
- [3] C. L. Cowan, F. Reines, F. B. Harrison, H. W. Kruse, and A. D. McGuire, "Detection of the Free Neutrino: a Confirmation," *Science*, vol. 124, no. 3212, pp. 103–104, 1956.
- [4] E. Fermi, "Versuch einer Theorie der β -Strahlen. I," *Zeitschrift für Physik*, vol. 88, no. 3, pp. 161–177, 1934.
- [5] S. L. Glashow, "Partial Symmetries of Weak Interactions," *Nucl. Phys.*, vol. 22, pp. 579–588, 1961.
- [6] A. Salam, "Renormalizability of gauge theories," *Phys. Rev.*, vol. 127, pp. 331–334, 1962.
- [7] S. Weinberg, "A model of leptons," *Phys. Rev. Lett.*, vol. 19, pp. 1264–1266, 1967.
- [8] C. D. Anderson and S. H. Neddermeyer, "Cloud chamber observations of cosmic rays at 4300 meters elevation and near sea-level," *Phys. Rev.*, vol. 50, pp. 263–271, 1936.
- [9] G. Danby, J.-M. Gaillard, K. Goulianos, L. M. Lederman, N. Mistry, M. Schwartz, and J. Steinberger, "Observation of high-energy neutrino reactions and the existence of two kinds of neutrinos," *Phys. Rev. Lett.*, vol. 9, pp. 36–44, 1962.
- [10] M. L. Perl *et al.*, "Evidence for anomalous lepton production in $e^+ - e^-$ annihilation," *Phys. Rev. Lett.*, vol. 35, pp. 1489–1492, 1975.
- [11] K. Kodama *et al.*, "Observation of tau neutrino interactions," *Phys. Lett.*, vol. B504, pp. 218–224, 2001.
- [12] S. Schael *et al.*, "Precision electroweak measurements on the Z resonance," *Phys. Rept.*, vol. 427, pp. 257–454, 2006.
- [13] M. Goldhaber, L. Grodzins, and W. Sunyar, "Helicity of Neutrinos," *Phys. Rev.*, vol. 109, p. 1015–1017, 1958.
- [14] R. Davis, D. S. Harmer, and K. C. Hoffman, "Search for neutrinos from the sun," *Phys. Rev. Lett.*, vol. 20, pp. 1205–1209, 1968.

- [15] J. N. Abdurashitov *et al.*, "Measurement of the solar neutrino capture rate with gallium metal. III: Results for the 2002–2007 data-taking period," *Phys. Rev.*, vol. C80, p. 015807, 2009.
- [16] W. Hampel *et al.*, "GALLEX solar neutrino observations: Results for GALLEX III.," *Phys. Lett.*, vol. B388, pp. 384–396, 1996.
- [17] A. Acker, J. G. Learned, S. Pakvasa, and T. J. Weiler, "A Single solution to the atmospheric and solar neutrino anomalies," *Phys. Lett.*, vol. B298, pp. 149–153, 1993.
- [18] W.-M. Yao and al., "Review of Particle Physics," *Journal of Physics G*, vol. 33, pp. 1+, 2006.
- [19] K. A. Olive *et al.*, "Review of Particle Physics," *Chin. Phys.*, vol. C38, p. 090001, 2014.
- [20] B. Pontecorvo, "Mesonium and anti-mesonium," *Sov. Phys. JETP*, vol. 6, p. 429, 1957. [*Zh. Eksp. Teor. Fiz.*33,549(1957)].
- [21] Z. Maki, M. Nakagawa, and S. Sakata, "Remarks on the unified model of elementary particles," *Progress of Theoretical Physics*, vol. 28, no. 5, pp. 870–880, 1962.
- [22] J. N. Bahcall, A. M. Serenelli, and S. Basu, "New solar opacities, abundances, helioseismology, and neutrino fluxes," *Astrophys. J.*, vol. 621, pp. L85–L88, 2005.
- [23] K. S. Hirata *et al.*, "Observation of ^8B solar neutrinos in the kamiokande-ii detector," *Phys. Rev. Lett.*, vol. 63, pp. 16–19, 1989.
- [24] S. P. Mikheev and A. Yu. Smirnov, "Resonance Amplification of Oscillations in Matter and Spectroscopy of Solar Neutrinos," *Sov. J. Nucl. Phys.*, vol. 42, pp. 913–917, 1985. [*Yad. Fiz.*42,1441(1985)].
- [25] C. Patrignani and P. D. Group, "Review of Particle Physics," *Chinese Physics C*, vol. 40, no. 10, p. 100001, 2016 and 2017 update.
- [26] Kajita Takaaki, "Atmospheric neutrinos and discovery of neutrino oscillations," *Proceedings of the Japan Academy. Series B, Physical and Biological Sciences*, vol. 86, pp. 303–321, Jan. 2010.
- [27] T. J. Haines *et al.*, "Calculation of Atmospheric Neutrino Induced Backgrounds in a Nucleon Decay Search," *Phys. Rev. Lett.*, vol. 57, pp. 1986–1989, 1986.
- [28] Y. Ashie *et al.*, "Evidence for an oscillatory signature in atmospheric neutrino oscillation," *Phys. Rev. Lett.*, vol. 93, p. 101801, 2004.
- [29] S. H. Ahn *et al.*, "Detection of accelerator produced neutrinos at a distance of 250-km," *Phys. Lett.*, vol. B511, pp. 178–184, 2001.
- [30] D. G. Michael *et al.*, "Observation of muon neutrino disappearance with the MINOS detectors and the NuMI neutrino beam," *Phys. Rev. Lett.*, vol. 97, p. 191801, 2006.
- [31] N. Agafonova *et al.*, "Observation of a first ν_τ candidate in the OPERA experiment in the CNGS beam," *Phys. Lett.*, vol. B691, pp. 138–145, 2010.
- [32] S. Abe *et al.*, "Precision Measurement of Neutrino Oscillation Parameters with KamLAND," *Phys. Rev. Lett.*, vol. 100, p. 221803, 2008.
- [33] F. P. An *et al.*, "New measurement of antineutrino oscillation with the full detector configuration at daya bay," *Phys. Rev. Lett.*, vol. 115, p. 111802, 2015.

-
- [34] N. Agafonova *et al.*, “New results on $\nu_\mu \rightarrow \nu_\tau$ appearance with the OPERA experiment in the CNGS beam,” *JHEP*, vol. 11, p. 036, 2013. [Erratum: JHEP04,014(2014)].
- [35] T. Nakaya and R. K. Plunkett, “Neutrino Oscillations with the MINOS, MINOS+, T2K, and NOvA Experiments,” *New J. Phys.*, vol. 18, no. 1, p. 015009, 2016.
- [36] R. Acciarri *et al.*, “Long-Baseline Neutrino Facility (LBNF) and Deep Underground Neutrino Experiment (DUNE),” 2016.
- [37] K. Abe *et al.*, “A Long Baseline Neutrino Oscillation Experiment Using J-PARC Neutrino Beam and Hyper-Kamiokande,” 2014.
- [38] F. An *et al.*, “Neutrino Physics with JUNO,” *J. Phys.*, vol. G43, no. 3, p. 030401, 2016.
- [39] M. G. Aartsen *et al.*, “PINGU: A Vision for Neutrino and Particle Physics at the South Pole,” *J. Phys.*, vol. G44, no. 5, p. 054006, 2017.
- [40] A. Kouchner, “KM3NeT - ORCA: measuring the neutrino mass ordering in the Mediterranean,” *Journal of Physics: Conference Series*, vol. 718, no. 6, p. 062030, 2016.
- [41] T. A. Mueller *et al.*, “Improved Predictions of Reactor Antineutrino Spectra,” *Phys. Rev.*, vol. C83, p. 054615, 2011.
- [42] P. Huber, “On the determination of anti-neutrino spectra from nuclear reactors,” *Phys. Rev.*, vol. C84, p. 024617, 2011. [Erratum: Phys. Rev.C85,029901(2012)].
- [43] G. Mention, “The reactor antineutrino anomaly,” *Journal of Physics: Conference Series*, vol. 408, no. 1, p. 012025, 2013.
- [44] G. Mention, M. Fechner, T. Lasserre, T. A. Mueller, D. Lhuillier, M. Cribier, and A. Letourneau, “The Reactor Antineutrino Anomaly,” *Phys. Rev.*, vol. D83, p. 073006, 2011.
- [45] S. Gariazzo, C. Giunti, M. Laveder, Y. F. Li, and E. M. Zavanin, “Light sterile neutrinos,” *J. Phys.*, vol. G43, p. 033001, 2016.
- [46] A. Aguilar-Arevalo *et al.*, “Evidence for neutrino oscillations from the observation of anti-neutrino(electron) appearance in a anti-neutrino(muon) beam,” *Phys. Rev.*, vol. D64, p. 112007, 2001.
- [47] V. H elaine, “Sterile neutrino search at the ILL nuclear reactor: the STEREO experiment,” in *Prospects in Neutrino Physics (NuPhys2015) London, UK, December 16-18, 2015*, 2016.
- [48] N. Ryder, “First results of the deployment of a SoLid detector module at the SCK-CEN BR2 reactor,” *PoS*, vol. EPS-HEP2015, p. 071, 2015.
- [49] G. Bellini *et al.*, “SOX: Short distance neutrino Oscillations with BoreXino,” *JHEP*, vol. 08, p. 038, 2013.
- [50] B. Pontecorvo, “Neutrino Experiments and the Problem of Conservation of Leptonic Charge,” *Sov. Phys. JETP*, vol. 26, pp. 984–988, 1968. [Zh. Eksp. Teor. Fiz.53,1717(1967)].
- [51] E. Majorana, “Teoria simmetrica dell’elettrone e del positrone,” *Il Nuovo Cimento (1924-1942)*, vol. 14, p. 171, Sep 2008.
-

- [52] T. D. Lee and C. N. Yang, "Parity nonconservation and a two-component theory of the neutrino," *Phys. Rev.*, vol. 105, pp. 1671–1675, Mar 1957.
- [53] J. Schechter and J. W. F. Valle, "Neutrino masses in $su(2) \otimes u(1)$ theories," *Phys. Rev. D*, vol. 22, pp. 2227–2235, 1980.
- [54] J. Schechter and J. W. F. Valle, "Neutrino Decay and Spontaneous Violation of Lepton Number," *Phys. Rev.*, vol. D25, p. 774, 1982.
- [55] C. Kraus *et al.*, "Final results from phase II of the Mainz neutrino mass search in tritium beta decay," *Eur. Phys. J.*, vol. C40, pp. 447–468, 2005.
- [56] V. M. Lobashev *et al.*, "Neutrino mass and anomaly in the tritium beta spectrum. Results of the 'Troitsk nu mass' experiment," *Nucl. Phys. Proc. Suppl.*, vol. 77, pp. 327–332, 1999.
- [57] A. Osipowicz *et al.*, "KATRIN: A Next generation tritium beta decay experiment with sub-eV sensitivity for the electron neutrino mass. Letter of intent," 2001.
- [58] K. Assamagan *et al.*, "Upper limit of the muon-neutrino mass and charged-pion mass from momentum analysis of a surface muon beam," *Phys. Rev. D*, vol. 53, pp. 6065–6077, 1996.
- [59] R. Barate *et al.*, "An Upper limit on the tau-neutrino mass from three-prong and five-prong tau decays," *Eur. Phys. J.*, vol. C2, pp. 395–406, 1998.
- [60] B. W. Lee and S. Weinberg, "Cosmological Lower Bound on Heavy Neutrino Masses," *Phys. Rev. Lett.*, vol. 39, pp. 165–168, 1977.
- [61] J. Lesgourgues and S. Pastor, "Massive neutrinos and cosmology," *Phys. Rept.*, vol. 429, pp. 307–379, 2006.
- [62] P. A. R. Ade *et al.*, "Planck 2013 results. XVI. Cosmological parameters," *Astron. Astrophys.*, vol. 571, p. A16, 2014.
- [63] C. F. V. Weizsacker, "Zur Theorie der Kernmassen," *Z. Phys.*, vol. 96, pp. 431–458, 1935.
- [64] M. Goeppert-Mayer, "Double beta-disintegration," *Phys. Rev.*, vol. 48, pp. 512–516, 1935.
- [65] G. Racah, "On the symmetry of particle and antiparticle," *Nuovo Cim.*, vol. 14, pp. 322–328, 1937.
- [66] M. Hirsch, H. V. Klapdor-Kleingrothaus, and S. G. Kovalenko, "Supersymmetry and neutrinoless double beta decay," *Phys. Rev.*, vol. D53, pp. 1329–1348, 1996.
- [67] M. C. Gonzalez-Garcia, M. Maltoni, and T. Schwetz, "Updated fit to three neutrino mixing: status of leptonic CP violation," *Journal of High Energy Physics*, vol. 2014, no. 11, p. 52, 2014.
- [68] P. Guzowski *et al.*, "Combined limit on the neutrino mass from neutrinoless double- β decay and constraints on sterile majorana neutrinos," *Phys. Rev. D*, vol. 92, p. 012002, 2015.
- [69] C. S. Wu, E. Ambler, R. W. Hayward, D. D. Hoppes, and R. P. Hudson, "Experimental test of parity conservation in beta decay," *Phys. Rev.*, vol. 105, pp. 1413–1415, 1957.
- [70] M. Doi, T. Kotani, H. Nishiura, and E. Takasugi, "Double beta decay," *Progress of Theoretical Physics*, vol. 69, no. 2, p. 602, 1983.

-
- [71] R. Arnold and al, "Probing new physics models of neutrinoless double beta decay with SuperNEMO," *The European Physical Journal C*, vol. 70, no. 4, pp. 927–943, 2010.
- [72] P. R. M. Gell-Mann and R. Slansky., "Complex spinors and unified theories," *Supergravity*, p. 315, 1979.
- [73] Y. Chikashige, R. N. Mohapatra, and R. D. Peccei, "Spontaneously broken lepton number and cosmological constraints on the neutrino mass spectrum," *Phys. Rev. Lett.*, vol. 45, pp. 1926–1929, 1980.
- [74] C.S. Aulakh and R.N. Mohapatra, "The neutrino as the supersymmetric partner of the majoron," *Physics Letters B*, vol. 119, no. 1, pp. 136–140, 1982.
- [75] G.B. Gelmini and M. Roncadelli, "Left-handed neutrino mass scale and spontaneously broken lepton number," *Physics Letters B*, vol. 99, no. 5, pp. 411–415, 1981.
- [76] P. Bamert, C.P. Burgess, and R.N. Mohapatra, "Multi-majoron modes for neutrinoless double-beta decay," *Nuclear Physics B*, vol. 449, no. 1, pp. 25–48, 1995.
- [77] S. P. Martin, "A Supersymmetry primer," 1997. [Adv. Ser. Direct. High Energy Phys.18,1(1998)].
- [78] N. Fatemi-Ghomi, *Measurement of the double beta decay half-life of Nd-150 and search for neutrinoless decay modes with NEMO-3 detector*. PhD thesis, Manchester U., 2009.
- [79] J. Menéndez, A. Poves, E. Caurier, and F. Nowacki, "Disassembling the nuclear matrix elements of the neutrinoless $\beta\beta$ decay," *Nuclear Physics A*, vol. 818, no. 3, pp. 139–151, 2009.
- [80] E. Caurier, F. Nowacki, and A. Poves, "Nuclear-structure aspects of the neutrinoless $\beta\beta$ -decays," *The European Physical Journal A*, vol. 36, no. 2, pp. 195–200, 2008.
- [81] E. Caurier, J. Menéndez, F. Nowacki, and A. Poves, "Influence of pairing on the nuclear matrix elements of the neutrinoless $\beta\beta$ decays," *Phys. Rev. Lett.*, vol. 100, p. 052503, 2008.
- [82] R. A. Sen'kov and M. Horoi, "Accurate shell-model nuclear matrix elements for neutrinoless double- β decay," *Phys. Rev. C*, vol. 90, p. 051301, 2014.
- [83] D.-L. Fang, A. Faessler, V. Rodin, and F. Simkovic, "Neutrinoless double beta decay of deformed nuclei within QRPA with realistic interaction," *Phys. Rev.*, vol. C83, p. 034320, 2011.
- [84] J. Terasaki, "Many-body correlations of quasiparticle random-phase approximation in nuclear matrix elements of neutrinoless double- β decay," *Phys. Rev.*, vol. C91, no. 3, p. 034318, 2015.
- [85] M. T. Mustonen and J. Engel, "Large-scale calculations of the double- β decay of ^{76}Ge , ^{130}Te , ^{136}Xe , and ^{150}Nd in the deformed self-consistent Skyrme quasiparticle random-phase approximation," *Phys. Rev.*, vol. C87, no. 6, p. 064302, 2013.
- [86] J. Barea, J. Kotila, and F. Iachello, "Nuclear matrix elements for double- β decay," *Phys. Rev. C*, vol. 87, p. 014315, 2013.
- [87] N. N. Bogolyubov, V. V. Tolmachev, and D. V. Shirkov, "A New method in the theory of superconductivity," *Fortsch. Phys.*, vol. 6, pp. 605–682, 1958.
- [88] P. K. Rath, R. Chandra, K. Chaturvedi, P. Lohani, P. K. Raina, and J. G. Hirsch, "Neutrinoless $\beta\beta$ decay transition matrix elements within mechanisms involving light majorana neutrinos, classical majorons, and sterile neutrinos," *Phys. Rev. C*, vol. 88, p. 064322, 2013.
-

- [89] J.F. Berger, M. Girod, and D. Gogny, "Microscopic analysis of collective dynamics in low energy fission," *Nuclear Physics A*, vol. 428, pp. 23–36, 1984.
- [90] T. R. Rodriguez and G. Martinez-Pinedo, "Energy density functional study of nuclear matrix elements for neutrinoless $\beta\beta$ decay," *Phys. Rev. Lett.*, vol. 105, p. 252503, 2010.
- [91] L. S. Song, J. M. Yao, P. Ring, and J. Meng, "Relativistic description of nuclear matrix elements in neutrinoless double- β decay," *Phys. Rev. C*, vol. 90, p. 054309, 2014.
- [92] A. Smolnikov and P. Grabmayr, "Conversion of experimental half-life to effective electron neutrino mass in $0\nu\beta\beta$ decay," *Phys. Rev. C*, vol. 81, p. 028502, 2010.
- [93] B. Kay *et al.*, "Valence neutron properties relevant to the neutrinoless double- β decay of ^{130}Te ," *Phys. Rev. C*, vol. 87, p. 011302, 2013.
- [94] J. D. Vergados, H. Ejiri, and F. Simkovic, "Theory of Neutrinoless Double Beta Decay," *Rept. Prog. Phys.*, vol. 75, p. 106301, 2012.
- [95] F. T. Avignone, S. R. Elliott, and J. Engel, "Double beta decay, majorana neutrinos, and neutrino mass," *Rev. Mod. Phys.*, vol. 80, pp. 481–516, 2008.
- [96] A. Garfagnini, "Neutrinoless Double Beta Decay Experiments," in *12th Conference on Flavor Physics and CP Violation (FPCP 2014) Marseille, France, May 26-30, 2014*.
- [97] H. V. Klapdor-Kleingrothaus *et al.*, "Latest results from the Heidelberg-Moscow double beta decay experiment," *Eur. Phys. J.*, vol. A12, pp. 147–154, 2001.
- [98] H.V Klapdor-Kleingrothaus, I.V Krivosheina, A. Dietz, and O. Chkvorets, "Search for neutrinoless double beta decay with enriched ^{76}Ge in Gran Sasso 1990–2003," *Physics Letters B*, vol. 586, no. 3–4, pp. 198–212, 2004.
- [99] C. E. Aalseth *et al.*, "Comment on evidence for neutrinoless double beta decay," *Mod. Phys. Lett.*, vol. A17, pp. 1475–1478, 2002.
- [100] C. E. Aalseth *et al.*, "Recent results of the IGEX ^{76}Ge double-beta decay experiment," *Physics of Atomic Nuclei*, vol. 63, no. 7, pp. 1225–1228, 2000.
- [101] M. Agostini *et al.*, "Results on neutrinoless double- β decay of ^{76}Ge from phase i of the gerda experiment," *Phys. Rev. Lett.*, vol. 111, no. 12, p. 122503, 2013.
- [102] M. Agostini *et al.*, "Background free search for neutrinoless double beta decay with GERDA Phase II," 2017. [Nature544,47(2017)].
- [103] N. Abgrall *et al.*, "The Majorana Demonstrator Neutrinoless Double-Beta Decay Experiment," *Adv. High Energy Phys.*, vol. 2014, p. 365432, 2014.
- [104] N. Abgrall *et al.*, "The Large Enriched Germanium Experiment for Neutrinoless Double Beta Decay (LEGEND)," in *Matrix Elements for the Double-beta-decay EXperiments (MEDEX'17) Prague, Czech Republic, May 29-June 2, 2017*, 2017.
- [105] B. H. Marik, "Semiconductor-based experiments for neutrinoless double beta decay search," *Nuclear Physics B - Proceedings Supplements*, vol. 229, pp. 141–145, 2012.

-
- [106] J. Ebert *et al.*, "Results of a search for neutrinoless double- β decay using the COBRA demonstrator," *Phys. Rev.*, vol. C94, no. 2, p. 024603, 2016.
- [107] S. Umehara *et al.*, "Neutrino-less double- β decay of ^{48}Ca studied by $\text{CaF}_2(\text{eu})$ scintillators," *Phys. Rev. C*, vol. 78, p. 058501, 2008.
- [108] A. S. Umehara *et al.*, "Search for neutrino-less double beta decay with candles," *AIP Conference Proceedings*, vol. 1441, pp. 448–450, 2012.
- [109] F. A. Danevich *et al.*, "Search for double beta decay of ^{116}Cd with enriched $^{116}\text{CdWO}_4$ crystal scintillators (Aurora experiment)," *J. Phys. Conf. Ser.*, vol. 718, no. 6, p. 062009, 2016.
- [110] A. Gando *et al.*, "Search for Majorana Neutrinos near the Inverted Mass Hierarchy Region with KamLAND-Zen," *Phys. Rev. Lett.*, vol. 117, no. 8, p. 082503, 2016. [Addendum: *Phys. Rev. Lett.* 117, no. 10, 109903 (2016)].
- [111] S. Junpei, "KamLAND-Zen: Status and Future," *Nuclear Physics B - Proceedings Supplements*, vol. 237, pp. 28–30, 2013.
- [112] S. Andringa *et al.*, "Current Status and Future Prospects of the SNO+ Experiment," *Adv. High Energy Phys.*, vol. 2016, p. 6194250, 2016.
- [113] E. Andreotti *et al.*, " ^{130}Te Neutrinoless Double-Beta Decay with CUORICINO," *Astropart. Phys.*, vol. 34, pp. 822–831, 2011.
- [114] Cuore Collaboration, "Status of the CUORE experiment," *Journal of Physics: Conference Series*, vol. 447, no. 1, p. 012066, 2013.
- [115] Cuore Collaboration, "LUCIFER: Neutrinoless Double Beta decay search with scintillating bolometers," *Journal of Physics: Conference Series*, vol. 335, no. 1, p. 012047, 2011.
- [116] E. Armengaud *et al.*, "Development of ^{100}Mo -containing scintillating bolometers for a high-sensitivity neutrinoless double-beta decay search," 2017.
- [117] "Search for neutrinoless double-beta decay in ^{136}Xe with EXO-200," *Phys. Rev. Lett.*, vol. 109, p. 032505, 2012.
- [118] J. J. Gomez-Cadenas *et al.*, "Present status and future perspectives of the NEXT experiment," *Adv. High Energy Phys.*, vol. 2014, p. 907067, 2014.
- [119] A. Gando *et al.*, "Limit on Neutrinoless $\beta\beta$ Decay of ^{136}Xe from the First Phase of KamLAND-Zen and Comparison with the Positive Claim in ^{76}Ge ," *Phys. Rev. Lett.*, vol. 110, no. 6, p. 062502, 2013.
- [120] R. Arnold *et al.*, "Measurement of the double-beta decay half-life and search for the neutrinoless double-beta decay of ^{48}Ca with the NEMO-3 detector," *Phys. Rev.*, vol. D93, no. 11, p. 112008, 2016.
- [121] M. Agostini *et al.*, "Results on $\beta\beta$ decay with emission of two neutrinos or Majorons in ^{76}Ge from GERDA Phase I," *The European Physical Journal C*, vol. 75, no. 9, p. 416, 2015.
- [122] J. Mott, *Search for double beta decay of ^{82}Se with the NEMO-3 detector and development of apparatus for low-level radon measurements for the SuperNEMO experiment*. PhD thesis, U. Coll. London, 2013-09-25.
-

- [123] J. Argyriades *et al.*, "Measurement of the two neutrino double beta decay half-life of Zr-96 with the NEMO-3 detector," *Nucl. Phys.*, vol. A847, pp. 168–179, 2010.
- [124] R. Arnold *et al.*, "First results of the search for neutrinoless double-beta decay with the nemo-3 detector," *Phys. Rev. Lett.*, vol. 95, p. 182302, 2005.
- [125] R. Arnold *et al.*, "Measurement of the Double Beta Decay Half-life of ^{130}Te with the NEMO-3 Detector," *Phys. Rev. Lett.*, vol. 107, p. 062504, 2011.
- [126] J. B. Albert *et al.*, "Improved measurement of the $2\nu\beta\beta$ half-life of ^{136}Xe with the EXO-200 detector," *Phys. Rev.*, vol. C89, no. 1, p. 015502, 2014.
- [127] R. Arnold *et al.*, "Measurement of the $2\nu\beta\beta$ decay half-life of ^{150}Nd and a search for $0\nu\beta\beta$ decay processes with the full exposure from the NEMO-3 detector," *Phys. Rev.*, vol. D94, no. 7, p. 072003, 2016.
- [128] R. Arnold *et al.*, "Results of the search for neutrinoless double- β decay in ^{100}Mo with the NEMO-3 experiment," *Phys. Rev.*, vol. D92, no. 7, p. 072011, 2015.
- [129] K. Alfonso *et al.*, "Search for neutrinoless double-beta decay of ^{130}Te with cuore-0," *Phys. Rev. Lett.*, vol. 115, p. 102502, 2015.
- [130] J. R. Wilson, "Double Beta Decay Measurement with COBRA," *Nuclear Physics B - Proceedings Supplements*, vol. 221, pp. 313–316, 2011.
- [131] F. Boehm and P. Vogel, *Physics of Massive Neutrinos*. 1992.
- [132] C. Berger *et al.*, "Experimental study of muon bundles observed in the fréjus detector," *Phys. Rev. D*, vol. 40, pp. 2163–2171, 1989.
- [133] D. Mei and A. Hime, "Muon-induced background study for underground laboratories," *Phys. Rev.*, vol. D73, p. 053004, 2006.
- [134] D. Dassie *et al.*, "Double beta decay prototype detector with multiwire drift tubes in the Geiger mode," *Nucl. Instrum. Meth.*, vol. A309, pp. 465–475, 1991.
- [135] R. Arnold *et al.*, "Performances of NEMO-2, a Prototype Tracking Detector for Double Beta Decay Measurements," *Nucl. Instrum. Meth.*, vol. A354, 1995.
- [136] R. Arnold *et al.*, "Technical design and performance of the NEMO 3 detector," *Nucl. Instrum. Meth.*, vol. A536, pp. 79–122, 2005.
- [137] R. Arnold *et al.*, "Observation of two neutrino double beta decay of Cd-116 with the tracking detector NEMO-2," *JETP Lett.*, vol. 61, pp. 170–174, 1995. [Pisma Zh. Eksp. Teor. Fiz.61,168(1995)].
- [138] S. R. Elliott, A. A. Hahn, M. K. Moe, M. A. Nelson, and M. A. Vient, "Double beta decay of Se-82," *Phys. Rev.*, vol. C46, pp. 1535–1537, 1992.
- [139] J. Tuli, "Nuclear Data Sheets for $A = 60$," *Nuclear Data Sheets*, vol. A309, pp. 347–481, 2003.
- [140] J. Argyriades *et al.*, "Measurement of the background in the NEMO 3 double beta decay experiment," *Nucl. Instrum. Meth.*, vol. A606, pp. 449–465, 2009.

-
- [141] R. Arnold *et al.*, "Measurement of the $2\nu\beta\beta$ Decay Half-Life and Search for the $0\nu\beta\beta$ Decay of ^{116}Cd with the NEMO-3 Detector," *Phys. Rev.*, vol. D95, no. 1, p. 012007, 2017.
- [142] D. Waters, "Latest Results from NEMO-3 & Status of the SuperNEMO Experiment," *J. Phys. Conf. Ser.*, vol. 888, no. 1, p. 012033, 2017.
- [143] R. Arnold *et al.*, "Search for neutrinoless quadruple- β decay of ^{150}Nd with the NEMO-3 detector," 2017.
- [144] J.J. Gomez-Cadenas *et al.*, "Physics case of supernemo with 82se source : Docdb 358-v2," 2008.
- [145] A. S. Barabash *et al.*, "The BiPo-3 detector for the measurement of ultra low natural radioactivities of thin materials," 2017.
- [146] M. Cascella, "The SuperNEMO Tracking Detector," in *Proceedings, Topical Research Meeting on Prospects in Neutrino Physics (NuPhys2014): London, UK, December 15-17, 2014*, 2015.
- [147] A. S. Barabash *et al.*, "Calorimeter development for the SuperNEMO double beta decay experiment," *Nucl. Instrum. Meth.*, vol. A868, pp. 98–108, 2017.
- [148] G. J. Feldman and R. D. Cousins, "A Unified approach to the classical statistical analysis of small signals," *Phys. Rev.*, vol. D57, pp. 3873–3889, 1998.
- [149] N. A., "Radon reduction and radon monitoring in the nemo experiment," *2nd Topical workshop in Low Radioactivity*, Feb. 2007.
- [150] M. S. Basunia, "Nuclear Data Sheets for $A = 210$," *Nuclear Data Sheets*, vol. 121, pp. 561–694, 2014.
- [151] H. Gomez, "Results from bipo measurements of source foil components. : Docdb3244," May 2014.
- [152] P. Loaiza, "Bipo measurement of the purified se-nat+pva pads : Docdb3731-v2," June 2015.
- [153] X. R. Liu, "Update of the latest c-section measurement results. : Docdb3772," June 2015.
- [154] Cern GEANT4, "Geant 4, <http://geant4.cern.ch>."
- [155] I. Nasteva *et al.*, "90-cell prototype performance : Docdb 803," June. 2009.
- [156] A. S. Barabash, "Precise half-life values for two-neutrino double- β decay," *Phys. Rev. C*, vol. 81, p. 035501, Mar 2010.
- [157] N. Kudomi *et al.*, "Double beta decays and elegant ν and ν_i at oto cosmo observatory," *Nuclear Physics A*, vol. 629, no. 1, pp. 527 – 530, 1998.
- [158] F. Danevich *et al.*, "Search for 2β decay of cadmium and tungsten isotopes: Final results of the solotvina experiment," *Phys. Rev. C*, vol. 68, p. 035501, 2003.
- [159] R. Arnold *et al.*, "Double-beta decay of Cd-116," *Z. Phys.*, vol. C72, pp. 239–247, 1996.
- [160] O. A. Ponkratenko, V. I. Tretyak, and Yu. G. Zdesenko, "The Event generator DECAY4 for simulation of double beta processes and decay of radioactive nuclei," *Phys. Atom. Nucl.*, vol. 63, pp. 1282–1287, 2000. [*Yad. Fiz.*63,1355(2000)].
-

- [161] R. Brun, F. Bruyant, M. Maire, A. C. McPherson, and P. Zancarini, *GEANT 3: user's guide Geant 3.10, Geant 3.11; rev. version*. Geneva: CERN, 1987.
- [162] S. Blot *et al.*, "Gamma identification and reconstruction in hereward, internal note : Docdb3151," 2014.
- [163] R. Brun and F. Rademakers, "ROOT: An object oriented data analysis framework," *Nucl. Instrum. Meth.*, vol. A389, pp. 81–86, 1997.
- [164] P. Speckmayer, A. Höcker, J. Stelzer, and H. Voss, "The toolkit for multivariate data analysis, TMVA 4," *Journal of Physics: Conference Series*, vol. 219, no. 3, p. 032057, 2010.
- [165] W. Fisher, "Systematics and limit calculations," 2006.
- [166] P. van Laarhoven and E. Aarts, "Simulated annealing: theory and applications.." *Mathematics and its Applications*, 37. Dordrecht etc.: D. Reidel Publishing Company, a member of the Kluwer Academic Publishers Group. XI, 186 p.; Dfl. 120.00; 49.00; 39.00 (1987)., 1987.
- [167] S. Blot, "Position paper for $^{150}\text{Nd} \rightarrow ^{150}\text{Sm}$ ground state analysis : Docdb3716," 2014.

Résumé

Les détecteurs NEMO-3 et SuperNEMO ont été conçus pour la recherche de décroissance double bêta sans émission de neutrinos. Ces détecteurs fournissent une approche unique dans la recherche des événements double bêta en combinant des mesures à la fois de trajectoires, de temps de vol et d'énergie. De plus, grâce à la séparation de la source double bêta du reste du système de détection, les détecteurs NEMO ont la possibilité d'étudier plusieurs isotopes double bêta avec une forte réjection du bruit de fond.

Cette thèse présente plusieurs études réalisées dans le cadre de l'optimisation et la préparation du détecteur SuperNEMO, successeur de NEMO-3. La première concerne l'optimisation des performances du détecteur en fonction de la configuration mécanique de ses feuilles sources. La conclusion de cette étude est que les deux configurations considérées sont équivalentes. La seconde étude s'intéresse à l'un des principaux bruits de fond que constitue le radon dans la recherche des désintégrations double bêta. Cette étude a été concrétisée par le développement et l'implémentation d'un algorithme permettant l'identification et la mesure des événements provenant de ce bruit de fond. Le deuxième volet de cette thèse rapporte l'analyse des données de NEMO-3 pour rechercher les décroissances double bêta avec et sans émission de neutrino du ^{116}Cd vers les états excités du ^{116}Sn . Ces décroissances n'ont jamais été observées à ce jour, et les limites obtenus sur les états excités (2^+) et (0^+) sont les premières utilisant le détecteur NEMO-3.

Mots clés

Neutrino, Double bêta, SuperNEMO, Feuille source, Radon, État excité, Cadmium-116

Abstract

The NEMO-3 and SuperNEMO detectors have been designed to search for neutrinoless double beta decays. These detectors provide a unique approach combining a calorimetric and a tracking measurement of double beta events emitted by a separated isotopic source. This approach allows to search for neutrinoless double beta decays among several isotopes with good background rejection.

This thesis presents many studies performed for the optimisation and the preparation of the SuperNEMO detector, successor of NEMO-3. The first study concerns the optimisation of the detector performances with respect to the design of the source foil. The conclusion of this study is that the two configurations considered are equivalent. The second study focuses on the radon which constitutes one of the main background to the search for double beta decays. In this study an algorithm has been developed and implemented to search for the alpha particle allowing the identification and the measurement of the radon events. The thesis is completed by an analysis of the NEMO-3 data to search for the double beta decay of ^{116}Cd via the excited state of ^{116}Sn . These decays have never been observed up to date and the limits set on the excited states (2^+) and (0^+) are the first using the NEMO-3 detector.

Key Words

Neutrino, Double beta decay, SuperNEMO, Source Foil, Radon, Excited State, Cadmium-116